High Resolution Anatomical and Functional Imaging

by

Rosa María Sánchez Panchuelo

Thesis submitted to
The University of Nottingham
for the degree of
Doctor of Philosophy

August 2009

Contents

Abstract

The signal-to-noise ratio available in Magnetic Resonance Imaging (MRI) is determined by the static magnetic field strength, causing a continued drive toward higher fields to enable faster image acquisition at finer spatial resolution. The work in this thesis is primarily concerned with the development of sequences for Ultra High Field Magnetic Resonance Imaging (7T) which allow the acquisition of images with high spatial resolution for study of the structure and function of the brain.

The methods developed here for high spatial resolution structural imaging allow the identification of regions of the cortex which exhibit layers of high myelin concentration within the cortical strip. This permits the investigation of the correspondence of functional regions in the visual cortex to their underlying structure *in vivo*.

A robust methodology for high resolution functional mapping over a restricted field of view is presented and the results of fMRI studies demonstrating 1 mm isotropic resolution in the primary somatosensory cortex S1 using this methodology are shown. BOLD responses to vibrotactile digit stimulation were investigated using a travelling wave paradigm to measure the topographic representation of the digits in S1 and an event related paradigm for characterization of the haemodynamic delay.

A spin-echo EPI acquisition has been optimized and tested to compare the BOLD response in GE and SE echo planar images by employing visual and motor tasks. The specificity of the BOLD responses of SE and GE data was found to be similar using a travelling wave paradigm.

Acknowledgements

I would like to take this opportunity to express my gratitude to all those who have helped me during my PhD study. First and foremost I would like thank my excellent supervisors Richard Bowtell and Sue Francis, for giving me the opportunity to work in this project and for their support and guidance throughout this time. A big thank you to Denis Schluppeck for teaching me about fMRI and a lot of other things.

I would like to thank the following people from the Sir Peter Mansfield Magnetic Resonance Centre at the University of Nottingham; Michael Poole for implementing the image-based shimming method in the Philips scanner, Olivier Mougin for his phase unwrapping skills, Clemente Cobos Sánchez and Roman Wesołowski for helping me to get started and the rest of my friends, especially the people and frequent visitors of the downstairs office, who created the perfect atmosphere to work in.

I would like to thank my good friends Olivier, Daniele, Caroline and Arianna who have coloured my PhD time with their exceptional culinary skills, *Bang* evenings and Tiramisu competitions.

Quisiera expresar mi mas profundo agradecimiento a mis padres y a mis hermanas por apoyarme en mi educación y animarme en todo momento.

Chapter 1

Introduction

Since the introduction of magnetic resonance imaging (MRI) in the 70's, this technique has developed rapidly into a standard clinical method. The excellent soft tissue contrast and high spatial resolution of MRI has made it a technique of choice for human neuroimaging. Using functional magnetic resonance imaging (fMRI) we can track changes in the local blood flow that occur in response to increased neuronal activity, allowing researchers to investigate not only the structure, but also the function of the human brain. MRI is limited in its spatial resolution by the available signal to noise ratio (SNR), which is determined principally by the strength of the magnetic field. Field strengths used in both research and clinical scanners have continued to increase over the past 30 years. There is growing interest in ultra high field systems, with 7T human imaging systems now installed at several sites around the world. This increase in field strength is accompanied by many technical challenges arising from interactions between the electromagnetic fields used by the MRI scanner and the object being scanned. The aim of this work is to exploit the the improved SNR and increased functional contrast available at 7 T to improve the spatial resolution of anatomical images and BOLD fMRI studies.

1.1 Overview of this thesis

The second chapter of this thesis describes the fundamental principles of nuclear magnetic resonance and magnetic resonance imaging. An overview of off-resonance effects and their implications for imaging is also given.

In Chapter 3 an overview of a typical magnetic resonance imaging system is given. A description of the main hardware components and their function is given.

Chapter 4 begins with an introduction to magnetic resonance imaging at ultra high field (7 T), outlining methodology used in the following chapters to acquire high resolution anatomical images and high resolution functional maps.

In Chapter 5, the relationship of functionally defined visual areas to the underlying brain structure is investigated. High resolution structural images reveal myelination patterns within the cortical grey matter. Retinotopic mapping is performed to identify visual borders between the primary visual cortex (V1) and V2, and a moving versus stationary localizer is used to identify motion selective area V5.

Chapter 6 investigates the GE-EPI neuronal responses to vibrotactile stimuli in order to study the topographic map of the digit representations in the primary somatosensory cortex at 1mm isotropic resolution. Using a travelling wave paradigm, the specificity of the GE BOLD response is improved. An event related paradigm was also used for characterization of the haemodynamic delay.

Chapter 7 presents the optimization of a sequence for spin echo (SE)-based fMRI. A study was performed to compare SE- and GE-BOLD activation maps for a visual and a motor task. The specificity of the BOLD responses of SE and GE data was found to be similar using a travelling wave paradigm.

Chapter 8 summarises the findings arising from the work described in this thesis and highlights some areas for further development.

Chapter 2

Nuclear Magnetic Resonance and Magnetic Resonance Imaging

This chapter outlines the physical principles pertinent to the work described in this thesis. The basic theories on which MRI are based have been extensively described in numerous texts, for example [1, 2]. Firstly, in Section 2.1, a description of the nuclear magnetic resonance phenomenon is given. The origin of nuclear magnetization is briefly discussed and the behaviour of a sample under an applied magnetic field described. This is followed in Section 2.2 by an introduction to how an MR image is formed. Signal localization is introduced and the concept of k-space is described. Some relevant imaging pulse sequences used in the experimental work in this thesis are then introduced. Finally, in Section 2.3, off-resonance effects and their implications for imaging are discussed.

2.1 NMR basic principles

Nuclear magnetic resonance (NMR) is the study of the resonant behavior of nuclei under the influence of a magnetic field. This section outlines the basic principles of NMR.

2.1.1 Introduction

The NMR phenomenon was discovered independently by Bloch [3] and Purcell [4] in 1946, for which they were jointly awarded the Nobel Prize for Physics in 1952. Nuclei with spin angular momentum (spin) can interact with a magnetic field. The resonant angular frequency or Larmor frequency, ω_L, of spins in an applied magnetic field of strength B_0 is:

$$\omega_L = \gamma \cdot B_0 \qquad (2.1)$$

where γ is the gyromagnetic ratio, which is a unique constant for each nuclear isotope possessing a spin. The gyromagnetic ratio may have either positive or negative sign. Most nuclei have positive γ, but a few nuclei such as ^{29}Si and ^{15}N have negative values of γ. NMR is primarily focused on elements of high gyromagnetic ratio, such as hydrogen, (^{1}H), carbon (^{13}C), nitrogen (^{14}N), sodium (^{23}Na) and phosphorus (^{31}P). The numerical values of the gyromagnetic ratio and natural abundance of these nuclei are given in Table 2.1. Hydrogen is generally used for imaging due to its high natural abundance and large concentration in biological samples. Since all experiments in this thesis are based on ^{1}H NMR, this is the only nucleus that will be discussed in detail.

nucleus	spin	γ (MHz/T)	relative sensitivity (to ^{1}H)	natural abundance (%)
^{1}H	1/2	42.58	1	99.8
^{13}C	1/2	10.71	1.59×10^{-2}	1.11
^{14}N	1	3.08	1.01×10^{-3}	99.6
^{23}Na	3/2	11.26	9.25×10^{-2}	100
^{31}P	1/2	17.24	6.63×10^{-2}	100

Table 2.1: Properties of nuclei used for magnetic resonance.

2.1.2 Nuclei, spin, energy levels

Hydrogen atoms consist of an electron orbiting a nucleus consisting of a single proton. All nuclei with unpaired nucleons (protons and neutrons) have
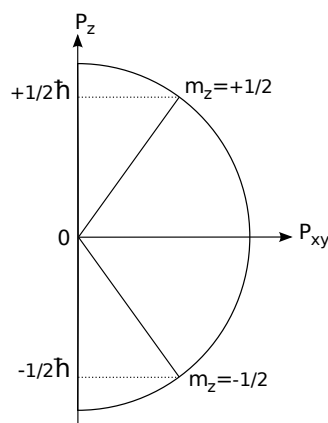
Figure 2.1: Angular momentum.

a net nuclear angular momentum. The angular momentum, $\mathbf{p}$, is quantised and is related to the spin quantum number, $\mathbf{I}$ by

$$\mathbf{p} = \hbar\sqrt{\mathbf{I}(\mathbf{I}+1)} \qquad (2.2)$$

where $\hbar = 1.054 \times 10^{-34} Js$ is the reduced Planck constant. The measurable values of the z-component of the angular momentum, p_z, are given by

$$p_z = \hbar m_z \qquad (2.3)$$

where m_z may take values $-I, -I+1, ..., I$. Since a proton has a spin quantum number of $\frac{1}{2}$, m_z can take values of $\frac{1}{2}$ or $-\frac{1}{2}$. Hydrogen nuclei also possess a positive charge. These rotating spins therefore generate magnetic dipole moments, $\boldsymbol{\mu} = \gamma\mathbf{I}$, whose z-component is

$$\mu_z = \gamma p_z = \gamma\hbar m_z \qquad (2.4)$$

with $\gamma = 2.675 \times 10^8 s^{-1}T^{-1}$ for ^1H. In a magnetic field, $\mathbf{B_0}$, the ^1H spin will tend to align 'parallel' or 'anti-parallel' with the direction of $\mathbf{B_0}$. This means that there are two possible spin states of the hydrogen nucleus, the 'up' or
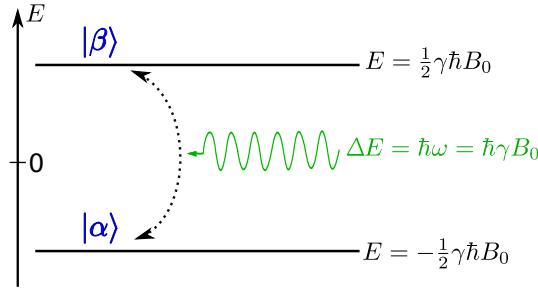
Figure 2.2: Energy level diagram of the hydrogen nucleus (spin $\frac{1}{2}$) in a magnetic field B_0. Transitions can be induced between spin states by irradiating with photons of energy E equal to the energy level splitting.

$|\alpha>$ state and the 'down' or $|\beta>$ state. The energy of a spin is given by

$$E = -\mu_z B_0 = -\gamma \hbar m_z B_0 \tag{2.5}$$

thus the energy difference between the two spin states is

$$\Delta E = \gamma \hbar B_0. \tag{2.6}$$

Quantisation of the nuclear angular momentum, $\mathbf{I}$, dictates that the magnetic moment vector, μ, cannot align exactly parallel to $\mathbf{B_0}$, rather it precesses about $\mathbf{B_0}$ at the Larmor frequency. Applying a radiofrequency wave made up with photons with energy equal to the energy level splitting, ΔE, of the two states, (Fig. 2.2), introduces transitions between the up and down spin states. For ^1H nuclei in a 7 Tesla (T) magnetic field, the Larmor frequency is 300 MHz, which is in the radio-frequency (RF) range of the electromagnetic spectrum. Only radiowaves of the correct frequency will drive transitions between states, hence the term 'resonance' in NMR.

2.1.3   Spins in a magnetic field

For nuclei with $\gamma > 0$ ($\gamma < 0$), the magnetic moment of a nucleus points in the same (opposite) direction as the spin polarization, i.e. the direction of the spin angular momentum. Consider hydrogen nuclei in a sample of water;
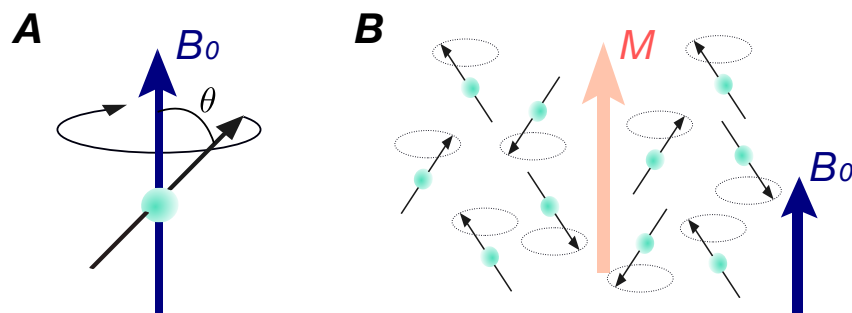
Figure 2.3: (A) Single spin and (B) ensemble of magnetic moments precessing in a magnetic field, B_0. At thermal equilibrium there are more spins in the lower energy state, resulting in a macroscopic net magnetisation, M, aligned with B_0.

in the absence of a magnetic field, all possible magnetic moment directions are equally represented and the total magnetic moment of the sample is close to zero. If a magnetic field is instantaneously applied, the magnetic moment of each spin precesses on a cone around the magnetic field axis at the Larmor frequency, keeping a constant angle between the spin magnetic moment and the field. This precession is shown in Fig. 2.3.A. For nuclei with positive γ, such as the proton, the precession is in the clockwise direction. The angle of the cone, θ, depends only on the spin state. Magnetic moments in an entire sample are slightly more likely to be aligned with the field rather than opposed to the field, causing the sample to acquire a small net magnetic moment along the field direction, i.e., a longitudinal bulk magnetisation, **M** (see Fig. 2.3.B.). This net or bulk magnetisation is the magnetisation that is available for the NMR experiment.

2.1.4 Boltzman statistics

The distribution of spins between the two energy states is described by Boltzmann statistics. Boltzmann statistics give the ratio of the number of nuclei in the high $|\beta>$, N_{down}, and low $|\alpha>$, N_{up}, energy states as a function

of the energy difference, ΔE, and the temperature, T, of the system,

$$\frac{N^{down}}{N^{up}} = e^{-\frac{\Delta E}{kT}} \qquad (2.7)$$

where $k = 1.38 \cdot 10^{-23} JK^{-1}$ is the Boltzmann constant. For hydrogen nuclei at 300 K and a 1 T magnetic field, the population difference is approximately 6 ppm; meaning there are 1,000,006 nuclei in the low energy level for every 1,000,000 in the high energy level state. This small net magnetization is one of the reasons for the intrinsically low signal to noise ratio of NMR experiments. The bulk magnetization increases with increasing B_0-field and decreasing temperature. Decreasing the temperature of the sample is not a viable option in clinical imaging. Therefore increasing the magnetic field strength is the best option for achieving a higher NMR signal amplitude. This is one of the reasons for the current interest in high field magnet systems, together with increased sensitivity to the BOLD effect (see Chapter 5) and the increased sensitivity to the chemical environment in spectroscopy.

2.1.5   Interaction with B_1 field

As stated in Section 2.1.2, applying a radio-frequency (RF) pulse at the Larmor frequency, ω_L, will induce transitions between spin states. In NMR, the spin experiences two magnetic fields; a static magnetic field, $\mathbf{B_0}$ and an oscillating RF field $\mathbf{B_1(t)}$. This oscillating field is many orders of magnitude smaller than the static field, but gives rise to a change in the spin state due to it being resonant with the precession of the spins. $\mathbf{B_1(t)}$ causes the phases of the precessing spins to align, the bulk magnetization vector, $\mathbf{M}$, then circulates around the z-axis in a process called nutation, as illustrated in Fig. 2.4.A. Since the $\mathbf{B_1}$ field and $\mathbf{M}$ both rotate about the z-direction at ω_L, a rotating frame of reference is introduced. By adopting a frame which rotates 'with the field', the $\mathbf{B_1(t)}$ field appears static. This is done mathematically by a change of the coordinate system from the laboratory frame (x, y, z) to a frame of reference rotating at the Larmor Frequency, known as the 'rotating frame',

denoted by co-ordinates (x', y', z'). The z-axis along which the static magnetic field is applied is the same in both reference frames. The transverse $\mathbf{B_1(t)}$ field, oscillating at angular frequency ω_L, can be described in the laboratory frame by two vectors; one rotating clockwise at a frequency ω_L, $B_1^+(t)$, and one rotating anticlockwise at a frequency $-\omega_L$, $B_1^-(t)$. In the rotating frame, the B_1^+ component rotating clockwise appears stationary, and the B_1^- component rotating anticlockwise, appears at frequency $-2\omega_L$ which is far from the resonant frequency and therefore can be ignored.

In the rotating frame (Fig. 2.4.B) the magnetisation vector $\mathbf{M}$ appears to tip from its equilibrium position, aligned with the z-axis, down towards the y'-axis. The angle, α, through which the magnetisation is tipped, the flip angle, is

$$\alpha = \int_0^\tau \gamma B_1(t) dt \tag{2.8}$$

where τ is the length of time that the RF pulse is applied. For a rectangular pulse envelope this reduces to

$$\alpha = \gamma B_1 \tau \tag{2.9}$$

A 90° pulse is an RF pulse which tips $\mathbf{M}$ entirely into the xy' plane. The net magnetization moment in this plane, perpendicular to the magnetic field, is called the transverse magnetization.

From this point on, the motion of magnetization vectors will be discussed using the rotating frame.

2.1.6   Relaxation

The term 'relaxation' is widely used in physical sciences to indicate the re-establishment of thermal equilibrium after some perturbation is applied. At equilibrium the system has a random phase and a spin population conforming to Boltzmann statistics. The macroscopic nuclear magnetization has an equilibrium value M_0 along the direction of the external field, i.e. the z-axis.
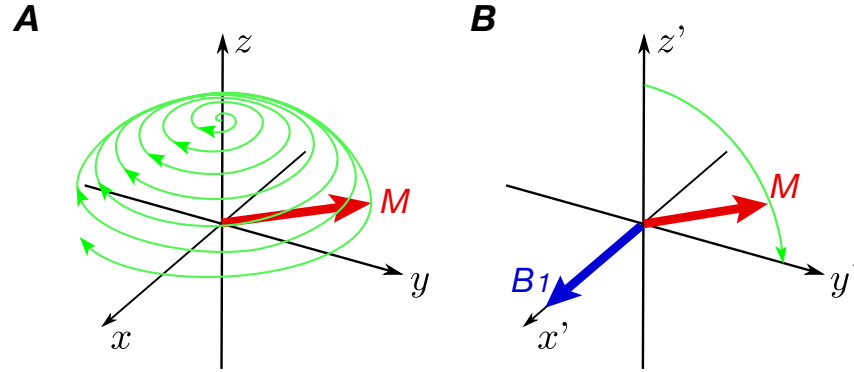
Figure 2.4: The evolution of the bulk magnetisation vector **M** under the application of an RF pulse at the resonant frequency in (A) the laboratory and (B) the rotating frame.

The application of an RF pulse can lead to transitions of the spins resulting in a non-equilibrium number of parallel and anti-parallel spins and a net phase. The spin population will then return to equilibrium by two processes. Spin-lattice relaxation returns the longitudinal magnetization to equilibrium and the spin-spin relaxation process acts to randomise the phase. The evolution of the magnetisation can be described by the Bloch equation:

$$\frac{d\mathbf{M}}{dt} = \gamma(\mathbf{M} \times \mathbf{B}) - \frac{(M_z - M_0)\mathbf{k}}{T_1} - \frac{M_x\mathbf{i} + M_y\mathbf{j}}{T_2} \qquad (2.10)$$

where T_1 is the spin-lattice relaxation time that governs the recovery of the longitudinal magnetisation, M_z, and T_2 is the spin-spin relaxation time that governs the decay of transverse magnetisation, M_{xy}.

The main mechanism for relaxation is dipole-dipole interaction. Spins precess at the Larmor frequency, however, the proximity of other spins and the molecular surroundings give rise to microscopic fluctuating magnetic fields which add to the applied macroscopic field, altering locally the Larmor frequency of each spin. These fluctuations in the dipole-dipole induced magnetic field induce transitions which contribute to the relaxation processes.

Longitudinal spin-lattice relaxation

The longitudinal or spin-lattice relaxation process equilibrates the spin population and thereby returns the longitudinal magnetization to its equilibrium value, M_0. This occurs as a result of the exchange of energy between the lattice and the spin system. Transitions are induced in the spin system by the fluctuations in the dipole-dipole induced magnetic field. Immediately after the RF pulse is switched off, at time=0, the magnetisation has a value $M_z(0)$, whose value will depend on the flip angle of the excitation pulse. The magnetization will then return to equilibrium in a manner described by

$$M_z(t) = M_0(1 - e^{-t/T_1}) + M_z(0)e^{-t/T_1} \qquad (2.11)$$

where t is the time after the RF pulse has been applied. A 90° RF pulse along the x axis will flip the entire magnetization vector M$_0$ into the xy plane, the system is then said to be excited or saturated. A saturation recovery is plot in Fig. 2.5.A (blue solid line); At time t=0 after the saturation pulse, the longitudinal magnetization takes a value of zero and then recovers to its initial value, M_0, with relaxation time, T_1. If a 180° or inversion pulse is used, the longitudinal magnetization is inverted and M_z begin to recover from $-M_0$ (red solid line). An inversion pulse reverses the equilibrium magnetization without inducing phase coherence, i.e., transverse magnetization. Inversion pulses are used to enhance contrast in MR images. In an inversion recovery sequence, the longitudinal magnetization is left to recover for a time TI after the inversion pulse. The available magnetization at this time, $M_0(1-2e^{-\frac{TI}{T_1}})$, is then flipped into the xy plane with a saturation pulse. With knowledge of the T_1 of tissues, the TI can be chosen to produce the desired contrast.

The T_1 of ^1H nuclei in water depends on the occurrence of fluctuations with frequency ω_L and $2\omega_L$ in the lattice and these vary with temperature and the chemical environment of the spins. Transitions with higher energy are necessary at higher fields and this is why T_1 values increase with increasing B_0 [5, 6, 7]. For example, in the study by Wright et al [6], T_1 values of white matter
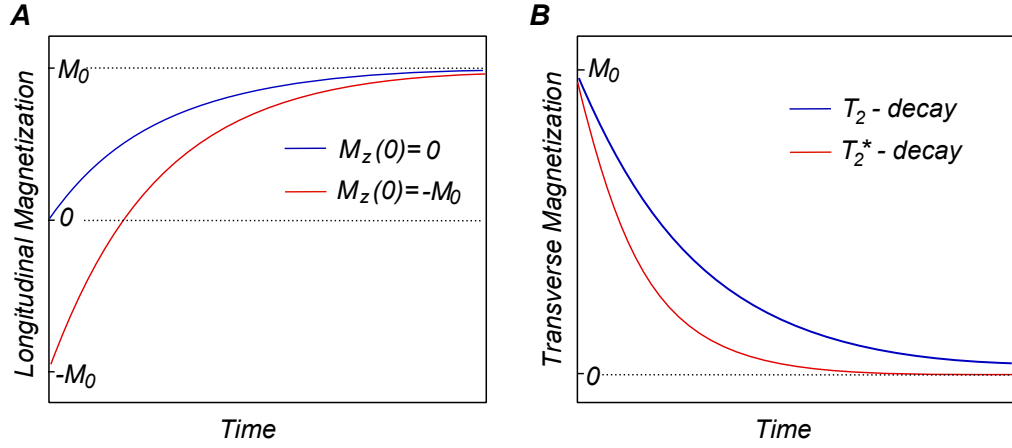
Figure 2.5: (A) Relaxation of the longitudinal magnetisation $M_z(t)$ for saturation (blue line) and inversion recovery (red line). (B) Relaxation of the transverse magnetisation $M_{xy}(t)$; $T_2^\star$ decay (red line) occurs at a faster rate than T_2 decay (blue line).

and grey matter were found to be 840/1600 ms at 3 T and 1130/1940 ms at 7 T. Nevertheless, Rooney et al [7] found that the T_1 value of the cerebrospinal fluid (CSF) did not change significantly with B_0, with its average value across magnetic field strengths of 0.2, 1, 1.5, 4, and 7 T being 4300±200 ms.

Transverse relaxation

The transverse magnetization created by an RF pulse will be dephased after the RF pulse is turned off due to interactions between spins, causing exchange of energy. The exchange of energy between spins leads to a loss of coherence of the transverse magnetization. The amplitude of the transverse magnetization decays from its initial value at time=0, $M_{xy}(0)$ to zero as:

$$M_{xy}(t) = M_{xy}(0)e^{-t/T_2} \tag{2.12}$$

If a saturation pulse is applied, the entire magnetization vector M_0 is tipped into the xy plane. The transverse magnetization, M_{xy}, will then decay from M_0 to zero due to T_2 relaxation as shown by the blue solid line in Fig. 2.5.B. In practice, the NMR signal decays faster than predicted from consideration of T_2 alone, as illustrated by the red solid line. This accelerated decay rate is

characterised by the relaxation time, $T_2^\star$, which is given by

$$\frac{1}{T_2^\star} = \frac{1}{T_2} + \frac{1}{T_2'} \tag{2.13}$$

where T_2' accounts for processes arising from inhomogeneities in B_0 which are reversible. Inhomogeneity in the B_0 field causes slight shifts in the local resonant frequency, leading to additional spin dephasing. This additional relaxation term is the basis of the $T_2^\star$ contrast mechanism. This provides unique information on tissue magnetic susceptibility (Section 2.1.9) and changes in susceptibility that occur with functional processes. The susceptibility effects around vascular structures in the brain provide an ideal mechanism for using $T_2^\star$ contrast to study brain function. Blood, as an endogenous contrast agent, makes the magnetic susceptibility of the vasculature different from the adjacent tissue. Any functional brain process or pathological alteration that changes the brain blood oxygenation distribution, can be directly observed using $T_2^\star$-contrast.

T_2 values in brain tissue decrease with increasing magnetic field strength. For example, on going from 3 to 7 T the T_2 values of cortical grey matter and white matter are reduced from 110/80 ms [8] to 55/46 ms [9]. The additional relaxation term $1/T_2'$ scales with the field strength because of increased magnetic susceptibility effects, and thus becomes dominant in $T_2^\star$ relaxation. Typical $T_2^\star$ values for grey matter and white matter are 60/55 ms at 3 T and 33/29 ms at 7 T [10].

The increase of $T_2^\star$ contrast with increasing magnetic field strength is the reason for the strong interest in $T_2^\star$ contrast applications at ultra high field. Gradient echo (GE) acquisition methods (Section 2.2.5), which are sensitive to microscopic variations in tissue susceptibility, were used to achieve this contrast in the experiments described later in this thesis.

2.1.7   NMR measurements

The transverse magnetisation of the precessing spins in the sample is detected using an RF coil. Often the same coil is used for RF detection as that which generates the RF excitation. Following the application of a short pulse of RF energy, modulated at the Larmor frequency, the magnetisation is tipped into the transverse plane (Figure 2.4). The resulting transverse magnetization precesses about the field producing a change in magnetic flux, which causes a detectable electromotive force oscillating at the precessional frequency to be induced in the coil. Once the RF source is switched off, this Free Induction Decay (FID) signal is detected in the receiver coil. This signal is very small and it therefore requires amplification in order to be detected. The amplified signal, which oscillates at the Larmor frequency, is then mixed with an oscillating reference signal with a frequency ω_{ref} in two quadrature (90° out of phase) phase sensitive detectors, producing two separate demodulated signals which are proportional in strength to the orthogonal components of the transverse magnetization, M_x and M_y. Their complex addition gives,

$$S(t) = S(0)e^{-t/T_2^\star} e^{i(\Delta\omega t + \phi)} \tag{2.14}$$

where $\Delta\omega$ is the resonance frequency offset $\omega_0 - \omega_{ref}$ and ϕ is the reference phase.

At the start of the FID the spins are in phase (coherent); this coherence is lost due to the relaxation processes described above and the signal decays in amplitude. When the spatially dependent phase shifts are momentarily nulled so that the signal from spins within the sample interfere positively, a relative increase in signal intensity or echo results. The echo was first studied by Hahn [11]. There are two commonly used echo formation methods; gradient echoes (GE) are formed using a linear gradient, this process is described in Section 2.2.4, and spin echoes (SE) are formed using refocusing pulses. A refocusing pulse, typically applied along the y-axis in the rotating frame, rotates the transverse magnetization by 180° in the xz plane, reversing the dephasing
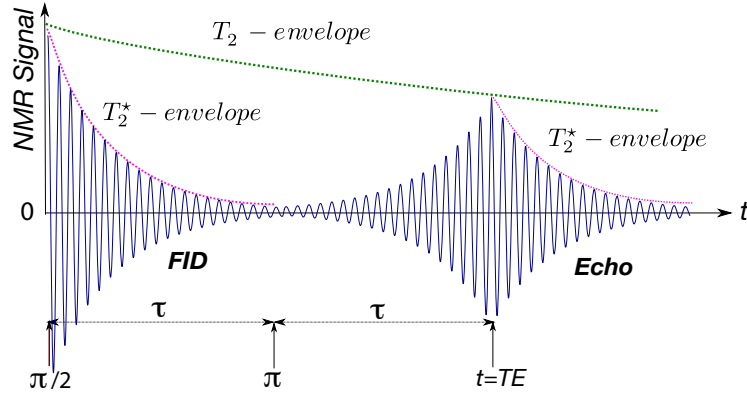
Figure 2.6: A free induction decay (FID) NMR signal (solid blue line)with its $T_2^\star$ decay envelope (dashed pink line) followed by the formation of an echo (solid blue line) at $t = TE = 2\tau$ with a peak amplitude dependent on the T_2 decay (green dashed line), due to the refocusing by a 180° pulse applied at t=τ.

caused by the T_2' term. The formation of spin echoes is discussed in more detail in Section 2.2.5.

2.1.8   Chemical shift

Nuclei in different chemical environments generally experience slightly different static magnetic fields due to varying degrees of electronic shielding. The effect of this shielding on the NMR frequency is known as the chemical shift. The effective field experienced by a spin is dependent on the applied external field and the induced field generated by the electrons of the molecule:

$$B_{eff} = (1 - \sigma)B_0 \tag{2.15}$$

where σ is the chemical shift shielding constant. The chemical shift parameter δ in parts per million (ppm) is given by

$$\delta = \frac{\omega - \omega_{ref}}{\omega_{ref}} \times 10^6 ppm \tag{2.16}$$

where ω_{ref} is a fixed reference frequency, generally set equal to the resonant frequency of ^1H nuclei in tetramethylsilane (TMS). Thus, a range of chemi-

cal shifts leads to a range of precessional frequencies. In NMR spectroscopy, information about the chemical environment of the nuclei in the sample is extracted from a single FID. The FID is Fourier transformed and the frequency spectrum analyzed. Since the shielding varies with the chemical environment, the variation of frequencies provides useful information, and forms the basis of NMR spectroscopy. In MRI such a range of precessional frequencies can produce chemical shift and water-fat shift artefacts (Section 2.3.2).

2.1.9 Susceptibility

Perturbation of the static magnetic field also arises when atoms and molecules are polarized by the magnetic field. The induced magnetization, $M_{Z,ind}$, can be written in terms of the magnetic susceptibility, χ:

$$M_{Z,ind} \approx \frac{\chi}{\mu_0} B_0 \tag{2.17}$$

where μ_0 is the permeability of free space. It is important to distinguish between nuclear susceptibility of the proton which is *paramagnetic* $(\chi > 0)$ and the bulk susceptibility of tissue which is generally *diamagnetic* $(\chi < 0)$. The nuclear susceptibility is very small because the magnetic moment of the nucleus is small and the total susceptibility of tissue is dominated by the much larger diamagnetic effect. The effective local magnetic field is given by

$$B_{eff} \approx (1 + \chi)B_0. \tag{2.18}$$

Susceptibility effects induce perturbations in the magnetic field which can cause artefacts in magnetic resonance images (Section 2.3.1). Depending on its orientation with respect to the magnetic field and its magnetic susceptibility, a blood vessel can modify the magnetic field in its vicinity. This effect is more intense near the interfaces of media with distinctively different magnetic susceptibility, such as brain tissues and air-containing bone structures. The largest field offsets are due to the air/tissue interfaces near the sinus cav-

ities. These macroscopic field distortions caused by tissue heterogeneity are unwanted, however microscopic field distortions around small vessels are the basis of both functional MRI and contrast agent studies. Functional MRI using the BOLD (Blood Oxygen Level dependent) effect relies on the susceptibility difference between oxygenated and deoxygenated blood to visualize brain activation [12, 13, 14, 15]. This is further discussed in Section 4.4.1. Paramagnetic rare earth elements such us ^{157}Gd whose susceptibility is extremely high, generate a magnetic field several thousand times greater than that of the proton magnetic moment. Such elements are used in MRI as contrast agents [16]. The magnitude of susceptibility effects vary with the type of imaging sequence and also scale linearly with the static field, leading to a greater impact on image artefacts and contrast formation at high field.

2.2 MRI: Principles of Imaging

NMR imaging was developed in the early 1970's. In 1973, Lauterbur proposed using a field gradient to localize the NMR signal [17]. A linear gradient was applied at different angles to a sample and the projections were combined using a back-projection method to produce 2D images of the sample.

One year later, selective excitation was proposed by Mansfield's group [18]. A variety of methods for selectively exciting a slice through a sample were described, including slice selection in the exact form it is used today.

Two years later, the first Fourier imaging method was published by Ernst's group [19], using non-selective excitation and orthogonal linear gradients to generate 2D Fourier encoded images.

From this gradient encoding technique a multitude of fast imaging methods have been developed. In 1977 Mansfield introduced a technique for fast imaging called Echo Planar Imaging (EPI) [20]. This is now routinely used and the method of choice for image acquisition in fMRI studies.

2.2.1 Signal localization

To create an image of a sample, a process for localization of the NMR signal is required. This is done by superimposing a small, spatially varying magnetic field onto the main B_0 magnetic field. This leads to the resonant frequency becoming a function of position. This additional field variation is produced with the use of three orthogonal linear field gradient coils, G_x, G_y and G_z, each designed to produce a linearly varying field along its respective axis, producing a total field gradient

$$\mathbf{G} = G_x \mathbf{i} + G_y \mathbf{j} + G_z \mathbf{k} \qquad (2.19)$$

The z-component of the magnetic field at point $\mathbf{r}$ is then given by

$$B_z(r) = B_0 + \mathbf{G} \cdot \mathbf{r} \qquad (2.20)$$

This introduces a spatial dependence to the Larmor frequency of the precessing spins in the sample;

$$w(r) = \gamma(B_0 + xG_x + yG_y + zG_z); \qquad (2.21)$$

Sections 2.2.2 and 2.2.3 introduce three methods for signal localisation using field gradients. Selective excitation is introduced via slice selection and localisation of the NMR signal is then described using frequency and phase encoding.

2.2.2 Slice Selection

Slice selection is a technique used to excite a thin slab of spins in a sample known as a 'slice'. The RF pulses described in Section 2.1.5 excite the whole sample since all the spins have the same Larmor frequency, thus the pulse is described as *non-selective*. However, when the pulse is applied in the presence of a field gradient, only spins in a plane with a Larmor frequency that

corresponds to the limited range of frequencies contained in the pulse will be tipped into the xy plane. This is called selective excitation. The gradient field, G_z, causes a linear variation of the Larmor frequency in the slice (z) direction across the sample,

$$w(z) = \gamma(B_0 + zG_z). \tag{2.22}$$

The position of the slice selected in the (z) direction can be changed by altering the frequency of the RF pulse, called the carrier frequency. The thickness of the slice, Δz is determined by the gradient amplitude,G_z, and the bandwidth of the pulse $\Delta \omega$:

$$\Delta z = \frac{\Delta \omega}{\gamma G_z}. \tag{2.23}$$

Using the small tip angle approximation [21], the response of the spins is approximately proportional to the Fourier Transform of the pulse. Therefore the time evolution of an RF pulse made up of equal contributions from a finite range of frequencies, (a rectangular slice profile) is a sinc-shaped pulse of 'infinite length' modulating a sine wave at the centre frequency ω_0. In practice, the duration of the RF pulse is limited by the need to avoid relaxation effects during excitation. A sinc pulse will therefore typically be limited to 3 or 5 lobes and filtering of the pulse is applied to improve the excited slice profile.

Application of a sinc pulse in the presence of a gradient results in a continuous phase shift across the slice. This phase shift must be corrected and this is performed by applying a reversed slice gradient for half the duration of the original slice select period, as shown in Fig. 2.7.B.

2.2.3 Fourier Imaging: spatial encoding

In the absence of relaxation, the signal emanating from a point $\mathbf{r}$ at a time t is proportional to the spin density, $\rho(\mathbf{r})$, and is also dependent on the evolution of the local Larmor frequency, $\omega_L(\mathbf{r}, t')$ from time $t' = 0$ to $t' = t$.

$$S(\mathbf{r,t}) \propto \rho(\mathbf{r})e^{i \int_0^t \omega_L(\mathbf{r},t')dt'}. \tag{2.24}$$
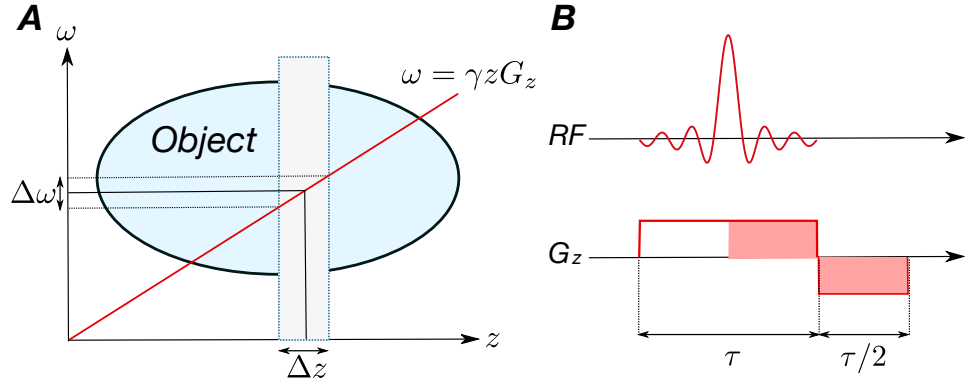
Figure 2.7: (A) When an RF pulse with a range of frequencies, $\Delta\omega$, is applied in the presence of a linear field gradient, G_z, a slice of thickness Δz is excited. (B) The slice selective excitation is followed by a negative gradient lobe to refocus the dephasing effects induced by the slice select gradient.

Signals are generally received from an extended region of the sample and therefore

$$S(t) \propto \int_V \rho(\mathbf{r})e^{i\int_0^t \omega_L(\mathbf{r},t')dt'}dV, \tag{2.25}$$

where $dV = dxdydz$ and V is the sample volume. Since the Larmor frequency is determined by the magnetic field experienced by the spins, that is related to the static magnetic field, B_0, and the three orthogonal gradients, G_x, G_y and G_z, the signal can be written in terms of the evolution of the gradients over time. Equation 2.26 shows this signal after the demodulation of the central Larmor frequency, ω_0, due to B_0;

$$S'(t) \propto \int_V \rho(\mathbf{r})e^{i\gamma\int_0^t \mathbf{r}\cdot\mathbf{G}(t')dt'}dV, \tag{2.26}$$

where $\mathbf{G}(t') = G_x(t')\mathbf{i} + G_y(t')\mathbf{j} + G_z(t')\mathbf{k}$. Defining:

$$\mathbf{k}(t) = \gamma\int_0^t \mathbf{G}(t')dt' \tag{2.27}$$

where the space that $\mathbf{k}(t)$ resides in is known as k-space (Section 2.2.4), Eq. 2.26 reduces to

$$S'(t) \propto \int_V \rho(\mathbf{r})e^{i\mathbf{r}\cdot\mathbf{k}(t)}dV. \tag{2.28}$$

This is now in the form of a 3D Fourier transform, meaning that by appropriate signal acquisition and gradient adjustment, information can be obtained about the spin density of objects from an inverse Fourier transform (IFT) of the received signal. This concept forms the basis of modern imaging techniques in MRI.

Frequency Encoding

Frequency encoding is a common spatial encoding method used in many MRI pulse sequences, including projection acquisition [17] and Fourier imaging [19, 22]. Frequency encoding uses the same principle as slice selection, but the field gradient is applied during image readout rather than excitation, influencing only those spins that have already being excited by slice selection. Applying a constant linear field gradient in one direction $\mathbf{G}(t') = G_x \mathbf{i}$ makes the precession frequency a function of position along that gradient axis:

$$\omega(x) = \gamma(B_0 + G_x x). \tag{2.29}$$

If the gradient is applied from $t' = 0$ to $t' = t$ while the signal is measured,

$$S'(t) \propto \int_V \rho(\mathbf{r})e^{i\gamma x G_x t}dV = \int_V \rho(\mathbf{r})e^{i x k_x}dV \tag{2.30}$$

using Eq. 2.27 yields

$$S'(t) \propto \int \int FT_x[\rho(r)]dydz. \tag{2.31}$$

If a thin slice has been selected (Section 2.2.2), the system is reduced to just two dimensional (2D) imaging,

$$S'(t) \propto \int FT_x[\rho(r)]dy. \tag{2.32}$$

The Larmor frequency varies across the sample in a linear way, so that the inverse Fourier transformation of the received, demodulated signal provides a
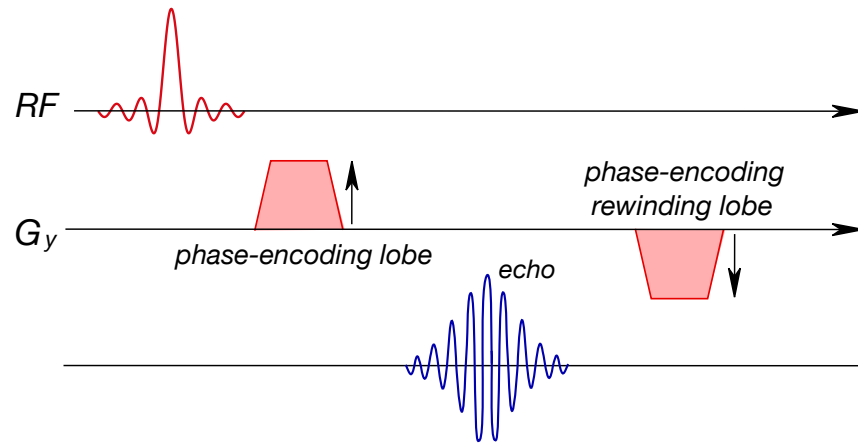
Figure 2.8: A pulse sequence that uses phase-encoding plus phase rewinding. For each phase encode step, the rewinding gradient area is the negative of the phase-encoding gradient area. Therefore the amplitudes of the two gradient lobes are stepped in opposite directions (arrows).

breakdown of the frequencies and therefore information about the distribution of spin density in the x-direction.

Phase Encoding

Phase encoding localizes the NMR signal orthogonal to the frequency encoding direction, so as two produce a two dimensional image. The idea behind phase encoding is to create a linear spatial variation of the phase of the magnetization. This is achieved by applying a y-gradient lobe, while the magnetization is in the transverse plane, prior to each frequency encoding acquisition. This modifies the phase before signal acquisition and by varying the area under the phase encoding gradient, different amounts of linear phase variation are introduced. The resulting signals can be reconstructed trough Fourier transformation to recover spatial information about the object.

Many pulse sequences such as Turbo Spin Echo (TSE) or Magnetization-Prepared Rapid Gradient Echo (MPRAGE) (Section 4.2.1) rewind the phase-encoding gradient after read-out (Fig. 2.8) to rephase the transverse magnetisation and to make it more consistent between phase encoding steps. By doing so, certain signal losses can be avoided and artefacts can be minimized.
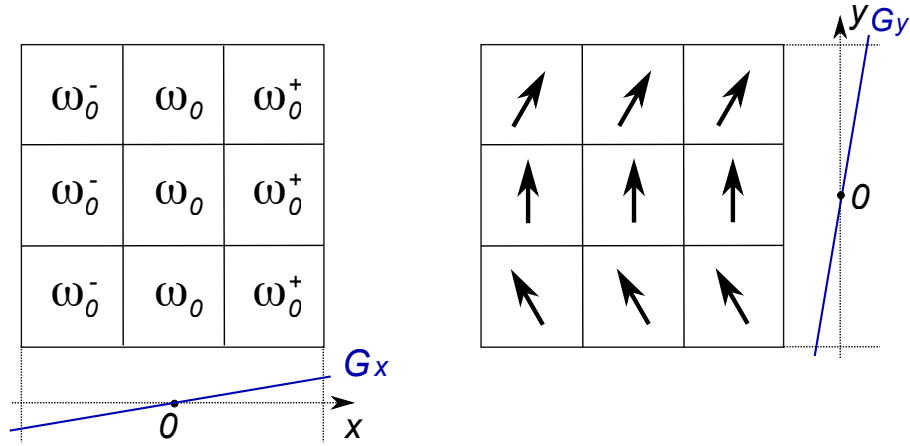
Figure 2.9: The frequency encoding gradient (left) makes the Larmor frequency of the spins dependent on their position along the x-axis. A phase encoding gradient (right) introduces a phase shift of the transverse magnetization which varies along the y-axis.

The amount of phase introduced to the signal due to a phase encoding gradient $\mathbf{G}(t') = G_y\mathbf{j}$ applied from $t' = 0$ to $t' = t_1$ is

$$\phi_y = \gamma y G_y t_1 = y k_y \tag{2.33}$$

so that the signal acquired in the time interval from $t' = t_1$ to $t' = t_2$ during which a gradient $\mathbf{G}(t') = G_x\mathbf{i}$ is applied can be written as

$$S'(t) \propto \int \int \rho(\mathbf{r}) e^{i\phi_y + ixk_x} dx dy \tag{2.34}$$

where $t = t' - t_1$. Again, using Eq. 2.27 yields

$$S'(t) \propto 2DFT_{xy}[\rho(r)]. \tag{2.35}$$

Phase encoding can also be applied in the slice direction in 3D volume acquisitions so that the object can be reconstructed by three dimensional inverse Fourier transformation.
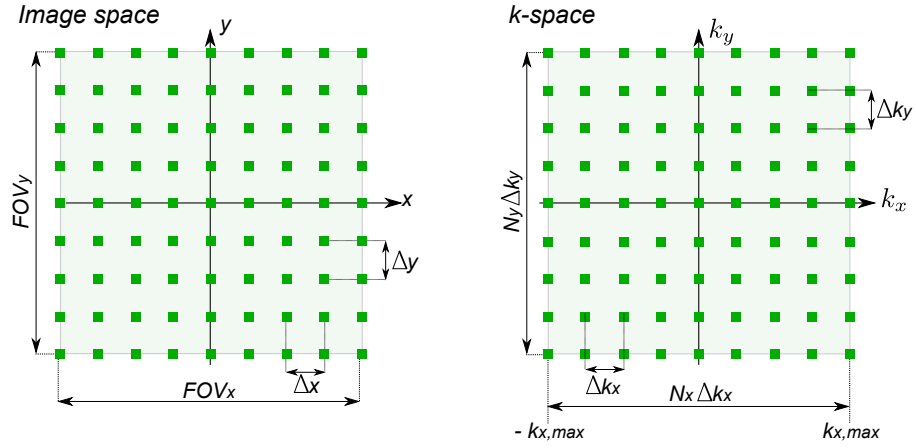
Figure 2.10: The relationship between image space (left) and k-space (right).

2.2.4 k-space

The concept of k-space was introduced in 1983 [23] as a way of visualizing the trajectories of the spins' phase under the influence of field gradients. k-space can be consider as the Fourier space (k_x, k_y, k_z) in which images are acquired, before being Fourier transformed into Cartesian image space (x,y,z). k-space represents the spatial frequency distribution of the MR image. Low spatial frequencies (coarse image structures) appear close to the origin while higher spatial frequencies (edges and fine detail) appear at the outer edges of k-space.

Applying field gradients in the correct way in the imaging plane encodes the spatial position of signals as frequencies and phases (Section 2.2.3). Immediately after excitation, the sampling position is at the centre of k-space and the position at a time, t, after excitation is proportional to the integrated gradient at that time. So, signal acquired in the presence of a constant x-gradient samples k-space along a line in the k_x-direction. Therefore, during frequency encoding, data points are recorded at regular intervals as k-space is swept, while during phase encoding the location in k-space is altered without sampling the signal, resulting in instantaneous jumps in the sampled trajectory. To sample an image, fully, all four quadrants of k-space must be covered by the readout trajectory.
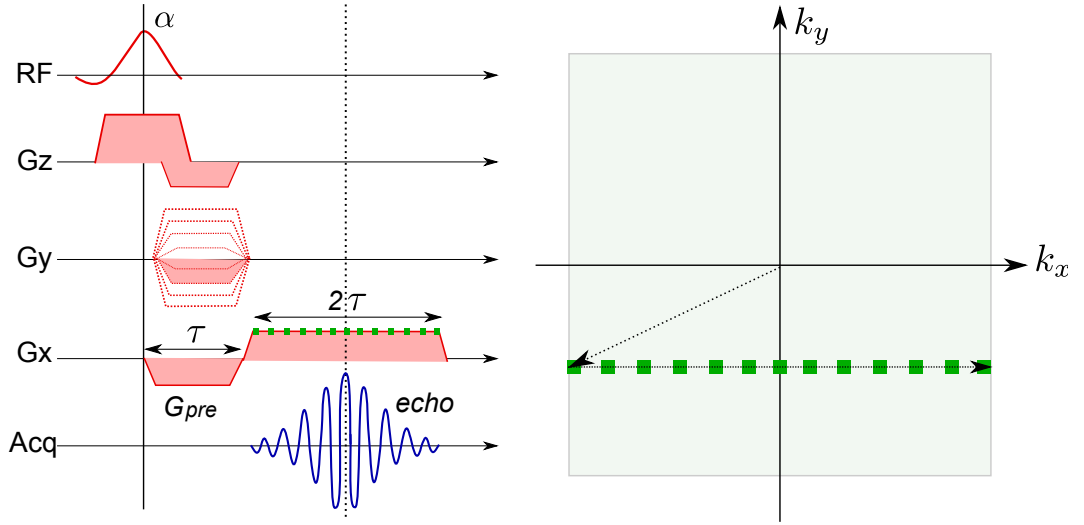
Figure 2.11: The basic gradient echo sequence (left diagram) and the corresponding discrete sampling of one line in k-space. The phase encoding gradient, G_y, applied in conjunction with the pre-excursion gradient, G_{pre}, shifts the position in k-space as shown by the dashed arrow. When the area under the positive lobe of the read out gradient, G_x, matches the area under the pre-excurion gradient, an echo is formed. The signal is sampled at the points indicated by the green squares.

Although k-space trajectories traverse a continuous path, the signal is sampled only at discrete intervals along the path. The spacing of the measurements made in k-space determines the field-of-view (FOV) of the resulting image:

$$\Delta k_{x,y} = \frac{1}{FOV_{x,y}}, \tag{2.36}$$

and the further from the centre of k-space one measures, the greater the resolution of the reconstructed image.

2.2.5 GE imaging

A gradient echo is formed by applying a linear field gradient across a sample. This gradient causes spins to precess at different rates at different positions across the sample, causing the bulk magnetization to dephase. Reversing the field gradient will then reverse the dephasing effect. Figure 2.11 shows the timing diagram for the gradient echo imaging version of the spin-warp sequence

[22] and the corresponding k-space trajectory. This is a 2D slice selective imaging sequence, now often referred as to Fourier imaging.

A frequency-selective RF pulse applied simultaneously with a z-gradient, rotates the magnetization in a thin slice by an angle, α, into the transverse plane. This is followed by a refocusing gradient lobe to remove the phase gradient over the selected slice (slice selection). After an evolution time which can be varied to change the contrast of the image, k-space is traversed using gradients applied along the x- and y-directions to ensure that sampling starts at the appropriate point in k-space. The frequency encoding gradient consists of two portions with opposite polarity; a pre-phasing (also called dephasing) gradient lobe, denoted G_{pre} in the diagram, and a readout gradient lobe. The pre-phasing gradient lobe is applied for a time τ, which causes a traversal of k-space to the extreme left of the sampled area ($-k_{x,max}$). The variable phase encoding gradient is applied in the y-direction at the same time to move the sampling position to $k_{y,n}$. The purpose of the pre-phasing gradient is to prepare the transverse magnetization so that an echo can be acquired at a latter time. Immediately after the RF pulse the excited spins have the same phase, but become dephased gradually due to $T_2^\star$ processes (Section 2.1.6) and the effects of the gradients. When the pre-phasing gradient is applied, the spins accumulate phase at different rates depending on their locations in the gradient field. Then the read out gradient is applied for a time, 2τ, while data are acquired at points along the k-space line. The polarity change between the pre-phasing and read-out gradients reverses the direction of phase accumulation of the spins; rapidly dephasing spins come back into phase with slowly dephasing spins, producing a gradient echo signal with a peak at a time τ after the read-out gradient is first applied(where the area under the read0out lobe equals the area under the prephasing lobe). The system is then allowed to relax to equilibrium before the sequence is repeated with a different strength of phase encoding (y) gradient so as to sample 2D k-space fully.

2.2.6 SE imaging

Spin echo imaging [11] is similar to gradient echo imaging (Section 2.2.5), but differs in the mechanism by which the echo is created. Figure 2.12 shows the timing diagram and k-space trajectory of a typical spin echo sequence and the principles underlying the formation of the spin echo are illustrated in Fig. 2.13. The 90° RF pulse flips the transverse magnetisation into the transverse plane. The spins are initially coherent in phase, but will steadily dephase due to $T_2^\star$ effects (Section 2.1.6) causing the detectable signal to decay. After a time τ, a 180° pulse is applied, which flips the spins, reversing the sign of the phase shift. A spin that has been precessing rapidly (slowly), and which has consequently built up a positive (negative) phase shift, will now show a negative (positive) phase shift. However, the local effects that cause it to precess rapidly (slowly) have not changed, and the spin will therefore tend to catch up (slow down) back to zero shift at time τ after the refocusing pulse (Fig. 2.13). A spin echo is thus formed at a time TE $= 2\tau$ after the excitation pulse. Whereas the gradient echo is unable to refocus field inhomogeneities, RF refocussing will eliminate field inhomogeneities and the measured signal will have T_2 weighting. Notice that only static inhomogeneities are eliminated in a spin echo sequence; signal decay due to diffusion in inhomogeneous magnetic fields (which gives rise to T_2 relaxation) is not recovered in either spin echo or gradient echo sequences.

2.2.7 Fast Imaging: EPI

In 1977, Mansfield [20] proposed echo-planar imaging (EPI), a fast imaging modality that traverses all of k-space after application of a single RF pulse (a single "shot") rather than using multiple RF excitations to sample k-space. This is still the most commonly used sequence for fMRI and it is a widely used in medical imaging [24]. A schematic diagram of the EPI sequence is shown in Fig. 2.14. After the radiofrequency excitation pulse, whose flip angle is normally 90°, repeated reversals of the measurement gradient, G_x, repeatedly
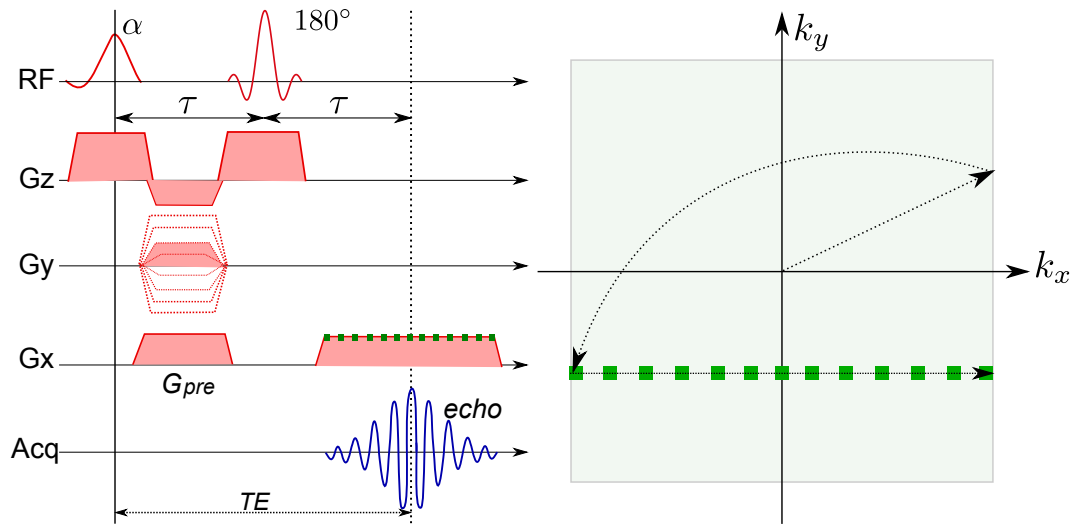
Figure 2.12: The basic spin echo sequence (left diagram) and the corresponding discrete sampling of one line in k-space. The dashed arrows represent the initial k-space shift due to the phase encoding, G_y, and pre-excursion, G_{pre}, gradients, and the effect of the refocusing pulse. The signal is acquired along the solid arrow at the position indicated by the green squares.
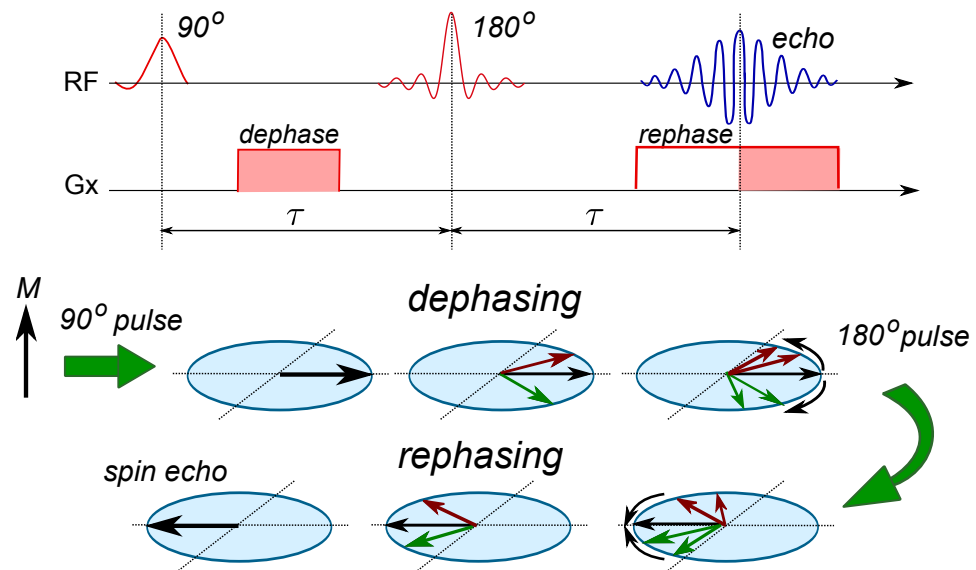
Figure 2.13: The refocusing effect of the 180° pulse in a spin echo sequence.
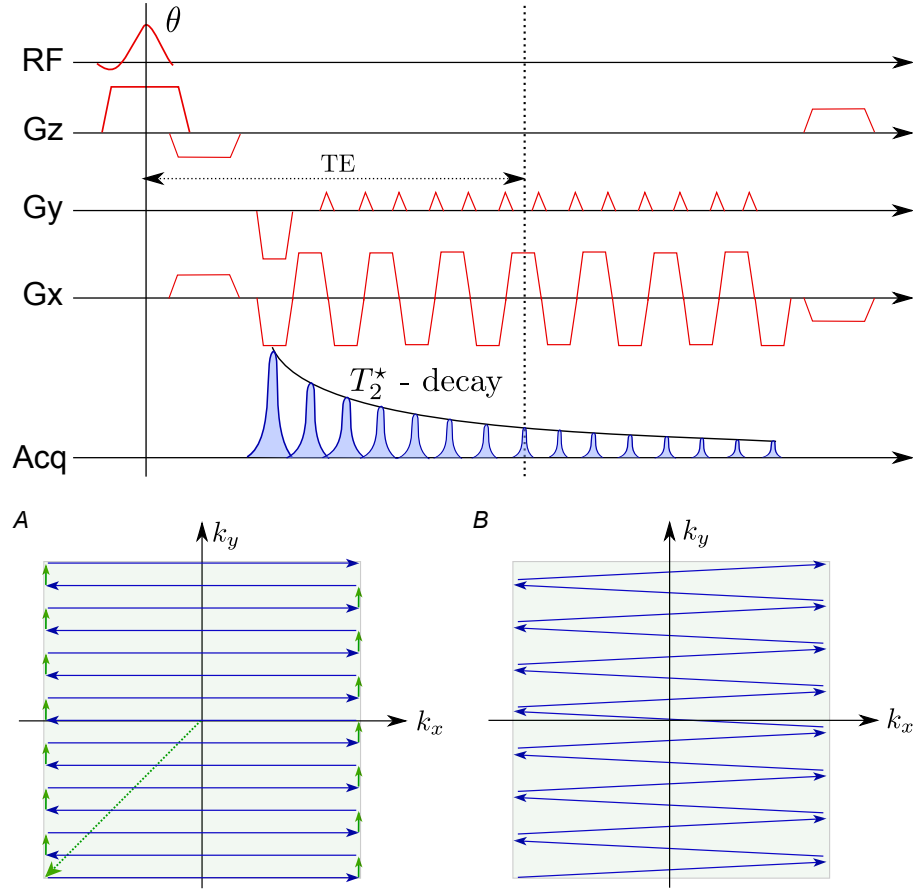
Figure 2.14: Echo planar imaging pulse sequence diagram (top) and k-space trajectories (bottom); (A) blipped and (B) zig-zag.

refocus the transverse magnetization to yield a train of gradient echoes. The gradient echo removes the dephasing effects due to the imaging gradient, but it does not rephase macroscopic or microscopic susceptibility effects. A large initial phase encode gradient is applied to place the first echo at the periphery of k-space. A constant gradient will progressively reduce the net phase gradient to zero and then increment it until it reaches the other side of k space, sampling the k-space in a zig-zag trajectory as shown in Fig. 2.14.B. A Modulus Blipped Echo-planar Single-pulse Technique, or MBEST [25], where k-space is sampled in a rectilinear fashion, Fig. 2.14.A, is commonly used nowadays. After the initial pre-excursion gradient the subsequent blips of the phase encoding gradient, as shown in Fig. 2.14, serve to step the acquired echoes through k-space.

Inhomogeneities of the B_0-field due to poor shimming and susceptibility ef-

fects induce geometric distortions in the image (Section 2.3.1). This influences
the evolution of the phase during the echo train, affecting the EP image more
severely than in conventional sequences. The presence of small gradient im-
perfections or eddy currents will cause the alternating polarity of the k-space
lines to produce a shift in the echo position. This appears in the reconstructed
image as the Nyquist ghost, a lower intensity ghost of the image shifted by half
the field of view in the phase encoding direction. EPI data also suffers from
signal drop-out in areas where throughslice gradients are found due to local
field inhomogeneities (Section 2.3.1). With EPI sequences, a phase variation
due to chemical shift also accumulates in the phase encode direction, and since
the voxel bandwidth is low in this direction, this component of the chemical
shift can cause substantial displacements of the signals such as that from fat
(Section 2.3.1).

2.3   Off-resonance effects

In this section, the effects of deviations in the static magnetic field from
its nominal value of B_0 will be discussed. There are two main sources of
off-resonance effects in MRI; namely susceptibility effects and chemical shift
effects. Chemical shift effects cause spatial displacements of the fat signal,
whilst susceptibility effects can give rise to geometric distortions as well as
signal loss.

2.3.1   Susceptibility effects: Implications for Imaging

Differences in local tissue susceptibility, for example due to air spaces of
the sinuses, can generate spatially varying magnetic field, giving rise to off-
sets in the resonant frequency. Since spatial encoding relies on a homogeneous
magnetic field, field inhomogeneity results in artefacts in MR images. Sus-
ceptibility effects give rise to geometric distortions, as well as signal loss and
image blurring in rapid imaging techniques [26, 27, 28, 29, 30]. The effects
of the magnetic field inhomogeneities depend on the extent and magnitude of
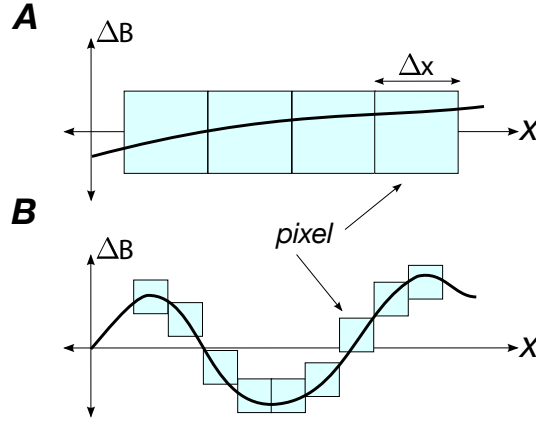
Figure 2.15: (A) Intravoxel dephasing effects which lead to signal loss and imaging blurring and (B) off-resonance effects which lead to geometric distortion.

the field perturbation rand on the pixel dimension and pixel bandwidth. The pixel bandwidth, BW, is the inverse of the time needed to acquire a full line of k- space data in a particular direction [31]. If the field perturbation occurs over a small distance relative to the voxel size, Fig. 2.15.A, the increased phase dispersion will give rise to an increase in the rate of signal decay. If instead the field perturbation occurs over a large distance relative to the voxel size, Fig. 2.15.B, then mainly signal misregistration occurs, since the field within a voxel can then be approximated to be constant, but shifted from its reference value, giving rise to geometric distortion.

Intravoxel dephasing

Reduction of the $T_2^\star$ relaxation time occurs when the phase dispersion due to field inhomogeneities within a voxel is large, giving rise to intravoxel dephasing. The increased rate of $T_2^\star$ relaxation due to the through-plane local gradients causes signal loss and imaging blurring. The signal-loss artifact is caused by intravoxel phase dispersion, $\delta\phi$, mainly resulting from local field gradients in the slice dimension [27]. Fig. 2.16.A shows a slice selection gradient, G_z and the corresponding phase evolution in the slice, $\Delta\phi$. The local susceptibility gradient, ΔG_z, shown in Fig. 2.16.B adds to the slice selection

gradient causing the phase of the magnetization of a voxel to dephase during the TE period; signals from pairs of spins with opposite phase cancel leading to signal loss in GE images. The amount of signal loss is dependent upon, G_z, ΔG_z, TE and the slice thickness [32]. The signal loss can be understood as a result of signal reduction at the effective TE where the signal from the centre of k-space is sampled. Due to a large difference in susceptibility between air and tissue, signal loss can be very large in the regions close to air-tissue interfaces, such as in cortical regions near to the sphenoid sinus in the frontal lobe. Effects are particularly large at high static field strengths [26], where ΔG_z is large. Changing the slice orientation can improve image orientation as field gradients around local field inhomogeneities are often not symmetric [33]. The increased rate of $T_2^\star$ relaxation also results in a strong modulation of the MR signal along the k-space trajectory of rapid imaging sequences. This modulation generally acts as a low-pass filter of the k-space signal, resulting in blurring in images produced using conventional rapid acquisition methods. The point spread function, PSF, caused by $T_2^\star$ decay is a Lorentzian with a full width at half maximum, FWHM, given by

$$\Delta x = \frac{2}{\gamma \langle G \rangle T_2^\star} \quad , \tag{2.37}$$

where $\langle G \rangle$ is the average value of the gradient strength. Due to the strong applied gradient in the read-out direction and short read time, T_{read}, the blurring due to the finite duration of signal sampling in the k_x-(read out) direction is generally much larger than the blurring due to $T_2^\star$ relaxation. For example, at 7 T the $T_2^\star$ value of gray matter is about 25 ms, for a mean gradient strength of $\langle G \rangle = 30$ mT/m, the FWHM is about 0.06 mm. For EPI images $T_2^\star$ blurring can be significant in the phase encoding direction. The effective gradient is proportional to the average velocity of movement through k-space, so that if N is the matrix size in the phase-encode direction:

$$\langle G_x \rangle \cong N \langle G_y \rangle, \tag{2.38}$$
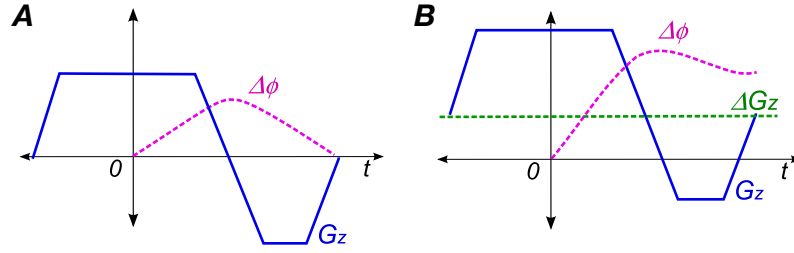
Figure 2.16: Evolution of the phase dispersion across a slice (pink dashed line) under the influence of (A) a refocused slice select gradient, G_z (blue dashed line) and (B) G_z plus an additional susceptibility induced gradient ΔG_z (green dashed line).

making the FWHM of the point spread function in the phase encoding direction N times larger than in the read-out direction ($\sim$ 4 mm if N=64 in the above example).

Signal miss-registration

Off-resonance effects form the dominant susceptibility artefact when the pixel bandwidth is small relative to the spatial extent of the field perturbation; the field variation within the voxel, $\Delta B_0(r)$, is then small, but the entire voxel may experience a frequency offset. In this case, the average field offset of a given voxel adds to the effective field in the z direction, B_z

$$B_z = B_0 + G_x(t)x + G_y(t)y + \Delta B_z(x, y, z), \qquad (2.39)$$

where $\Delta B_z(x, y, z)$ is the total susceptibility induced field shift within the voxel ($\approx \Delta B_0$). For conventional GE and SE sequences the phase offset due to ΔB_z in the phase encoding direction is constant for all phase encoding steps and does not introduce any modulation of the signal. Thus the spatial distortions in conventional GE and SE sequences will always occur along the frequency encoding direction. The magnitude of the spatial distortion due to ΔB_z along the read-out gradient can then be expressed in terms of the applied read out gradient strength as

$$\Delta x = \Delta B_0 / G_x, \qquad (2.40)$$

where Δx is the shift in the pixel due to a susceptibility induced field ΔB_0 and G_x is the applied read gradient. The pixel dimension in the read-out direction can be expressed as

$$\delta x = \frac{2\pi}{\gamma G_x T_{read}}, \tag{2.41}$$

where T_{read} is the total read-out time, i.e., the inverse of the pixel bandwidth (BW$=\frac{1}{T_{read}}$). In order to have a negligible shift, the shift in position should be much smaller than the pixel dimension, $\Delta x \ll \delta x$, i.e, the pixel bandwidth must be large relative to the susceptibility induced frequency shift

$$BW \gg \frac{\gamma \Delta B_0}{2\pi}. \tag{2.42}$$

Therefore, one way of increasing the pixel bandwidth is to increase the gradient strength and reduce the read-out time, which reduces the SNR. Alternatively the voxel size can be increased, but this reduces image resolution and may also increase the intravoxel dephasing.

Geometric distortion artefact in EPI

Single shot echo planar imaging, (EPI), requires the acquisition of a long train of echoes in which phase errors accumulate, therefore geometric distortion due to field inhomogeneity is more prominent with this sequence. The geometric distortions present in EPI are caused by the frequency shift of the MR signal due to the in-plane local field variation during the elongated k-space trajectory. The velocity at which k-space is traversed in the k_y (phase-encode) direction is much smaller than in the k_x (read) direction. Therefore the frequency shift of the MR signal results in a pixel shift in the EP image which is more severe in the phase-encoding direction, since the pixel bandwidth in this direction is relatively small. In our experiments at 7 T for example, the typical pixel bandwidth in the frequency encoding direction is about 1-2 kHz, which is large compared with the B_0-field inhomogeneities, which are usually less than 100 Hz. The pixel bandwidth in the phase encoding direction is usually of 20-30 Hz, which results in misregistration of a few pixels. One way

of alleviating this problem is using parallel imaging techniques, such as Sensitivity encoding (SENSE) imaging which is implemented on a Philips system [34, 35, 36]. The use of multiple coils allows the number of phase encoding steps to be reduced while maintaining the same k-space sampling area. In this way, the acquisition time is reduced compared with the conventional EPI method, and this reduces the cumulative effect of field inhomogeneity. Field inhomogeneity taking the form of a gradient in the phase encoding direction also causes a shift of the apparent echo time leading to spatial variation in the sensitivity to BOLD contrast. Deichmann et al. [37] applied preparation phase encoding pulses in combination with z-shimming to restore these shifted echoes and thereby mitigate the loss of BOLD sensitivity.

Since susceptibility-induced field inhomogeneity scales linearly with static magnetic field strength, B_0 [26], susceptibility induced image distortions and signal loss become more severe at high field. Shimming techniques therefore become crucial in overcoming magnetic field inhomogeneities at 7 T and are discussed further in Section 4.3.3.

2.3.2 Water fat shift

The water fat shift artefact, due to the difference in the resonant frequencies of water and fat, is the most prominent chemical shift artefact. The artefact manifests itself as a misregistration of the signal from fatty tissues, since fat and water spins in the same voxel are encoded as being located in different voxels. For water and fat, the chemical shift difference, $\Delta\delta$, is approximately 3.4 ppm, and the frequency separation (Δf) increases with the static magnetic field strength B_0;

$$\Delta f = \frac{\gamma B_0}{2\pi} \times \Delta\delta[ppm] \times 10^{-6} \tag{2.43}$$

which corresponds to a frequency separation of $\sim 440 Hz$ at 3 T and $\sim 1013 Hz$ at 7 T. In order to avoid excessive misregistration of pixels containing fat, we need to have a pixel bandwidth which is large relative to the frequency offset
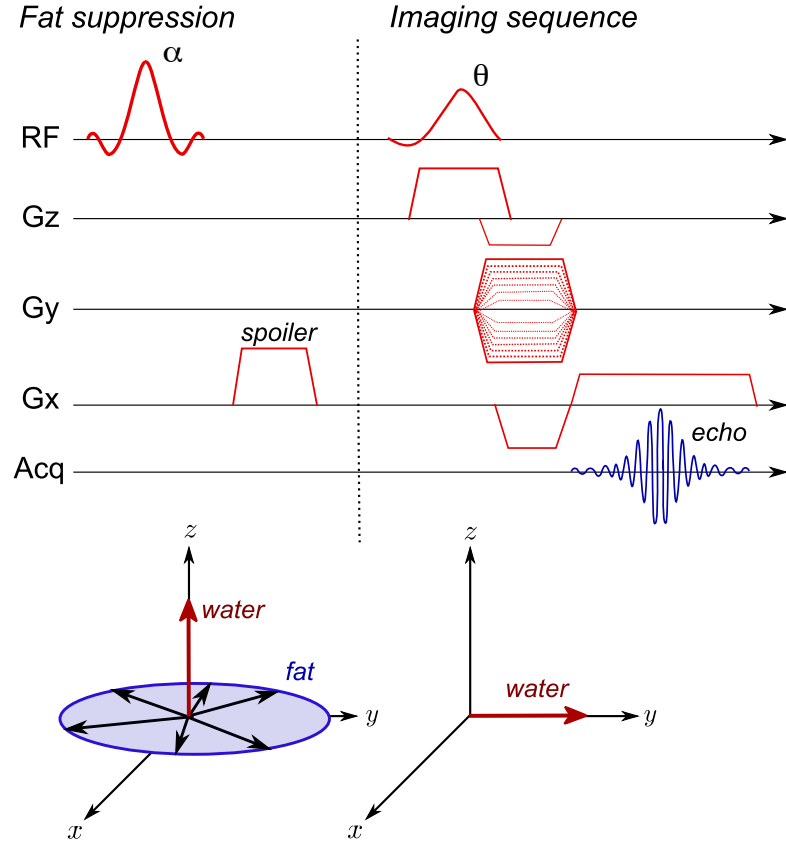
Figure 2.17: Diagram of a fat suppression sequence applied immediately before the imaging sequence. A spectrally selective pulse of flip angle α excites only the fatty tissues, and the subsequent spoiler gradient destroys the transverse magnetization. The excitation pulse of the imaging sequence is applied before the longitudinal magnetization of fat has had time to recover, so that only water spins are excited.

of fat ($BW \geq \Delta f$). Taking into account Equation 2.41, the water-fat shift for a given read out gradient can be expressed as:

$$\delta x = \frac{B_0}{G_x} \times \Delta\delta[ppm] \times 10^{-6}. \tag{2.44}$$

As an example, at 7 T with G_x=30mT/m, the water-fat shift is 0.79 mm in the x-direction. For EP images, where $< G_y >=< G_x > /N$, with a matrix size of N=64 in phase encoding direction, the water fat shift will be $\delta y \approx N\delta x = 50.6mm$. This will cause large water fat shift in the phase encoding direction. Fat signal appears bright in T_2-weighted images. Since

the T_2 relaxation time of fat is short (52 ms at 7 T [38]), one way of alleviating this artefact is to use a longer TE. However this will reduce sensitivity to BOLD contrast particularly at 7 T, as the T_2 of tissue is also short. The most efficient way to eliminate the fat artefact is to use fat suppression. This can be achieved with spectrally selective pulses, as illustrated in Fig. 2.17. Prior to the imaging sequence, the signal from lipids is suppressed in the following way: the spectrally selective pulse flips the lipid magnetization into the transverse plane, while leaving the water magnetization unperturbed along the longitudinal axis. The spectral profile of the RF pulse must be broad enough to cover the majority of the lipid resonance frequencies, but not wide enough to affect the water signal. One or more spoiler gradient pulses are subsequently applied to dephase the excited fat signals. The spoiler gradient has no effect on water signals because the water magnetization is stored along the longitudinal axis. The subsequent excitation pulse of the imaging sequence will only affect water, since the fat longitudinal magnetization is zero. Since the T_1 of the lipids is relatively short, longitudinal magnetization of the fatty tissue can regrow during the sequence. To offset the rapid lipid signal recovery, a bigger flip angle rather than 90° is often used in fat suppression pulses. This is the case for the Spectral Pre-saturation with Inversion Recovery (SPIR) [39] and Spectral Attenuation with Inversion Recovery (SPAIR) [40] methods implemented in the Philips scanner. In contrast to SPIR (see Chapter 7), for SPAIR the selective presaturation is performed with an adiabatic excitation pulse. An alternative method to suppress the signal from fat, also implemented in the Philips scanner, is the ProSet Water-only Selection Technique (WAST) [41, 42]. This technique uses a binomial pulse to excite the water signal, while lipid spins are left in equilibrium, thereby producing no signal.

The signal from fat can also be eliminated with a Slice Selective Gradient Reversal (SSGR) technique [43], which is described in detail in Chapter 7. Very recently, the use of a refocusing pulse of long duration has demonstrated excellent fat suppression at 7 T [44]. As the refocusing pulse increases in duration the bandwidth decreases and signal from fat is therefore not refocussed. Since
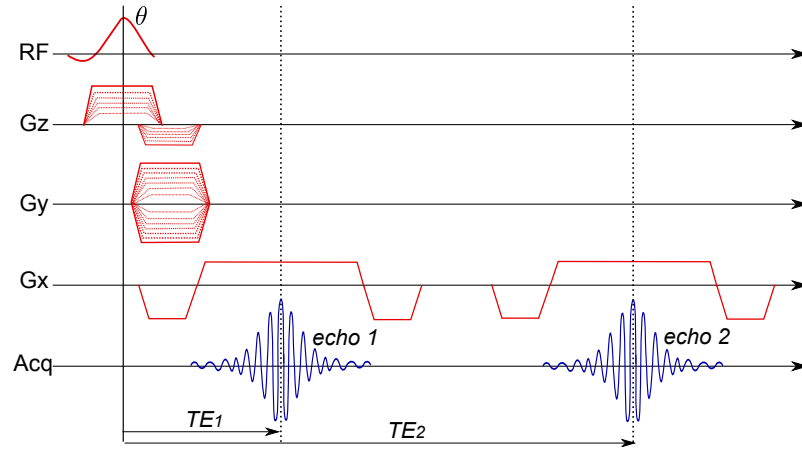
Figure 2.18: Timing diagram for a double echo - gradient echo field mapping sequence. The applied gradients cause echo 1 and echo 2 to be formed along the same k-space line.

the RF power deposition also increases as the refocusing pulse is lengthened, this technique has also the potential to reduce the SAR.

2.3.3   Field map acquisition

It is possible to measure the field inhomogeneities with a field mapping sequence. In the most common sequence two gradient echo images are acquired with slightly different echo times, for example 6 and 7 ms. A double gradient echo sequence with echo times TE_1 and TE_2 is shown in Fig. 2.18. Local magnetic field offsets, ΔB_z, will modify the phase of the spins in that area. The phase difference from one image to another, $\Delta\phi(r)$, is proportional to both the field inhomogeneity in that voxel and the echo time difference ΔTE,

$$\Delta\phi(r) = \gamma \cdot \Delta B_z(r) \cdot \Delta TE. \tag{2.45}$$

The field offset can therefore be calculated from the measured phase difference;

$$\Delta B_z(r) = \frac{\Delta\phi(r)}{\gamma \cdot \Delta TE} \ . \tag{2.46}$$

Field maps generated using this method can be used to correct distortions in EP images and this process is described in Section 4.3.3.

Bibliography

[1] M. H. Levitt. *Spin Dynamics: Basics of Nuclear Magnetic Resonance.* John Wiley and Sons, Ltd., (2001).

[2] R. H. Hashemi and W. G. Bradley. *MRI: The Basics.* Lippincott Williams and Willkins., (19997).

[3] F. Bloch, W. W. Hansen, and M. Packard. Nuclear Induction. *Physical Review*, **69**(3068), 127, (1946).

[4] E. M. Purcell, H. C. Torrey, and R. V. Pound. Resonance Absorption by Nuclear Magnetic Moment in a Solid. *Physical Review.*, **69**, 37–38, (1946).

[5] S. Clare and P. Jezzard. Rapid T1 mapping using multislice echo planar imaging. *Magn Reson Med*, **45**(4), 630–634, (2001).

[6] P. J. Wright, O. E. Mougin, J. J. Totman, A. M. Peters, M. J. Brookes, R. Coxon, P. E. Morris, M. Clemence, S. T. Francis, R. W. Bowtell, and P. A. Gowland. Water proton T1 measurements in brain tissue at 7, 3, and 1.5 T using IR-EPI, IR-TSE, and MPRAGE: results and optimization. *MAGMA*, **21**(1-2), 121–130, (2008).

[7] W. D. Rooney, G. Johnson, X. Li, E. R. Cohen, S.-G. Kim, K. Ugurbil, and C. S. Springer. Magnetic field and tissue dependencies of human brain longitudinal 1H2O relaxation in vivo. *Magn Reson Med*, **57**(2), 308–318, (2007).

[8] J. P. Wansapura, S. K. Holland, R. S. Dunn, and W. S. Ball. NMR relaxation times in the human brain at 3.0 tesla. *J Magn Reson Imaging*, **9**(4), 531–538, (1999).

[9] E. Yacoub, T. Q. Duong, P.-F. V. D. Moortele, M. Lindquist, G. Adriany, S.-G. Kim, K. Ugurbil, and X. Hu. Spin-echo fMRI in humans using high spatial resolutions and high magnetic fields. *Magn Reson Med*, **49**(4), 655–664, (2003).

[10] A. M. Peters, M. J. Brookes, F. G. Hoogenraad, P. A. Gowland, S. T. Francis, P. G. Morris, and R. Bowtell. T2* measurements in human brain at 1.5, 3 and 7 T. *Magn Reson Imaging*, **25**(6), 748–753, (2007).

[11] E. L. Hahn. Spin Echoes. *Physical Review*, **80**, 580–594, (1950).

[12] R. Turner, D. L. Bihan, C. T. Moonen, D. Despres, and J. Frank. Echo-planar time course MRI of cat brain oxygenation changes. *Magn Reson Med*, **22**(1), 159–166, (1991).

[13] S. Ogawa, D. W. Tank, R. Menon, J. M. Ellermann, S. G. Kim, H. Merkle, and K. Ugurbil. Intrinsic signal changes accompanying sensory stimulation: functional brain mapping with magnetic resonance imaging. *Proc Natl Acad Sci U S A*, **89**(13), 5951–5955, (1992).

[14] K. K. Kwong, J. W. Belliveau, D. A. Chesler, I. E. Goldberg, R. M. Weisskoff, B. P. Poncelet, D. N. Kennedy, B. E. Hoppel, M. S. Cohen, and R. Turner. Dynamic magnetic resonance imaging of human brain activity during primary sensory stimulation. *Proc Natl Acad Sci U S A*, **89**(12), 5675–5679, (1992).

[15] P. A. Bandettini, E. C. Wong, R. S. Hinks, R. S. Tikofsky, and J. S. Hyde. Time course EPI of human brain function during task activation. *Magn Reson Med*, **25**(2), 390–397, (1992).

[16] J. W. Belliveau, D. N. Kennedy, R. C. McKinstry, B. R. Buchbinder, R. M. Weisskoff, M. S. Cohen, J. M. Vevea, T. J. Brady, and B. R. Rosen. Functional mapping of the human visual cortex by magnetic resonance imaging. *Science*, **254**(5032), 716–719, (1991).

[17] P. C. Lauterbur. Image formation by induced local interactions. Examples employing nuclear magnetic resonance. *Nature*, **242**, 190–191, (1973).

[18] A. N. Garroway, P. K. Grannel, and P. Mansfield. Image formation in NMR by a selective irradiative process. *Journal of Physics C: Solid State Physics*, **7**, 457–462, (1974).

[19] A. Kumar, D. Welti, and R. R. Ernst. NMR Fourier zeugmatography. *NMR Fourier zeugmatography.*, **18**, 69–83, (1975).

[20] P. Mansfield. Multi-planar image formation using NMR spin echoes. *J Phys C*, **10**(6), L55–L58, (1977).

[21] J. M. Pauly, D. G. Nishimura, and A. Macovski. A k-Space Analysis of Small-Tip-Angle Excitation. *J Magn Reson*, **81**, 43–56, (1989).

[22] W. A. Edelstein, J. M. Hutchison, G. Johnson, and T. Redpath. Spin warp NMR imaging and applications to human whole-body imaging. *Phys Med Biol*, **25**, 751–756, (1980).

[23] S. Ljungren. A Simple Graphical Representatio of Fourier-Based Imaging Methods. *Journal of Magnetic Resonance*, **54**, 338–343, (1983).

[24] M. K. Stehling, R. Turner, and P. Mansfield. Echo-planar imaging: magnetic resonance imaging in a fraction of a second. *Science*, **254**(5028), 43–50, (1991).

[25] A. M. Howseman, M. K. Stehling, B. Chapman, R. Coxon, R. Turner, R. J. Ordidge, M. G. Cawley, P. Glover, P. Mansfield, and R. E. Coupland. Improvements in snap-shot nuclear magnetic resonance imaging. *Br J Radiol*, **61**(729), 822–828, (1988).

[26] K. Farahani, U. Sinha, S. Sinha, L. C. Chiu, and R. B. Lufkin. Effect of field strength on susceptibility artifacts in magnetic resonance imaging. *Comput Med Imaging Graph*, **14**(6), 409–413, (1990).

[27] J. Frahm, K. D. Merboldt, and W. Hnicke. Direct FLASH MR imaging of magnetic field inhomogeneities by gradient compensation. *Magn Reson Med*, **6**(4), 474–480, (1988).

[28] Z. H. Cho and Y. M. Ro. Reduction of susceptibility artifact in gradient-echo imaging. *Magn Reson Med*, **23**(1), 193–200, (1992).

[29] E. M. Haacke, J. A. Tkach, and T. B. Parrish. Reduction of T2* dephasing in gradient field-echo imaging. *Radiology*, **170**(2), 457–462, (1989).

[30] Q. X. Yang, G. D. Williams, R. J. Demeure, T. J. Mosher, and M. B. Smith. Removal of local field gradient artifacts in T2*-weighted images at high fields by gradient-echo slice excitation profile imaging. *Magn Reson Med*, **39**(3), 402–409, (1998).

[31] T. G. Reese, T. L. Davis, and R. M. Weisskoff. Automated shimming at 1.5 T using echo-planar image frequency maps. *J Magn Reson Imaging*, **5**(6), 739–745, (1995).

[32] I. R. Young, I. J. Cox, D. J. Bryant, and G. M. Bydder. The benefits of increasing spatial resolution as a means of reducing artifacts due to field inhomogeneities. *Magn Reson Imaging*, **6**(5), 585–590, (1988).

[33] R. Deichmann, J. A. Gottfried, C. Hutton, and R. Turner. Optimized EPI for fMRI studies of the orbitofrontal cortex. *Neuroimage*, **19**(2 Pt 1), 430–441, (2003).

[34] K. P. Pruessmann, M. Weiger, M. B. Scheidegger, and P. Boesiger. SENSE: sensitivity encoding for fast MRI. *Magn Reson Med*, **42**(5), 952–962, (1999).

[35] X. Golay, K. P. Pruessmann, M. Weiger, G. R. Crelier, P. J. Folkers, S. S. Kollias, and P. Boesiger. PRESTO-SENSE: an ultrafast whole-brain fMRI technique. *Magn Reson Med*, **43**(6), 779–786, (2000).

[36] R. Bammer, S. L. Keeling, M. Augustin, K. P. Pruessmann, R. Wolf, R. Stollberger, H. P. Hartung, and F. Fazekas. Improved diffusion-weighted single-shot echo-planar imaging (EPI) in stroke using sensitivity encoding (SENSE). *Magn Reson Med*, **46**(3), 548–554, (2001).

[37] R. Deichmann, O. Josephs, C. Hutton, D. R. Corfield, and R. Turner. Compensation of susceptibility-induced BOLD sensitivity losses in echo-planar fMRI imaging. *Neuroimage*, **15**(1), 120–135, (2002).

[38] J. Ren, I. Dimitrov, A. D. Sherry, and C. R. Malloy. Composition of adipose tissue and marrow fat in humans by 1H NMR at 7 Tesla. *J Lipid Res*, **49**(9), 2055–2062, (2008).

[39] E. Kaldoudi, S. C. Williams, G. J. Barker, and P. S. Tofts. A chemical shift selective inversion recovery sequence for fat-suppressed MRI: theory and experimental validation. *Magn Reson Imaging*, **11**(3), 341–355, (1993).

[40] P. Muertz, C. Krautmacher, F. Trber, J. Gieseke, H. H. Schild, and W. A. Willinek. Diffusion-weighted whole-body MR imaging with background body signal suppression: a feasibility study at 3.0 Tesla. *Eur Radiol*, **17**(12), 3031–3037, (2007).

[41] C. H. Meyer, J. M. Pauly, A. Macovski, and D. G. Nishimura. Simultaneous spatial and spectral selective excitation. *Magn Reson Med*, **15**(2), 287–304, (1990).

[42] F. Schick, J. Forster, J. Machann, P. Huppert, and C. D. Claussen. Highly selective water and fat imaging applying multislice sequences without sensitivity to B1 field inhomogeneities. *Magn Reson Med*, **38**(2), 269–274, (1997).

[43] J. M. Gomori, G. A. Holland, R. I. Grossman, W. B. Gefter, and R. E. Lenkinski. Fat suppression by section-select gradient reversal on spin-echo MR imaging. Work in progress. *Radiology*, **168**(2), 493–495, (1988).

[44] D. Ivanov, A. Schaefer, M. Streicher, R. Trampel, and R. Turner. Fat Suppresion with Low SAR for SE EPI fMRI at 7 T. *Proceedings of the 17th Annual Meeting of ISMRM, Honolulu, USA, 1547.*, (2009).

Chapter 3

Overview of an MRI system

This Chapter gives a brief overview of a magnetic resonance imaging system with particular reference to the 7 T Philips system at which the work in this thesis was performed. Figure 3.1 shows an schematic diagram with the principal components. The most significant part of any MR system is the main magnet. The bore of the magnet contains the shim and gradient coils. The 7T Philips system has a patient bore size of 58 cm with the RF coil attached to the patient bed, inserted into the magnet. The operation of the principal components is described in the following sections.

3.1 Main magnet

In current commercial MRI systems an electro-magnet provides the static B_0 field. To produce an intense homogenous magnetic field, such as 7 T, a coil of super-conducting material such as Niobium- Titanium (Nb3 Ti) is usually used. Nb3 Ti becomes superconducting at temperatures below 10K, therefore the wires are held in a superconducting state by immersion in liquid helium at 4K. An MRI system requires the main magnet to produce a highly spatially uniform magnetic field and have good temporal stability. For the Philips 7 T system, the field stability is of the order of 0.10 ppm in a 25 cm diameter spherical volume.

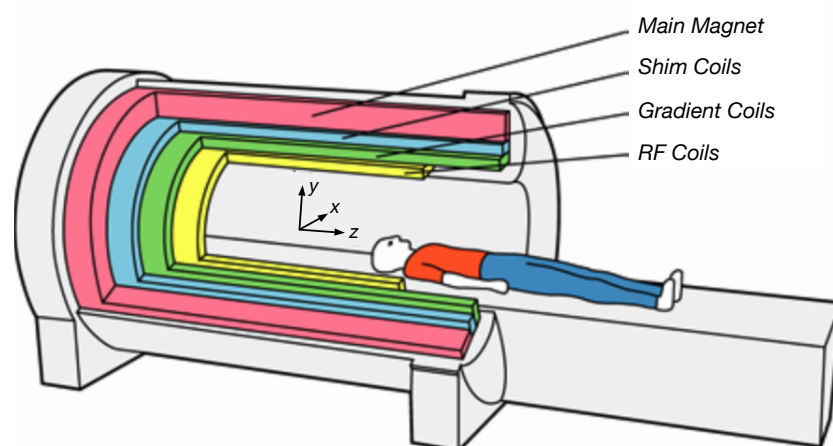Another important property of a magnet is how far the fringe field (the

Figure 3.1: Schematic of a whole-body MRI scanner with cut-away section to show the principal components. Reproduced from [1].

field outside the scanner bore) stretches. For safety reasons, access must be restricted to areas exposed to more than 0.5 mT (to prevent interference with pacemakers, for example). The Nottingham 7 T system is surrounded by 200 tonnes of passive iron shielding to reduce the size of the fringe field.

3.2   Shim coils

When a subject is placed into the static B_0-field, the field is distorted by susceptibility differences between different materials in the subject. To ensure the magnetic field generated by the main electromagnet is as homogeneous as possible, a set of shim coils are placed within the bore of the magnet.

The process of homogenising the magnetic field is done through both passive and active shimming. Passive shimming involves the placement of ferromagnetic blocks of material in the magnet's bore that correct for minor inhomogeneities of the field. After placing a subject in the scanner, active shimming is performed by adjusting currents in the shim coils. On the Philips systems, an auto-shimming routine is included in the pulse sequence set-up process. Automatic FID shimming was first proposed by Ernst [2], and successfully implemented by Tochtrop [3] and Holz [4]. Field homogeneity is

measured by examining an FID signal in the absence of field gradients and adjusting the shim currents to produce a large amplitude exponentially decaying FID. An alternative field map based shimming is explained in Section 4.3.3.

3.3 Gradient coils

Gradient coils are large resistive coils, usually positioned inside the shim coils, used to produce magnetic fields in the the x-, y-, and z-directions. These fields are used for spatially encoding the NMR signal for MRI as described in Section 2.2.3. Due to the high current carried by coils during an imaging sequence (~ 600 A), the coils are often water cooled to prevent over heating. The Philips gradient systems produce a peak field strength of 40 mT/m using a slew rate of 200 mT/m/ms. However during this work this was limited to 33 mT/m using a slew rate of 166 mT/m/ms. However it was found that due to Peripheral Nerve Stimulation (PNS) issues it was necessary to further reduce the gradient strength to 30 mT/m and the slew rate to 100 mT/m/ms.

3.4 RF system

The RF system generates the oscillating B_1-field to excite the sample and detect the resulting NMR signal. The RF coil is located within the gradient coils closest to the object that is to be scanned. The RF signal is generated by the spectrometer. An adjustable frequency synthesizer produces the pure radio frequency signal ω_0, which is then mixed with a pulse envelope (for example a sinc function) and amplified: the Nottingham Philips 7 T system is equipped with a 4 kW amplifier. The RF probe then converts the electrical signal from the power amplifier into a homogeneous oscillating magnetic field inside the sample. Following excitation, the system switches to receive mode. The receive probe detects the weak rotating magnetic field generated by the precessing spins after excitation and converts it back to an electrical signal via Farady induction. The signal is amplified and passed to the spectrometer

which uses two quadrature phase sensitive detectors, as described in Section 2.1.7., to demodulate the signal.

The same RF coil may be used for both transmission and reception. A volume transmit/receive head coil supplied by the manufacturer was used as both transmitter and receiver for the experiments described in Section 4.2.2. A NOVA head coil with 16 independent receive channels become available in early 2007, which was used for the remainder of the experiments in this thesis, allowing the implementation of parallel imaging [5, 6].

Bibliography

[1] M. Poole. *Improved Equipment and Techniques for Dynamic Shimming in High Field MRI.* PhD thesis, University of Nottingham, (2007).

[2] R. R. Ernst. Measurement and Control of Magnetic Field Homogeneity. *Review of Scientific Instruments*, **39 (7)**, 998–1012, (1968).

[3] M. Tochtrop, W. Vollmann, D. Holz, and C. Leussler. Automatic Shimming of Selected Volumes in Patients. *Proceedings of the Society for Magnetic Resonance in Medicine*, **6**, 816, (1987).

[4] D. Holz, D. Jensen, R. Proksa, M. Tochtrop, and W. Vollmann. Automatic shimming for localized spectroscopy. *Med Phys*, **15**(6), 898–903, (1988).

[5] K. P. Pruessmann, M. Weiger, M. B. Scheidegger, and P. Boesiger. SENSE: sensitivity encoding for fast MRI. *Magn Reson Med*, **42**(5), 952–962, (1999).

[6] D. K. Sodickson and W. J. Manning. Simultaneous acquisition of spatial harmonics (SMASH): fast imaging with radiofrequency coil arrays. *Magn Reson Med*, **38**(4), 591–603, (1997).

Chapter 4

Methods for high resolution brain imaging at ultra-high field

This chapter describes the methodology used in Chapters 5, 6 and 7 of this thesis. It begins with an introduction to magnetic resonance imaging at ultra-high field (7T). The imaging sequences and the methods used and developed in this thesis to acquire structural images with fine spatial resolution and high-resolution BOLD-based activation maps are then discussed. Finally, the methods used to unfold cortical surfaces to provide improved visualization and interpretation of activation maps, and delineation of anatomically defined borders is described.

4.1   Ultra-high field imaging

Commonly used Magnetic Resonance Imaging (MRI) scanners operate at field strengths of 1.5 or 3 Tesla (T). At these field strengths it is possible to obtain high quality images of brain anatomy, but the low signal to noise ratio (SNR) limits the evaluation of subtle abnormalities. Ultra-high field imaging provides improved SNR and BOLD contrast, as well as lengthened longitudinal relaxation times, but also poses many technical challenges, since field inhomogeneities and thus image distortions are increased. The main technical issues are listed in the following sections.

Signal to noise ratio (SNR)

The image signal to noise ratio (SNR) available in MRI increases with the static magnetic field strength, B_0. At magnetic fields up to 4 T, the increase is approximately linearly [1, 2]. At magnetic fields greater than 4 T, the SNR dependence becomes complex because B_1-inhomogeneities results in the gain in sensitivity being position dependent. In one comparison between 4 and 7 T human brain imaging using a transverse electromagnetic (TEM) volume head coil, an average increase of 1.76 in SNR was recorded [3]. However, the increase was not spatially uniform, with the measured gain varying from a value of 2.1 at the centre of the head to 1.4 at the periphery. The overall increase in SNR at ultra-high field can be traded for increased spatial resolution or reduced image acquisition time.

However, in functional MRI, in addition to the inherent thermal image noise, sensitivity is also affected by noise due to physiological signal fluctuations, such as those associated with the cardiac cycle and respiration [4]. This physiological noise increases with magnetic field strength [5, 6]. In a study comparing noise in functional MRI time series across field strengths of 1.5, 3 and 7 T [6], it was found that the ratio of physiological noise to thermal image noise increases from 0.61/0.89 at 1.5/3 T, to 2.23 at 7 T for a spatial resolution of 3×3×3mm^3 (TR=3 s). At this spatial resolution, the increase in image SNR at 7 T consequently only produces a modest increase in temporal SNR . However, it was found that the ratio of physiological to thermal noise at 7 T was significantly reduced to 0.91 by increasing the resolution to 1×1×3 mm^3. Therefore, at high resolution the physiological noise contribution is reduced to a level where the increased sensitivity available at ultra-high field translates into a considerable improvement in the SNR of fMRI time series.

B_1 homogeneity

Human brain images acquired at ultra high-field (4 T and higher) with an RF coil with volume coverage are generally characterized by a hyperintense re-

gion at the centre of the image compared to the periphery due to an increased B_1-amplitude at the centre of the brain [7, 8, 3]. This phenomenon has been investigated experimentally and through simulations [9, 10, 11, 12], suggesting that interferences between standing waves and/or dielectric resonance effects are responsible for the non-uniform signal intensities observed at ultra-high field. Dielectric effects become relevant as the RF wavelength becomes comparable to the dimension of the target object [7]. Resonant frequency increases linearly with magnetic field strength and at 7 T, the proton resonant frequency is 300 MHz, yielding a wavelength of approximately 13 cm in tissue. Since this wavelength is smaller than the dimensions of the human head, the strength and phase of the radiofrequency B_1 field can vary considerably with position within the sample, producing field cancellation due to interference. Thus, the RF magnetic field inside the human brain exhibits a standing wave behavior, destroying the otherwise homogeneous field produce by an unloaded coil [2, 10]. Under these circumstances, the electrical properties, geometry, and relative position of the sample in the coil become important factors in determining the RF distribution inside the sample [10]. Various methods are being investigated to reduce these strong transmit B_1 - homogeneities, such as counterbalancing by RF shimming techniques [13, 14] or use of multiple RF transmitter coils in transmit SENSE[15, 16].

Power deposition

Theoretical calculations predict that the RF power required for signal excitation increases quadratically with field strength up to approximately 200 MHz, at which point it then increases more slowly [17]. This has also been confirmed experimentally [8, 3]. For example, the required RF power increases by a factor of 1.8 from 4 to 7 T [3], rather than the factor of 3 predicted by the standard square-law. The increased RF power deposition results in a high Specific Absorption Rate (SAR) at high and ultra-high field. SAR, defined as RF power absorbed per unit of mass of an object, describes the potential for heating of the patient's tissue and can therefore lead to a significant restriction

for pulse sequences employing multiple refocusing pulses.

4.2 Anatomical imaging

Anatomical images of brain tissue generally rely on the contrast induced by differences in the T_1 and T_2 relaxation times of different tissues. At higher field the spin-lattice relaxation time, T_1, increases, whereas the spin-spin relaxation time, T_2, is slightly reduced (See Chapter 2 for further details). Therefore standard clinical MR sequences must be adapted at ultra-high field to achieve the desired contrast. It has been shown that the Turbo Spin Echo (TSE) sequence enables the acquisition of images with high resolution and tissue contrast in the brain in relatively short scan times [18, 19, 20]. The insensitivity to local B_0-field variation, due to the multiple refocusing pulses of the TSE sequence, which refocus macroscopic field inhomogeneities, makes it an ideal candidate for T_2-weighted imaging at ultra-high field, however SAR may be an issue. Rapid acquisition of high resolution images of the human brain with high T_1 contrast has been accomplished with three dimensional magnetization prepared fast spoiled gradient echo (MPRAGE) imaging [21, 22, 23, 24]. $T_2^\star$-weighted images suffer less from artifacts related to inhomogeneous RF excitation fields and require a relatively low RF power, but need to be performed at sufficiently high resolution to avoid through-plane dephasing artefacts related to macroscopic susceptibility effects, which otherwise can obscure fine anatomical detail. $T_2^\star$ contrast increases dramatically with field strength. This mechanism has been proved to be useful for visualising vessels containing deoxyhaemoglobin [25, 26], to provide contrast between brain tissues such as grey and white matter [27], to reveal tissue heterogeneity within white matter [28] and to map iron containing subcortical structures [29, 30, 31]. It has also been shown that the use of MR signal phase in gradient echo images can improve contrast in specific human brain structures such as veins and iron rich regions [32, 33, 31, 34, 35, 36], and also provides good contrast between grey and white matter [33, 31, 36].

4.2.1   Imaging sequences

2D Fast-Low Angle SHot

Fast-Low Angle SHot (FLASH) [37] is a gradient echo pulse sequence primarly used for fast anatomical scanning. Figure 4.1 shows a schematic diagram of the FLASH sequence with two dimensional cartesian encoding. The sequence consists of a train of RF pulses of flip angle, α, with pulses separated by a time TR. Since the sequence uses an excitation pulse of flip angle, α, which is usually of 20°-30°, much less than 90°, a short period for recovery of the longitudinal magnetization can be used and thus a short repetition time (TR). Each excitation pulse is applied in conjunction with a slice select z-gradient, to create a given amount of transverse magnetization in the selected slice which then produces a FID. The FID is rephased into a gradient echo using the readout gradient (G_x). The y-gradient trace shows the phase-encoding lobe applied before the acquisition, and a phase rewinder lobe of opposite polarity applied after the acquisition to return the spins to zero phase. To produce $\mathrm{T}_2^\star$- weighting contrast, the TE is made relatively long (approximately 20 ms at 7 T), and the TR is at least four to five times T_2, so that the transverse magnetization M_{xy} decays to zero between excitation pulses. If $\mathrm{TR} \ll 5\mathrm{T}_2$, spoiling has to be used. In a multi-slice technique, several slices are acquired within the TR period. The length of TR determines the number of slices that can be sampled. When low flip angles are used, an appreciable amount of transverse magnetization is created, but the longitudinal magnetization is relatively unperturbed.

It is important to examine how the longitudinal magnetization responds to the series of RF excitation pulses and approaches a steady state [38]. The magnetization in the imaging slice experiences a series of identical excitation pulses with flip angle, α, evenly spaced in time by TR. After a sufficient number of excitation pulses, the longitudinal magnetization M_z, reaches a steady state. For a spin ensemble with density M_0 and longitudinal relaxation time T_1, if we assume perfect spoiling of transverse magnetization before each RF pulse,
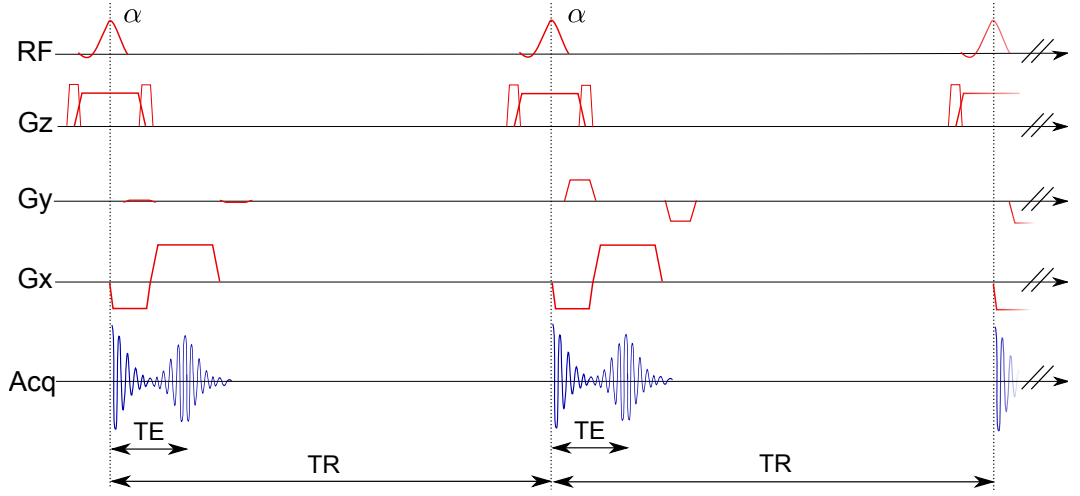
Figure 4.1: (A) 2D FLASH pulse sequence diagram.

the longitudinal magnetization after each subsequent excitation pulse can be calculated recursively from

$$M_z(i+1) = M_0 \left(1 - e^{-\frac{TR}{T_1}}\right) + M_z(i)\cos(\alpha)e^{-\frac{TR}{T_1}}, \qquad (4.1)$$

The steady state for the longitudinal magnetization is reached when $M_z(i) = M_z(i+1)$, so that

$$M_z(i) = M_0 \frac{1 - e^{-\frac{TR}{T_1}}}{1 - \cos(\alpha)e^{-\frac{TR}{T_1}}} \qquad (4.2)$$

Figure 4.2 illustrates the approach to steady state for various flip angle and for TR values of 0.1 and 0.01 times T_1. The approach to steady state is faster for larger values of the flip angle. It is of practical importance to predict how long it takes for the steady state to be established. This can be used to estimate how many start-up pulses (i.e, those applied without data collection) to play out so as not to collect k-space data during the approach to steady state.

(i) Magnitude Image

In conventional gradient echo imaging, a magnitude image is formed, and shows contrast which depends upon transverse T_2 relaxation, as well as an
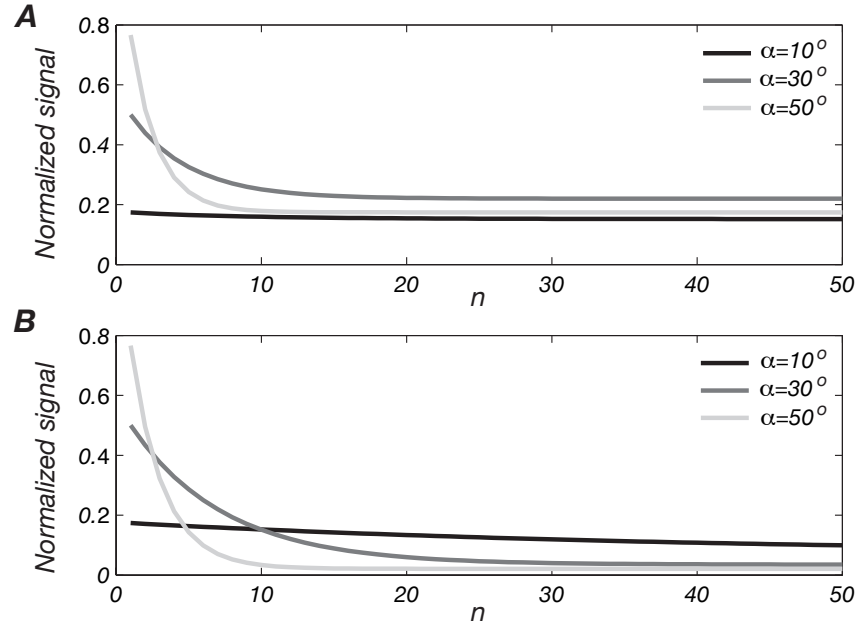
Figure 4.2: The approach to steady state for a spoiled GE pulse sequence plot versus the number of excitation pulses that the magnetization experiences (A) $TR/T_1=0.1$, which corresponds to an Ernst angle of 25.2° and (B) $TR/T_1=0.01$ with corresponding Ernst angle of 8°.

additional signal loss originating from intra-voxel dephasing due to susceptibility induced field variation. This additional relaxation term scales with field strength because of the increased magnetic susceptibility effects at high field, resulting in $T_2^\star$ contrast dominating. $T_2^\star$ contrast provides unique information on tissue magnetic susceptibility which can be used to study brain iron concentration [39, 40, 41], hemorrhage and calcification [42, 43] as well as any functional brain process or pathological alteration that changes the brain blood oxygenation distribution. However, $T_2^\star$-weighted images are prone to large signal void artefacts in the inferior frontal and inferiolateral temporal lobes produced by the susceptibility differences between tissue and other air-containing structures. Small field gradients arising from the heterogenous magnetic susceptibility of tissue can also cause distortions in the image.

The relevant signal $S(i)$ in a gradient echo sequence depends on the gradient

rephasing of the FID at echo time, TE, and is given by:

$$S(i) = \frac{M_0 \sin(\alpha)(1 - e^{-\frac{TR}{T_1}})}{1 - \cos(\alpha)e^{-\frac{TR}{T_1}}} e^{-\frac{TE}{T_2^\star}}. \tag{4.3}$$

The maximum signal can be obtained for a flip angle α_E, the Ernst angle, where

$$\alpha_E = \arccos(e^{-\frac{TR}{T_1}}). \tag{4.4}$$

The Ernst angle lies between 0 and 90° and increases with the ratio TR/T_1.

(ii) Phase Image

MR data is complex so it has phase as well as magnitude. It has been shown recently that the phase of the gradient echo signal can be used to form anatomical images. The phase in a MR image depends on the echo time and field offset, ΔB

$$\phi = \gamma \Delta B \cdot TE. \tag{4.5}$$

Therefore, to achieve sensitivity to small local variations in field, images must be acquired with long echo times (TE) or at high field so as to increase the magnitude of ΔB. Unfortunately it is not simple to use phase images directly to investigate anatomy as there are unwanted phase variations originating from poor shimming and background phase effects in images caused by air-tissue interfaces. Dephasing across a voxel can be reduced by using very small voxels, so that the phase variation from background field inhomogeneity can be reduced to less than 2π across the voxel [25]. Since the phase is only defined in the range of $(-\pi, +\pi)$, phase unwrapping must be applied to phase images before all further processing steps. Phase-unwrapping algorithms that preserve all phase information have been developed and applied to MR imaging [44, 45, 46]. Field variations from imperfect shimming or distant large air cavities, which usually have low spatial frequencies, can be removed by applying a high-pass filter to the phase images [47, 48] or by estimating their magnitude and distribution from a low-order polynomial fit to the phase data [36].
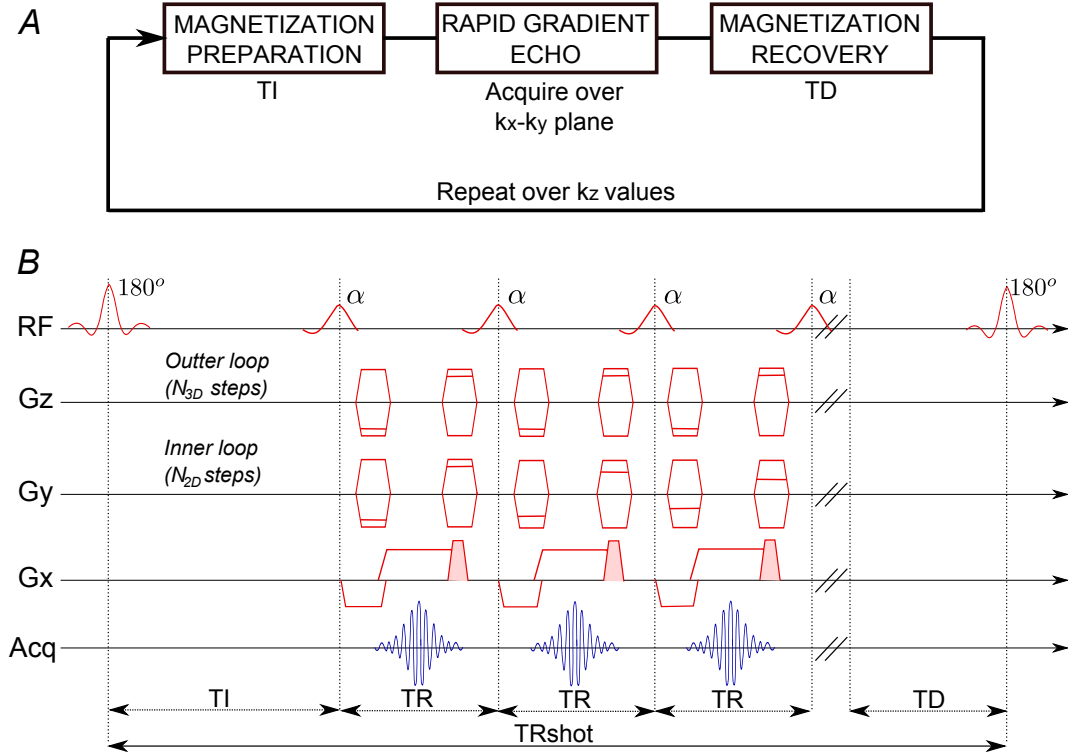
Figure 4.3: (A) Schematic diagram of the MPRAGE sequence and (B) MPRAGE pulse sequence diagram. Shaded gradients indicate spoilers.

MPRAGE

Magnetization-Prepared Rapid Gradient Echo (MPRAGE) imaging, also known as three dimensional Fast Field Echo (3D FFE) imaging [49], is an alternative technique for structural imaging. A schematic representation of this technique is shown in Fig.4.3.a. The sequence consists of three time periods. The first is a magnetization preparation period which introduces contrast into the image; to produce T_1 contrast this preparation period consists of an RF pulse of flip angle θ followed by a delay, TI. Most frequently θ values of 120° and 180° (inversion) are used. The magnetization preparation period is followed by an acquisition period, during which the data are acquired over a given plane using a spoiled FLASH sequence. After the acquisition period, the magnetization is allowed to recover for a time TD before the next inversion pulse is applied. This is termed the magnetization recovery period.

An MPRAGE pulse sequence diagram is shown in Fig. 4.3.b. In a 3D

acquisition method, two phase encoding gradients are applied, for example, as shown in Fig.4.3.b, one in the k_y direction and a second in the k_z direction, the latter being referred to as the slice (or partition) encoding gradient. The matrix size during image acquisition is given by N_R (Read) $\times$ N_{2D} (Phase) $\times N_{3D}$ (Partition). In conventional MPRAGE sequences k-space data are acquired over k_x-k_z planes during the acquisition period. However, if a small number of slices are to be imaged, the scanning time can be significantly reduced by changing the phase encoding gradients so that the slice encoding direction is stepped through in the outer loop and the phase encoding varied through the acquisition train, hence acquiring data over k_x-k_y planes instead. Usually the N_{2D} loop is segmented into a few acquisition trains.

The FLASH sequence consists of a train of radio frequency excitation pulses of low flip angle, α, separated by a short repetition time TR. During this short TR, the transverse magnetization does not have time to decay to zero, therefore a spoiling gradient module is applied following the readout gradient to destroy the remaining transverse magnetization (See Fig.4.3.b). Through the acquisition segment, the G_z gradient is applied at a constant level whilst the G_y phase encoding amplitude gradient varies with each TR period. If n is the number of excitation pulses in the train, named the TFE-factor on Philips scanners, then the shot repetition time, i.e., the time from one inversion pulse to the next one, is given by TI + nTR + TD.

The image contrast depends on the preparation flip angle, θ, TI and α and the order in which k-space is sampled. This order depends on the sequence in which the G_y phase-encoding gradient amplitude is varied. In a linear phase encoding scheme, where k-space is filled from the bottom (highest negative spatial frequency) to the top (highest positive spatial frequency), the zero spatial frequency is sampled at the middle of the acquisition period (see Fig. 4.4.A). With a centric (low-high) phase encoding order, as shown in Fig. 4.4.B, the zero spatial frequency is sampled first and sampling then proceeds in an alternating fashion from negative and positive, low to high spatial frequencies. This is preferred for optimizing image contrast because the image intensity is mainly
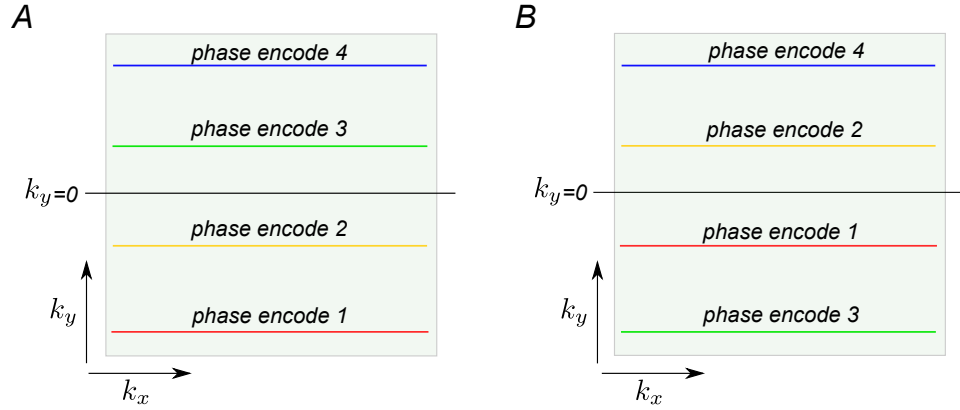
Figure 4.4: Cartesian k-space sampling trajectories with (A) linear and (B) centric (also termed low-high) phase encoding order. Each line shown on k-space corresponds to a frequency-encoded readout.

determined by the value of the longitudinal magnetization when the central k -space lines are acquired. However the variability of the signal intensity as a function of the spatial frequency (phase- encoding step) leads to a spatial filtering of the data in the phase encoding direction [50]. Although image data are acquired during the approach to steady state, a given number of start up pulses with increasing flip angle are played out before the acquisition segment to make the change in longitudinal magnetization smoother. Other k-space coverage strategies such as radial projection acquisition can also be used.

Inversion recovery Turbo Spin Echo

Turbo Spin Echo [51] is a fast imaging sequence consisting of an RF excitation pulse followed by a train of refocusing pulses which produce multiple spin echoes that are distinctively phase encoded. In this way multiple k-space lines can be sampled following each excitation pulse. An IR-TSE sequence is schematically shown in Fig. 4.5. Generally in IR-TSE, complete k-space filling is accomplished in a multi-shot acquisition. The number of refocusing pulses applied after the excitation pulse is called the echo train length (ETL), it is also known as the 'turbo factor' since this provides the factor by which the total scan time is reduced compared to a conventional spin echo sequence. However, for multi-slice acquisition the time gain may not be as large as the
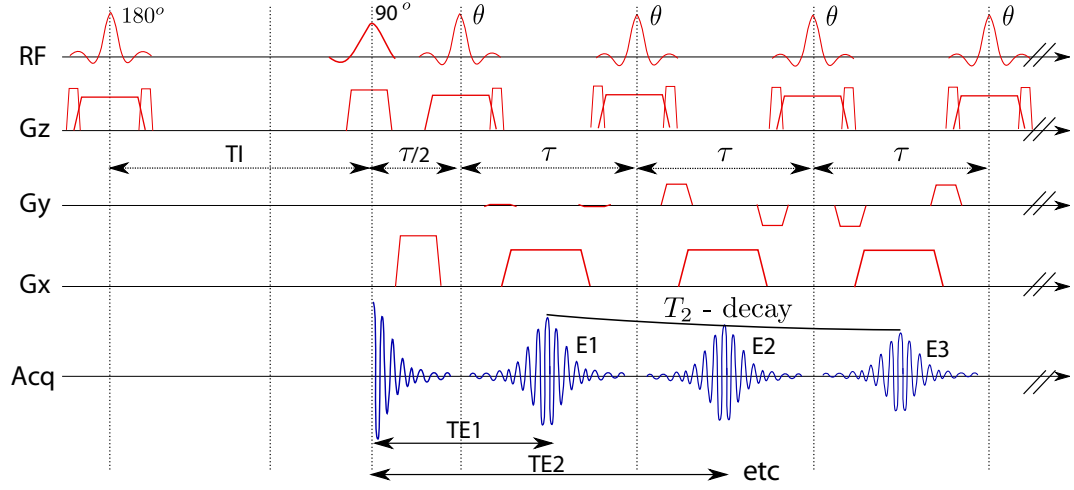
Figure 4.5: Inversion Recovery Turbo Spin Echo pulse sequence diagram

ETL, since the generation of multiple echoes leaves less time to acquire data from multiple slices within the TR-period.

In brain imaging the contrast between grey and white matter can be enhanced by preceding the TSE acquisition with an inversion recovery to produce mixed T_1 and T_2 contrast, as shown in Fig. 4.5. For 2D sequences the inversion, excitation and refocusing RF pulses are all slice selective. The repetition time (TR) is the time from one 180° inversion to the next inversion pulse. The 180° inversion pulse is followed after a delay time (TI) by a 90° excitation pulse which flips the longitudinal magnetization into the x-y plane. Each RF refocusing pulse, of flip angle, θ, is surrounded by balanced crusher gradient pulses applied in the slice select direction. If every refocusing pulse has a flip angle of 180° the spin echo signal amplitude is maximized. However in practice smaller angles are chosen to reduce the SAR, particularly at high and ultra-high field. The interval between the refocusing pulses, τ, is called the echo spacing and it is twice as long as the time delay between the excitation and the first refocusing pulse.

The echo amplitude within one train is modulated by T_2 relaxation effects, causing the echo peak amplitude to decay according to the following equation:

$$S_n \sim \rho \left(1 - 2e^{-\frac{TI}{T_1}} + e^{-\frac{TR-N}{T_1}} \right) (\sin^2(\frac{\theta}{2}))^n e^{-\frac{TE_n}{T_2}}, \tag{4.6}$$

where n is the echo index, N is the number of echoes in the train and ρ, T_1 and T_2 are the tissue proton density, longitudinal and transverse relaxation times respectively. The variable echo time $TE_n = n\tau$ results in k-space data with a non-uniform T_2 weighting. As a consequence the image is blurred in the phase encoding direction by a point spread function which depends on the properties of the tissue and the scan parameters [52]. Tissues with a short T_2 suffer more blurring than tissues with a long T_2. Image blurring by this mechanism does not occur for conventional spin echo sequences because all points along k_y have equal T_2-weighting. To minimize blurring, the echo spacing τ is kept to a minimum. The extent of the blurring increases with increasing ETL and hence it is more severe for single shot TSE acquisitions. k-space is usually therefore covered in multiple segments to reduce blurring from T_2 relaxation, but this can have the effect of introducing other artifacts in the image due to discontinuities in the signal level from one segment to the next.

On the Philips scanner the collection of an IR-TSE image is defined by a number of parameters, including TI, TR, ETL and the echo time (TE). ETL denotes the number of lines of k-space obtained per slice per TR. Image contrast is determine by TI and the effective TE; the TE selected by the user is an effective echo time and refers to the time between the excitation pulse and the formation of the echo located nearest to the centre of k-space (in the k_y- direction). Since image contrast is mainly determined by the information collected at the centre of k-space, echoes generated close to the centre of k-space determine the effective echo time and hence the image contrast. The profile order has also to be considered in order to set the effective TE to the desired value. Linear phase encoding ordering gives a long effective TE, introducing T_2-weighted contrast. To produce a T_1 weighted or proton density weighted image, centric phase encoding order is used to sample the central k-space with the earlier echoes so that the effective TE takes its minimum value. Fig. 4.6 shows the k-space trajectory for (A) linear and (C) centric phase encode order. Since the read-out gradient is not reversed, all lines in
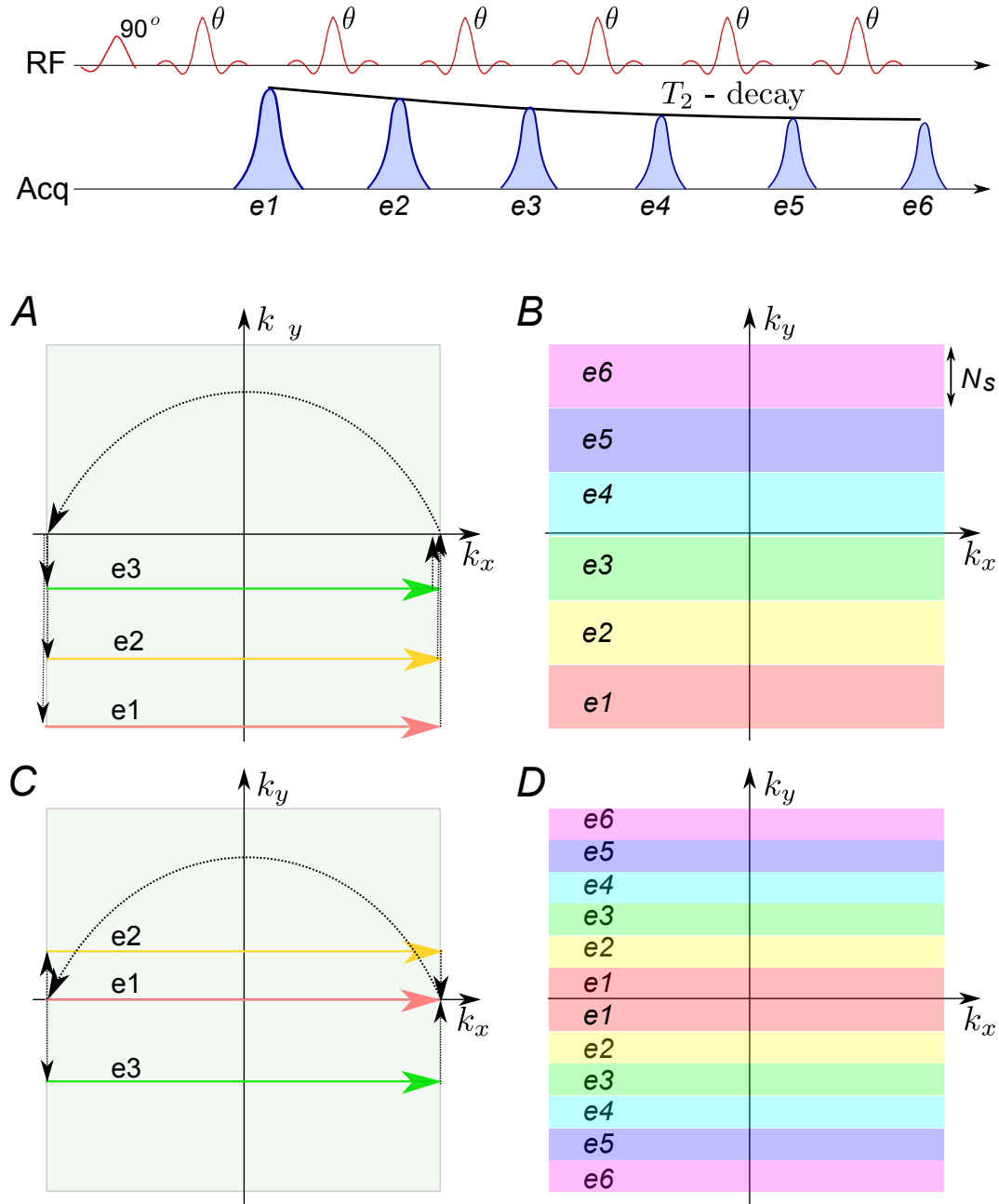
Figure 4.6: Turbo spin-echo k-space filling method. (A,C) k-space trajectory and (B,D) k-space encoded into bands for linear and centric phase encoding order, respectively.

k-space are acquired in the same direction. In Fig 4.6.A, since the ETL is an even number, the effective TE will be within either the 3rd or the 4th echo, depending on which was acquired with k_y=0. For an odd ETL like 7, the effective TE will be within the 4th echo (effective TE=$4\times\tau$). Echoes at the same position in the echo train from different acquisitions are assigned to the same region of k-space. Each echo within the train is therefore phase encoded into a k-space band as illustrated in Fig. 4.6.(B, D). The number of phase encoding lines in each of these bands corresponds to the number of shots (N_s) necessary to fill the whole of k-space: e.g, for a 48×48 matrix, 8 shots will fill k-space if an ETL of 6 echoes is used. In the case of centric phase encoding order, each echo band has half of the phase encoding lines in the top half ($+k_y$) of k-space and half in the bottom half (-k_y).

In TSE images the contrast between grey and white matter arises not only from T_2 differences, but also from other factors [52] such as the substantiable proton density difference between gray and white matter, the T_1 weighting introduced by the presence of stimulated echoes and the magnetization transfer effects. Stimulated echoes compensate for the signal loss of the spin echoes throughout the echo train due to T_2 relaxation. The combined echo amplitude of the primary and stimulated spin echoes is dependent on T_1 as well as T_2 [53, 54]. Magnetization transfer (MT) effects increase contrast by preferentially attenuating myelinated tissue. These effects arise in the multislice TSE sequence because of the repetition of numerous refocusing pulses applied close to the resonance frequency of the imaged tissue during the acquisition of neighbouring planes [55].

The length of TR determines the number of slices that can be sampled within the TR period in 2D multi slice imaging. If the number of slices exceeds the optimal number for a given TR, then the slices are distributed equally between 2 acquisition segments (packages).
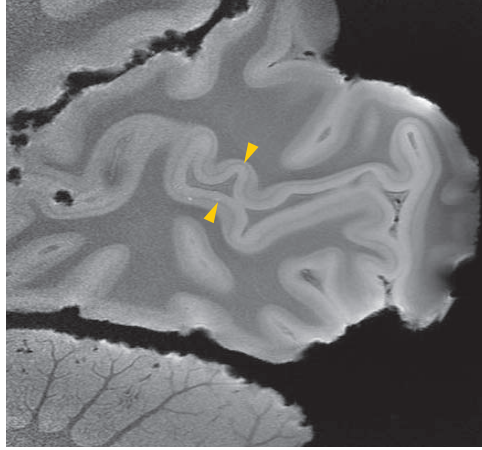
Figure 4.7: Sagittal section of ex-vivo human occipital lobe from a 3D isotropic proton density-weighted FLASH scan acquired at 7 T with 120 μm isotropic resolution [57]. The stria of Gennari defining Brodmann area 17 can be seen as a darker signal area) in the proton-density weighted scan as a result of an increase in myelin content.

4.2.2 Imaging with the volume T/R coil

The gains in sensitivity obtained with the introduction of human ultra-high field MR scanners can be exploited to allow acquisition of images with higher spatial resolution and therefore greater anatomical detail. The increased signal to noise ratio at 7 T makes it possible to achieve a level of spatial resolution to visualize fine structures within the cortex. One such structure is the stria of Gennari, a dense band of myelination found in layer IVb within the cortical grey matter of primary visual cortex (Brodmann's area 17) as shown in Fig. 4.7. Due to this myeloarchitecture, Brodmann's area 17 is also called the striate cortex, whilst the other cortical regions which do not exhibit a myelin layer are called extra-striate cortex. MRI sequences providing contrast between grey and white matter potentially allow detection of the stria, but since the thickness of this myelin band is of the order of 300 μm [56], this can only be accomplished at very high resolution.

The IR-TSE and MPRAGE pulse sequences described above were optimized at 7 T in order to allow the acquisition of images with high spatial resolution with the desired contrast to allow visualization of the stria of Gen-

nari.

Due to the increase of the T_1 relaxation time at 7 T, small flip angles are required to obtain maximum signal to noise ratio with the MPRAGE acquisition. The inversion time and the phase encoding order also have a strong effect on the image contrast. Centre-out phase-encode ordering was chosen to maximize SNR, but this comes at the expense of a small degree of blurring in the phase encoding direction[58, 50]. The optimum contrast between gray matter and stria of Gennari was found to be for a sequence using a 180° preparation pulse followed after a delay of 260 ms by a train of 12° excitation pulses with a 14 ms repetition time (TR) and a 4.1 ms echo time (TE). The shot repetition time was 3000 ms with 170 steps in the acquisition segment, requiring three segments (shots) to cover the 512 phase encoding steps. In the 2D-phase encoding loop k-space coverage was centre-out: lines 0, -2, 3, -5, 6,... are covered by the first segment, lines -1, 2, -4, 5, -7,... by the second segment and lines 1, -3, 4, -6, 7,... by the third segment. Simulations of this contrast using appropriate values for ρ, T_1 [59] and $T_2^\star$ [60] based on measured values at 7 T show that for this sequence the full width at have maximum (FWHM) of the point spread functions in the phase encode direction werw 378 and 368 μm for WM and GM respectively.

In an IR-TSE sequence, the dependence of image contrast on TE is not straightforward, as it depends on tissue T_1 and T_2 relaxation times, as well as magnetization transfer effects [20, 52, 55]. In a study at 4.7 T, Thomas et al[18] showed that the GM to WM contrast does not vary substantially with effective TE. Therefore, an effective echo time of 10 ms was used to maximize signal to noise ratio. In order to implement this short TE, centric phase encoding order was used. A refocusing RF pulse angle of 160° rather than 180° was chosen to reduce the RF power deposition. Simulations at 4.7 T demonstrated that a reduction of the refocusing pulse from 180° to 165° results in a significant RF power reduction without compromising the image SNR [18]. At 7 T, the optimal contrast was found to be produced for a delay time (TI) of 320 ms and a repetition time of 3200 ms and an echo train length (ETL) of 16, resulting

in a TSE shot duration of 160 ms. On the Philips scanner, the choice of the above parameters results in a protocol with an echo spacing τ of 10 ms.

Four subjects were scanned on a 7 T Philips Achieva system using a volume transmit-receive (T/R) coil for both MPRAGE and IR-TSE sequences with the optimized parameters. At the time this data was collected there was no parallel receive capability at 7 T. Image data sets with 1.5 mm slice thickness aligned perpendicular to the plane of the calcarine sulcus were acquired with both imaging sequences. The in-plane resolution was 0.35×0.35 mm^2 (matrix size: 512×512). Each subject was scanned twice; the IR-TSE imageswere acquired in the first session and the MPRAGE data in the second. In order to avoid subject motion, the total duration of the high resolution scanning was restricted to approximately 20 minutes in each scan session. For the IR-TSE sequence, six averages were acquired in total, by acquiring 3 individual data sets of 4 slices each formed from two averages (NSA=2). Each of these data sets was acquired in 422 seconds, leading to a total scan time of 21 minutes for 4 slices. For the MPRAGE sequence, three individual data sets comprising 20 slices aligned perpendicular to the plane of the calcarine sulcus were acquired. Each individual data set consisted of two averages and took 6 min 47 sec to acquire, resulting in a total scanning time of 20 min 21 sec for the six averages covering 20 slices. The 3 individual data sets were realigned to correct for motion before averaging.

The total acquisition time for both sequences was approximately the same. Since several averages need to be acquired to increase the signal to noise ratio, the slice coverage is limited for both sequences, particulary for the IR-TSE sequence. The specific absorption rate (SAR) imposed a limit on the implementation of the IR-TSE sequence because of the energy deposited from the multiple refocusing RF pulses. This resulted in the acquisition being split into several packages, therefore increasing the total scanning time.

A hypo-intense band within the cortical grey matter indicating the stria of Gennari was visible in the visual cortex for all four subjects. Figure 4.8 shows example images acquired with the IR-TSE sequence and Fig.4.9 shows similar
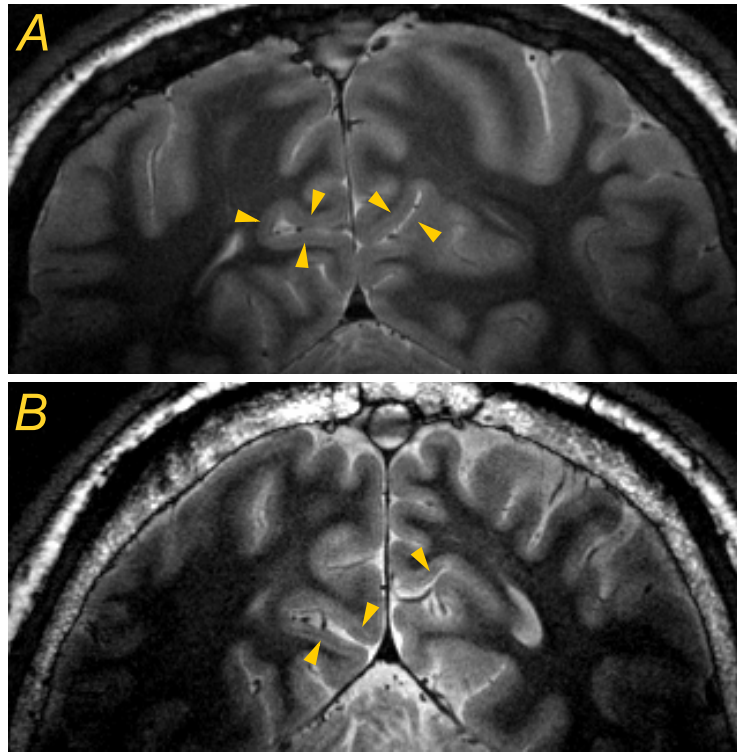
Figure 4.8: High resolution images acquired with the IR-TSE sequence (TE=10 ms, TR=3200 ms, TI=320 ms, ETL=16) for two subjects A and B. Image resolution is $0.35 \times 0.35 \times 1.5$ mm^3.

images acquired with the MPRAGE sequence. In both sets of data, the highest signal intensity occurs in CSF, with grey matter appearing with significantly higher intensity than white matter. A hypo-intense band can be seen in the cortical grey matter in the visual cortex (indicated by the arrows). One can see the difference in the contrast and signal between the images acquired using MPRAGE and the IR-TSE sequences, with the IR-TSE sequence allowing better visualization of the stria.

Fig. 4.10 shows IR-TSE data acquired from one subject. The image on the right shows a magnification of the region where the stria was visible; a dark band can clearly be seen within parts of the grey matter along the calcarine sulcus. Intensity profiles were measured across the sulci at different locations where the stria was most evident. Profiles A and C were measured from the edge of the white matter across the CSF to the edge of the white matter and B from the edge of white matter (WM) to the edge of the CSF (from left to
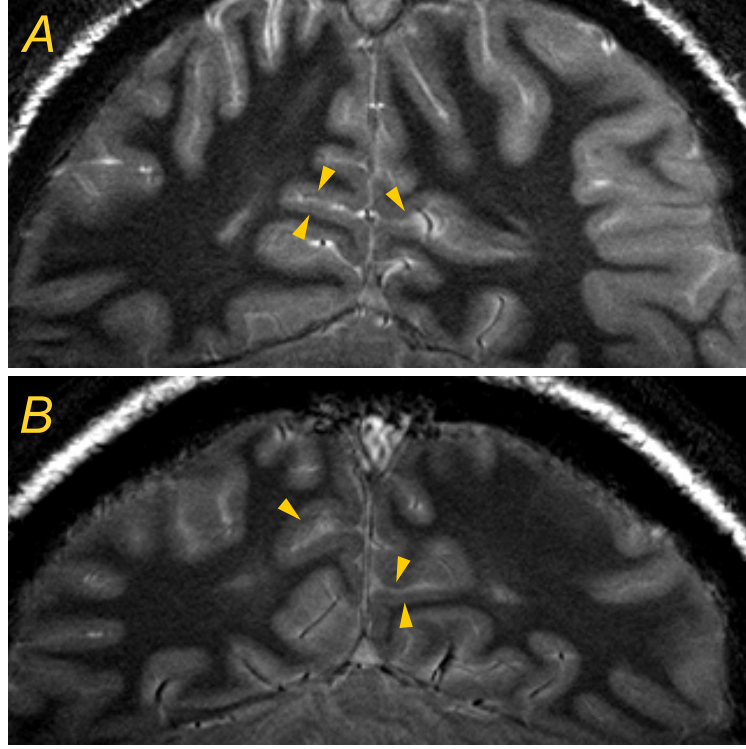
Figure 4.9: High resolution images acquired with the MPRAGE sequence (TE=4.1 ms,TR=14 ms, TI=260 ms, FA=12°) for two subjects A and B. Image resolution is $0.35 \times 0.35 \times 1.5$ mm^3.

right). A dip in signal intensity, shown by the arrows, is present in all of these profiles, indicating the presence of a band of myelination.

The contrast to noise ratio (CNR) was also calculated in the following manner: a small region of interest was selected in the stria of Gennari, and in grey and white matter. The signal S for these regions was measured in the average image of the N registered individual scans. The noise was measured as the mean standard deviation, σ, for these regions of interest in images resulting from subtracting the successive individual scans. The contrast to noise between tissue types 1 and 2, was then calculated by

$$CNR_{12} = \frac{S_1 - S_2}{\sigma/\sqrt{N-1}} \qquad (4.7)$$

Table 4.1 details the mean contrast to noise ratio (CNR) across subjects between grey and white matter, and grey matter and the myelinated band. It
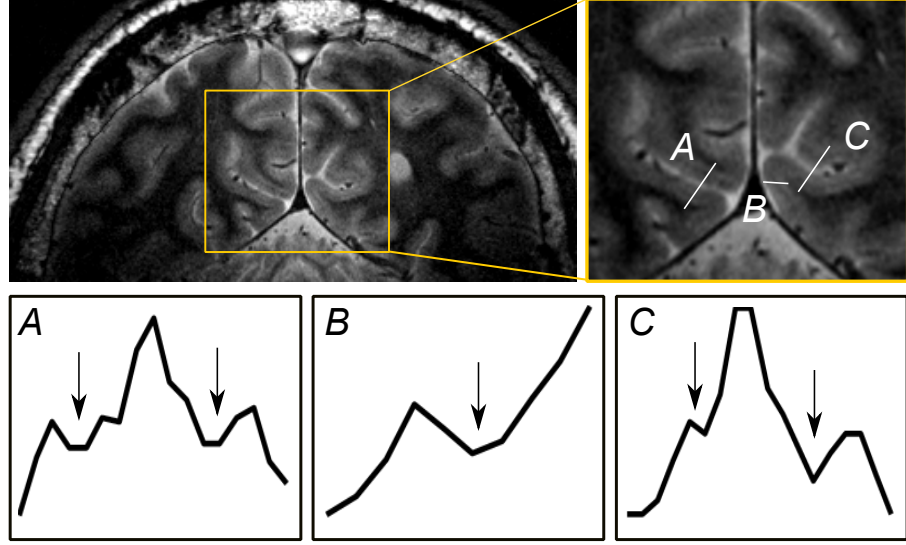
Figure 4.10: High resolution IR-TSE image showing the Stria of Gennari. On the right a magnified region showing the position of line profiles (A,B,C). The boxes A, B and C show line profiles through sulci along the lines marked on the image.

	IR-TSE	MPRAGE
GM/WM	9.2 ± 1.4	6.7 ± 1.3
GM/Stria	4.0 ± 1.4	2.9 ± 1.2

Table 4.1: Mean ratio of the contrast between GM/noise to WM/noise and GM/noise to stria of Gennari/noise at both field strengths for the IR-TSE and MPRAGE sequences.

can be seen that the CNR is significantly greater for the IR-TSE sequence than for the MPRAGE sequence. However it must be noted that when measuring the contrast to noise for these sequences at 7T, B_1-inhomogeneities mean that the contrast to noisse varies within each image and across the slices. It must also be notice that for a similar acquisition time, the coverage achieved by the MPRAGE sequence is 5 times larger than with the IR-TSE sequence.

4.2.3   Imaging with the 16 Channel Receiver Coil

The benefits of multiple receiver coils have been well established for both, increasing SNR [61] and increased spatial resolution via parallel imaging techniques [62, 63]. It has also been successfully demonstrated that parallel imaging
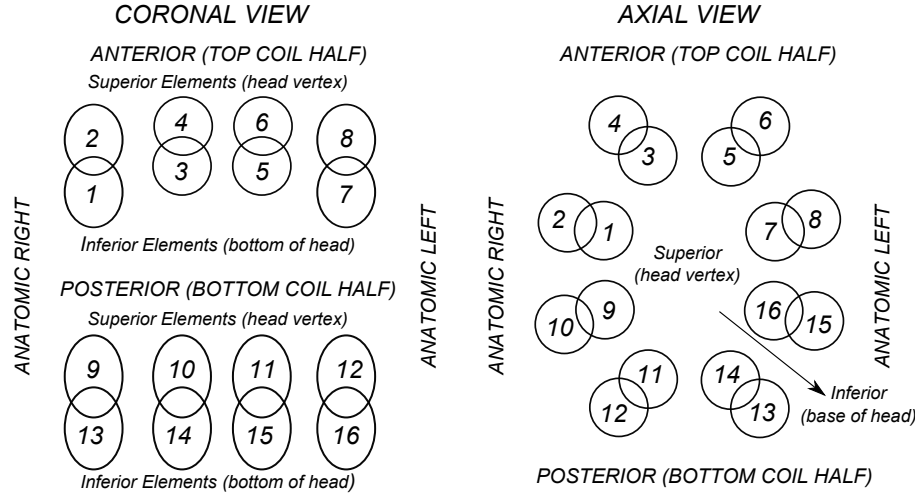
Figure 4.11: 16 channel array element layout.

performance increases with magnetic field strength beyond ~ 4 T [64], suggesting the need for the use of even larger numbers of receiver coil elements at high field [65]. The reduced wavelength at high field reduces the overlap in the receptivity distributions from the separate receiver coils [66, 67]. One immediate advantage of parallel imaging for brain studies at high field is that the use of surface coils in parallel results in increased signal receptivity towards the periphery of the brain, offsetting the tendency for central brightening [66, 67].

A 16 - channel NOVA array coil (Fig. 4.11) for the Nottingham 7 T scanner became available early in 2007. To compare the performance of this coil with the volume transmit-receive (T/R) coil, IR-TSE images were acquired with identical protocols using (i) the volume T/R coil as both transmitter and receiver, and (ii) a volume coil to transmit and a 16-channel array coil to receive. Figure 4.12.A shows an image acquired using the volume T/R coil to transmit and receive and Fig.4.12.B and C show images acquired using the volume transmit coil, with 16-channel array coil as a receiver, with no acceleration factor (B) and an acceleration factor of 2 (C) in the right-left direction. The use of a SENSE factor of 2, reduces the acquisition time for the IR-TES sequence from 422 s to 218 s and therefore to maintain equal imaging time two individual scans with SENSE factor 2 were acquired and
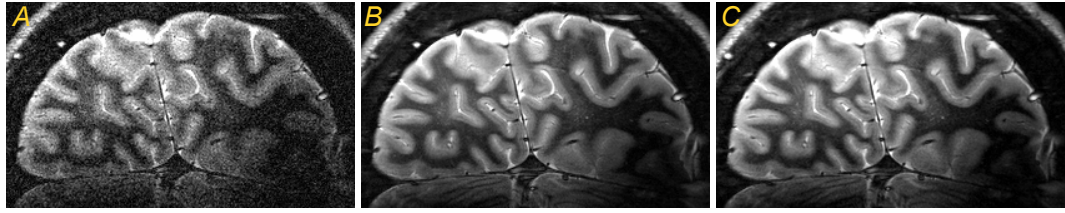
Figure 4.12: IR-TSE images acquired using (A) a Volume T/R coil for signal reception and a receiver 16-channel SENSE coil with (B) no acceleration factor and (C) an acceleration factor of 2 in the right-left direction. Image resolution: $0.35 \times 0.35 \times 1.5$ mm ^{3}.

then averaged together. The images acquired with the array coil clearly exhibit a considerable increase in SNR with respect to the image acquired with the T/R coil, for both data acquired with and without SENSE acceleration (Figure 4.12). The measured contrast to noise ratio between grey and white matter increased from 9.9 with the volume T/R coil (A) to 41.2 with the 16-channel coil using no SENSE acceleration (B) and 42.5 with a SENSE acceleration factor of 2 (C). Therefore, the use of the array coil provides approximately a 4-fold improvement in SNR.

The main benefit of parallel imaging is the speeding up of the imaging sequences. The IR-TSE sequence benefits from parallel imaging since less refocusing pulses are required. However the benefits of using SENSE acquisition are more significant for the 3D MPRAGE technique, where the coverage can be increased with no time penalty. For example, 20 slices were acquired with the MPRAGE sequence in 208 seconds with no SENSE acceleration factor. But using a SENSE acceleration factor of two, the coverage can be doubled and allowing the acquisition of 40 slices in 223 seconds. The measured signal to noise ratio of the resulting images was similar; 3.8 for white matter in both cases, and 10.8/11.5 for grey matter for the 20/40 slices coverage respectively.

Adiabatic Inversion Pulse

The images shown in Fig. 4.12 exhibit a severe drop in signal intensity at the bottom right corner due to the spatial inhomogeneity of the B_1-field. The

inhomogeneous B_1-field results in spatial variations of the flip angle across the image. Adiabatic pulses do not obey the relationship described in Eq. 2.8 between the angle and the B_1-field amplitude. Instead, the flip angle of an adiabatic pulse depends on how the B_1-field varies in amplitude and modulation frequency during the pulse. Adiabatic inversion pulses require a relatively long pulse with and a high B_1-amplitude. As long as the B_1-field amplitude exceeds a minimum threshold, theoretically the resultant magnetization vector becomes nearly immune to B_1-field variations, leading to a spatially uniform inversion of the magnetization. A commonly used adiabatic inversion pulse is the hyperbolic secant (HSC) pulse [68], which results in an almost perfect inversion, and is represented by:

$$H(t) = Asech^{1+i\mu}(\beta t). \tag{4.8}$$

In order to ensure that the adiabatic inversion pulse works within the adiabatic regime, a series of MPRAGE images were collected with increasing B_1 power. An image acquired with the default scanner settings is shown in Fig. 4.13.A. The arrow points to the area with poor inversion. Increasing the power by factors of 1.2 and 1.4 (Fig.4.13.B and C) relative to the default value can be seen to significantly improve the quality of the contrast in this area. A further increase to a factor of 1.6 does not result in any significant improvement (Fig.4.13.D), particularly when assessed against the increased SAR. The adiabatic regime is therefore reached across the slice by setting the B_1-field power to 1.4 relative to the default value.

$T_2^\star$ contrast

Ideally, $T_2^\star$-weighted images should be sensitive to small local susceptibility effects without being affected by undesired macroscopic susceptibility effects which obscure fine anatomical detail. The increased sensitivity of the 16-channel receiver array can be exploited to increase the resolution of $T_2^\star$-weighted images to a resolution of $0.25\times 0.25\times 1$ mm^3, giving a 0.0625 mm^3
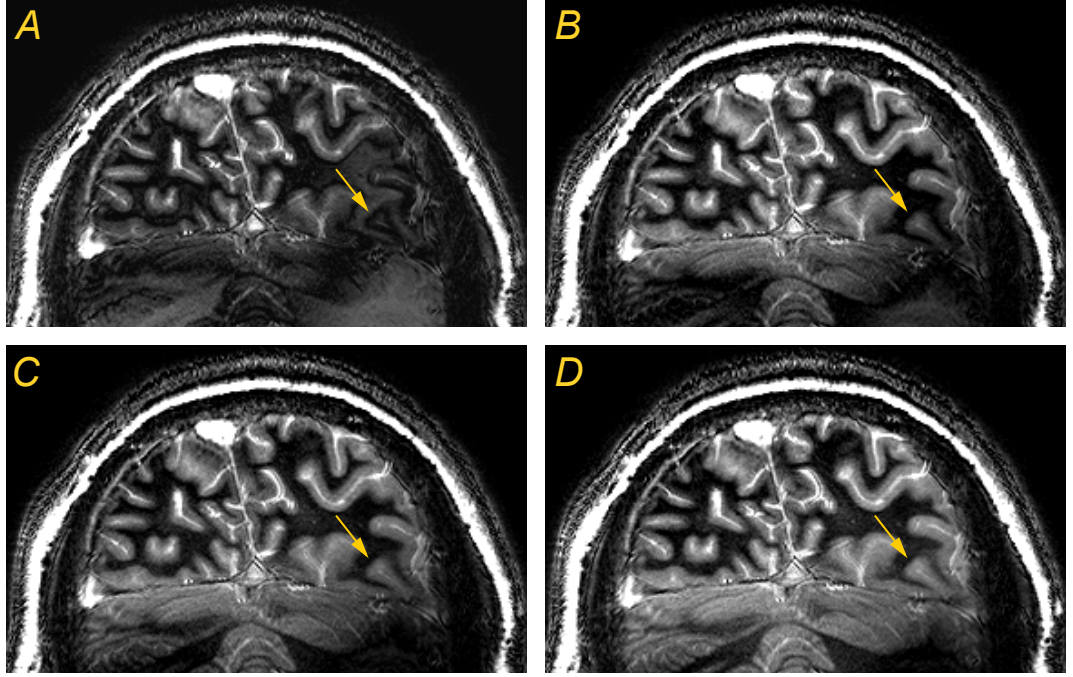
Figure 4.13: Images acquired using the MPRAGE imaging sequence with increasing power of the adiabatic inversion pulse by factors of: (A) 1, (B) 1.2, (C) 1.4 and (D) 1.6 relative the default value. Arrow indicates area of poor inversion for default scanner setting.

voxel size. The multi-slice FLASH sequence described in Section 4.2.1 has been implemented and used to acquire high resolution $T_2^\star$-weighted images. An in-plane resolution of 250 μm with a slice thickness of 1 mm was achieved using a 1024×616 matrix over a 192×154 mm^2 field of view. The length of TR determines the number of slices which can be acquired. The minimum TR required to accommodate 10 slices was 320 ms. To optimize the image contrast, the flip angle was set to 32°, which is approximately equal to the Ernst angle for a TR of 320 ms assuming an average T_1 of 1.8 s for grey matter at 7 T [69]. The choice of TE affects the amount of $T_2^\star$-weighting and should be chosen to be in the relevant range for the prevalent tissues. Various TE values were assessed in the range of 15 to 30 ms and a TE of 20 ms was found to produce good grey-white matter contrast. In order to improve the SNR of the $T_2^\star$-weighted images, 3 averages were acquired, leading to a total scanning time of approximately ten minutes. Both modulus and phase

data were acquired. Post-processing of the phase data was needed; first, the 2π phase jumps present in the data were unwrapped using a fast and robust custom written in house algorithm (Mougin, SPMMRC). Secondly, the unwrapped phase data were spatially high-pass filtered to remove the unwanted low spatial frequency variations due to macroscopic susceptibility effects. This was achieved by smoothing the unwrapped phase data with a Gaussian function of 5 pixels width, and subtracting this smoothed data from the original unwrapped phase data.

Figure 4.14.A and B show representative $T_2^\star$- weighted modulus (left) and phase (right) images of the occipital lobe of two subjects, A and B, acquired with spatial resolution of $0.25 \times 0.25 \times 1$ mm^3. The modulus images show excellent detail of the venous microvasculature. The $T_2^\star$ of grey matter is slightly longer than that of white matter, therefore grey matter appears brighter. Both modulus and phase images also demonstrate clearly delineated boundaries between grey matter and white matter and CSF. There is also clear evidence of banding within the cortical grey matter indicating the presence of the stria of Gennari. Intensity profiles for both modulus and phase images were measured at locations indicated by the lines in the magnified region of the modulus data from subject B. Figure 4.14 subplots 1 and 2 show the intensity profiles across the grey matter. The dips indicating the presence of the myelin band are indicated by the arrows. The highest intensity corresponds to CSF. The dip in the centre of the CSF in profile 2 corresponds to the vessel which can be clearly seen as a dark region in the magnified region. Modulus and phase of $T_2^\star$-weighted axial images including the central and post-central sulcus are also displayed in Fig. 4.15 for two subjects (A,B). This region is of interest because the motor and somatosensory cortices lie on opposite banks of the central sulcus. The somatosensory cortex is studied in Chapter 6 to assess somatotopic mapping and the motor cortex is studied in Chapter 7. Both modulus and phase images show fine detail across the cortical grey matter. The contrast between grey and white matter in the modulus data is variable and appears to vanish in the central sulcus, highlighted by the arrow. This region appears slightly darker
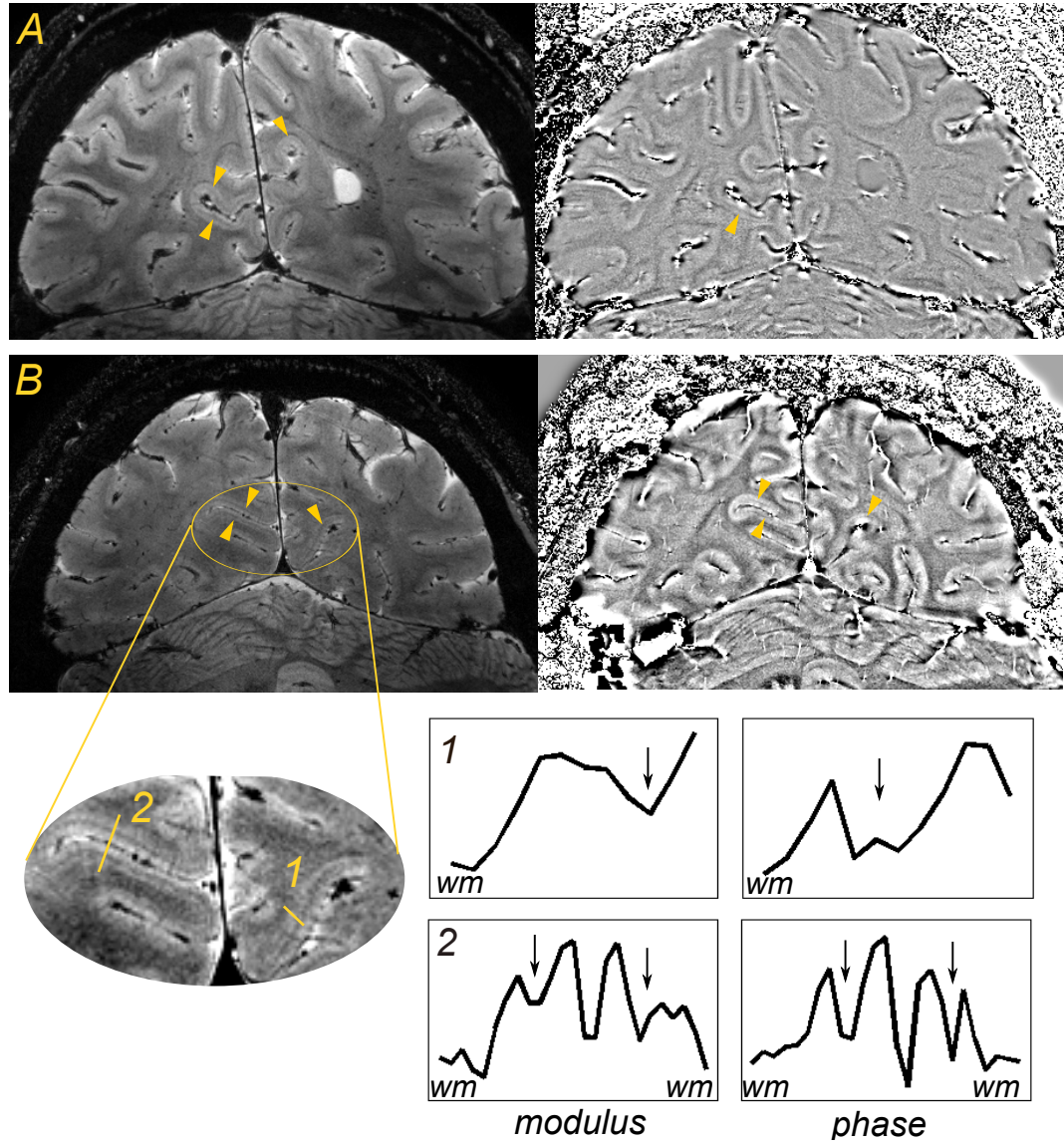
Figure 4.14: $T_2^\star$-weighted modulus (left) and phase (right) images of the occipital lobe acquired with the multi-slice FLASH protocol for subject (A) and (B). Image resolution is $0.25 \times 0.25 \times 1$ mm^3. (1,2) line profiles through sulci for the modulus and phase data along the lines marked on the magnified region of subject (B) shown on the left.

Figure 4.15: Modulus (left) and phase (right) of axial $T_2^\star$-weighted images acquired in a slice spanning the central sulcus using the multi-slice FLASH protocol for two (A and B) different subjects. Image resolution is $0.25{\times}0.25{\times}1$ mm^3. Phase images are shown with contrast reversed.

Figure 4.16: Axial images acquired to include the central and post-central sulcus using (A) TSE and (B) MPRAGE imaging sequences. (C) Corresponding T_1 map.

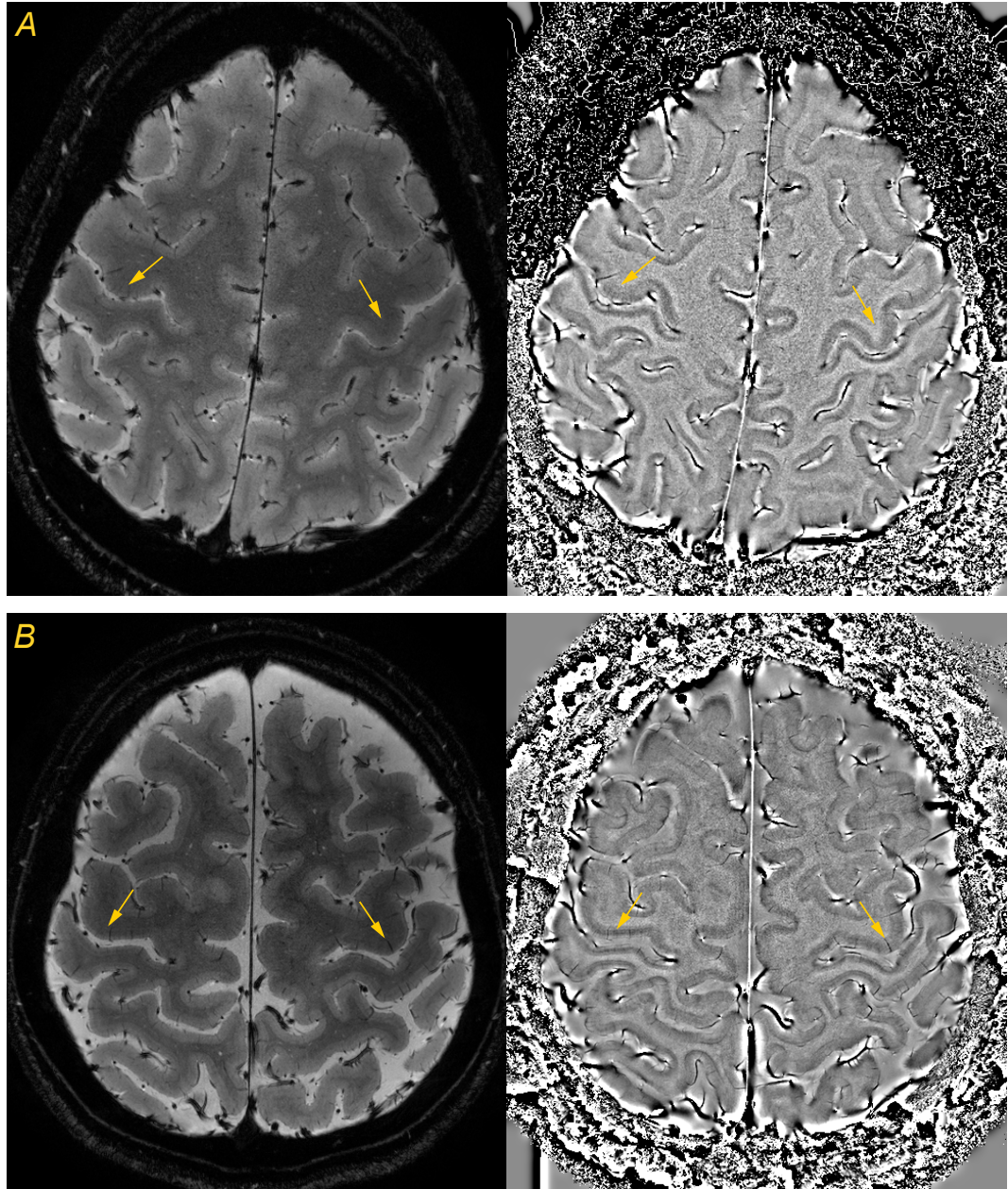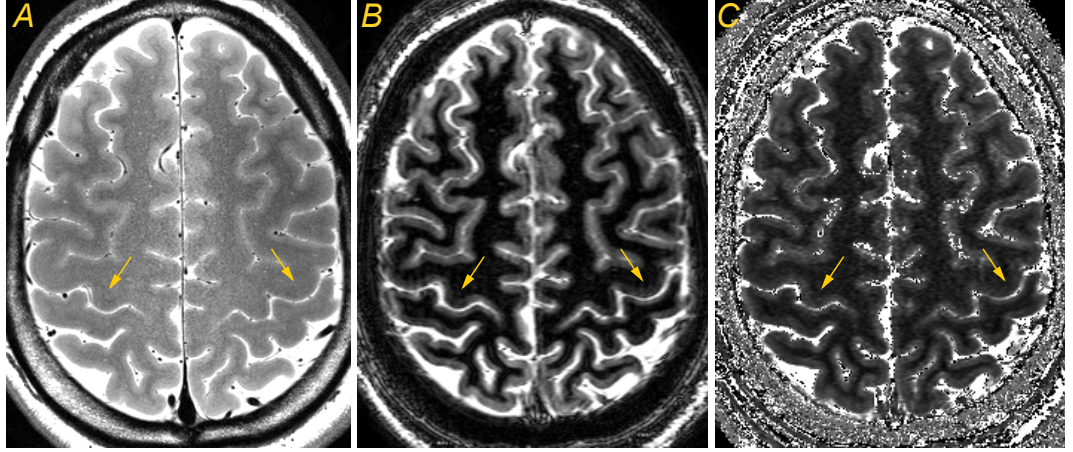than other grey matter areas in the phase data. Figure 4.16 shows a comparison between (A) a T_2-weighted and (B) T_1-weighted axial images spanning the central sulcus, acquired using turbo spin echo and MPRAGE respectively. The arrows point to the central sulcus, which appears hypointense with respect to other grey matter regions in both images. The corresponding T_1 map is shown in Fig. 4.16.C. This high resolution ($0.5\times 0.5\times 1$ mm^3) T_1 map has been calculated from a set of MPRAGE images acquired with inversion times of: 300, 600, 1500, 2500 and 3500 ms [59]. The measured T_1 across a region of interest in the central sulcus, 1820 ± 160 ms is shorter than the values 2080 ± 190 ms measured in brighter grey matter regions (superior frontal sulcus). The mean white matter T_1 was measured as 1390 ± 130 ms in this map. However, the water content of brain tissue also influences T_2 and T_1. These shortened T_1's in white matter agree with theory as on average, there is a water content of 72% in white matter and 84% in grey matter [70, 71]. Lower water content results in reduced T_2 and T_1 relaxation times. Paramagnetic iron also decreases T_2 [72] and T_1 relaxation times [73, 74], but it has been suggested that water content correlates better with T_1 than iron content, therefore the reduced contrast in the central sulcus is probably due to a poor water content in this area.

A decrease in T_2 would suggest that shorter TE values should be used in spin echo functional magnetic resonance imaging when mapping the somatosensory and motor cortices with respect to other cortical regions. This is examined in Chapter 7.

The imaging sequences described in this section benefit from parallel imaging, with the speeding up of the imaging sequences being the main benefit. However, the benefits of using SENSE acquisition are more significant for the 3D MPRAGE and the FLASH techniques than for the IR-TSE sequence, where the high level of SAR due to the energy deposited by refocusing pulses is still an issue. The slice coverage of the IR-TSE sequence is limited by the available scanning time, but the IR-TSE yields the best grey to white matter contrast to noise ratio, and therefore it should be used to study structures where a big slice coverage is not necessary. In order to study structures where slice coverage is necessary, as it is the case in Chapter 5, the MPRAGE or FLASH techniques should be used, which allow a far grater coverage than the IR-TSE sequence while maintaining a reasonable contrast to noise ratio.

4.3   Functional Imaging

Functional MRI attempts to localize the increased neuronal activation in the brain arising from specific tasks so as to produce maps of neuronal function. There are several MRI methods which can be used to detect the increased metabolic demand associated with activity; the blood oxygenation level dependent (BOLD) contrast [75, 76, 77, 78], cerebral blood volume (CBV) alterations [79, 80, 81] and cerebral blood flow (CBF) changes measured using arterial spin labeling (ASL) [77, 82, 83, 84].

Functional MRI based on BOLD contrast is the most sensitive of these techniques and it has become the most commonly used methodology for mapping brain function since it was introduced in 1992 [75, 76, 77, 78].

Making precise quantitative predictions about the size and amplitude of the BOLD response is difficult since it results from a combination of several

haemodynamic effects. fMRI based on BOLD contrast is therefore limited to semi-quantitative measurements of brain activity. The following paragraphs review some pertinent background theory to provide understanding of the various factors influencing the BOLD response, allowing the reader to understand the goals and complications of the experiments described in the following chapters.

4.3.1 Measuring brain function with BOLD contrast

The signal measured in BOLD fMRI depends on the magnetic properties of haemoglobin and the dependence of these properties on oxygenation state. When bound to oxygen, haemoglobin is diamagnetic with a similar susceptibility to that of water, whereas deoxygenated haemoglobin is paramagnetic [85]. The magnetic field is thus distorted in the vicinity of deoxygenated red blood cells [75, 86]. These distortions create magnetic field gradients around capillaries and veins. The change in susceptibility induced by changes in oxygenation therefore leads to local changes of the magnetic field of a few hundredths of a part per million [87, 88]. For deoxygenated blood, the resulting field gradients shorten $T_2^\star$ and reduce the amplitude of the MR signal in $T_2^\star$-weighted images. During brain activation the brain over-compensates in supplying blood flow to active brain tissue and the oxygen content of blood is therefore increased. With less deoxyhaemoglobin the susceptibility of the blood becomes closer to that of the surrounding tissue and the field gradients are reduced. The $T_2^\star$ therefore lengthens, increasing the measured MR signal in $T_2^\star$-weighted images by a few percent, dependent on field strength. Hence, blood oxygenation dependent differences provide the contrast mechanism in BOLD fMRI used to reveal areas of functional activity. The vast majority of fMRI experiments are performed by acquiring a series of $T_2^\star$-weighted gradient echo (GE), echo planar images while a subject performs a certain task or experiences some type of stimulation. Only a few studies at high field have used spin echo (SE), echo planar acquisitions [89, 90, 91, 92, 93, 94]. The differences of GE and SE fMRI
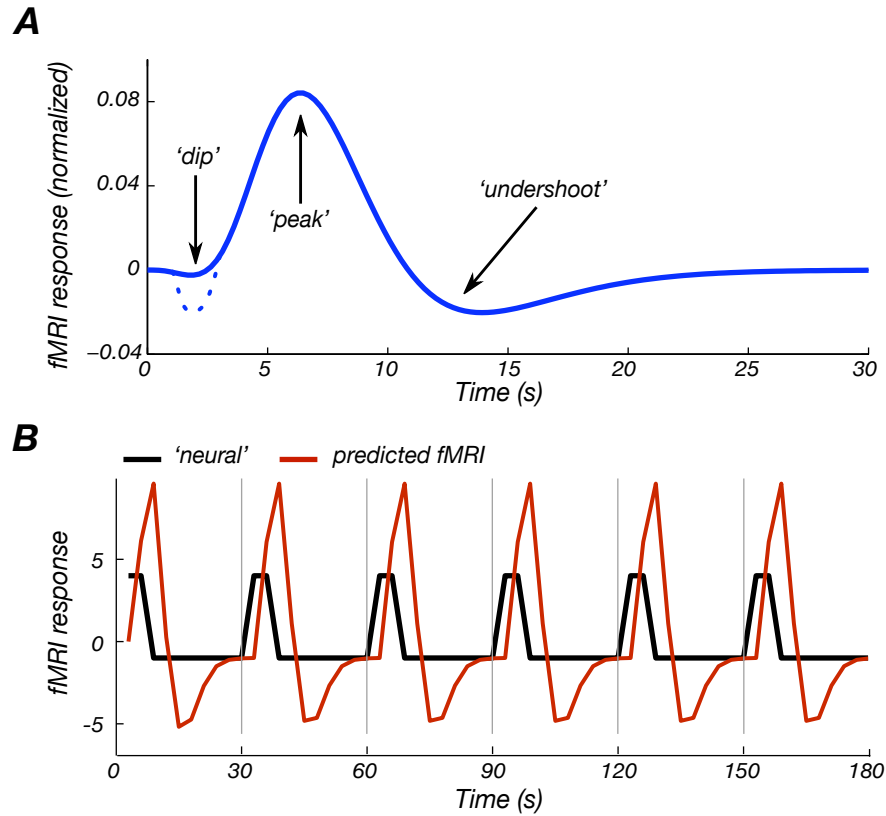
Figure 4.17: (A) Haemodynamic response function (HRF) to an event, approximated by the Friston function [95] with a time to peak of 6 seconds (a_1=6, a_2=12, b_1=0.9 s, b_2=0.9 s, c=0.35). (B) The modeled BOLD response (solid red line) is obtained by convolving the stimulus input (solid black line) with the HRF (A).

will be discussed later in this section and experimentally in Chapter 7.

The measured BOLD signal change that results as a consequence of stimulation does not reflect neuronal activity directly. Approximately two seconds after stimulus onset, there is an initial decrease in BOLD signal [96, 97, 90]. This 'initial dip', whose origin stills remains contentious, is hypothesised to be a result of initial activity in neurons drawing oxygen from the capillaries. This leads to an initial increase in the local concentration of deoxyhaemoglobin in the close vicinity of the active cells, which results in a reduction in $T_2^\star$. The brain vasculature reacts to this increased activity by increasing the local (cortical) blood supply, the Cerebral Blood Flow (CBF), to the active region, overcompensating for the increased Cerebral Metabolic Rate of Oxygen

consumption, (CMRO$_2$), leading to a decrease in the concentration of deoxy-haemoglobin in the active areas and in the veins draining away from it. The BOLD response to a brief period of elevated neuronal activity is well predicted by a 'haemodynamic response function' (HRF). A typical BOLD response to a single 'impulse' of stimulation or 'event', is shown in Fig. 4.17. This has been described by Friston et al [95] as a function defined by:

$$H(t) = \left(\frac{t}{d_1}\right)^{a_1} e^{-\frac{t-d_1}{b_1}} - c\left(\frac{t}{d_2}\right)^{a_2} e^{-\frac{t-d_2}{b_2}} \tag{4.9}$$

where $d_i = a_i b_i$ and H(t) is often termed the 'canonical' HRF. The response peaks approximately 6 seconds after the onset of the stimulation. After stimulus cessation, the BOLD signal decreases over a few seconds to a level below the initial baseline (the post-stimulus 'undershoot') from which it then recovers slowly over a further few seconds to return to baseline. Overall, even for a brief stimulus, the time from onset to return of the signal intensity to baseline may be as long as 30 seconds.

The BOLD contrast to noise ratio (CNR) is also influenced by paradigm design. A BOLD fMRI experiment can be classified as a block design, event-related design, or mixed design, which as the name suggests is an intermediate between block and event-related designs. In a block design, a stimulus is continuously applied or multiple trials of a particular condition are grouped together, resulting in a fixed sequence of different blocks such as visual checkerboard stimulus alternating between 'ON' and 'OFF' periods or a stimulus alternating between the left and right visual fields. In event related designs brief stimulus events, 'trials', are presented. A single button press followed by rest (OFF) periods of random duration is an example of an event related design. In an fMRI experiment the typical measurement interval of a dynamic scan, TR, is less than the duration of the BOLD response. fMRI data recorded in a session is treated as a time series. The BOLD signal is assumed to be the output of a linear time-invariant system [98], according to which the response to an arbitrary sequence of stimuli is equal to the summation of the responses

to each of the individual stimuli. This assumption allows the use of the HRF concept, such that the predicted fMRI response, $X(t)$, is obtained as the convolution of the stimulus input function, $s(t)$, with the haemodynamic response function, $h(t)$:

$$X(t) = s(t) \otimes h(t) = \int_0^\tau s(t - \tau)h(\tau)d\tau \qquad (4.10)$$

The stimulus input function is usually a top-hat function, as shown by the black solid line in Fig. 4.17.B, encoding the occurrence of an event or epoch. In this case, a top-hat function of 6 seconds duration appearing every 30 seconds has been used. This is then convolved with the HRF shown in Fig. 4.17.A. to obtain the model function (solid red line) for BOLD signal changes.

Signal changes in EPI BOLD

The EPI sequence described in Chapter 2 is a fast and intrinsically $T_2^\star$-weighted gradient echo imaging method, allowing images to be acquired in less than 100 ms. EPI is the most commonly used acquisition method for fMRI. The $T_2^\star$ of a voxel is determined by the $T_2^\star$ relaxation processes, which include the effect of microscopic field heterogeneity due to the presence of deoxyhaemoglobin and the macroscopic field inhomogeneity due to large vessels and imperfect shimming. The decay rate $R_2^\star$, equal to $1/T_2^\star$, can be expressed as;

$$R_2^\star = R_2 + R_2', \qquad (4.11)$$

where R_2 reflects the T_2-decay rate and R_2' represents the dephasing term due to microscopic and macroscopic field inhomogeneity. Maximum BOLD CNR is achieved when the echo-time (TE) is approximately equal to the $T_2^\star$ of the grey matter being imaged. However, the BOLD sensitivity does not depend critically on TE and the use of a longer echo time can still result in good CNR, although the overall image SNR decreases with increasing echo time (see Fig. 4.18).
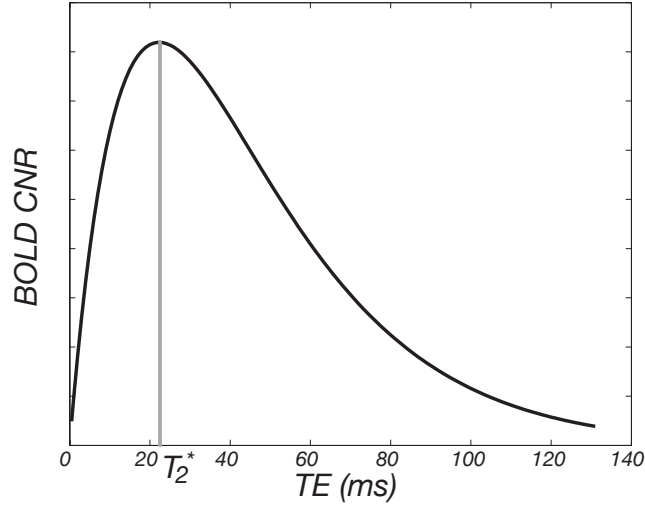
Figure 4.18: BOLD contrast to noise ratio as a function of TE, for $T_2^\star$=25 ms.

In gradient echo imaging, the signal decays exponentially with $T_2^\star$ as:

$$S = S_0 e^{\frac{-TE}{T_2^\star}} = S_0 e^{-TE \cdot R_2^\star}. \qquad (4.12)$$

For small changes in $R_2^\star$, written as $\Delta R_2^\star$, the predicted BOLD signal change, ΔS, between activation (S_a) and rest (S_r) at echo time TE can be expressed as

$$\frac{\Delta S}{S} \approx -TE \cdot \Delta R_2^\star \qquad (4.13)$$

where ΔS=S_a-S_r and S=(S_a+S_r)/2.

BOLD signal changes can also be observed using a spin echo (SE) pulse sequence which produce images that are T_2-weighted. In a SE-EPI pulse sequence (Fig. 4.19), a 180° radiofrequency pulse is applied before the gradient echo train, at time τ after the radiofrequency excitation pulse. The phase offsets due to precession in inhomogeneous fields are refocused at the centre of the spin echo, which occurs at time 2τ. Pure T_2-weighting can therefore be produced by arranging the centre of the gradient echo train to coincide with the spin echo, i.e., TE equals 2τ. At the centre of the spin echo there are also no phase shifts due to macroscopic field inhomogeneities, resulting in reduced
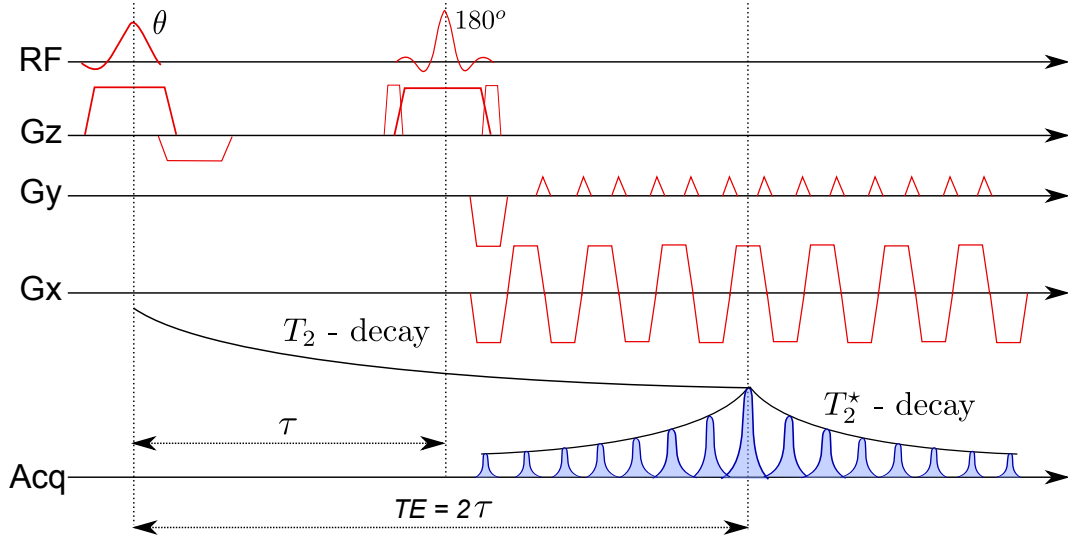
Figure 4.19: Spin-echo, echo planar imaging pulse sequence diagram.

signal loss in the image. The attenuation of the signal with increasing echo time is determined by T_2 rather than $T_2^\star$, and the optimum BOLD contrast is obtained when TE is equivalent to the T_2 of grey matter.

Analogous to gradient echo BOLD, the spin echo BOLD signal change is proportional to the change of the decay rate R_2 $(=1/T_2)$ on activation:

$$\frac{\Delta S}{S} \approx -TE\Delta R_2 \tag{4.14}$$

The use of a spin-echo, as well as the removal of the effects of macroscopic field inhomogeneities, reduces the contributions of microscopic field inhomogeneities to the BOLD effect. The BOLD effect in spin echo imaging is sensitive to vessel size, being more specific to activation in and around capillaries [89, 91]. However, spin echo sequences produce a weaker BOLD signal, for a given TE, than gradient echo sequences since $\Delta R_2 < \Delta R_2^\star$. Use of SE BOLD contrast thus trades reduced sensitivity for increased specificity. The increased signal to noise ratio combined with the reduced venous draining vein blood signal means that SE-based fMRI is best implemented at high and ultra-high field.

Magnetic field dependence of GE and SE BOLD signals

The BOLD signal is composed of intravascular and extravascular contributions, both of which can arise from small and large vessels. The relative contributions of intravascular and extravascular signals to the BOLD signal are dependent on magnetic field strength, image acquisition method (GE vs SE), echo time and blood-vessel diameter.

The intravascular BOLD component originates from the change in T_2 and $T_2^\star$ of water in blood as the content of deoxyhaemoglobin is altered by elevated neuronal activity.

The extravascular component originates from the water molecules present in the tissue surrounding the vessel. On activation, the blood oxygenation increases and the reduction in field gradients in the tissue immediately surrounding the blood vessel cause an increase in T_2 and $T_2^\star$, which increases the MR signal in T_2- and $T_2^\star$-weighted images. The extravascular signal increase depends on the change in blood oxygenation and volume, as well as the proximity to vessels and the orientation of those vessels relative to the magnetic field. Diffusion of water molecules through the field gradients around vessels affects both the SE and GE signal. Diffusion effects depend on the distance travelled by the water molecule during the echo time relative to the vessel size and are explained in more detail in Chapter 7. Briefly, water protons surrounding capillaries will move a considerable distance relative to the capillary diameter in a time TE, and hence will experience a range of field gradients in an echo time. This dynamic dephasing is a random process that can not be refocused by a spin echo. As the vessel size increases, water protons will tend to experience a similar magnetic field during TE. In this case dephasing is largely due to local variations in magnetic field across the voxels. These static dephasing effects around large vessels will be refocused by the 180° pulse in spin echo (SE) BOLD. GE imaging is sensitive to extravascular BOLD effects around small and large vessels, while SE is relatively insensitive to extravascular effects around large vessels. Hence, SE BOLD contrast is more specific

to activation in and around capillaries (provided the intravascular signal from large vessels is suppressed).

The effect of field strength on BOLD contrast is not straightforward to characterise, as field strength influences the BOLD response in several ways. $\Delta R_2^\star$ in both the intra- and extravascular compartments increases with increasing field strength. However the changes in T_2 relaxation rate for intravascular water increase linearly with field strength, whilst the increase in $T_2^\star$ relaxation rate for extravascular water is supra-linear with field strength [99]. Hence, the relative proportion of BOLD signal arising from tissue rather than veins increases with the applied static magnetic field strength [100]. The intra- and extravascular contributions to the BOLD effect in functional images can be experimentally examined with the use of bipolar gradients. The effect of these gradients, introduced to study diffusion [101], is to dephase randomly moving spins, consequently suppressing the intravascular signal. Experiments comparing the BOLD signal with and without diffusion weighting have confirmed that at field strengths of 1.5-3 T a substantial fraction of the gradient echo signal arises from intravascular or blood-related effects [102, 103, 104]. Similar experiments at 7 T [91] have shown that blood contributions to the BOLD effect are virtually eliminated at typical TE values that correspond to the $T_2^\star$ of grey matter [91]. Blood contributions are suppressed at high magnetic field due to the dramatic shortening of blood T_2 relative to tissue T_2 or $T_2^\star$ [88, 100]. Blood T_2 can be described by

$$\frac{1}{T_2} = A_o + K(1 - Y)^2, \tag{4.15}$$

where A_0 is a field independent constant term, while K scales quadratically with the magnetic field and depends also on the echo time [105] and Y is the fraction of oxygenation in venous blood. At 1.5 T, the apparent T_2 of venous blood is dependent on Y taking values of 90-180 ms [105, 106], which are comparable or longer than the T_2 of grey matter tissue (80-90 ms [107]). However, at 7 T the intrinsic T_2 of deoxygenated blood ($\sim$12 ms [99, 108]) is

much shorter than the T_2 of grey matter (55 ms [89]).

Numerical simulations of the extravascular signal attenuation show that signal changes due to the capillary bed increase quadratically with magnetic field strength [109, 110, 102, 111]. Since dynamic averaging applies to vessels of the size of capillaries, signal changes specific to the microvasculature increase relative to those resulting from macrovasculature as field strength increases [89]. High magnetic fields therefore provide an improvement in spatial specificity of BOLD contrast, which is valuable for high resolution fMRI.

All these factors together suggest that ultra-high magnetic field can provide the capability of providing robust, tissue-based BOLD maps with increased contrast and specificity. The increase in BOLD signal changes at elevated field [100, 96] in conjunction with the increased intrinsic signal to noise ratio can be exploited to improve the spatial resolution and/or to decrease the number of trials in functional mapping.

Spatial resolution and specificity

BOLD fMRI has been widely exploited to map brain function on the spatial scale of several millimetres to a centimetre in humans. While this scale is suitable for investigating a large number of questions in psychology, it is inadequate to study functional segregation which occurs at the millimetre level. 'High resolution' in fMRI experiments is typically used to describe studies in which voxels are of the order of a few millimetres cubed in volume. The spatial resolution of the BOLD effect depends on the intrinsic resolution of the imaging experiment and on the volume over which haemodynamic regulation occurs. Degradation of specificity in BOLD fMRI can arise from the coupling between functional changes and detectable signals containing non-specific contributions, such as those coming from large draining veins [112, 113, 114]. Deoxyhaemoglobin concentration changes due to increased neuronal activity are initiated at the point of altered neuronal activity in the capillary bed and propagate down the vasculature to large draining vessels which pool blood from a large cortical area. Therefore the source of neuronal activation may

be mis-localised by as much as millimetres distant to the site of elevated neuronal activity. The effects due to larger veins are largely suppressed at 7 T [83, 108] compared to lower fields because of the dramatic shortening of blood T_2. However, extravascular effects can persist in the small venules and veins that immediately drain the capillary bed. Most fMRI studies in humans employ GE imaging because this provides the highest BOLD contrast to noise ratio. Despite this, the presence of residual contributions from venules and small veins in GE fMRI even at 7 T suggest that submillimetre functional organization may be outside the reach of measurements based on GE BOLD contrast.

It has been suggested that the point spread function in GE BOLD contrast may have a limit of the order of 2 mm at 7 T [115]. In order to improve the specificity at such high resolution, several approaches can be adopted: 1: the employment of differential imaging techniques to eliminate the non-specific activation; 2: the use of SE BOLD contrast at ultra high field; 3: 'initial dip' imaging and 4: CBF imaging. The initial increase in deoxyhaemoglobin content which gives rise to the initial dip is thought to have spatial specificity on the millimetre to sub-millimetre scale [96, 116, 117]. However, fMRI signal changes associated with this phenomenon are small and difficult to detect. CBF changes have been shown to have sufficient specificity to allow the production of maps of sub-millimetre columnar organization in the cat visual cortex [118], but the contrast to noise ratio of perfusion-based functional maps is relatively poor. Improvements in the spatial specificity of the SE BOLD response with respect to GE BOLD contrast have been demonstrated in human visual cortex [89, 90, 91]. Using bipolar gradients to eliminate the blood contribution to the BOLD response, Yacoub et al [108] reported $\Delta R_2^\star$ changes induced by activation in the visual cortex 2.1 times larger at 7 than 4 T, whereas ΔR_2 changes measured with SE BOLD were 2.6 times larger at 7 than 4 T [89]. These results suggest that SE BOLD contrast at high magnetic fields represents a viable method for functional mapping with very high resolution and high specificity.

Increasing the spatial resolution also results in increased contrast-to-noise in the BOLD response due to reduced partial volume effects. With decreasing voxel sizes, the contribution from white matter and cerebrospinal fluid to grey matter voxels is reduced leading to larger and more consistent haemodynamic response modulations arising from cortical grey matter. The capillary level activation is expected to become independent of voxel size when the voxels are small enough that they are fully occupied by grey matter without any partial volume effects. However, increasing the resolution also results in a decrease of SNR.

4.3.2   EPI sequence optimisation

The implemention of high spatial resolution EPI gives rise to a number of challenges at 7 T. In EPI, the acquisition time for a given spatial resolution is proportional to the field of view (FOV) in the phase encoding direction and thus to the number of k-space lines acquired. Hence, increasing spatial resolution generally requires an increase in the data acquisition time, and consequently a reduction of the pixel bandwidth in the phase encoding direction. Geometric distortions in EPI occur as a result of the very low effective bandwidth in the phase encoding direction and increase with magnetic field strength. The shortening of T_2 and $T_2^{\star}$ relaxation times at 7 T limits the usable echo time for fMRI as it is not possible to sample the entire k-space with a long echo train length and retain an optimal TE. High resolution also poses heavy demands on the gradients and due to the use of high slew rates can cause peripheral nerve stimulation (PNS) in the subject. In work performed for this thesis, it was found that restricting the maximum gradient amplitude to 30 mT/m and the slew rate to 100 T/m/s allowed the acquisition of high resolution EP images without producing PNS in the majority of subjects.

High spatial resolution fMRI requires a compromise to be made between contrast-to-noise ratio, volume coverage and temporal resolution. In order to acquire high spatial resolution EP images with the boundary condition of

short TE ($\sim$ $T_2^\star$ of grey matter for fMRI), the acquisition is often segmented [119, 120, 121, 122, 123, 124] using several excitations to cover the whole of k-space. This leads to a lower temporal resolution since the time needed to acquire an image is proportional to the number of segments, and any movement between segments can significantly degrade image quality.

Partial Fourier sampling or parallel imaging techniques, described in Section 2.3.1, enable the echo train length to be shortened while maintaining the same resolution (and same field of view, FOV) at the expense of reducing the available signal to noise ratio.

An alternative method to achieve high resolution is to reduce the field of view in the phase encoding direction, since this reduces the number of echoes that need to be acquired. However, if the spatial resolution of an MR image is increased to an extent where the object extends beyond the field of view, aliasing or wrap-around artifacts will occur. The aliased signals wrap back into the field of view and superimpose on the true image, obscuring detail [125]. This artifact is shown schematically in Fig. 4.20. The dark areas indicate where aliasing has occurred. Unwanted signal from tissues responsible for aliasing artifacts can be removed by using Outer Volume Suppression (OVS) methods [126, 127, 128, 129, 83, 130] or alternatively not excited by using inner volume selection techniques [131].

However, aliasing artifacts can arise from imperfect outer-volume suppression (OVS) in zoomed (reduced FOV) imaging or from imperfect data reconstruction when using parallel imaging techniques. The combination of outer volume suppression with parallel imaging has shown to improve the image quality of single-shot EPI acquisitions, enabling high resolution fMRI at ultra-high field strength [132].

For the work in this thesis, high resolution (up to 1 mm^3 voxels) functional MRI protocols at 7 T were implemented using the combination of a reduced field of view in the phase encoding direction and outer volume suppression, and parallel imaging with a 16 channel array coil and SENSE factor of two to reduce the number of phase encoding steps. An additional benefit of the
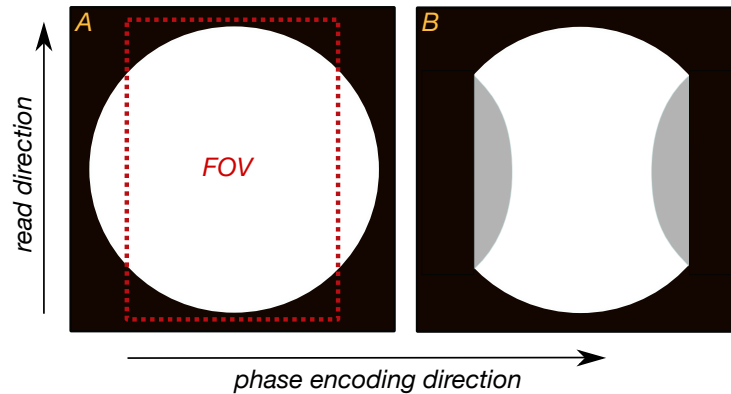
Figure 4.20: Object imaged at low resolution (A) and at higher resolution and reduced FOV (B) as shown by the red dotted box. Wrap around artefact occurs in the phase encode direction.

reduced read-out length is an increase of the bandwidth in the phase encoding direction, thus reducing geometric distortions. In order to further minimize the geometric distortions, an image-based shimming technique was developed in- house by Poole and Bowtell to correct for field inhomogeneity [133].

Outer Volume Suppression

The principle of OVS is to use a spatially selective saturation (i.e. 90°) RF pulse to flip the longitudinal magnetization into the transverse plane over one or more independently defined saturation slabs which can have a different plane orientation than used for imaging (see Fig. 4.21.A). Wrap-around aliasing artefact can be suppressed by selectively exciting broad slabs displaced along the phase-encoding axis just outside the FOV, thus, the signal from tissue that would otherwise alias into the image is suppressed.

Following the RF pulse we intentionally create phase dispersion across the saturated band by applying spoiler gradient pulses (Fig. 4.21.B). Under the influence of the spoiler gradient, the transverse magnetization dephases along the direction of the gradient, leading to signal cancelation within a voxel. Meanwhile, the longitudinal magnetization experiences no effect from the spoiler gradients. The spoiler pulse is usually applied along two of the gradient axes to give additional phase dispersion in orthogonal directions. The saturation
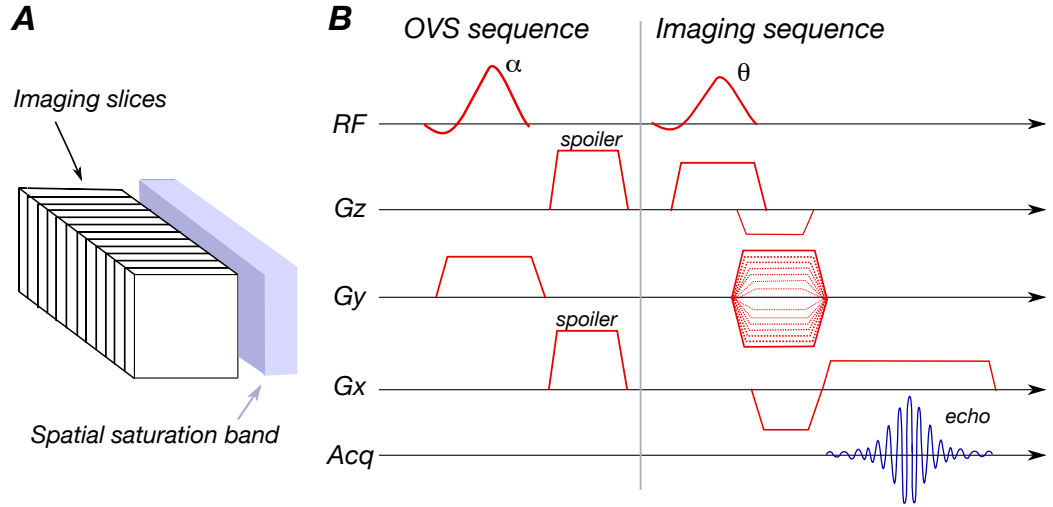
Figure 4.21: (A) A spatial saturation slab placed to the right side of the imaging slices. (B) An outer volume suppression sequence followed by a gradient-echo imaging sequence. The α RF pulse is used to define a saturation slab. Slab selection is accomplished by applying a gradient pulse in y. The spoilers destroy residual transverse magnetization. The θ excitation pulse of the gradient echo sequence that follows has a different carrier frequency from the saturation pulse.

pulse is immediately followed by excitation and imaging of the desired area before the longitudinal magnetization has sufficient time to recover.

At 7 T, the number of pre-saturation pulses used for outer volume suppression often has to be limited so as to ensure that the RF power deposition in the brain does not exceed SAR levels. In the work presented in this thesis, a train of three pulses with a flip angle of 94° was used which gives good outer volume suppression in slab width of up to 8 cm.

RF pulse power

Optimization of the RF power to generate a requested flip angle can be performed in two ways on the Philips scanner; either by monitoring the signal from a 1 cm transverse plane located at the isocenter of the magnet or by monitoring signal from the imaging plane. If power optimisation (PO) is performed in the transverse plane (which is the default), the power is optimised for a 1 cm transverse volume centered at the isocentre of the imaging coil. If
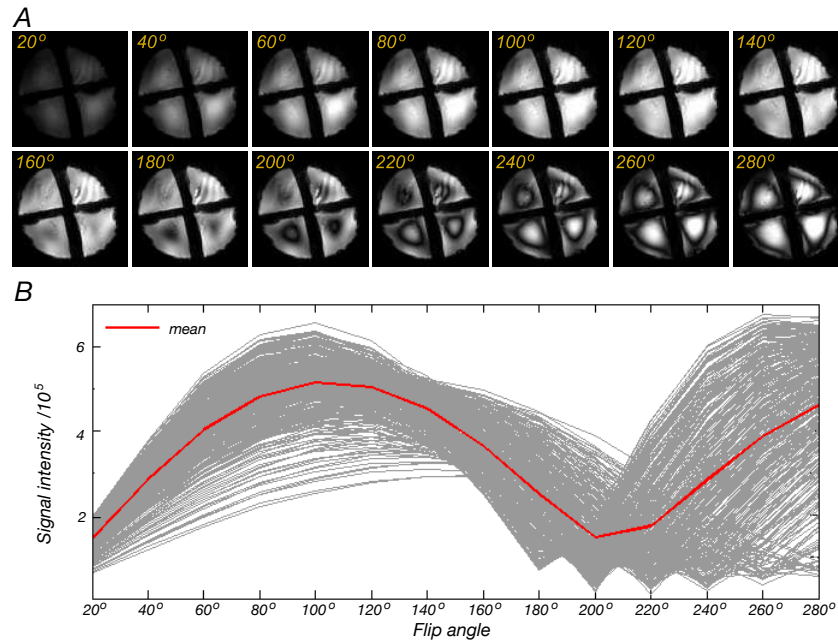
Figure 4.22: GE EP images of a phantom showing the variation of the MR signal intensity with the requested excitation flip angle. The graph shows MR signal intensity versus excitation flip angle for each voxel (grey) in a region of interest (ROI) in the upper right quadrant and for the mean across voxels. It can be seen that an optimal excitation pulse requires a requested $100°$ flip angle to be set on the flip angle slider.

the imaging plane is selected, PO will be performed for a transverse volume centered at the centre of the imaging stack. The imaging plane setting was used work performed in this thesis. Due to the B_1 field variability across the imaging volume, the effective RF pulse flip angle will vary across the imaging volume.

The scanner aims to set a flip angle of $90°$ for the excitation pulse, but in practice this pulse will not be equal to the $90°$ requested flip angle. In order to determine the optimal flip angle for the excitation pulse, we acquired a series of axial GE-EP images of a phantom using a range of flip angles. The resulting images for one representative slice and a plot of the MR image intensity versus flip angle for a region of interest in the upper right quadrant of the phantom are shown in Fig. 4.22. As expected, the MR signal intensity has a sinusoidal dependence on the flip angle, but this dependence varies slightly different across voxels (grey lines). The mean across voxels (red line) suggests
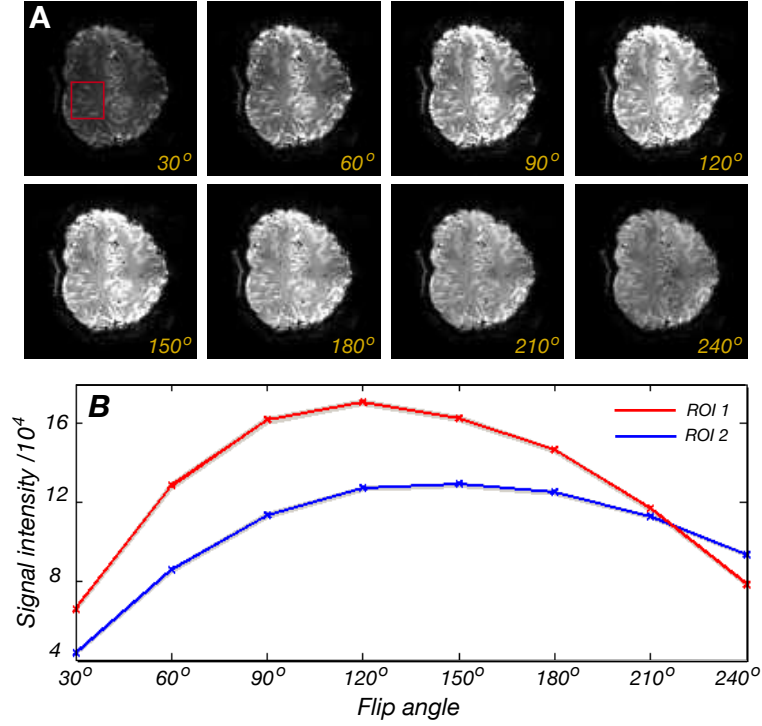
Figure 4.23: (A) GE MR signal intensity for various flip angles of the excitation pulse and (B) graph of the MR image intensity versus flip angle for an ROI (as shown in Figure A) in a slice at the inferior (red) and superior (blue) part of the brain.

that in order to achieve an average excitation flip angle of $\sim 90°$ over the region of interest, the flip angle of the excitation pulse needs to be set to $110°$ in the EPI protocol.

These experiments to determine excitation 'flip angle' were repeated on a human head. The resulting GE images are shown in Fig. 4.23.A for a representative slice. In order to determine the optimal refocusing pulse for SE EPI, a series of SE echo planar images were also acquired with different settings for the flip angle of the refocusing pulse. The SE images for the corresponding slice are shown in Fig. 4.24.A. In order to illustrate the variability across slices, graphs of the image intensity versus excitation and refocusing flip angles are shown in Fig. 4.23.B and 4.24.B for two regions of interest, 1 and 2, defined in the inferior and superior part of the brain respectively. The curves for ROI1 (red) and ROI2 (blue) show that in the EPI protocol the excitation flip angle
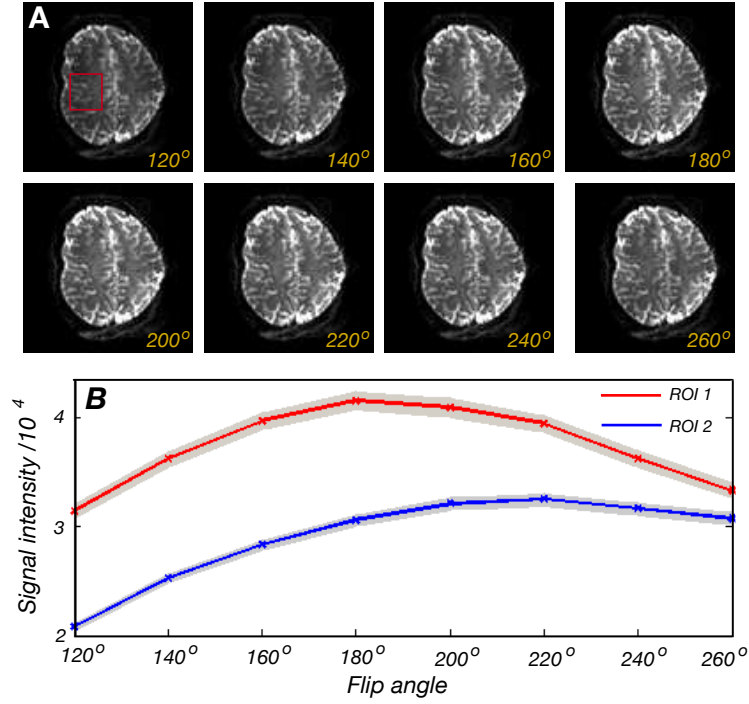
Figure 4.24: (A) SE MR signal intensity for various flip angles of the refocusing pulse and (B) graph of the MR image intensity versus flip angle for an ROI in a slice at the inferior (red) and superior (blue) part of the brain.

must be set to 120° and 150° respectively in order to maximize the signal intensity, and the refocusing flip angle should be set to 180° and 220° in order to achieve an optimized refocusing effect in ROI 1 and 2 respectively. The values of excitation and refocusing flip angles for ROI1 are closer to the expected value than ROI2 as the ROI in the inferior part of the brain (lower slice) is closer to the isocentre of the coil, which is where the power optimization performs the best.

4.3.3   Shimming methods

Magnetic resonance imaging requires a homogeneous magnetic field, B_0, with constant magnitude over the whole region of interest (ROI). However, there are always deviations in the static magnetic field, ΔB_0, originating from various sources causing off-resonant effects. The final homogeneity required for the collection of good quality images requires an additional level of con-

trol and correction of field inhomogeneity which is known as *shimming*. Any magnetic field can be represented as an infinite series of orthogonal functions. The spherical harmonics [134] form such a series, and are commonly used to represent the field in NMR and MRI. When the field is represented in this way, the magnitude of the amplitudes of the spherical harmonics tend to zero with increasing order, n [135]. ΔB_0 can therefore be reduced by compensating a few orders of spherical harmonics. MR scanners are equipped with a set of shim coils, each designed to provide a low order, pure spherical harmonic contributions to the main field. The shimming coil currents can be individually and systematically set to produce the correction field needed to minimize ΔB_0. Prammer et al [136] introduced the approach of measuring the spatial variation of ΔB_0, analysing the spherical harmonic content and setting the currents in the shim coils to minimize the measured field inhomogeneity.

The shim currents, I^{shim}, can be determined by pseudo inversion, †, of a matrix describing the field produced by the shim coils, B_0^{shim}, multiplied by the field required to maximally null, ΔB_0

$$I^{shim} = -\Delta B_0 \cdot (B_0^{shim})^\dagger, \qquad (4.16)$$

where $I^{shim} = [I^{\{0,0\}}, I^{\{1,0\}}, I^{\{1,1\}}, ..., I^{\{n,m\}}]$, $I^{\{n,m\}}$ is the current to be passed though the shim coil that produces the spherical harmonic with order n and degree m, $B_0^{shim} = [B_0^{\{0,0\}}, B_0^{\{1,0\}}, B_0^{\{1,1\}}, ..., B_0^{\{n,m\}}]$ and $B_0^{\{n,m\}}$ is the magnetic field generated by passing a current through the n, m shim coil.

The FASTMAP, fast automatic shimming technique which is based on mapping the field along projections, and its derivatives [137, 138, 139], is a time efficient method that is commonly used in clinical MR scanners involving measurement of ΔB_0 along 6 'pencil beam' lines to acquire the required information to optimally set the shim coil currents.

Field inhomogeneities give rise to severe geometric distortions in the phase encoding direction of EP images due to the small pixel bandwidth in this direction. In order to minimize the geometric distortions of the fMRI data,
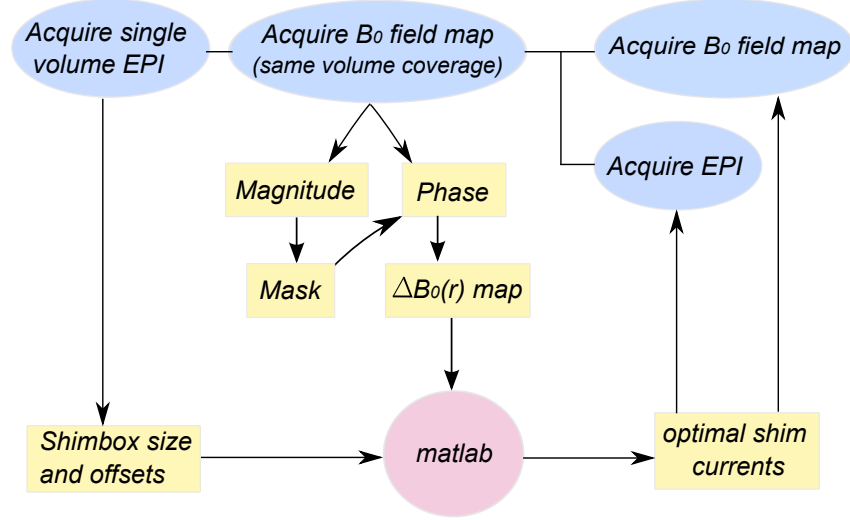
Figure 4.25: Schematic of the shimming process. Processes shown in oval are scans acquired.

an image-based shimming technique was used here to correct field inhomogeneities [133]. This technique involves computing the shim coil currents up to the second order which minimize the magnetic field inhomogeneity over a cuboidal region of interest using a prior acquired field map. This process is shown schematically in Fig. 4.25. First, a single EPI volume is acquired to define the region over which shimming is applied. Maps of the magnetic field inhomogeneity, $\Delta B_0(r)$, are then acquired using the standard, B_0-mapping sequence available on the Philips scanner, which is based on acquisition of two gradient echo images with echo times of TE_1=6 ms and TE_2=6.5 ms as described in Section 2.3.3. The resulting data are exported for shim calculation in Matlab (The Mathworks, Inc) running on a separate PC. The magnitude images are skull-stripped using the Brain Extraction Tool (BET) in FSL [140] and thresholded to generate a brain-only mask which is then applied to the phase data to produce a map of $\Delta B_0(r)$ in the brain.

Shim $\Delta B_0(r)$ maps are then generated from pure spherical harmonics in the same image space and collated into a matrix which is pseudo-inverted and multiplied by the measured $\Delta B_0(r)$ map to find the shim strengths required to maximize the field homogeneity in the cuboidal shim region [136]. If the
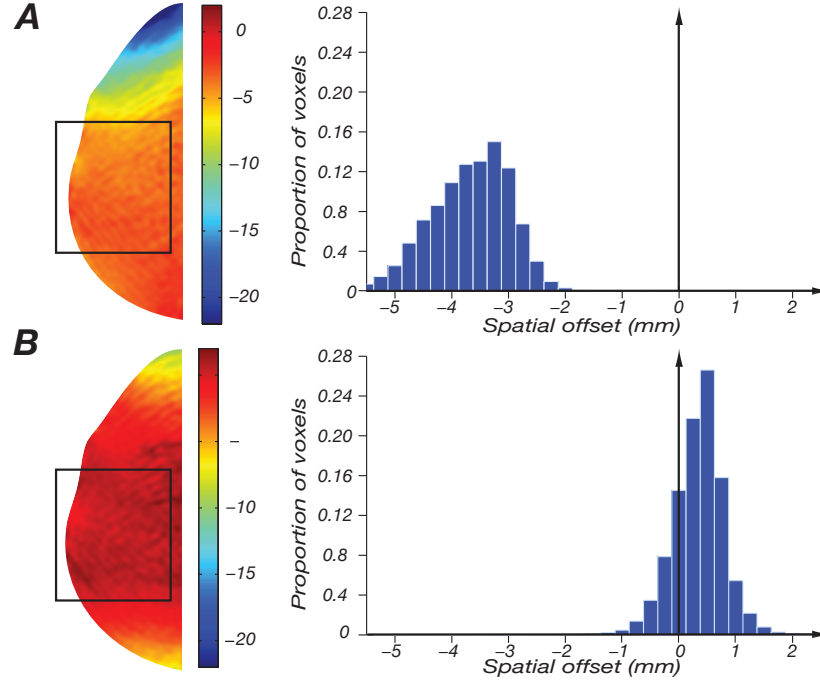
Figure 4.26: Field map obtained with the (A) conventional pencil-beam and (B) image-based shimming method in pixel units. The colour scale indicates the geometric distortion in the phase encoding (right-left) direction. The black square represent the border of the shimming box, which extends ~ 20 mm in the superior-inferior direction. A histogram of the pixel displacement for each map is shown on the left. The y-axis represents the fraction of number of voxels within the shimming cuboidal region.

shim box is small and there is some large second order inhomogeneity present, the algorithm performs a constrained fit taking into account the limits of the amount of current that can be passed through each coil [141]. The calculated optimal shim values are then transferred back to the scanner and fixed for the remainder of the data acquisition. The speed of the shim calculation was measured overall to be less than 30 s in Matlab R2007 on a 2.0 GHz Pentium 4 processor, making it a useable shimming tool for standard MRI experiments. The effective local geometric distortion in high resolution, 1 mm isotropic, EP images due to inhomogeneities in the magnetic field was assessed for the imaged-based shimming technique and the conventional pencil-beam (PB) approach implemented on the scanner [138] by calculating a field map for each and converting to a geometric distortion or spatial offset map
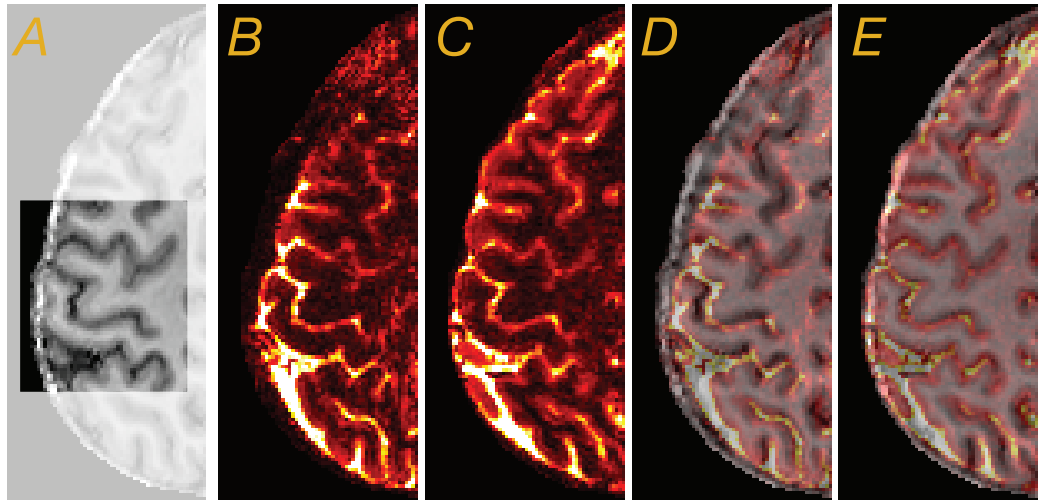
Figure 4.27: Skull-stripped undistorted MPRAGE image (A). Highlighted square indicates shimming volume. Echo-planar image acquired with (B) conventional pencil-beam and (C) imaged-based shimming method and in (D,E) image from (B,C), hot colors, superimposed on MPRAGE image from (A), greyscale.

in pixel units (deviations in Hz were converted to pixels using the 22.8 Hz bandwidth per pixel of the EPI sequence). Figure 4.26 shows the spatial offset map in pixel units acquired with pencil-beam (A) and image-based (B) shimming techniques. The colour bar encodes the pixel shift in the right-left direction. The shimming was optimized for the pre- and post-central gyri (areas of interest to Chapter 6 and 7) which are included in the region of interest represented by the rectangular box. The reduction of local geometric distortion is illustrated by the histograms, which highlight that distortions of less than one voxel (1 mm) can be achieved over the shimming region using the imaged-based shimming technique.

The effect of both shimming methods on geometric distortion in EP images is shown in Fig. 4.27. The phase encoding (and hence field inhomogeneity related pixel shift) is in the right-left direction. The image-based shimming technique (C,E) shows a better correspondence between EPI data and (undistorted) anatomical MPRAGE images than the conventional pencil-beam shimming method (B,D) as implemented on the Philips scanner.

4.3.4 Inversion recovery EPI acquisition

One aim of the high resolution fMRI study was to assess the spatial localisation of the measured BOLD signal changes at ultra-high field. To aid the segmentation of the EPI images into grey matter, white matter and CSF so as to classify activated voxels into tissue types and thus determine the 'spatial spread' of activation, an additional inversion recovery (IR) data set was acquired. An inversion recovery pulse sequence with a delay (TI) before the EPI acquisition introduces T_1-weighting to the EP images. Figure 4.28.A shows a
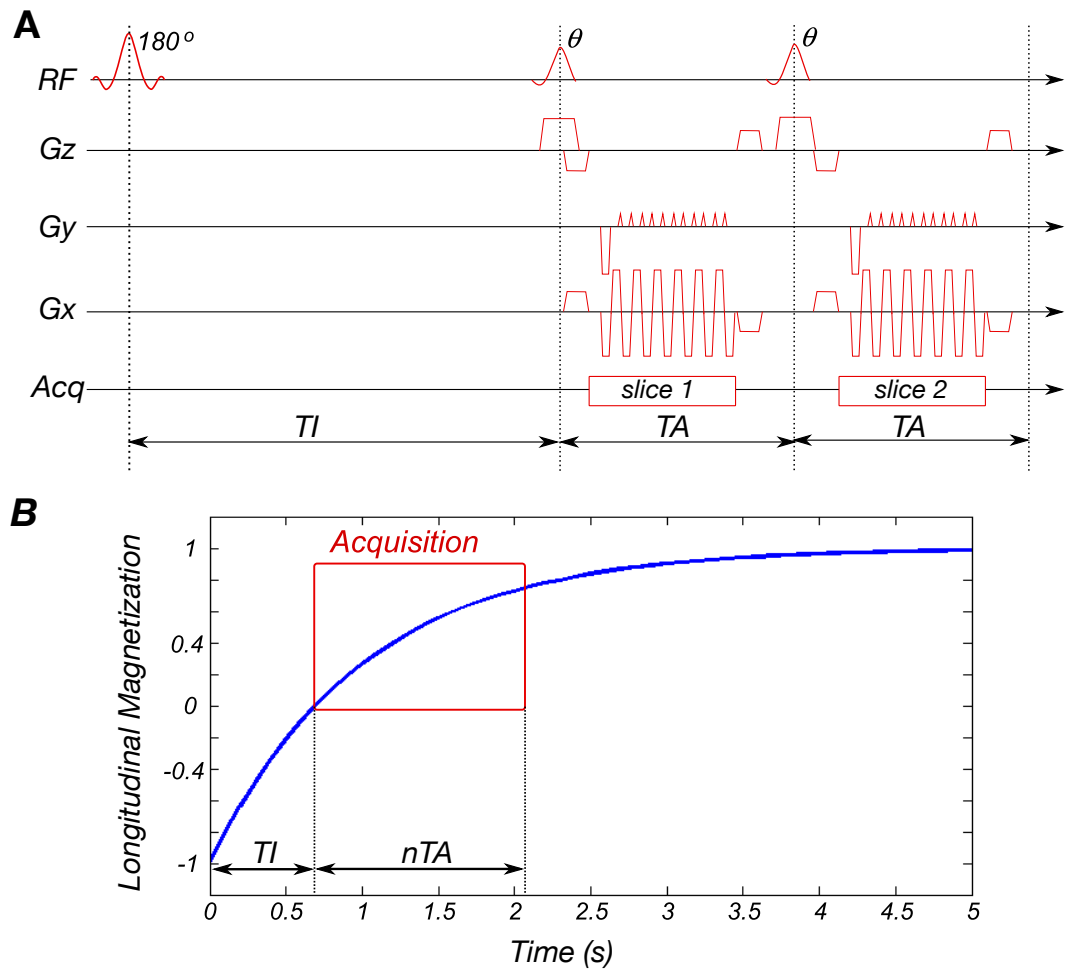

Figure 4.28: (A) An IR followed by multislice EPI acquisition sequence diagram and (B) the evolution of the longitudinal magnetization for white matter. The first slice is acquired after a time TI following the inversion pulse. TA is the acquisition time for a single slice and the total acquisition time for n slices is n times TA.

multi-slice acquisition following a single inversion pulse. By altering the time from the inversion pulse to the excitation pulse (TI) the signal of a given tissue type can be nulled. However, if multiple EPI images are acquired following each TI, the contrast will vary across slices in the multislice data set. This is illustrated in Fig. 4.28.B, for which the longitudinal magnetization of white matter is plotted throughout the total acquisition time of a simulated multi-slice set. The first slice is acquired a time TI after the inversion pulse. At this time the value of the longitudinal magnetization of white matter is close to the null point, however through the total acquisition of all n slices the longitudinal magnetization has time to recover. We can see from the graph that after the 1.4 s that it takes to acquire 24 slices (TE= 25 ms, EPI factor=39) the longitudinal magnetization has recovered to almost 80% of the equilibrium value. Therefore in order to maintain the same contrast across the different slices, a simpler sequence was used. This is a variation of the conventional EPI sequence, where only one slice is acquired per TR, with a slice selective inversion pulse applied at a time TI earlier. This ensures that the inversion delay is the same for all n slices in the multislice set, mantaining constant contrast across the slices. However this method does increase the time taken to acquire a multi-slice data set, with the acquisition time being n times that of a conventional multi-slice EPI sequence. An alternative method is fast IR for rapid T_1-mapping [142], but this is not currently available on the Philips system.

To improve the performance of the adiabatic inversion pulse, particularly in regions such as the visual cortex where the B_1-field is reduced, the RF pulse power was increased (as described in Section 4.2.3). A value of 120 % of the scanner calculated level was used to obtain the IR images shown in Fig. 4.29.(A,B,C). It should be noticed that since this sequence employs a long TR, then for high resolution imaging where a rest-slab is required to prevent fold over, the power of the RF pulse used in saturating the outer volume (denoted here as the 'rest-slab power') should be increased to null the signal adequately compared to that used for the fMRI acquisition where a lower
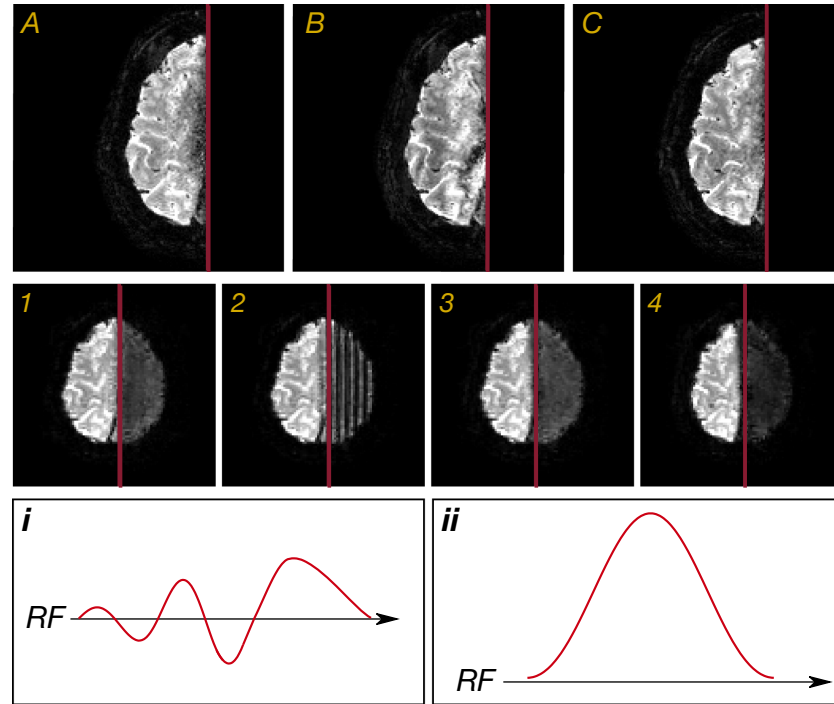
Figure 4.29: Images, top: Comparison of a GE-EP image with rest slab power 1 (A) to an EP image acquired using the TR of the IR-EPI sequence with REST slab power 1 (B) and 4 (C). Image resolution is 1 mm isotropic with FOV (AP × RL): 192 mm × 72 mm. Bottom: Effect of rest slab power on EP image (with TR of IR-EPI). The position of the slab is to the right of the red line. Diagrams: (i) conventional (power 1) and (ii) broadband (power 3) REST pulse shapes.

steady state signal is reached. Also note htat a rest slab of power 4 would significantly increase SAR for fMRI acquisitions which have much shorter TR and so limit slice coverage. When the rest slab power is low, signal outside the FOV folds over into the EP image (Figure 4.29.B) compared to the GE EP image (Figure 4.29.A). To show the effect of the rest-slab power over the region outside the FOV where the signal should be suppressed (and will wrap around at higher resolution), an image with a coarse in-plane resolution of 2 × 2 mm^2 was acquired with the rest-slab in the same position as for the high resolution image. This is shown in Fig. 4.29 (bottom) for a range of rest slab powers from 1 to 4: power 1 corresponds to a train of three pulses of increasing flip angle as shown in Fig. 4.29.i; power 2 corresponds to this sequence applied twice back-to-back: power 3 corresponds to a broadband pulse of flip angle
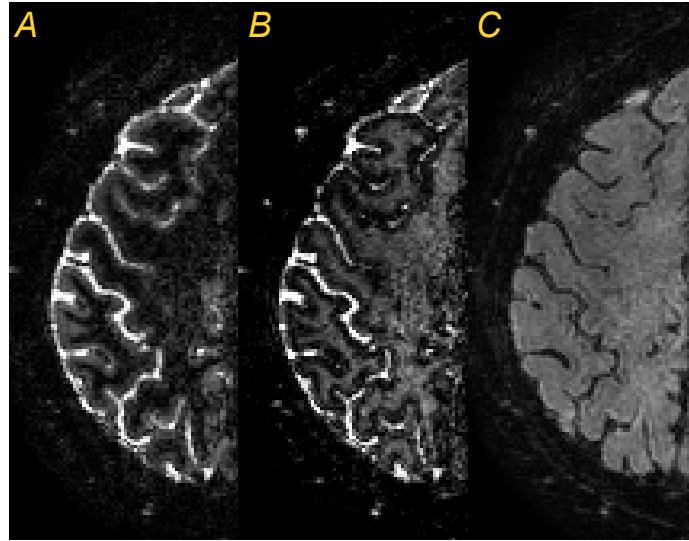
Figure 4.30: Single slice showing the different contrast achievable for inversion times (A) 450 ms (B) 1200 ms and (C) 2300 ms. Image resolution is 1 mm isotropic with FOV (AP × RL): 192 mm × 72 mm.

$458°$, as shown in Fig. 4.29.ii, and power 4 corresponds to the broadband pulse applied twice back-to-back.

Power 4 can be seen to be optimal to suppress the signal and was thus used for IR experiments. When power 4 is applied, the wrap- around artefact in the high resolution image is reduced (Figure 4.29.C). In order to best null the white matter, grey matter and CSF, delay times between the inversion and acquisition pulse of 450 ms, 1200 ms and 2300 ms respectively were used. Figure 4.30 shows images of the same slice where (A) white matter, (B) grey matter and (C) CSF have been nulled. These images can be used to segment the grey matter, white matter, and CSF, and subsequently to mask the functional statistical maps to hide false activity approximately occuring in either the white matter or the CSF, or to localize activity by plotting a histogram of activated voxels versus tissue type.

4.4   Unfolding of cortical surfaces

Topographic organization of cortical areas can only be properly understood in the context of the intrinsic two-dimensional structure of the cortical surface. One approach to visualize grey matter is to create a surface model of the grey matter-pial boundary; the cortical grey matter is rendered in three dimensions as a tesselated surface and mainly those portions of the exterior brain surface are seen. Since much of the cortical grey matter is buried deep within the folds of the brain, and therefore obscured from view, visualization of neural activity by fMRI within sulci requires novel visualization techniques, such as the use of a flattened representation of the cortex, in which the 3D surface is projected onto a 2D sheet by cortical unfolding. Using a flattened representation, one can appreciate the activity across a large region of the cortex within a single image. This method has been applied to the high resolution fMRI data shown in the following chapters. In this work, the portion of the grey matter representation in the cortical layer of interest that falls along the grey-white matter boundary is flattened.

In order to create a flattened representation of the grey matter surface, one must first identify and extract the cortical surface. Computational methods have recently been developed [143, 144, 145, 146] to extract and unfold the cortical surface from high-resolution anatomical MR images. In the work described in this thesis, custom written software developed by Larsson [147] (SurfRelax) has been used to obtain accurate reconstructions of the cortical surface. The main advantage of this tool over a number of other publicly available methods is that it yields a topologically correct surface that at the same time preserves the detailed shape of the cortex.

The method for cortical surface extraction developed by Larsson uses a deformable template that is voxel-based, rather than surface-based. Briefly, a template is deformed voxel by voxel to the white matter surface in a series of steps designed to make the deformation insensitive to noise but able to capture detailed sulcal geometry. The surface of the deformed template is
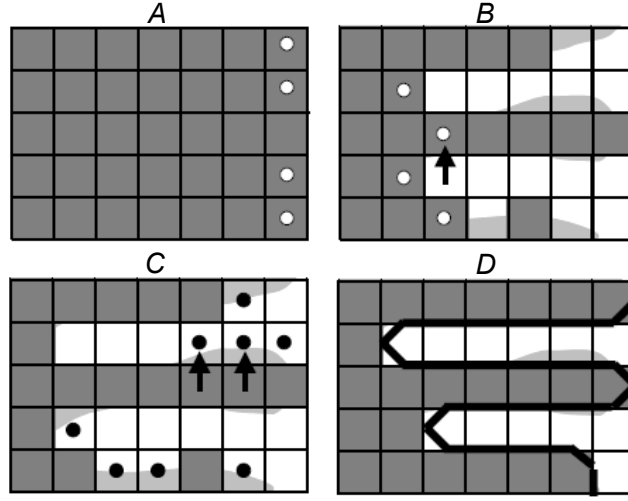
Figure 4.31: Schematic description of topologically constrained deformation adapted from [147]. (A) Initial template (grey) superimposed on input volume. The white circles represent voxels with subthreshold values, which are scheduled for removal). (B) Result after five rounds of erosion using a high threshold. (C) Result of completed erosion. The black circles represent voxels scheduled to be added in a subsequent dilation process. (D) Result of completed dilation.

then extracted and refined against the original image.

4.4.1   Larsson's algorithm for topologically constrained deformation

The method deforms an elastic surface to the target shape by iteratively moving individual vertices guided by the local tissue intensity in the target image. In voxel space, this corresponds to adding or removing (inverting) voxels along the surface of a binary-valued image volume, guided by the voxel values in the target image. Voxel inversions that result in a change of the local topology are not allowed. The relationship which monitors the change in the topology is given by the Euler-Poincaré formula:

$$2 - 2g = \chi = F + V - E, \qquad (4.17)$$

where g is the topology or genus, equivalent to the number of handles/holes, and the Euler Characteristic χ of a polygonal surface is related to the number of surface primitives; vertices V, edges E and faces F. For instance, the Euler Characteristic of a sphere is two and for a torus is zero. As can be seen in the above relationship, a local operation that change the number of surface primitives, but does not change the global Euler Characteristic does not affect the topology of the surface. The efficient use of this formula to test for topological changes in 3D volume relies on the method used to extract a surface from the voxellated data. The method used in this application for extracting a surface from the 3D volume is a discretized version of the Marching Cubes algorithm [148] developed to specify the surface configuration for every cube of eight voxels uniquely.

The deformation may be guided by smoothness constraints which prevent the deformable volume from converging too quickly and becoming stuck in local minima. The voxels of the template define a closed single surface which by definition cannot self-intersect. The algorithm is iterated a specified number of times or until no more voxels can be changed without changing the topology. Figure 4.31 describes the algorithm schematically. Figure 4.31.A shows the initial template, which is superimposed on the input volume. The outer boundary of the template is to the right of the image. The boundary voxels with subthreshold values (i.e. voxels scheduled for removal) are indicated with a white circle. The result after five rounds of erosion using a high threshold is shown in Fig. 4.31.B. Note that removal of the voxel indicated by the arrow, which is below threshold and thus is scheduled to be removed in the next round, would cause a topological change. Therefore this voxel will not be removed. Figure 4.31.C shows the result of the completed erosion. Voxels scheduled for adding in a subsequent dilation process using a high threshold are indicated with a black circle. Note that adding the voxels indicated by the arrows will change the topology, hence the voxels will not be added. Fig. 4.31.D shows the result of the complete dilation. Because of the topology constraints, the volume preserves the overall shape of the input. The position

of the extracted surface is indicated by a black line. The surface generated this way provides a very good starting estimate for subsequent surface-based deformation to capture the fine details of the surface.

Note that for the work performed in this thesis, cortical segmentations (Section 5.4 and Section 6.3) were obtained of high-resolution T_1-weighted anatomical images acquired at 3 T, which displayed less B_1-inhomogeneity-related signal intensity variation than images acquired at 7T.

4.4.2   Reconstruction of cortical surface with SurfRelax

There are various steps involved in the surface reconstruction and deformation process. The process of reconstructing the cortical surface with SurfRelax begins with a series of pre-processing steps applied to the original T_1-weighted anatomical MPRAGE image of the brain; the first step corrects for intensity variations due to B_1-field inhomogeneities. Fig. 4.32.A shows the original image. Fig. 4.32.B shows the intensity corrected image. Note that the intensity variations across the image, especialy at the centre, have been reduced compared to the original image Fig. 4.32.A. Next non-brain tissues are removed by a deformable surface algorithm similar to that described by Dale *et al.* [143], where the white matter component is deformed into the shape of the inner surface of the skull. Fig. 4.32.C shows the skull stripped-intensity corrected image superimposed on the intensity corrected image. Next, subcortical structures such as the basal ganglia, the thalamus and the ventricles are automatically identified and assigned the mean intensity of the white matter in order to obtain a smooth surface in the medial aspect of each hemisphere. Finally, the hemispheres are segmented from each other and from the cerebellum and brainstem by a series of automated processes whereby the topologically constrained algorithm is applied. This results in a single filled volume for each cortical hemisphere. Fig. 4.32.D shows the resulting surfaces superimposed on the skull stripped image and colour coded so that the left hemisphere is green and the right hemisphere yellow. These surfaces are used to segment the white
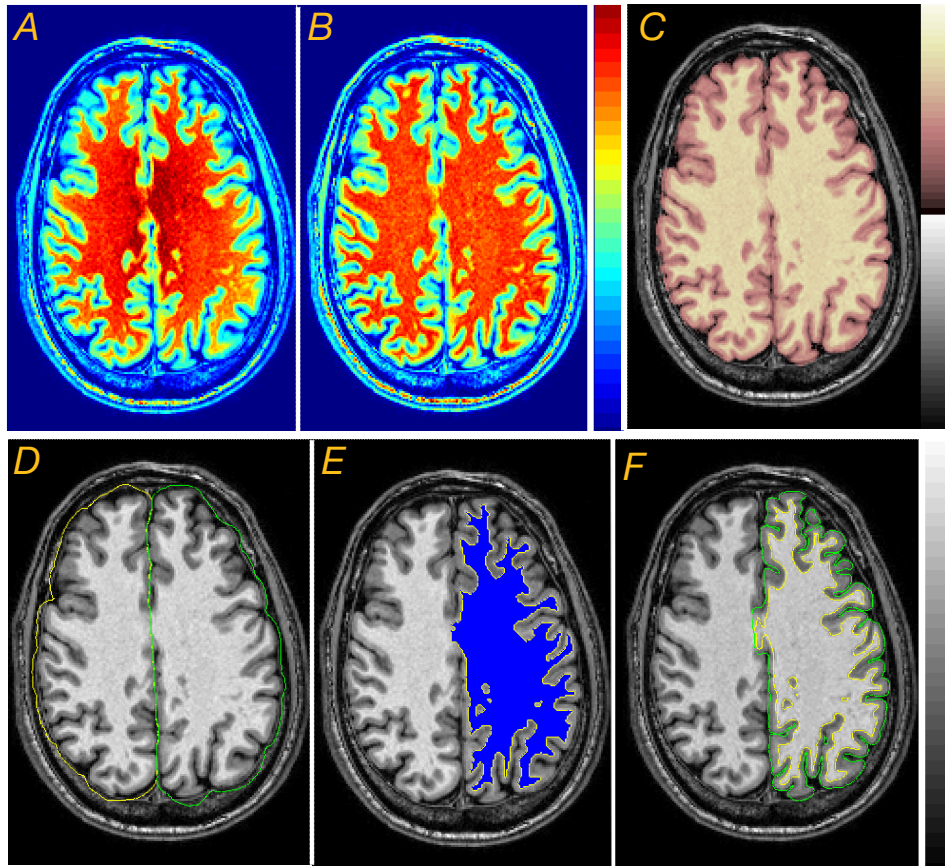
Figure 4.32: Different steps in the cortical surface extraction process. (A) Original T_1-weighted anatomical image (1x1x1 mm^3 spatial resolution).(B) Corresponding intensity-corrected image.(C) Skull- stripped image (pink map) superimposed on to the intensity corrected image (grey map). (D) Right (yellow) and left (green) hemisphere surfaces (E) Extracted white matter surface of the left hemisphere (yellow) and corresponding white matter volume (blue). (F) Optimized inner cortical surface (green) and outer cortical surface (yellow) of the left hemisphere.

matter of each hemisphere in the surface extraction process. The first step in this process is the generation of a topologically correct template volume using the surface extraction algorithm described above with minor modifications. This is a method similar to that employed in mrUnfold [146]. A template volume with spherical topology is generated directly from the filled white matter compartment of each hemisphere generated in the previous step. This template is then deformed onto the filled white matter volume by a series of topologically constrained erosions and dilations. Fig. 4.32.E shows the extracted white

matter surface of the left hemisphere and its corresponding volume. The resulting surface is a good approximation to the grey-white matter interface. However, to improve the fit in regions of high curvature and to generate a surface representation of the outer grey matter surface, the extraction is followed by an optimization step; the surface is iteratively deformed in three stages onto the original intensity normalized image [143]. First, the surface is expanded a few millimetres towards the middle of the cortex. In the second stage, the surface is shrunk back onto the white matter to ensure that small fragments of white matter which may have been missed in the surface extraction step are accounted for. Third, the surface is expanded from the middle of the cortex to the grey-CSF boundary. The resulting reconstructed grey-white matter and grey matter-pial boundary surfaces for the left hemisphere are shown in Fig. 4.32.F.

4.4.3 Surface visualization

Much of the human cortical surface is obscured from view by the complex pattern of foldings, making the spatial relationship between different surface locations hard to interpret (see Fig. 4.33.A.). The final surfaces need to be transformed to an inflated or flattened representation for visualization of functional data. Figure 4.33.A shows a folded grey matter surface of the
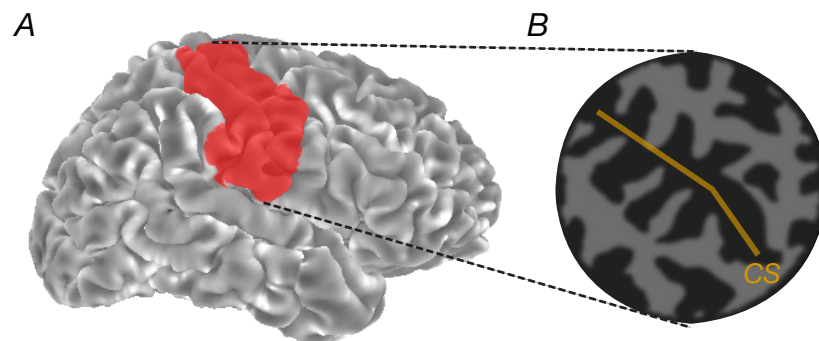
Figure 4.33: (A) Folded grey matter surface of the right hemisphere and (B) flattened representation of red patch shown in (A). The main curvature has been overlayed for better visualization of the sulci (dark region) and gyri (bright region).

right hemisphere. Flattening is performed over a selection or patch of the folded surface, such as the red region around the central sulcus. The corresponding flattened patch, obtained using custom written software (mrTools, NYU, http://www.cns.nyu.edu/heegerlab/wiki/; VISTA, Stanford), is shown in Fig. 4.33.B. The main curvature of the surface is overlaid on the patch so that the dark grey region represents the sulci and the lighter grey region the gyri. Once the cortical surface has been inflated or flattened, it can be used to display functional data or for morphometric analysis.

Bibliography

[1] W. A. Edelstein, G. H. Glover, C. J. Hardy, and R. W. Redington. The intrinsic signal-to-noise ratio in NMR imaging. *Magn Reson Med*, **3**(4), 604–618, (1986).

[2] D. I. Hoult and R. Richards. The signal-to-noise ratio of the nuclear magnetic resonance phenomenon. *J Magn Reson*, **24**(1), 71–85, (1976).

[3] J. T. Vaughan, M. Garwood, C. M. Collins, W. Liu, L. DelaBarre, G. Adriany, P. Andersen, H. Merkle, R. Goebel, M. B. Smith, and K. Ugurbil. 7T vs. 4T: RF power, homogeneity, and signal-to-noise comparison in head images. *Magn Reson Med*, **46**(1), 24–30, (2001).

[4] R. M. Weisskoff, J.Baker, J. Belliveau, T. L.Davis, K. K. Kowng, M. S. Cohen, and B. R. Rosen. Power spectrum analysis of functionally-weighted MR data: What's noise? *Proc. 12th Metting Soc. Mag. Res. Med, New York,* **7**, (1993).

[5] G. Krueger and G. H. Glover. Physiological noise in oxygenation-sensitive magnetic resonance imaging. *Magn Reson Med*, **46**(4), 631–637, (2001).

[6] C. Triantafyllou, R. D. Hoge, G. Krueger, C. J. Wiggins, A. Potthast, G. C. Wiggins, and L. L. Wald. Comparison of physiological noise at 1.5 T, 3 T and 7 T and optimization of fMRI acquisition parameters. *Neuroimage*, **26**(1), 243–250, (2005).

[7] H. Bomsdorf, T. Helzel, D. Kunz, P. Roeschmann, O. Tschendel, and J. Wieland. Spectroscopy and imaging with a 4 tesla whole-body MR system. *NMR Biomed*, **1**(3), 151–158, (1988).

[8] P. M. Robitaille, A. M. Abduljalil, A. Kangarlu, X. Zhang, Y. Yu, R. Burgess, S. Bair, P. Noa, L. Yang, H. Zhu, B. Palmer, Z. Jiang, D. M. Chakeres, and D. Spigos. Human magnetic resonance imaging at 8 T. *NMR Biomed*, **11**(6), 263–265, (1998).

[9] A. Kangarlu, B. A. Baertlein, R. Lee, T. Ibrahim, L. Yang, A. M. Abduljalil, and P. M. Robitaille. Dielectric resonance phenomena in ultra high field MRI. *J Comput Assist Tomogr*, **23**(6), 821–831, (1999).

[10] Q. X. Yang, J. Wang, X. Zhang, C. M. Collins, M. B. Smith, H. Liu, X.-H. Zhu, J. T. Vaughan, K. Ugurbil, and W. Chen. Analysis of wave behavior in lossy dielectric samples at high field. *Magn Reson Med*, **47**(5), 982–989, (2002).

[11] C. M. Collins, W. Liu, W. Schreiber, Q. X. Yang, and M. B. Smith. Central brightening due to constructive interference with, without, and despite dielectric resonance. *J Magn Reson Imaging*, **21**(2), 192–196, (2005).

[12] P.-F. V. de Moortele, C. Akgun, G. Adriany, S. Moeller, J. Ritter, C. M. Collins, M. B. Smith, J. T. Vaughan, and K. Ugurbil. B1 destructive interferences and spatial phase patterns at 7 T with a head transceiver array coil. *Magn Reson Med*, **54**(6), 1503–1518, (2005).

[13] J. T. Vaughan, H. P. Hetherington, J. O. Otu, J. W. Pan, and G. M. Pohost. High frequency volume coils for clinical NMR imaging and spectroscopy. *Magn Reson Med*, **32**(2), 206–218, (1994).

[14] G. Adriany, P.-F. V. de Moortele, J. Ritter, S. Moeller, E. J. Auerbach, C. Akguen, C. J. Snyder, T. Vaughan, and K. Ugurbil. A geometrically adjustable 16-channel transmit/receive transmission line array for improved RF efficiency and parallel imaging performance at 7 Tesla. *Magn Reson Med*, **59**(3), 590–597, (2008).

[15] U. Katscher, P. Boernert, C. Leussler, and J. S. van den Brink. Transmit SENSE. *Magn Reson Med*, **49**(1), 144–150, (2003).

[16] Y. Zhu. Parallel excitation with an array of transmit coils. *Magn Reson Med*, **51**(4), 775–784, (2004).

[17] P. A. Bottomley and E. R. Andrew. RF magnetic field penetration, phase shift and power dissipation in biological tissue: implications for NMR imaging. *Phys Med Biol*, **23**(4), 630–643, (1978).

[18] D. L. Thomas, E. D. Vita, S. Roberts, R. Turner, T. A. Yousry, and R. J. Ordidge. High-resolution fast spin echo imaging of the human brain at 4.7 T: implementation and sequence characteristics. *Magn Reson Med*, **51**(6), 1254–1264, (2004).

[19] E. D. Vita, D. L. Thomas, S. Roberts, H. G. Parkes, R. Turner, P. Kinchesh, K. Shmueli, T. A. Yousry, and R. J. Ordidge. High resolution MRI of the brain at 4.7 Tesla using fast spin echo imaging. *Br J Radiol*, **76**(909), 631–637, (2003).

[20] R. Turner, A.-M. Oros-Peusquens, S. Romanzetti, K. Zilles, and N. J. Shah. Optimised in vivo visualisation of cortical structures in the human brain at 3 T using IR-TSE. *Magn Reson Imaging*, **26**(7), 935–942, (2008).

[21] V. P. Clark, E. Courchesne, and M. Grafe. In vivo myeloarchitectonic analysis of human striate and extrastriate cortex using magnetic resonance imaging. *Cereb Cortex*, **2**(5), 417–424, (1992).

[22] N. B. Walters, G. F. Egan, J. J. Kril, M. Kean, P. Waley, M. Jenkinson, and J. D. G. Watson. In vivo identification of human cortical areas using high-resolution MRI: an approach to cerebral structure-function correlation. *Proc Natl Acad Sci U S A*, **100**(5), 2981–2986, (2003).

[23] H. Bridge, S. Clare, M. Jenkinson, P. Jezzard, A. J. Parker, and P. M. Matthews. Independent anatomical and functional measures of the V1/V2 boundary in human visual cortex. *J Vis*, **5**(2), 93–102, (2005).

[24] S. Clare and H. Bridge. Methodological issues relating to in vivo cortical myelography using MRI. *Hum Brain Mapp*, **26**(4), 240–250, (2005).

[25] J. R. Reichenbach, M. Essig, E. M. Haacke, B. C. Lee, C. Przetak, W. A. Kaiser, and L. R. Schad. High-resolution venography of the brain using magnetic resonance imaging. *MAGMA*, **6**(1), 62–69, (1998).

[26] G. A. Christoforidis, E. C. Bourekas, M. Baujan, A. M. Abduljalil, A. Kangarlu, D. G. Spigos, D. W. Chakeres, and P. M. Robitaille. High resolution MRI of the deep brain vascular anatomy at 8 Tesla: susceptibility-based enhancement of the venous structures. *J Comput Assist Tomogr*, **23**(6), 857–866, (1999).

[27] E. M. Haacke, Y. Xu, Y.-C. N. Cheng, and J. R. Reichenbach. Susceptibility weighted imaging (SWI). *Magn Reson Med*, **52**(3), 612–618, (2004).

[28] T.-Q. Li, P. van Gelderen, H. Merkle, L. Talagala, A. P. Koretsky, and J. Duyn. Extensive heterogeneity in white matter intensity in high-resolution T2*-weighted MRI of the human brain at 7.0 T. *Neuroimage*, **32**(3), 1032–1040, (2006).

[29] E. C. Bourekas, G. A. Christoforidis, A. M. Abduljalil, A. Kangarlu, D. W. Chakeres, D. G. Spigos, and P. M. Robitaille. High resolution MRI of the deep gray nuclei at 8 Tesla. *J Comput Assist Tomogr*, **23**(6), 867–874, (1999).

[30] R. E. Burgess, Y. Yu, G. A. Christoforidis, E. C. Bourekas, D. W. Chakeres, D. Spigos, A. Kangarlu, A. M. Abduljalil, and P. M. Robitaille. Human leptomeningeal and cortical vascular anatomy of the cerebral cortex at 8 Tesla. *J Comput Assist Tomogr*, **23**(6), 850–856, (1999).

[31] E. M. Haacke, N. Y. C. Cheng, M. J. House, Q. Liu, J. Neelavalli, R. J. Ogg, A. Khan, M. Ayaz, W. Kirsch, and A. Obenaus. Imaging iron stores in the brain using magnetic resonance imaging. *Magn Reson Imaging*, **23**(1), 1–25, (2005).

[32] N. Yamada, S. Imakita, T. Sakuma, and M. Takamiya. Intracranial calcification on gradient-echo phase image: depiction of diamagnetic susceptibility. *Radiology*, **198**(1), 171–178, (1996).

[33] A. M. Abduljalil, P. Schmalbrock, V. Novak, and D. W. Chakeres. Enhanced gray and white matter contrast of phase susceptibility-weighted images in ultra-high-field magnetic resonance imaging. *J Magn Reson Imaging*, **18**(3), 284–290, (2003).

[34] N. D. Wycliffe, J. Choe, B. Holshouser, U. E. Oyoyo, E. M. Haacke, and D. K. Kido. Reliability in detection of hemorrhage in acute stroke by a new three-dimensional gradient recalled echo susceptibility-weighted imaging technique compared to computed tomography: a retrospective study. *J Magn Reson Imaging*, **20**(3), 372–377, (2004).

[35] A. Rauscher, J. Sedlacik, M. Barth, H.-J. Mentzel, and J. R. Reichenbach. Magnetic susceptibility-weighted MR phase imaging of the human brain. *AJNR Am J Neuroradiol*, **26**(4), 736–742, (2005).

[36] J. H. Duyn, P. van Gelderen, T.-Q. Li, J. A. de Zwart, A. P. Koretsky, and M. Fukunaga. High-field MRI of brain cortical substructure based on signal phase. *Proc Natl Acad Sci U S A*, **104**(28), 11796–11801, (2007).

[37] A. Haase, D. Matthaei, W. Haenicke, and J. Frahm. Dynamic digital subtraction imaging using fast low-angle shot MR movie sequence. *Radiology*, **160**(2), 537–541, (1986).

[38] W. Haenicke, K. D. Merboldt, D. Chien, M. L. Gyngell, H. Bruhn, and J. Frahm. Signal strength in subsecond FLASH magnetic resonance imaging: the dynamic approach to steady state. *Med Phys*, **17**(6), 1004–1010, (1990).

[39] B. Drayer, P. Burger, R. Darwin, S. Riederer, R. Herfkens, and G. A. Johnson. MRI of brain iron. *AJR Am J Roentgenol*, **147**(1), 103–110, (1986).

[40] R. J. Ordidge, J. M. Gorell, J. C. Deniau, R. A. Knight, and J. A. Helpern. Assessment of relative brain iron concentrations using T2-weighted and T2*-weighted MRI at 3 Tesla. *Magn Reson Med*, **32**(3), 335–341, (1994).

[41] J. M. Gorell, R. J. Ordidge, G. G. Brown, J. C. Deniau, N. M. Buderer, and J. A. Helpern. Increased iron-related MRI contrast in the substantia nigra in Parkinson's disease. *Neurology*, **45**(6), 1138–1143, (1995).

[42] M. Henkelman and W. Kucharczyk. Optimization of gradient-echo MR for calcium detection. *AJNR Am J Neuroradiol*, **15**(3), 465–472, (1994).

[43] S. W. Atlas, R. I. Grossman, D. B. Hackney, J. M. Gomori, N. Campagna, H. I. Goldberg, L. T. Bilaniuk, and R. A. Zimmerman. Calcified intracranial lesions: detection with gradient-echo-acquisition rapid MR imaging. *AJR Am J Roentgenol*, **150**(6), 1383–1389, (1988).

[44] S. Chavez, Q.-S. Xiang, and L. An. Understanding phase maps in MRI: a new cutline phase unwrapping method. *IEEE Trans Med Imaging*, **21**(8), 966–977, (2002).

[45] R. Cusack and N. Papadakis. New robust 3-D phase unwrapping algorithms: application to magnetic field mapping and undistorting echoplanar images. *Neuroimage*, **16**(3 Pt 1), 754–764, (2002).

[46] A. Rauscher, M. Barth, J. R. Reichenbach, R. Stollberger, and E. Moser. Automated unwrapping of MR phase images applied to BOLD MR-venography at 3 Tesla. *J Magn Reson Imaging*, **18**(2), 175–180, (2003).

[47] J. R. Reichenbach, R. Venkatesan, D. J. Schillinger, D. K. Kido, and E. M. Haacke. Small vessels in the human brain: MR venography with deoxyhemoglobin as an intrinsic contrast agent. *Radiology*, **204**(1), 272–277, (1997).

[48] Y. Wang, Y. Yu, D. Li, K. T. Bae, J. J. Brown, W. Lin, and E. M. Haacke. Artery and vein separation using susceptibility-dependent phase in contrast-enhanced MRA. *J Magn Reson Imaging*, **12**(5), 661–670, (2000).

[49] J. P. Mugler and J. R. Brookeman. Three-dimensional magnetization-prepared rapid gradient-echo imaging (3D MP RAGE). *Magn Reson Med*, **15**(1), 152–157, (1990).

[50] J. P. Mugler, F. H. Epstein, and J. R. Brookeman. Shaping the signal response during the approach to steady state in three-dimensional magnetization-prepared rapid gradient-echo imaging using variable flip angles. *Magn Reson Med*, **28**(2), 165–185, (1992).

[51] J. Hennig, A. Nauerth, and H. Friedburg. RARE imaging: a fast imaging method for clinical MR. *Magn Reson Med*, **3**(6), 823–833, (1986).

[52] R. T. Constable and J. C. Gore. The loss of small objects in variable TE imaging: implications for FSE, RARE, and EPI. *Magn Reson Med*, **28**(1), 9–24, (1992).

[53] J. Hennig. Echoes - how to generate, recognize, use or avoid them in MR-imaging sequences. *Conc Magn Reson*, **3**, 273–276, (1991).

[54] C. F. Williams, T. W. Redpath, and F. W. Smith. The influence of stimulated echoes on contrast in fast spin-echo imaging. *Magn Reson Imaging*, **14**(4), 419–428, (1996).

[55] P. S. Melki and R. V. Mulkern. Magnetization transfer effects in multislice RARE sequences. *Magn Reson Med*, **24**(1), 189–195, (1992).

[56] E. L. Barbier, S. Marrett, A. Danek, A. Vortmeyer, P. van Gelderen, J. Duyn, P. Bandettini, J. Grafman, and A. P. Koretsky. Imaging cortical anatomy by high-resolution MR at 3.0T: detection of the stripe of Gennari in visual area 17. *Magn Reson Med*, **48**(4), 735–738, (2002).

[57] P. M. Robitaille and L. J. Berliner. *Ultra High Field Magnetic Resonance Imaging.* Biological Magnetic Reonance 26, (2006).

[58] R. Deichmann, O. Josephs, C. Hutton, D. R. Corfield, and R. Turner. Compensation of susceptibility-induced BOLD sensitivity losses in echo-planar fMRI imaging. *Neuroimage*, **15**(1), 120–135, (2002).

[59] P. J. Wright, O. E. Mougin, J. J. Totman, A. M. Peters, M. J. Brookes, R. Coxon, P. E. Morris, M. Clemence, S. T. Francis, R. W. Bowtell, and P. A. Gowland. Water proton T1 measurements in brain tissue at 7, 3, and 1.5 T using IR-EPI, IR-TSE, and MPRAGE: results and optimization. *MAGMA*, **21**(1-2), 121–130, (2008).

[60] A. M. Peters, M. J. Brookes, F. G. Hoogenraad, P. A. Gowland, S. T. Francis, P. G. Morris, and R. Bowtell. T2* measurements in human brain at 1.5, 3 and 7 T. *Magn Reson Imaging*, **25**(6), 748–753, (2007).

[61] P. B. Roemer, W. A. Edelstein, C. E. Hayes, S. P. Souza, and O. M. Mueller. The NMR phased array. *Magn Reson Med*, **16**(2), 192–225, (1990).

[62] D. K. Sodickson and W. J. Manning. Simultaneous acquisition of spatial harmonics (SMASH): fast imaging with radiofrequency coil arrays. *Magn Reson Med*, **38**(4), 591–603, (1997).

[63] K. P. Pruessmann, M. Weiger, M. B. Scheidegger, and P. Boesiger. SENSE: sensitivity encoding for fast MRI. *Magn Reson Med*, **42**(5), 952–962, (1999).

[64] F. Wiesinger, P.-F. V. de Moortele, G. Adriany, N. D. Zanche, K. Ugurbil, and K. P. Pruessmann. Parallel imaging performance as a function of field strength–an experimental investigation using electrodynamic scaling. *Magn Reson Med*, **52**(5), 953–964, (2004).

[65] S. Moeller, P. van de Moortele, G. Adriany, C. Snyder, P. Andersen, J. Strupp, J. T. Vaughan, and K. Ugurbil. Parallel Imaging performance for densely spaced coils in phase arrays at ultra high field strength. *Proceedings of the 12th Annual Meeting of ISMRM. 2388.*, (2004).

[66] M. A. Ohliger, A. K. Grant, and D. K. Sodickson. Ultimate intrinsic signal-to-noise ratio for parallel MRI: electromagnetic field considerations. *Magn Reson Med*, **50**(5), 1018–1030, (2003).

[67] F. Wiesinger, P. Boesiger, and K. P. Pruessmann. Electrodynamics and ultimate SNR in parallel MR imaging. *Magn Reson Med*, **52**(2), 376–390, (2004).

[68] M. S. Silver, R. I. Joseph, and D. I. Hoult. Highly selective pi/2 and pi pulse generation. *J Magn Reson*, **59**, 347–351, (1984).

[69] J. Pfeuffer, H. Merkle, M. Beyerlein, T. Steudel, and N. K. Logothetis. Anatomical and functional MR imaging in the macaque monkey using a vertical large-bore 7 Tesla setup. *Magn Reson Imaging*, **22**(10), 1343–1359, (2004).

[70] R. M. Torack, H. Alcala, M. Gado, and R. Burton. Correlative assay of computerized cranial tomography CCT, water content and specific gravity in normal and pathological postmortem brain. *J Neuropathol Exp Neurol*, **35**(4), 385–392, (1976).

[71] H. Takagi, K. Shapiro, A. Marmarou, and H. Wisoff. Microgravimetric analysis of human brain tissue: correlation with computerized tomography scanning. *J Neurosurg*, **54**(6), 797–801, (1981).

[72] J. Vymazal, R. A. Brooks, C. Baumgarner, V. Tran, D. Katz, J. W. Bulte, R. Bauminger, and G. D. Chiro. The relation between brain iron and NMR relaxation times: an in vitro study. *Magn Reson Med*, **35**(1), 56–61, (1996).

[73] J. Vymazal, M. Hajek, N. Patronas, J. N. Giedd, J. W. Bulte, C. Baumgarner, V. Tran, and R. A. Brooks. The quantitative relation between T1-weighted and T2-weighted MRI of normal gray matter and iron concentration. *J Magn Reson Imaging*, **5**(5), 554–560, (1995).

[74] R. J. Ogg and R. G. Steen. Age-related changes in brain T1 are correlated with iron concentration. *Magn Reson Med*, **40**(5), 749–753, (1998).

[75] R. Turner, D. L. Bihan, C. T. Moonen, D. Despres, and J. Frank. Echo-planar time course MRI of cat brain oxygenation changes. *Magn Reson Med*, **22**(1), 159–166, (1991).

[76] S. Ogawa, D. W. Tank, R. Menon, J. M. Ellermann, S. G. Kim, H. Merkle, and K. Ugurbil. Intrinsic signal changes accompanying sensory stimulation: functional brain mapping with magnetic resonance imaging. *Proc Natl Acad Sci U S A*, **89**(13), 5951–5955, (1992).

[77] K. K. Kwong, J. W. Belliveau, D. A. Chesler, I. E. Goldberg, R. M. Weisskoff, B. P. Poncelet, D. N. Kennedy, B. E. Hoppel, M. S. Cohen, and R. Turner. Dynamic magnetic resonance imaging of human brain activity during primary sensory stimulation. *Proc Natl Acad Sci U S A*, **89**(12), 5675–5679, (1992).

[78] P. A. Bandettini, E. C. Wong, R. S. Hinks, R. S. Tikofsky, and J. S. Hyde. Time course EPI of human brain function during task activation. *Magn Reson Med*, **25**(2), 390–397, (1992).

[79] J. B. Mandeville, J. J. Marota, J. R. Keltner, B. E. Kosofsky, R. Weissleder, B. R. Rosen, and R. M. Weisskoff. CBF functional imaging in rat brain using iron oxide agent at steady state concentration. *Proceedings of the 12th Annual Meeting of ISMRM 292*, (1996).

[80] S.-G. Kim and K. Ugurbil. High-resolution functional magnetic resonance imaging of the animal brain. *Methods*, **30**(1), 28–41, (2003).

[81] H. Lu, X. Golay, J. J. Pekar, and P. C. M. V. Zijl. Functional magnetic resonance imaging based on changes in vascular space occupancy. *Magn Reson Med*, **50**(2), 263–274, (2003).

[82] S. G. Kim. Quantification of relative cerebral blood flow change by flow-sensitive alternating inversion recovery (FAIR) technique: application to functional mapping. *Magn Reson Med*, **34**(3), 293–301, (1995).

[83] J. Pfeuffer, P.-F. van de Moortele, E. Yacoub, A. Shmuel, G. Adriany, P. Andersen, H. Merkle, M. Garwood, K. Ugurbil, and X. Hu. Zoomed functional imaging in the human brain at 7 Tesla with simultaneous high spatial and high temporal resolution. *Neuroimage*, **17**(1), 272–286, (2002).

[84] J. A. Detre and J. Wang. Technical aspects and utility of fMRI using BOLD and ASL. *Clin Neurophysiol*, **113**(5), 621–634, (2002).

[85] L. Pauling and C. D. Coryell. The Magnetic Properties and Structure of Hemoglobin, Oxyhemoglobin and Carbonmonoxyhemoglobin. *Proc Natl Acad Sci U S A*, **22**(4), 210–216, (1936).

[86] S. Ogawa, T. M. Lee, A. R. Kay, and D. W. Tank. Brain magnetic resonance imaging with contrast dependent on blood oxygenation. *Proc Natl Acad Sci U S A*, **87**(24), 9868–9872, (1990).

[87] R. M. Weisskoff and S. Kiihne. MRI susceptometry: image-based measurement of absolute susceptibility of MR contrast agents and human blood. *Magn Reson Med*, **24**(2), 375–383, (1992).

[88] K. R. Thulborn, J. C. Waterton, P. M. Matthews, and G. K. Radda. Oxygenation dependence of the transverse relaxation time of water protons in whole blood at high field. *Biochim Biophys Acta*, **714**(2), 265–270, (1982).

[89] E. Yacoub, T. Q. Duong, P.-F. V. D. Moortele, M. Lindquist, G. Adriany, S.-G. Kim, K. Ugurbil, and X. Hu. Spin-echo fMRI in humans using high spatial resolutions and high magnetic fields. *Magn Reson Med*, **49**(4), 655–664, (2003).

[90] T. Q. Duong, E. Yacoub, G. Adriany, X. Hu, K. Ugurbil, J. T. Vaughan, H. Merkle, and S.-G. Kim. High-resolution, spin-echo BOLD, and CBF fMRI at 4 and 7 T. *Magn Reson Med*, **48**(4), 589–593, (2002).

[91] T. Q. Duong, E. Yacoub, G. Adriany, X. Hu, K. Ugurbil, and S.-G. Kim. Microvascular BOLD contribution at 4 and 7 T in the human brain: gradient-echo and spin-echo fMRI with suppression of blood effects. *Magn Reson Med*, **49**(6), 1019–1027, (2003).

[92] C. R. Michelich, A. W. Song, and J. R. Macfall. Dependence of gradient-echo and spin-echo BOLD fMRI at 4 T on diffusion weighting. *NMR Biomed*, **19**(5), 566–572, (2006).

[93] E. Yacoub, P.-F. V. D. Moortele, A. Shmuel, and K. Ugurbil. Signal and noise characteristics of Hahn SE and GE BOLD fMRI at 7 T in humans. *Neuroimage*, **24**(3), 738–750, (2005).

[94] S. P. Lee, A. C. Silva, K. Ugurbil, and S. G. Kim. Diffusion-weighted spin-echo fMRI at 9.4 T: microvascular/tissue contribution to BOLD signal changes. *Magn Reson Med*, **42**(5), 919–928, (1999).

[95] K. J. Friston, P. Fletcher, O. Josephs, A. Holmes, M. D. Rugg, and R. Turner. Event-related fMRI: characterizing differential responses. *Neuroimage*, **7**(1), 30–40, (1998).

[96] E. Yacoub, A. Shmuel, J. Pfeuffer, P. F. V. D. Moortele, G. Adriany, K. Ugurbil, and X. Hu. Investigation of the initial dip in fMRI at 7 Tesla. *NMR Biomed*, **14**(7-8), 408–412, (2001).

[97] E. Zarahn. Spatial localization and resolution of BOLD fMRI. *Curr Opin Neurobiol*, **11**(2), 209–212, (2001).

[98] G. M. Boynton, S. A. Engel, G. H. Glover, and D. J. Heeger. Linear systems analysis of functional magnetic resonance imaging in human V1. *J Neurosci*, **16**(13), 4207–4221, (1996).

[99] S. Ogawa, R. S. Menon, D. W. Tank, S. G. Kim, H. Merkle, J. M. Ellermann, and K. Ugurbil. Functional brain mapping by blood oxygenation level-dependent contrast magnetic resonance imaging. A comparison of signal characteristics with a biophysical model. *Biophys J*, **64**(3), 803–812, (1993).

[100] J. S. Gati, R. S. Menon, K. Ugurbil, and B. K. Rutt. Experimental determination of the BOLD field strength dependence in vessels and tissue. *Magn Reson Med*, **38**(2), 296–302, (1997).

[101] E. O. Stejskal and J. E. Tanner. Spin diffusion measurements: spin echoes in the presence of a time-dependent field gradient. *J Chem Phys*, **42**, 288–292, (1965).

[102] J. L. Boxerman, P. A. Bandettini, K. K. Kwong, J. R. Baker, T. L. Davis, B. R. Rosen, and R. M. Weisskoff. The intravascular contribution to fMRI signal change: Monte Carlo modeling and diffusion-weighted studies in vivo. *Magn Reson Med*, **34**(1), 4–10, (1995).

[103] A. W. Song, E. C. Wong, S. G. Tan, and J. S. Hyde. Diffusion weighted fMRI at 1.5 T. *Magn Reson Med*, **35**(2), 155–158, (1996).

[104] R. B. Buxton, E. C. Wong, and L. R. Frank. Dynamics of blood flow and oxygenation changes during brain activation: the balloon model. *Magn Reson Med*, **39**(6), 855–864, (1998).

[105] G. A. Wright, B. S. Hu, and A. Macovski. 1991 I.I. Rabi Award. Estimating oxygen saturation of blood in vivo with MR imaging at 1.5 T. *J Magn Reson Imaging*, **1**(3), 275–283, (1991).

[106] M. Barth and E. Moser. Proton NMR relaxation times of human blood samples at 1.5 T and implications for functional MRI. *Cell Mol Biol (Noisy-le-grand)*, **43**(5), 783–791, (1997).

[107] R. K. Breger, A. A. Rimm, M. E. Fischer, R. A. Papke, and V. M. Haughton. T1 and T2 measurements on a 1.5-T commercial MR imager. *Radiology*, **171**(1), 273–276, (1989).

[108] E. Yacoub, A. Shmuel, J. Pfeuffer, P. F. V. D. Moortele, G. Adriany, P. Andersen, J. T. Vaughan, H. Merkle, K. Ugurbil, and X. Hu. Imaging brain function in humans at 7 Tesla. *Magn Reson Med*, **45**(4), 588–594, (2001).

[109] R. M. Weisskoff, C. S. Zuo, J. L. Boxerman, and B. R. Rosen. Microscopic susceptibility variation and transverse relaxation: theory and experiment. *Magn Reson Med*, **31**(6), 601–610, (1994).

[110] J. L. Boxerman, L. M. Hamberg, B. R. Rosen, and R. M. Weisskoff. MR contrast due to intravascular magnetic susceptibility perturbations. *Magn Reson Med*, **34**(4), 555–566, (1995).

[111] N. Fujita. Extravascular contribution of blood oxygenation level-dependent signal changes: a numerical analysis based on a vascular network model. *Magn Reson Med*, **46**(4), 723–734, (2001).

[112] S. Lai, A. L. Hopkins, E. M. Haacke, D. Li, B. A. Wasserman, P. Buckley, L. Friedman, H. Meltzer, P. Hedera, and R. Friedland. Identification of vascular structures as a major source of signal contrast in high resolution 2D and 3D functional activation imaging of the motor cortex at 1.5T: preliminary results. *Magn Reson Med*, **30**(3), 387–392, (1993).

[113] C. Segebarth, V. Belle, C. Delon, R. Massarelli, J. Decety, J. F. L. Bas, M. Decorps, and A. L. Benabid. Functional MRI of the human brain: predominance of signals from extracerebral veins. *Neuroreport*, **5**(7), 813–816, (1994).

[114] R. Turner. How much cortex can a vein drain? Downstream dilution of activation-related cerebral blood oxygenation changes. *Neuroimage*, **16**(4), 1062–1067, (2002).

[115] A. Shmuel, E. Yacoub, D. Chaimow, N. K. Logothetis, and K. Ugurbil. Spatio-temporal point-spread function of fMRI signal in human gray matter at 7 Tesla. *Neuroimage*, **35**(2), 539–552, (2007).

[116] T. Q. Duong, D. S. Kim, K. Ugurbil, and S. G. Kim. Spatiotemporal dynamics of the BOLD fMRI signals: toward mapping submillimeter cortical columns using the early negative response. *Magn Reson Med*, **44**(2), 231–242, (2000).

[117] D. S. Kim, T. Q. Duong, and S. G. Kim. High-resolution mapping of iso-orientation columns by fMRI. *Nat Neurosci*, **3**(2), 164–169, (2000).

[118] T. Q. Duong, D. S. Kim, K. Ugurbil, and S. G. Kim. Localized cerebral blood flow response at submillimeter columnar resolution. *Proc Natl Acad Sci U S A*, **98**(19), 10904–10909, (2001).

[119] A. T. Lee, G. H. Glover, and C. H. Meyer. Discrimination of large venous vessels in time-course spiral blood-oxygen-level-dependent magnetic-resonance functional neuroimaging. *Magn Reson Med*, **33**(6), 745–754, (1995).

[120] S. G. Kim, X. Hu, G. Adriany, and K. Ugurbil. Fast interleaved echo-planar imaging with navigator: high resolution anatomic and functional images at 5 Tesla. *Magn Reson Med*, **35**(6), 895–902, (1996).

[121] K. R. Thulborn, S. Y. Chang, G. X. Shen, and J. T. Voyvodic. High-resolution echo-planar fMRI of human visual cortex at 3.0 tesla. *NMR Biomed*, **10**(4-5), 183–190, (1997).

[122] R. S. Menon and B. G. Goodyear. Submillimeter functional localization in human striate cortex using BOLD contrast at 4 Tesla: implications for the vascular point-spread function. *Magn Reson Med*, **41**(2), 230–235, (1999).

[123] W. Chen and K. Ugurbil. High spatial resolution functional magnetic resonance imaging at very-high-magnetic field. *Top Magn Reson Imaging*, **10**(1), 63–78, (1999).

[124] F. G. Hoogenraad, M. B. Hofman, P. J. Pouwels, J. R. Reichenbach, S. A. Rombouts, and E. M. Haacke. Sub-millimeter fMRI at 1.5 Tesla: correlation of high resolution with low resolution measurements. *J Magn Reson Imaging*, **9**(3), 475–482, (1999).

[125] D. A. Feinberg, J. C. Hoenninger, L. E. Crooks, L. Kaufman, J. C. Watts, and M. Arakawa. Inner volume MR imaging: technical concepts and their application. *Radiology*, **156**(3), 743–747, (1985).

[126] J. P. Felmlee and R. L. Ehman. Spatial presaturation: a method for suppressing flow artifacts and improving depiction of vascular anatomy in MR imaging. *Radiology*, **164**(2), 559–564, (1987).

[127] R. R. Edelman, D. J. Atkinson, M. S. Silver, F. L. Loaiza, and W. S. Warren. FRODO pulse sequences: a new means of eliminating motion, flow, and wraparound artifacts. *Radiology*, **166**(1 Pt 1), 231–236, (1988).

[128] P. L. Roux, R. J. Gilles, G. C. McKinnon, and P. G. Carlier. Optimized outer volume suppression for single-shot fast spin-echo cardiac imaging. *J Magn Reson Imaging*, **8**(5), 1022–1032, (1998).

[129] Y. Luo, R. A. de Graaf, L. DelaBarre, A. Tanns, and M. Garwood. BISTRO: an outer-volume suppression method that tolerates RF field inhomogeneity. *Magn Reson Med*, **45**(6), 1095–1102, (2001).

[130] B. J. Wilm, J. Svensson, A. Henning, K. P. Pruessmann, P. Boesiger, and S. S. Kollias. Reduced field-of-view MRI using outer volume suppression for spinal cord diffusion imaging. *Magn Reson Med*, **57**(3), 625–630, (2007).

[131] Y. Yang, V. S. Mattay, D. R. Weinberger, J. A. Frank, and J. H. Duyn. Localized echo-volume imaging methods for functional MRI. *J Magn Reson Imaging*, **7**(2), 371–375, (1997).

[132] R. M. Heidemann, R. Trumpel, D. Ivanov, F. Fasano, J. Pfeuffer, and R. Turner. Isotropic sub-millimetre fMRI of V5 in human at 7 T. *Proceedings of the 17th Meeting ISMRM. 1546*, (2009).

[133] M. Poole and R. Bowtell. Volume parcellation for improved dynamic shimming. *MAGMA*, **21**(1-2), 31–40, (2008).

[134] F. Romeo and D. I. Hoult. Magnet field profiling: analysis and correcting coil design. *Magn Reson Med*, **1**(1), 44–65, (1984).

[135] D. F. Hillenbrand, K. M. Lo, W. F. B. Punchard, T. G. Reese, and P. M. Starewicz. High-Order MR Shimming: A Simulation Study of the Effectiveness of Competing Methods. Using an Establish Susceptibility Model of hte Human Head. *Applied Magnetic Resonance*, **29**, 39–64, (2005).

[136] M. G. Prammer, J. C. Hasselgrove, M. Shinnar, and J. S. Leigh. A New Approach to Automatic Shimming. *Journal of Magnetic Resonance*, **77**, 40–52, (1988).

[137] R. Gruetter and C. Boecsh. Fast, Noniterative Shimming of Spatially Localized Signals. In Vivo Analyis of the Magnetic Field along Axes. *Journal of Magnetic Resonance*, **96**, 323–334, (1992).

[138] R. Gruetter. Automatic, localized in vivo adjustment of all first- and second-order shim coils. *Magn Reson Med*, **29**(6), 804–811, (1993).

[139] L. M. Klassen and R. S. Menon. Robust automated shimming technique using arbitrary mapping acquisition parameters (RASTAMAP). *Magn Reson Med*, **51**(5), 881–887, (2004).

[140] S. M. Smith. Fast robust automated brain extraction. *Hum Brain Mapp*, **17**(3), 143–155, (2002).

[141] H. Wen and F. A. Jaffer. An in vivo automated shimming method taking into account shim current constraints. *Magn Reson Med*, **34**(6), 898–904, (1995).

[142] N. J. Shah, M. Zaitsev, S. Steinhoff, and K. Zilles. A new method for fast multislice T1 mapping. *Neuroimage*, **14**(5), 1175–1185, (2001).

[143] A. M. Dale, B. Fischl, and M. I. Sereno. Cortical surface-based analysis. I. Segmentation and surface reconstruction. *Neuroimage*, **9**(2), 179–194, (1999).

[144] B. Fischl, M. I. Sereno, and A. M. Dale. Cortical surface-based analysis. II: Inflation, flattening, and a surface-based coordinate system. *Neuroimage*, **9**(2), 195–207, (1999).

[145] N. Kriegeskorte and R. Goebel. An efficient algorithm for topologically correct segmentation of the cortical sheet in anatomical mr volumes. *Neuroimage*, **14**(2), 329–346, (2001).

[146] B. A. Wandell, S. Chial, and B. T. Backus. Visualization and measurement of the cortical surface. *J Cogn Neurosci*, **12**(5), 739–752, (2000).

[147] J. Larsson. *Imaging Vision*. PhD thesis, Karolinska Institute,Stockholm, Sweden., (2001).

[148] W. E. Lorensen and H. E. Cline. Marchiing Cubes: A high resolution 3D surface construction algorithm. *Computer Graphics*, **21**(5), 163–169, (1987).

Chapter 5

Applications I: Comparison of retinotopic maps with cortical areas identified using high-resolution, T$_2^\star$-weighted images

5.1 The visual cortex

The visual cortex, situated in the occipital lobe of the brain, receives and processes neural inputs from the eyes. Figure 5.1 shows a schematic representation of the visual pathways. The first stages of visual information processing occur in the retina, a layer of cells at the back of the eye. The image projected onto the retina is inverted as it passes through the lens of the eyes. The visual field is divided into right and left hemifields and each eye receives information from both hemifields, with the image falling on one nasal retina and one temporal retina. The optic nerves convey visual information formed in the retina on to the brain. At the optic chiasm fibres from the nasal retina cross to the opposite hemisphere whereas fibres from the temporal retina continue
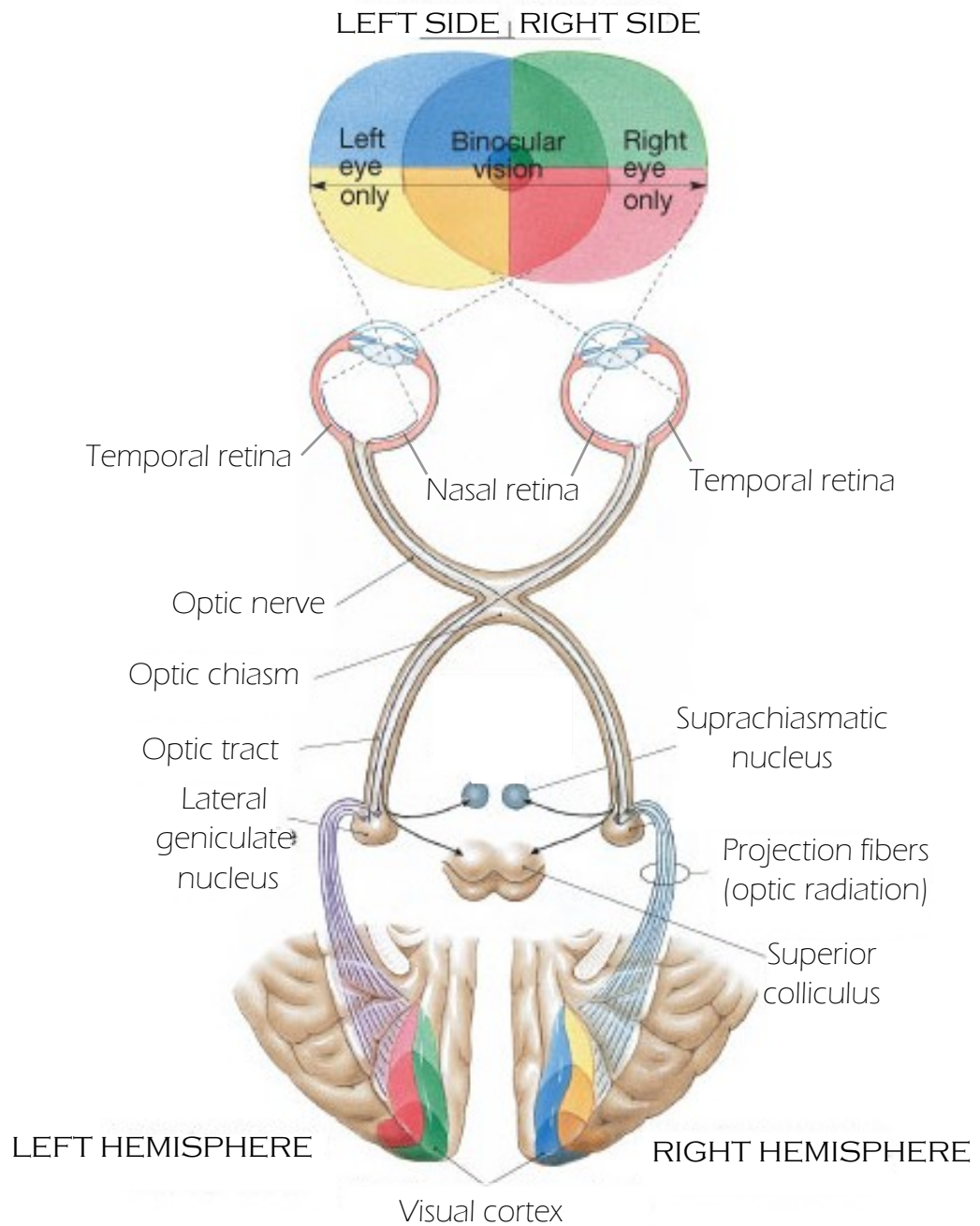
Figure 5.1: Visual pathways. Reproduced from www.iupucanatomy.com.

to the same hemisphere. This splitting and crossing re-organizes the retinal outputs so that the left hemisphere processes information from the right visual field, and the right hemisphere processes information from the left visual field. Beyond the optic chiasm the visual pathway is referred to as the optic tract. Most axons of the optic tract terminate on cells in the lateral geniculate nucleus (LGN). From there, the LGN axons fan out through the deep white matter of the brain as the optic radiations, which will ultimately travel to the primary visual cortex, V1, at the posterior of the brain. The function of V1 is to determine the localization and position of edges. Then from V1, further nerves fibers connect it to the secondary visual cortex V2, which decodes visual messages at a higher level than the V1 such as contours, and V3. From there, signals fan out to "higher" areas of cortex that process more global aspects of visual information. Some areas seem specialized for processing a certain aspect of visual information, such as area V4 for colour [1] and area V5 for motion [2]. Visual area V5 is also called MT+ because it is the human homologue of the macaque MT, plus other areas such as MTS and STS. In humans, V5 is located in the inferior temporal sulcus.

The spatial structure of the retinal image is preserved as neurons from the retina connect to the LGN, and is still preserved further along in the cortex. As a consequence, different areas of the visual field are mapped in an orderly fashion at the various levels of the visual system, with adjacent points of the visual field/retinal image mapped onto (or processed by) adjacent neurons. This property is known as retinotopy and it is a criteria for classifying visual areas.

5.2 Mapping the visual cortex with retinotopy

Visual areas can be differentiated according to their topographic organization, i.e retinotopy. Each distinct visual area has its own retinotopic map. Figure 5.2 shows the different visual areas that can be defined with retinotopic mapping paradigms. Mapping of the visual field by retinotopy is possible be-
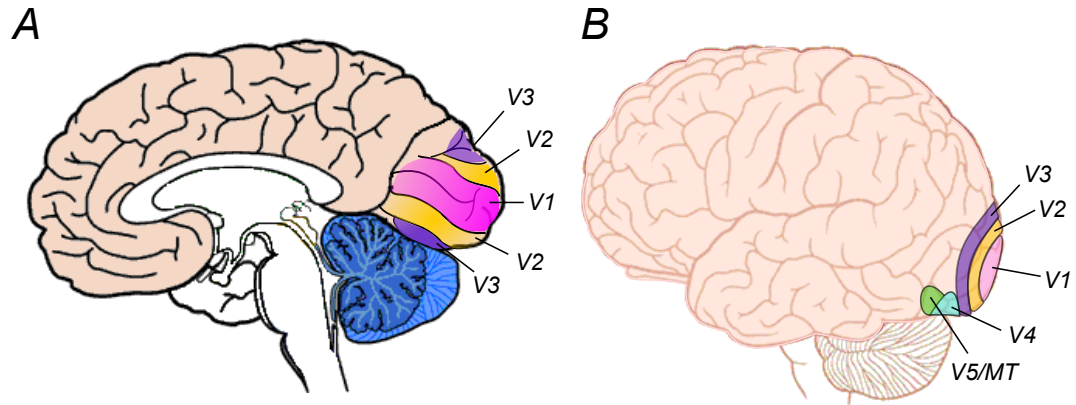
Figure 5.2: (A) Medial and (B) lateral diagram of the brain showing the representation of visual areas as determined by retinotopic mapping.

cause the retinal signal is projected to the cortex in an organised manner: adjacent points in the retina project to adjacent points in the cortex with the right visual field projecting to the left cerebral hemisphere and the left visual field projecting to the right cerebral hemisphere. There are two dimensions of retinotopic organization; eccentricity and angular dimension. Eccentricity shows the shift of the visual representation from the centre to the periphery of the visual field which is mapped from the posterior to the anterior of the visual cortex or calcarine sulcus. The angular dimension shows the shift of the visual representation from the upper (UVM) to the lower (LVM) vertical meridian along a path that traverses from the ventral to the dorsal bank of the calcarine sulcus. This is illustrated in Fig. 5.3; the icons indicating the visual field positions of the central fixation *(black dot, white surround)* and periphery *(white dot, black surround)* together with the representation of angular dimension are superimposed on the sketch of the occipital lobe to indicate the retinotopic organizations within areas V1 and V2. In the following it will be described how to measure retinotopic organization and how retinotopic maps allow the identification of borders between different visual areas.
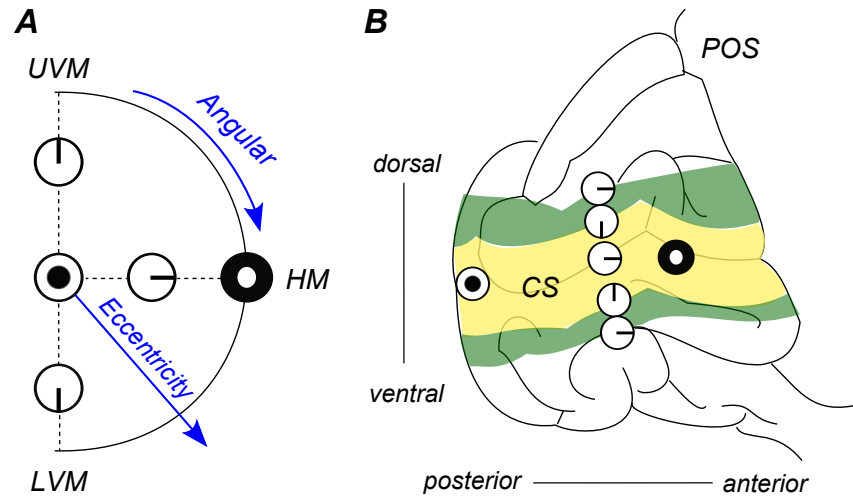
Figure 5.3: Retinotopic organization of visual areas in the left hemisphere. (A) Representation of the visual field. Central fixation is represented by the black dot in white surround and the periphery by the white dot in black surround. Eccentricity, upper vertical meridian (UVM), lower vertical meridian (LVM) and horizontal meridian (HM) are also labelled. (B) Sketch of the medial surface of the left occipital lobe showing approximate positions of areas V1 *(yellow area)* and V2 *(green area)*. The positions of the calcarine sulcus (CS) and parieto occipital sulcus (POS) are also shown. Adapted from [3].

5.2.1 Stimuli

The method to produce retinotopic maps is based on the delivery of visual stimuli which vary in position with time. The paradigms are designed to produce a travelling wave of neuronal activity within retinotopically organised visual areas. Fourier analysis of the functional image time series is then performed to produce maps of the phase of the BOLD response relative to the stimulus, with phase corresponding to specific locations in the visual field. Stimuli that are typically used for retinotopic mapping are shown in Fig. 5.4. To measure eccentricity, a flickering ring that contracts from the periphery to the centre of the visual field is used (Fig. 5.4.A). When the ring reaches the centre, it is replaced by a new ring at the edge. This creates a travelling wave of neuronal activity that expands along the eccentricity dimension which is mapped from the anterior to the posterior regions of the calcarine cortex. A flickering wedge rotating in an anticlockwise manner about a fixation point
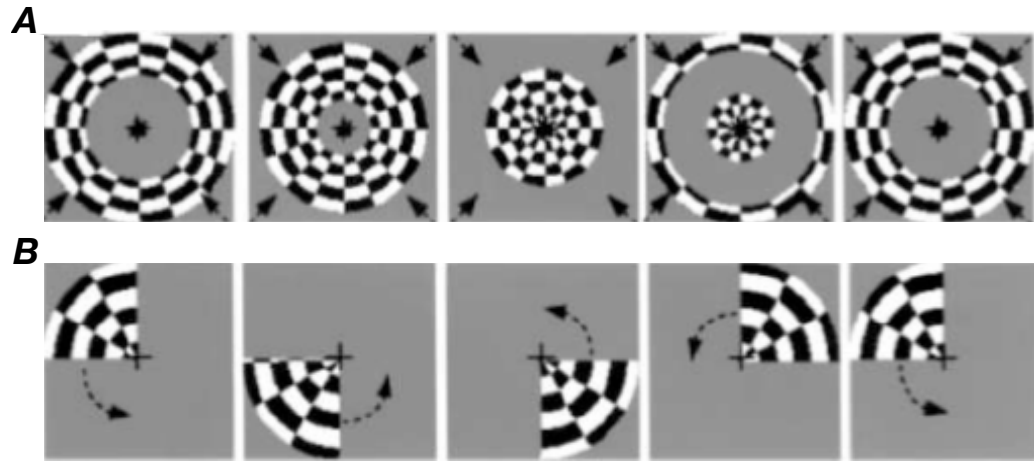
Figure 5.4: Images of the stimuli used for phase-based measurements of retinotopic organization. (A) Contracting ring and (B) rotating wedge are shown at different moments in time *(arrows)*.

(+) (Fig. 5.4.B) creates a travelling wave of activation that spreads from the ventral to the dorsal lip of the calcarine and it is used to measure retinotopic organization with respect to polar angle. This method is based on the assumption that neurons have a limited receptive field. For the receptive field of each neuron, the visual field alternates between the flashing checkerboard and the grey background. Since the stimulus moves at a constant velocity the frequency of the response is the same for all points in the visual field. However the temporal phase of the response differs (in the case of the contracting ring shown in Fig. 5.4.A, neurons with receptive fields in the periphery respond earlier than neurons with receptive fields near the centre). The phase of the response defines the receptive field position, and the progress across each visual field area indicates a topographic organization of the visual field on the cortex. The haemodynamic delay of the BOLD response creates a phase shift of the response that needs to be corrected. This is done by combining the responses of two stimuli moving in opposing directions [4].

5.2.2   Identification of visual borders

Because of the folded complexity of the human cortical surface it is difficult to interpret spatial locations and visualise functional data. In order to improve visualisation of the retinotopic map to understand the spatial organization of visual areas, a flattened representation of the cortex is needed (Section 4.4). A flattened representation of the cortical surface can be obtained from anatomical MR images with good contrast between grey and white matter. The first step of cortical unfolding is the segmentation of white and grey matter. Following segmentation, the surface between grey and white matter is extracted and flattened. Further details of the unfolding process are provided in Section 4.4.

The primary visual cortex, V1, occupies an area on the occipital lobe which falls on the cortical surface at the dorsal and ventral bank of the calcarine sulcus. Area V1 in the cortex of each hemisphere represents an entire hemifield in visual space. V1 is bordered by two cortical regions which form V2; the dorsal V2 (V2d) representing the lower visual field and the ventral V2 (V2v) representing the upper visual field. V2d and V2v each represent one quarter of the visual field.

Areas V1 and V2 share a similar retinotopic organization with respect to eccentricity, but have different angular representation. Thus, mapping the polar angle reveals the boundary between V1 and V2 [4] (See Fig. 5.5). Within the area of foveal confluence, shown by the circle, the foveal representations of areas V1, V2 and V3 converge [5], and cannot be segmented. The angular representation of the visual field is also reversed in the cortex, the upper visual field is represented in the lower part of the brain whereas the lower visual field is represented in the upper part of the brain. As one moves from the lower (ventral) to the upper (dorsal) bank of the calcarine, the representation of the visual field shifts from the UVM through the horizontal meridian (HM) to the LVM.

The polar angle maps in adjacent visual areas share a common eccentricity representation and are mirror images of each other so that phase progression
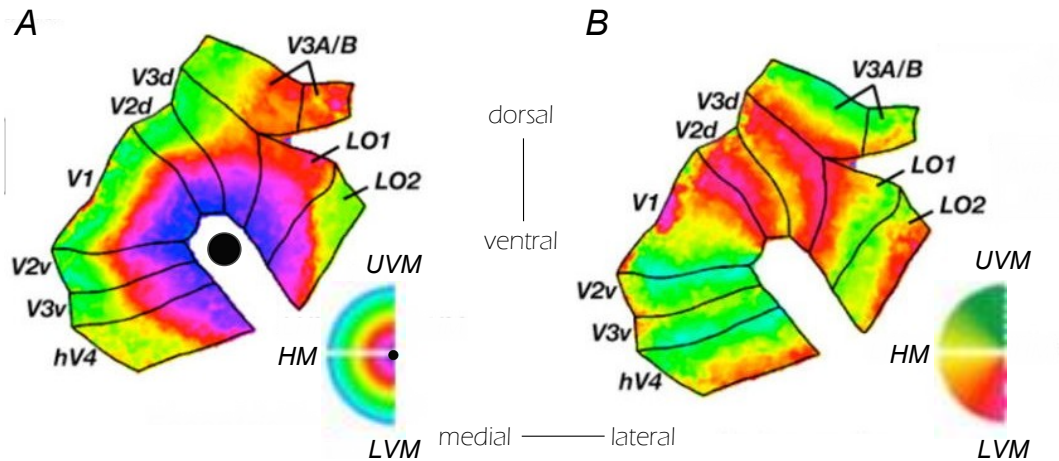
Figure 5.5: Retinotopic organization of visual areas in the right hemisphere (A) Areas V1, V2, V3 have a shared common eccentricity. The area within the circle is that of foveal confluence. (B) Retinotopy with respect to polar angle using a rotating wedge stimulus. Colour codes indicate the polar angle as shown in the colour map. Reversals in the polar angle are shown by the solid lines and can be used to identify the border between V1 and V2. Adapted from [7].

occurs in opposite directions along the cortical surface, with a phase reversal at their shared boundary. By identifying the locations of the travelling wave phase reversals, the boundaries of visual areas can be located [4, 6]; This is illustrated in Fig. 5.5.(B). The colour at each point represents the phase of the travelling wave at the position shown by the colour map. V1 comprises an entire hemifield centred on the calcarine sulcus. As one moves from the middle of V1 to the V1/V2 border, the receptive field locations change from the horizontal (HM) to the vertical (VM) meridian. As one crosses the border and continues to V2, the receptive field locations move in the opposite direction from the vertical meridian back towards the horizontal meridian (HM). The V1/V2d (dorsal) boundary is formed by the representation of the lower vertical meridian (LVM) while the V1/V2v (ventral) boundary is formed by the representation of the upper vertical meridian (UVM). The orderly progression of the map reverses direction again at the representation of the horizontal meridian, forming the V2/V3 border.

Note that V5 has its own retinotopic map of the visual field, however, the

receptive fields of V5 neurons are much larger than neurons in V1 [8]. (i.e., MT-neuron receptive fields cover or "see" a patch of visual space 100 times the size of V1 neuron receptive fields), suggesting that they are able to integrate more global motion signals.

5.3 Introduction

One of the major aims of neuroscience is a detailed understanding of the relationship between anatomy and function of different regions in the human brain. As discussed in Section 4.2.2, Brodmann's area 17, situated in the calcarine sulcus, can be distinguished from neighbouring regions by the presence of the stria of Gennari. It was Clark et al.[9] who first show that lamination patterns within the grey matter observed on MR images of striate cortex (using proton density weighted, spin echo imaging) correlate with this myelination pattern of striate cortex. More recent studies have visualized the stria of Gennari using high resolution T_1-weighted images [10, 11, 12, 13, 14] and IR-TSE data [15]. There is also evidence of distinct myelination patterns in the occipital extension of the inferior temporal lobe [12, 16, 17], thought to be the human homologue of monkey middle temporal area (MT). However, identifying regions based on the visual appearance of anatomy in MR image data does not necessarily mean that the regions also have a distinct function. The ability to detect myelin within the cortex of the living human subject opens up the ideal opportunity to investigate whether the myeloarchitecture-based divisions correspond to those determined functionally.

To be able to relate structural and functional definitions it is necessary to form functional maps of the visual cortex. Retinotopic mapping is routinely used to define visual areas [4, 18, 19, 20]. Previous MR studies have defined visual cortical regions V1 [13, 14] and V5 [12] anatomically in vivo using high resolution T_1-weighted images. Here we study the correspondence of functionally defined primary visual cortex (V1) and motion selective (V5) regions to the underlying structural anatomy assessed using high resolution $T_2^\star$-weighted

and T_1-weighted imaging at 7 T.

5.4 Methods

Four volunteers participated in the study which was performed at 7 T. All subjects had normal vision and were experienced in functional magnetic resonance (fMRI) experiments. Each of the subjects participated in two scanning sessions: one session to acquire high resolution anatomical data and one session to perform functional MRI to identify MT and to measure the angular component of the retinotopic map.

In an additional scanning session a whole brain T_1-weighted MPRAGE image data set with 1 mm isotropic resolution was acquired at 3 T (3D MPRAGE, 1 mm isotropic resolution, linear phase encoding order, TE= 3.7 ms, TR= 8.13 ms, TI=960 ms FA= 8°). These anatomical images were acquired at 3 T as they displayed less B_1-inhomogeneity-related signal intensity variation than those images acquired at 7T, allowing cortical unfolding. Images were first automatically segmented into grey and white matter compartments using FSL, FMRIB Software Library [21]. The grey matter surface was extracted and then flattened using custom written software (SurfRelax, Larsson [22]), as described in detail in Section 4.4, for ease of displaying regions of functional activation and anatomical areas.

Anatomical imaging

In order to structurally characterise the extent of the stria of Gennari, an isotropic resolution, which results in reduced partial volume effects compared to highly anisotropic voxels, is required. Image sequences which have been optimized to detect the stria of Gennari have been discussed in Chapter 4. The IR-TSE sequence produces high contrast-to-noise ratio but slice coverage is limited, even when using parallel imaging, due to the high energy deposited by the refocusing pulses. For example, to acquire 0.4 mm isotropic images with a volume coverage of $152 \times 140 \times 40$ mm^3, a 3D-IR-TSE sequence (IR

delay=320 ms, TR=2 s, TE=15 ms, TSE factor=16, centric phase encoding order) takes 16 min 32 sec for a single average. To obtain adequate signal-to-noise ratio at least 4 averages are required, requiring a scanning time of over one hour. Therefore this sequence was not used in this study and instead $T_2^\star$ data and MPRAGE data were collected.

Anatomical data collection

In the anatomical scanning session, high resolution $T_2^\star$ - weighted structural images were acquired. A 3D spoiled, gradient echo sequence with a TR of 50 ms, a TE of 20 ms and a flip angle of 16° was used to obtain 100 coronal slices at 0.4 mm isotropic resolution aligned perpendicular to the calcarine sulcus and spanning a $152 \times 144 \times 40$ mm^3 volume (Fig. 5.6.a). A single scan of $T_2^\star$-weighted data was acquired in 15 min. T1-weighted MPRAGE image data sets with the same slice prescription and in-plane resolution, but 0.6 mm slice thickness were also acquired for comparison. 4 sets of individual scans were acquired, each consisting of 2 averages (NSA=2), which were then co-registered and averaged together (20 minutes total scanning time).

The regions that display a dark band within the cortex were identified manually. Lines were drawn on the $T_2^\star$-weighted image over the dark band using VolumeViewer within the SurfRelax tools, Larsson [22]. These lines were then exported as image files and dilated (using the dilation function of the FSL tools with a 3×3×3 neighbourhood) to approximately cover the grey mater in that region.

Functional Imaging

Stimuli and Paradigm

The visual stimulus was projected onto a screen positioned at the end of the scanner bed, near the subject's feet. Subjects viewed the screen through prism goggles and were instructed to focus on the fixation cross displayed at the centre of the stimulus. The scanner bore restricted the extent of the
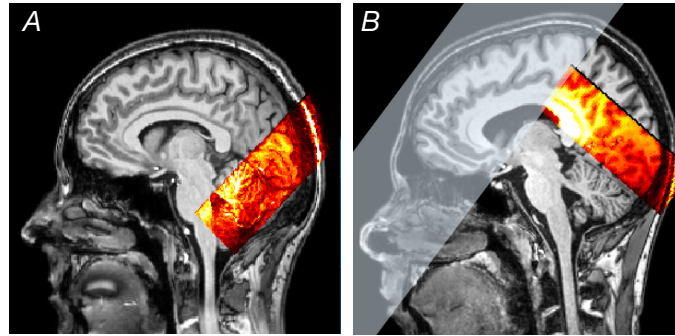
Figure 5.6: MPRAGE image showing slice prescription for (A) anatomical and (B) functional experiment. Slab used for outer volume suppression during collection of functional data is shown in blue.

stimulus to approximately 7.6 ^{o} visual angle. In order to localize the motion selective visual area V5, a stimulus that alternated in time between moving and stationary dots was used [2, 23, 24]. White dots were distributed on a black background around a yellow fixation cross at the centre of the visual field, as shown in Fig. 5.7.a. In a 12 second period, dots alternated every second between expanding and contracting motion, and remained stationary for the following 12 second period to complete a 24 second cycle. Retinotopic mapping was performed using a stimulus that rotated slowly through the visual field about a central fixation cross. The retinotopic stimulus was a circular aperture filled with white dots on a black background. Similar to the MT+ localizer stimulus, the dots within a 45° wedge, moved radially towards and away from fixation, alternating direction every second, while the remainder of the dots remained stationary, as shown in Fig. 5.7.b. This motion-defined wedge rotated 45° every 3 seconds, completing a full rotation every 24s. Similar flickering and flashing wedges have been routinely used in retinotopic mapping to identify visual areas (V1,V2, V3), [4, 18, 19, 25]. This paradigm evokes a travelling wave of activity in retinotopically organized visual areas width the temporal phase of the fMRI response corresponding to the cortical representation of angular position. The amplitude of the fMRI signal can also be interpreted as an indirect measurement of the size of neuron's receptive fields [8]. Neurons with small receptive fields will be stimulated only during a small fraction of
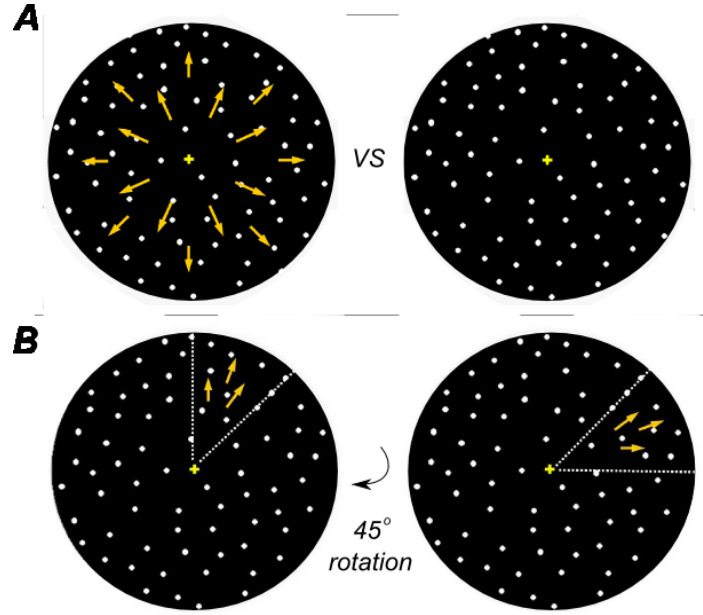
Figure 5.7: Stimuli: (A) V5 localiser; 12 seconds moving (radially inward and outward, alternating direction every second) versus 12 seconds stationary dots. (B) Retinotopy; A 45° rotating wedge containing moving dots which rotates 45° every 3 seconds to complete a full cycle every 24 seconds [7]. A fixation cross (+) is displayed at the centre of the stimulus.

the period of wedge rotation. Hence, this paradigm will produce a strong modulation of neuronal activity in area MT within V5 [8], which contains neurons with relatively small receptive fields.

Functional data collection

Single shot, gradient echo - echo planar imaging, GE-EPI, with TE = 25 ms and TR = 3 s was used for functional imaging. Acquisition used the optimisation methods described in sections 4.3.2 and 4.3.3. An RF pulse with a nominal flip angle of 100° was found to produce the highest signal to noise ratio in the visual cortex due to increased B_1 inhomogeneities at 7 T in lower brain regions, seen as a signal drop-off in B_1-amplitude in these areas. For the functional acquisition a total of 26 contiguous axial slices orientated parallel to the calcarine sulcus, as shown by the red stack in Fig. 5.6.b, were acquired with 1.5 mm isotropic resolution. A rectangular field of view (FOV) of 144

mm in the right-left (RL) direction and 126 mm in the anterior- posterior (AP) direction was used. The reduced FOV in the AP phase encoding (PE) direction required the used of an outer volume suppression [26], slab shown in blue in Fig. 5.6.b. A SENSE factor of 2 was used in the AP direction to reduce the number of phase encoding steps required.

Functional data sets consisting of 80 volumes of EPI data were acquired in 240 seconds, corresponding to 10 repeats of both the MT+ localizer and the rotating wedge stimuli (each using a 24 s cycle). Each functional scan was repeated twice for both types of stimuli. The shim currents were set using the calculated values from the image-based shimming method (described in more detail in Section 4.3.3) for all functional scans. This assured that geometric distortions were fixed throughout the functional experiment (as long as the subject does not move).

A T_1-weighted anatomical image with the same slice prescription, coverage, and resolution as the functional data (MPRAGE with linear phase encoding order, TE=2.14 ms, TR=14 ms, FA=10°, TI=960 ms, 2 averages) was acquired at the end of the scanning session.

Functional data analysis

All fMRI data analysis was performed with a combination of custom-written software (mrTools, NYU, http://www.cns.nyu.edu/heegerlab/wiki/; VISTA, Stanford) running in Matlab (Mathworks, Natick, MA) and FSL (FM-RIB, Oxford [21]. A motion correction algorithm was applied to the functional data [27] to correct for residual head motion. The fMRI data time series were then high-pass filtered to compensate for slow signal drift [28, 29] and each voxel's time series was divided by its mean intensity to convert the data from image intensity to units of percent signal change. The individual time series for the retinotopy (V5 localizer) paradigm were averaged together to create an average retinotopy (V5 localizer) time series with increased SNR.

The fMRI data were analyzed using standard methods for retinotopic mapping [25] reviewed in [3]. At each voxel the Fourier-transform of the time series

gives the coherence and the phase of the best fitting sinusoid at the stimulus repetition frequency. The coherence measures signal-to-noise [18, 25], taking a value near 1 when the fMRI signal modulation at the stimulus/cue period is large relative to the noise (at the other frequency components) and a value near 0 when there is no signal modulation or when the signal is small compared with noise. The phase of the periodic fMRI response measures the temporal delay of the fMRI signal with respect to stimulus onset, providing information about the angular position of the stimulus in the visual field to which the voxel responded. For the V5 localizer there are only two phase conditions, corresponding either to moving or stationary stimuli.

The functional maps were not spatially smoothed to avoid unnecessary blurring od the data. The coherence coefficient was used as a thresholding measure. The choice of coherence threshold does not have an effect on the phase values. Lowering the threshold, will only increase the number of voxels in the image with low coherence value (noise) which have a random phase, and therefore the definition of the visual borders from the phase reversals (described in section 5.2.2) is independent of the choice of coherence threshold.

Cortical flattening

To display activation on a cortically-flattened surface, the in-plane MPRAGE anatomical images acquired at the end of the functional session (which were in the same space as the co-registered fMRI data), an image registration algorithm [27] was used to align These MPRAGE images were then registered to the whole head 3T MPRAGE data. Visual area V5 was identified from the V5 localizer scan and the boundaries of V1 were identified from the phase reversals of the flattened retinotopic map.

As with the functional data, the manually labeled regions of banding were transformed into flattened cortical space. In order to transform the high resolution anatomical data to whole head anatomical space, the high-resolution averaged MPRAGE 7 T data was aligned to the whole head 3T MPRAGE

data. This transformation was also applied to the $T_2^\star$-weighted data, so that the corresponding binary image representing the location of myelin bands could then then be transformed into flattened cortical space.

5.5 Results

A hypointense band, conforming to the expected anatomical location of the stria of Gennari, was evident within the cortical grey matter in the visual cortex of all subjects scanned using the high resolution $T_2^\star$-weighted imaging. This band appears bright in the T_1-weighted MPRAGE data, but it is easier to visualized as a dark band in the contrast-inverted MPRAGE data. Figure 5.8 shows example $T_2^\star$-weighted (i) and contrast-inverted MPRAGE data (ii) acquired from subject 1. A hypointense band is clearly visible within the cortical grey matter at the calcarine sulcus (A,B), as well as in more lateral regions of the occipital lobe (C,D). Intensity profiles measured across the yellow lines in the zoomed images are also shown. Profiles (A,B) are measured across the calcarine sulcus (from WM to WM across the CSF) in the $T_2^\star$-weighted and contrast-inverted MPRAGE images respectively. The highest intensity peak at the centre of the profile corresponds to CSF, with the lowest intensity at the edges corresponding to WM. An intensity dip within the cortical grey matter, indicating the presence of the myelinetion band, is present in both images profiles (indicated by the arrows), and it is more pronounced in the $T_2^\star$-weighted image profile (A), (with dip 5 times larger than in MPRAGE data). Profiles (C,D) are measured across the cortical layer from WM to CSF in the $T_2^\star$-weighted and contrast inverted image MPRAGE data respectively. Again, the arrows mark a dip in intensity which is more obvious in the $T_2^\star$-weighted data (with dip 5.9 times larger than in MPRAGE data).

Figure 5.9.A shows phase colour maps of the retinotopy wedge paradigm overlaid on the average of the GE EPI data for subject 2 for a coherence threshold of c > 0.5. Figure 5.9.B shows the coherence map (for a coherence threshold c > 0.5) of the V5 localizer for the same subject for comparison.
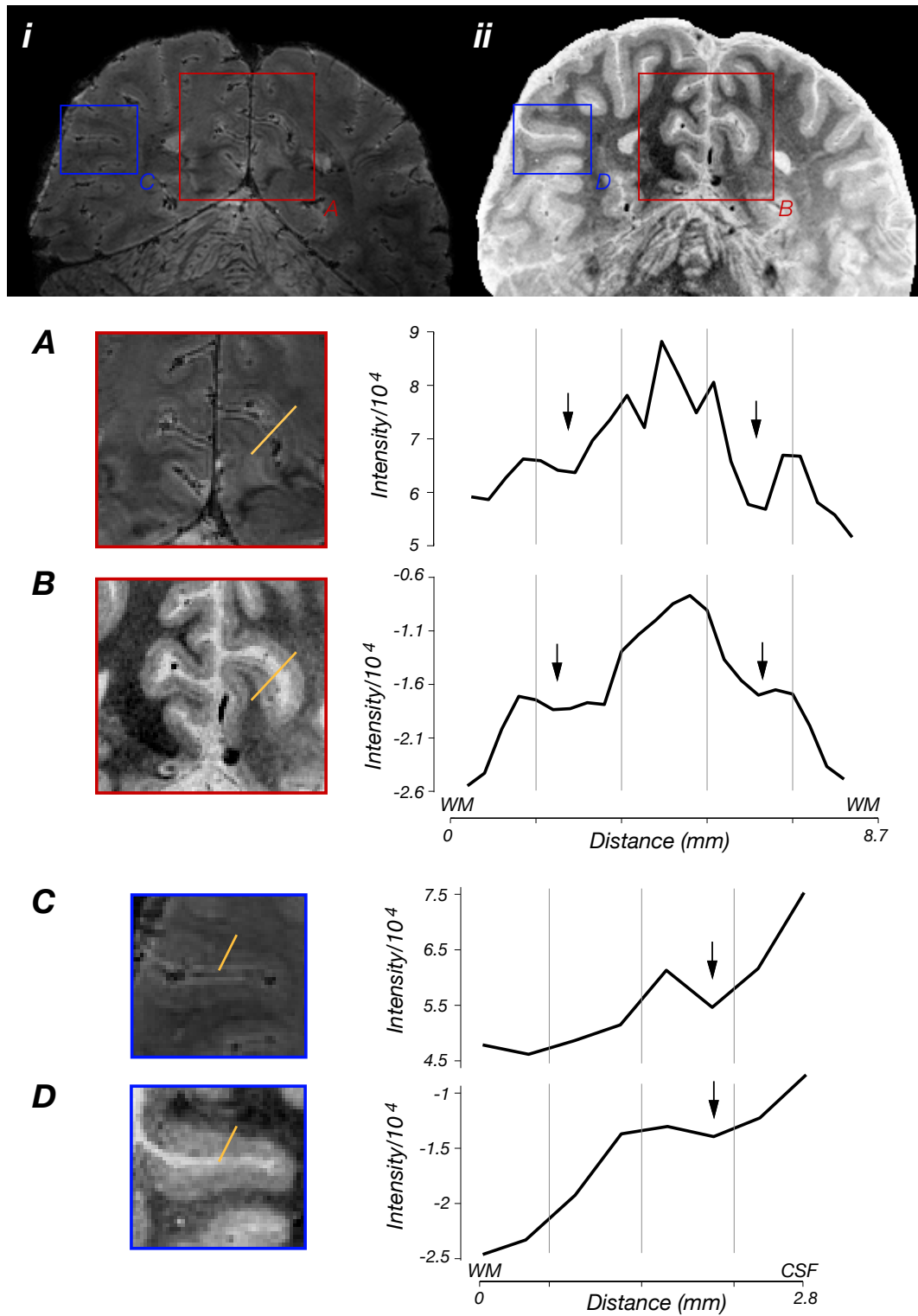
Figure 5.8: i) $T_2^\star$ high resolution image (0.4 mm isotropic) showing a hypointense band within the grey matter and (ii) corresponding contrast-inverted T_1-weighted MPRAGE slice (0.6 mm slice thickness) for the same subject in identical native space. (A,B,C,D) Intensity profiles measured through the yellow line marked in the zoomed images.
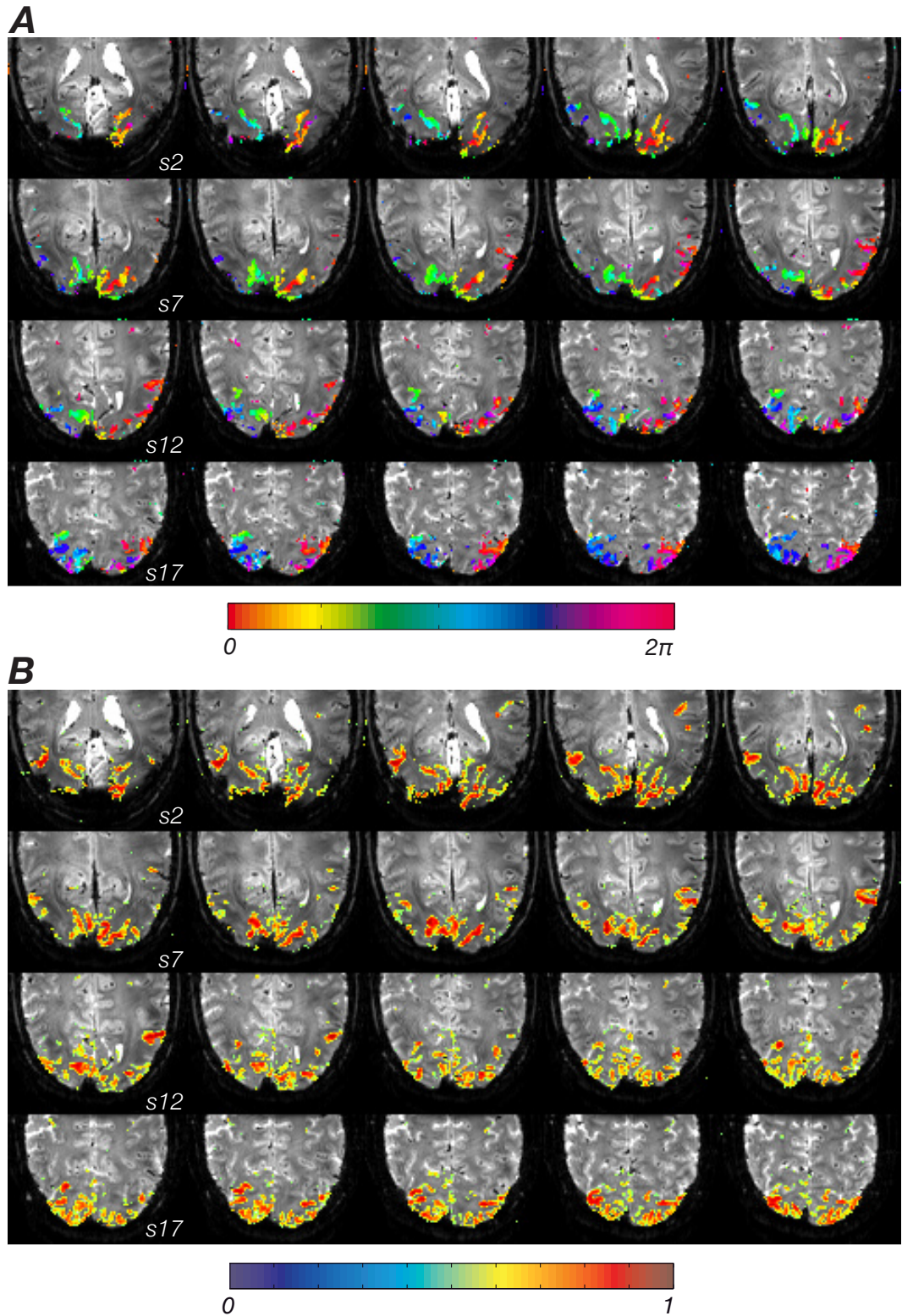
Figure 5.9: (A) Phase images colour maps (data shown for two motion corrected averages) of the rotating wedge paradigm for a coherence threshold of 0.5 and (B) coherence map (threshold 0.5) superimposed on the mean GE EPI image for a subset of the imaged slices.
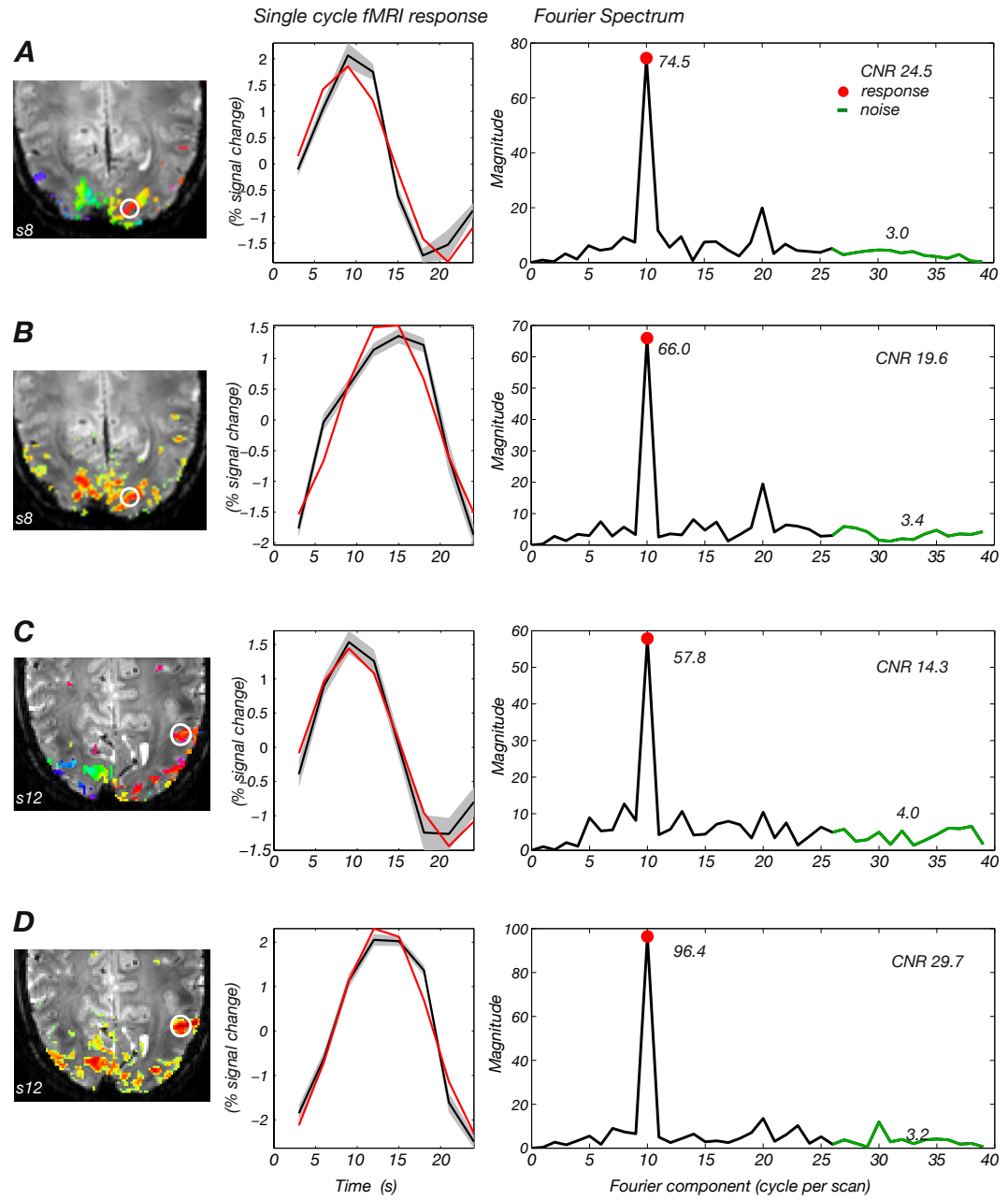
Figure 5.10: Mean cycle fMRI response and corresponding Fourier spectrum for (A,C) wedge paradigm and (B,D) V5 localizer paradigm for an ROI in V1 (A,B) and an ROI in V5 (C,D). The shaded grey area represents the standard error.
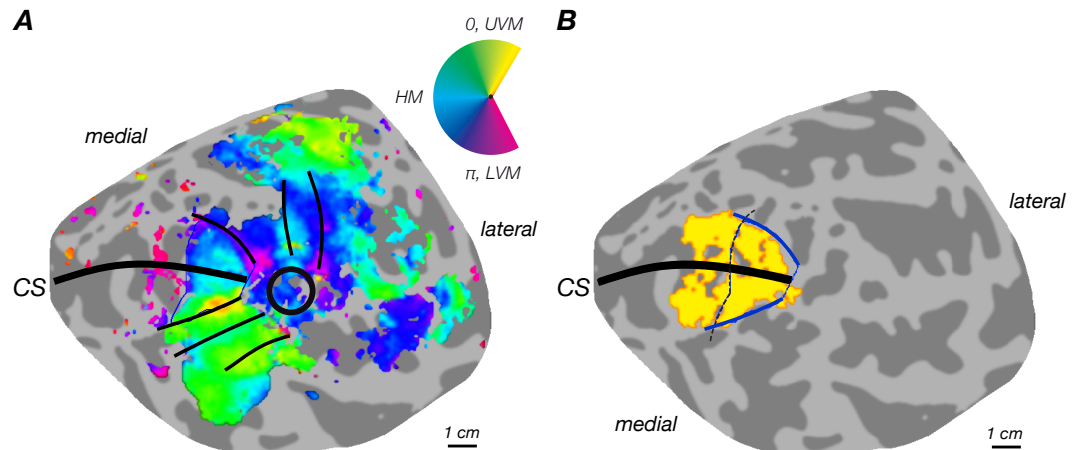
Figure 5.11: (A) Retinotopic organization of visual areas in the right hemisphere. Colour encodes the representation of the visual field as shown in top-right diagram. The black lines show the phase reversals which represent the borders of the various visual areas. The positions of the calcarine sulcus (CS) and visual fovea (black circle) are also shown. (B) Structural and functional maps of the striate cortex in the right hemisphere. Yellow, manual labels of structural, hypointense bands. Blue lines, outline of functionally defined area V1. Dashed line, extent of the visual field spanned by the stimulus.

The V5 localizer paradigm also produces high signal modulation in early visual areas. This is also illustrated by Fig. 5.10.B, which shows the fMRI response of the mean cycle (average across cycle) and the corresponding Fourier spectrum for an small ROI over V1 (marked by the white circle) for the V5 localizer paradigm. The signal modulation in this ROI for the wedge paradigm is higher (Fig. 5.10.A), with a temporal contrast to noise ratio of 24.5 (CNR is 19.6 for the V5 localizer). V5 is known to be highly responsive to motion. Comparing the response of this brain area to both paradigms, in can be seen that the rotating wedge paradigm produces a moderate signal modulation in visual area V5 (with a CNR of 14.3), as shown in Fig. 5.10.C, compared to the much stronger response (CNR 29.7) to motion versus stationary stimuli, shown in Fig. 5.10.D.

The retinotopic organization is clear when maps are transformed into a flattened representation of the cortex, as shown in Figure 5.11.A, which shows the angular component of the retinotopic map of the right hemisphere. Light
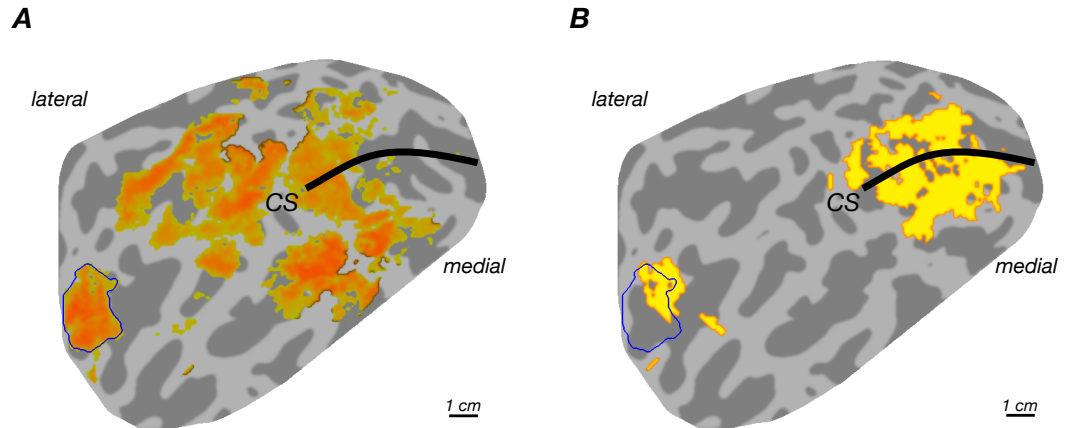
Figure 5.12: (A) Functional statistical map of MT localizer in the left hemisphere. (B) Structural and functional maps of striate cortex. Yellow, manual labels of structural, hypointense bands. Blue line, outline of functionally defined area MT.

areas represent the gyri and dark areas the sulci. The borders of the primary visual cortex, V1, were identified by the phase reversals at the lower vertical meridian (LVM) and the upper vertical meridian (UVM). The retinotopic mapping allows only the definition of the lateral borders, but not anterior-posterior extent. Anterior extent is limited by the size of the visual field viewed by the subject. Fig. 5.11.B shows the boundary of V1/striate cortex determined from the retinotopic maps (blue line) transformed onto inflated representations of the cortex for the same subject. The yellow region, which overlaps the V1 area defined via retinotopic mapping, represents the areas in which the hypointense band was identified in the $T_2^\star$-weighted data. This region extends further than the functionally defined area V1 in the anterior direction, due to the limited extent of the visual field spanned by the stimulus (7.6°), compared to the full extent of the visual field (80°). The mean across subjects of the total amount of striate cortex identified as a percentage of the V1 area defined from the retinotopic map was 87±9%.

In order to estimate the accuracy of the delineated band, additional drawings by independent observers would have been desirable in order to compare the extent of the bands delineated by each independent observer. Given the big amount of data acquired for each subject, the process of drawing lines over the
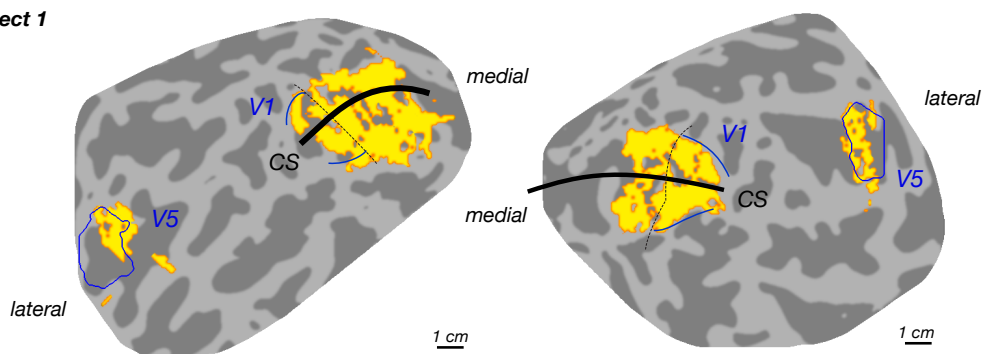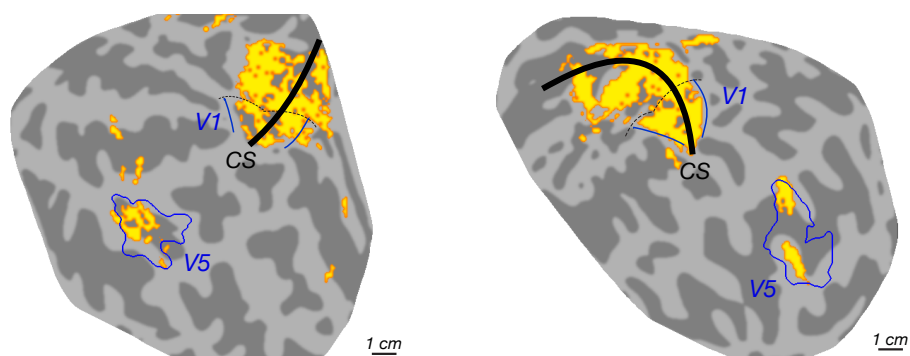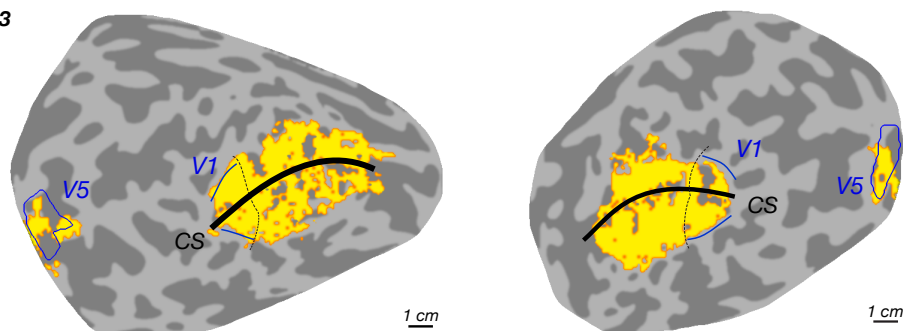
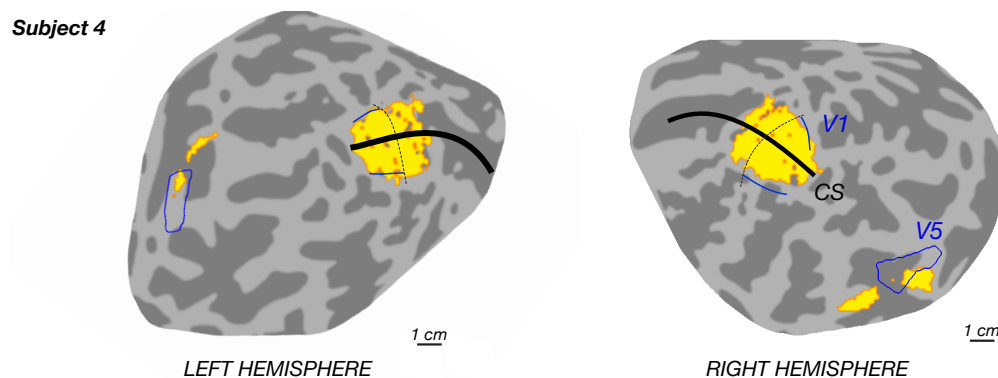Figure 5.13: Structural and functional maps of the striate cortex in the both hemispheres for all subjects. Yellow, manual labels of structural, hypointense bands. Blue line, outline of functionally defined areas V1 and MT. Dashed lines, extent of the visual field spanned by the stimulus.

dark band was slow and tiring, requiring several hours for each subject along two or three days. Therefore repeating the precess for each subject would have required an additional PhD student.

Figure 5.12.A shows the statistical map of the V5 localizer for subject 2 in the left hemisphere. A hypointense band was also evident in a portion of the functionally identified V5 region (Fig. 5.12.B). Fig. 5.13 shows the functional and structural maps in both hemispheres for all subjects. While a dark band was evident on both banks of the superior temporal sulcus, within the functionally defined area V5, this band was absent at the fundus of the sulcus (Fig. 5.13, subject 1, right hemisphere), presumably due to the high curvature [14]. A similar phenomenon can be seen in some regions of the calcarine sulcus. The mean across subjects of the total amount of myelinated cortex identified as a percentage of V5 area defined from the functional scan was 33±16%, which is considerably less than the proportion of striate cortex found within V1. The lower contrast to noise ratio of GM to myelin band in this area (5.1±0.4%) compared to V1 area (20.1±0.5%) makes it more difficult to detect the myelin band.

5.6   Discussion

We have shown that high resolution $T_2^\star$-weighted images acquired at 7 T can be used to identify banding within cortical grey matter in reasonable measurement times. A hypointense band of signal intensity in the grey matter of the occipital lobe was seen in all four subjects scanned. Regions where this band was identified overlapped with the functionally defined V1 area. The percentage of stria found within the boundaries of functionally defined V1 was 66%, a slightly higher percentage than that reported using T_1-weighted MPRAGE at 3 T [14], with a mean across subjects of 56%. In this previous study, the authors achieved 0.3×0.3 mm^2 in-plane resolution by expanding the slice thickness to 1.5 mm, and therefore needed to combine data from three orientations, which required up to 75 minutes scanning time, in order to improved detection

of the stria. A very recent study [15] has demonstrated detection of the stria using IR-TSE at 3 T with a resolution of $0.4\times0.4\times0.5$ mm^3, highlighting the need for isotropic resolution for the reliable detection of the stria of Gennari. The total scanning time in that study, using an acceleration factor of 2, was 40 minutes. The increased SNR available at 7 T, allows the acquisition of T$_2^\star$ images over a similar volume coverage in just 14 minutes. The shorter scanning time at 7 T provides potential for acquiring data with different image contrast within a single scanning session. The combination of such images with various contrast could then help the detection of layering within the grey matter with automated tools. The stria of Gennari has been visualised recently in vivo using gradient echo phase images [30]. Although the protocol was optimized for modulus image, we did also observed occasional patterns of myelination within the striate cortex in the phase images from the T$_2^\star$-weighted data. Recently, a novel method has been developed in this lab [31] to acquire magnetisation transfer data at 7 T within the SAR limits. MT brain images are very sensitive to myelin, and could be optimized to detect the stria of Gennari.

Evidence of banding was also found in the functionally defined V5 area. The proportion of myelinated cortex found within this area is significantly smaller than the proportion of the banded tissue found in V1. A previous study by Walters et al [12] showed evidence of the myelination within area V5 (MT+) identified using a moving checkerboard paradigm, similar to the V5 locazier paradigm used in this work. They measured intensity profiles through the grey matter, however, quantitative correspondence between functional activation and structure was not defined in detail. The discrepancy between functionally defined V5 area and the myelinated cortex in this work could be explained in part because the paradigm activated an area which extends outside the myelinated cortex, whose origin may not be purely MT. Huk et al [8] demonstrated the subdivision of area V5 into an area which exhibited a clear retinotopic organization, identified as the MT homologue of the macaque, and an area that did not exhibit clear retinotopic organization, but responded to peripheral ipsilateral stimulation, identified as the MST homologue of the

macaque. The V5 localizer would therefore activate both MST and MT areas, but the retinotopy wedge paradigm used here, which is identical to the one used by Huk et al, should produce an organized retinotopy map only in area MT which should correspond to the myelinated area. However, we did not find a distinction of two areas with different retinotopic organization within the area V5 defined by the motion versus stationary paradigm. The use of a paradigm which identifies functional area MST, and the acquisition of images with higher spatial resolution will help to identify visual area MT within the V5 (MT+) complex. A recent retinotopic mapping study at ultra-high field has demonstrated the benefits of high spatial resolution measurements at 7 T for producing visual field maps with higher coherence [32]. Here we have used 1.5 mm isotropic voxels in order to cover V5 as well as the earlier visual areas. An isotropic spatial resolution of 1 mm could be achieved by restricting the FOV to only include the V5 areas of both hemispheres. A 32-channel array head coil would allow the acquisition of images with increased acceleration factor, removing the restriction on limited FOV.

Bibliography

[1] S. M. Zeki. Colour coding in rhesus monkey prestriate cortex. *Brain Res*, **53**(2), 422–427, (1973).

[2] J. D. Watson, R. Myers, R. S. Frackowiak, J. V. Hajnal, R. P. Woods, J. C. Mazziotta, S. Shipp, and S. Zeki. Area V5 of the human brain: evidence from a combined study using positron emission tomography and magnetic resonance imaging. *Cereb Cortex*, **3**(2), 79–94, (1993).

[3] B. A. Wandell. Computational neuroimaging of human visual cortex. *Annu Rev Neurosci*, **22**, 145–173, (1999).

[4] M. I. Sereno, A. M. Dale, J. B. Reppas, K. K. Kwong, J. W. Belliveau, T. J. Brady, B. R. Rosen, and R. B. Tootell. Borders of multiple visual areas in humans revealed by functional magnetic resonance imaging. *Science*, **268**(5212), 889–893, (1995).

[5] R. F. Dougherty, V. M. Koch, A. A. Brewer, B. Fischer, J. Modersitzki, and B. A. Wandell. Visual field representations and locations of visual areas V1/2/3 in human visual cortex. *J Vis*, **3**(10), 586–598, (2003).

[6] M. I. Sereno, C. T. McDonald, and J. M. Allman. Analysis of retinotopic maps in extrastriate cortex. *Cereb Cortex*, **4**(6), 601–620, (1994).

[7] J. Larsson and D. J. Heeger. Two retinotopic visual areas in human lateral occipital cortex. *J Neurosci*, **26**(51), 13128–13142, (2006).

[8] A. C. Huk, R. F. Dougherty, and D. J. Heeger. Retinotopy and functional subdivision of human areas MT and MST. *J Neurosci*, **22**(16), 7195–7205, (2002).

[9] V. P. Clark, E. Courchesne, and M. Grafe. In vivo myeloarchitectonic analysis of human striate and extrastriate cortex using magnetic resonance imaging. *Cereb Cortex*, **2**(5), 417–424, (1992).

[10] E. L. Barbier, S. Marrett, A. Danek, A. Vortmeyer, P. van Gelderen, J. Duyn, P. Bandettini, J. Grafman, and A. P. Koretsky. Imaging cortical anatomy by high-resolution MR at 3.0T: detection of the stripe of Gennari in visual area 17. *Magn Reson Med*, **48**(4), 735–738, (2002).

[11] S. Eickhoff, N. B. Walters, A. Schleicher, J. Kril, G. F. Egan, K. Zilles, J. D. G. Watson, and K. Amunts. High-resolution MRI reflects myeloarchitecture and cytoarchitecture of human cerebral cortex. *Hum Brain Mapp*, **24**(3), 206–215, (2005).

[12] N. B. Walters, G. F. Egan, J. J. Kril, M. Kean, P. Waley, M. Jenkinson, and J. D. G. Watson. In vivo identification of human cortical areas using high-resolution MRI: an approach to cerebral structure-function correlation. *Proc Natl Acad Sci U S A*, **100**(5), 2981–2986, (2003).

[13] H. Bridge, S. Clare, M. Jenkinson, P. Jezzard, A. J. Parker, and P. M. Matthews. Independent anatomical and functional measures of the V1/V2 boundary in human visual cortex. *J Vis*, **5**(2), 93–102, (2005).

[14] S. Clare and H. Bridge. Methodological issues relating to in vivo cortical myelography using MRI. *Hum Brain Mapp*, **26**(4), 240–250, (2005).

[15] R. Turner, A.-M. Oros-Peusquens, S. Romanzetti, K. Zilles, and N. J. Shah. Optimised in vivo visualisation of cortical structures in the human brain at 3 T using IR-TSE. *Magn Reson Imaging*, **26**(7), 935–942, (2008).

[16] S. Clarke and J. Miklossy. Occipital cortex in man: organization of callosal connections, related myelo- and cytoarchitecture, and putative boundaries of functional visual areas. *J Comp Neurol*, **298**(2), 188–214, (1990).

[17] R. B. Tootell and J. B. Taylor. Anatomical evidence for MT and additional cortical visual areas in humans. *Cereb Cortex*, **5**(1), 39–55, (1995).

[18] S. A. Engel, G. H. Glover, and B. A. Wandell. Retinotopic organization in human visual cortex and the spatial precision of functional MRI. *Cereb Cortex*, **7**(2), 181–192, (1997).

[19] E. A. DeYoe, G. J. Carman, P. Bandettini, S. Glickman, J. Wieser, R. Cox, D. Miller, and J. Neitz. Mapping striate and extrastriate visual areas in human cerebral cortex. *Proc Natl Acad Sci U S A*, **93**(6), 2382–2386, (1996).

[20] B. A. Wandell, S. O. Dumoulin, and A. A. Brewer. Visual field maps in human cortex. *Neuron*, **56**(2), 366–383, (2007).

[21] S. M. Smith, M. Jenkinson, M. W. Woolrich, C. F. Beckmann, T. E. J. Behrens, H. Johansen-Berg, P. R. Bannister, M. D. Luca, I. Drobnjak, D. E. Flitney, R. K. Niazy, J. Saunders, J. Vickers, Y. Zhang, N. D. Stefano, J. M. Brady, and P. M. Matthews. Advances in functional and structural MR image analysis and implementation as FSL. *Neuroimage*, **23 Suppl 1**, S208–S219, (2004).

[22] J. Larsson. *Imaging Vision*. PhD thesis, Karolinska Institute, (2001).

[23] S. Zeki, J. D. Watson, C. J. Lueck, K. J. Friston, C. Kennard, and R. S. Frackowiak. A direct demonstration of functional specialization in human visual cortex. *J Neurosci*, **11**(3), 641–649, (1991).

[24] R. B. Tootell, J. B. Reppas, K. K. Kwong, R. Malach, R. T. Born, T. J. Brady, B. R. Rosen, and J. W. Belliveau. Functional analysis of human MT and related visual cortical areas using magnetic resonance imaging. *J Neurosci*, **15**(4), 3215–3230, (1995).

[25] S. A. Engel, D. E. Rumelhart, B. A. Wandell, A. T. Lee, G. H. Glover, E. J. Chichilnisky, and M. N. Shadlen. fMRI of human visual cortex. *Nature*, **369**(6481), 525, (1994).

[26] J. Pfeuffer, P.-F. van de Moortele, E. Yacoub, A. Shmuel, G. Adriany, P. Andersen, H. Merkle, M. Garwood, K. Ugurbil, and X. Hu. Zoomed functional imaging in the human brain at 7 Tesla with simultaneous high spatial and high temporal resolution. *Neuroimage*, **17**(1), 272–286, (2002).

[27] O. Nestares and D. J. Heeger. Robust multiresolution alignment of MRI brain volumes. *Magn Reson Med*, **43**(5), 705–715, (2000).

[28] B. Biswal, A. E. DeYoe, and J. S. Hyde. Reduction of physiological fluctuations in fMRI using digital filters. *Magn Reson Med*, **35**(1), 107–113, (1996).

[29] B. Biswal, A. G. Hudetz, F. Z. Yetkin, V. M. Haughton, and J. S. Hyde. Hypercapnia reversibly suppresses low-frequency fluctuations in the human motor cortex during rest using echo-planar MRI. *J Cereb Blood Flow Metab*, **17**(3), 301–308, (1997).

[30] J. H. Duyn, P. van Gelderen, T.-Q. Li, J. A. de Zwart, A. P. Koretsky, and M. Fukunaga. High-field MRI of brain cortical substructure based on signal phase. *Proc Natl Acad Sci U S A*, **104**(28), 11796–11801, (2007).

[31] O. Mougin, R. Cox, A. Pitiot, and P. A. Gowland. Magnetization transfer phenomenon in the human brain at 7T. *Neuroimage*, (2009).

[32] M. B. Hoffmann, J. Stadler, M. Kanowski, and O. Speck. Retinotopic mapping of the human visual cortex at a magnetic field strength of 7T. *Clin Neurophysiol*, **120**(1), 108–116, (2009).

Chapter 6

Applications II: Mapping the somatosensory cortex

6.1 The somatosensory cortex

Somatotopic sensation consists of the signals received from the various sensory receptors that perceive touch, pain, preoprioception and temperature or thermal sense. This chapter focus on the perception of touch to a flutter stimulus. The sensation of touch is primarily mediated by mechanoreceptors. Flutter, a touch sensation occuring in the frequency range of 30-50 Hz, is detected by Merkel's disks (a type of slowly-adapting mechanoreceptor found in the cutaneous tissue). Pacinian corpuscles, another type of mechanoreceptor, are most sensitive to vibrations with a frequency of approximately 250-300 Hz. These are fast-adapting cutaneous mechanoreceptors, sensitive to changes in stimulation, rather than continuous stimulation.

Figure 6.1 shows the two major ascending fibre systems in the somatosensory system; the Dorsal Column-Medial Lemniscal (DCML) pathway (red line), composed of fibres processing touch and proprioception, and the Spino-Thalamic (ST) pathway (blue line), composed of fibres processing pain and temperature. Information carried in each pathway remains segregated until it reaches the cortex. In the DCML pathway information ascends through
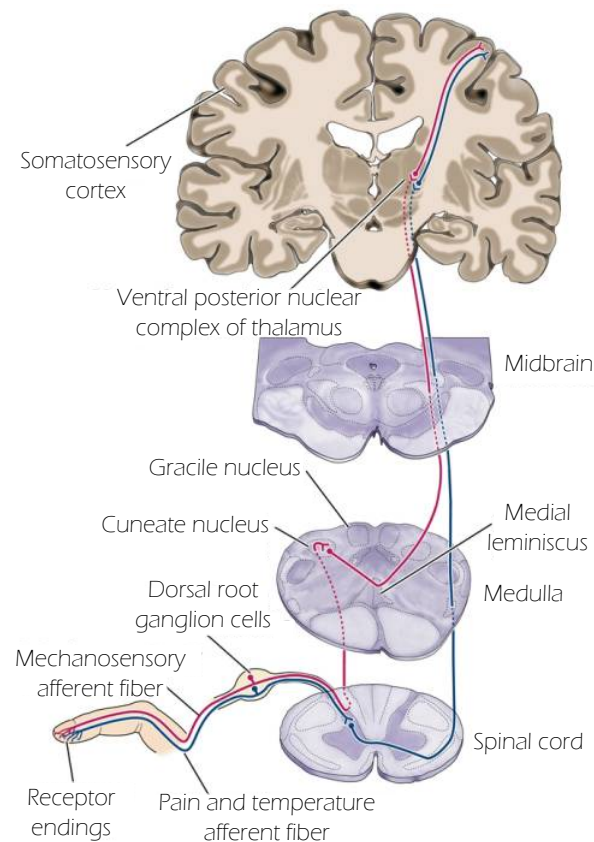
Figure 6.1: Sensory pathways. Reproduced from www.rci.rutgers.edu.

the dorsal column on the ipsilateral side of the spinal cord, it synapses in the medulla and ascends via the medial lemniscus to the thalamus. In the ST Pathway information crosses to the contralateral side in the spinal cord and ascends via the spinothalamic tract to the thalamus. As fibres from both tracks ascend towards the cortex they synapse with neurons in the thalamus. The ventral posterior nucleus in the thalamus receives the information and projects to the somatosensory cortex.

The human somatosensory cortex consists of two cortical areas : a primary somatosensory area (S1) covers the posterior bank of the central sulcus (CS) and a secondary somatosensory area (S2) is buried in the lateral sulcus. (See Fig. 6.2.A.). The central sulcus separates the parietal from the frontal lobe. S1 and the primary motor cortex (M1), Brodmann area 4, which drives the voluntary part of the muscular system, lie on opposite sides of the central
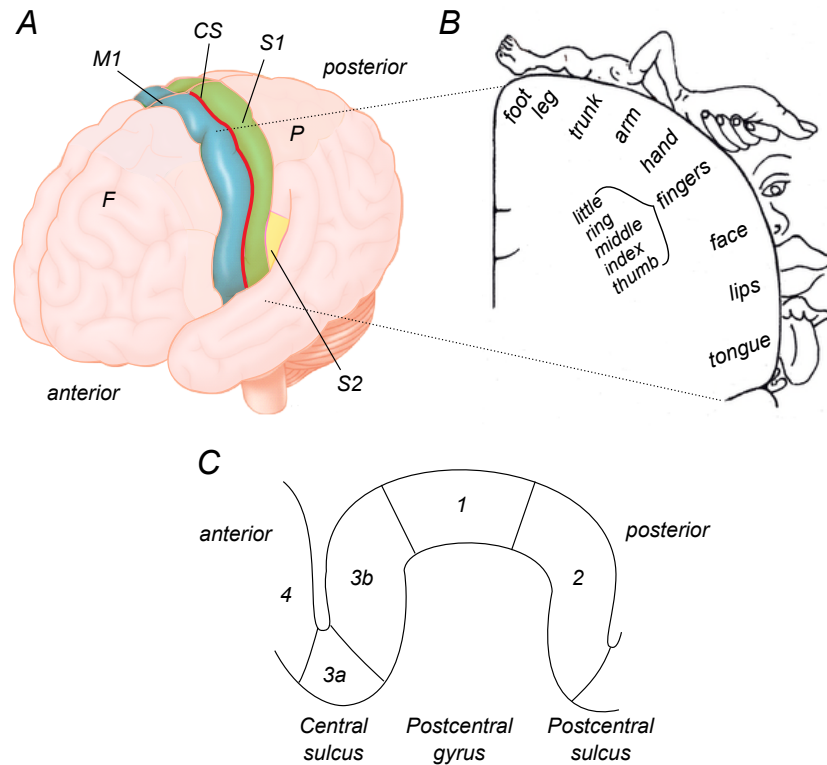
Figure 6.2: (A) Schematic drawing of the human brain. CS=central sulcus, S1=primary somatosensory cortex, S2=secondary somatosensory cortex, M1=primary motor cortex, F=frontal lobe, P=parietal lobe. Adapted from http://www.brainconnection.com/ (B) Diagram of the sensory homunculus. Reproduced from http://synergysci.wordpress.com/2007/05/31/brain-insight/. (C) Schematic drawing of the somatosensory cortex. Brodmann areas 1, 2, 3a and 3b are indicated.

sulcus. S1 spans the posterior bank of the central sulcus to the anterior bank of the postcentral sulcus and it has been shown cytoarchitectonically to be divided into Brodmann areas 1, 2, 3a and 3b. A schematic profile of S1 is shown in Fig. 6.2.B. Area 3a lies in the fundus and area 3b in the posterior bank of central sulcus. Area 1 lies on the crown of the postcentral gyrus and area 2 occupies the posterior wall of the postcentral gyrus. Activation in S1 is primairly in the hemisphere that is contralateral to the site of stimulation, with weak activation in the ipsilateral S1. S2 receives inputs from Brodmann area 1 and 3b. Neurons in S2 have a bilateral receptive field, unlike the neurons in S1. In this study we deliver flutter stimulus to a subject's finger using a piezoelectric device and the strongest activation is expected in areas 1 and 3b

of S1, and in S2, as this type of stimulus targets cutaneous mechanoreceptors. Brodmann area 4 is part of the motor-cortex and is close to the somatosensory cortex, covering nearly all of the precentral gyrus, from the anterior bank of the central sulcus to the precentral sulcus.

The responsiveness within primary sensory cortex is organized into a map known as the sensory homunculus (with positions of the body surface mapped to corresponding positions within the cortical field), neurons with similar response properties are grouped together and the size of a body surface is defined by the density of receptors and neurons devoted to that region. Therefore the hands, especially the digits tips, occupy a relatively large part of the cortex. A schematic of the sensory homunculus is shown in Fig. 6.2.B. A number of studies have investigated the representation of the body in human somatosensory cortex. Penfield and Boldrey [1] were the first to describe the somatosensory map (homunculus) in human subjects using direct stimulation of the cortical surface and verbal reports of sensation. In recent years with the advent of neuroimaging techniques several fMRI studies have now been performed to begin to map the somatosensory cortex [2, 3, 4, 5, 6, 7, 8, 9], however most of these studies are at relatively coarse resolution.

6.2 Introduction

High resolution measurements of the somatotopic mapping of the hand in human cerebral cortex have many important potential applications: understanding disturbed sensory representations in neurological disorders such as dystonia [10], interpreting cortical changes following hand injuries or tracking cortical re-organization during rehabilitation. Knowledge of the exact spatial layout of somatosensory cortex is also crucial for a detailed understanding of how top-down influences, such as attention, may modulate sensory inputs at the level of primary somatosensory cortex.

With the advent of modern, non-invasive, neuroimaging techniques, especially functional magnetic resonance imaging (fMRI), early measurements of

the representation of the body in human somatosensory cortex have been revisited. Several fMRI studies have concentrated on mapping the representation of the hand by applying sensory stimuli to the glabrous skin of the fingertips (phalangeal digits) and measuring the resulting cortical responses. Sensory stimuli are usually delivered by piezoelectric [5, 7] or pneumatic [6, 8, 9] apparatus. However, most of these earlier studies are limited to low spatial resolution [2, 3, 4, 5] and only a few studies have attempted to obtain a map of all fingers in the primary somatosensory cortex (S1) [3, 4, 7, 8]. In addition these studies include data that is averaged across subjects or registered into a standard space (Talairach, MNI) which leads to spatial blurring. A recent study [9] evaluated the effects of voxel size (2 mm and 3 mm isotropic) and smoothing on BOLD sensitivity to finger somatotopy. The results demonstrated, not surprisingly, that higher spatial resolution led to improvements on the quality of somatotopic maps. High spatial resolution is particularly important when studying somatosensory responses, because the maps in S1 are much smaller than for example those in visual cortex, and the postcentral gyrus (PCG) is prone to significant partial volume effects (PVE) due to its large surface-to-volume ratio [11] and narrow width ($\sim$ 3mm) [12].

Obtaining high-spatial resolution measurements with fMRI, however, is not trivial. As spatial resolution is increased, image signal to noise ratio is reduced and the blood oxygenation level dependent (BOLD) CNR is reduced. It has shown that there is a complex relationship between physiological noise with spatial resolution and field strength [13]. BOLD CNR can be limiting, particularly for studies using tactile stimulation where the amplitude of the BOLD response has previously been shown to be low [14] and the detectability of finger representations has been shown to be limited even at coarse resolution with good levels of SNR [3]. A recent high spatial resolution fMRI study of functional organization of the fingers used multi-echo FLASH at 3 T [7] with 1 mm in-plane resolution and 2 mm slice thickness. In that study, a low resolution localizer scan was first acquired and a second fMRI session followed to acquire targeted high spatial resolution data using multiple imaging stacks.

The reduced CNR (and therefore reduced statistical power) led to the need for an increase in the number of repeated measurements, but still not all subjects showed statistically significant BOLD responses [7]. fMRI at ultra-high field (7 T) overcomes some of these limitation as BOLD sensitivity is markedly increased (see Section 4.3.1).

BOLD CNR is also influenced by paradigm design. Most previous fMRI studies of somatosensory cortex have used block or event related designs, stimulating individual digits in separate scans [3, 4, 7, 8]. Here a travelling wave paradigm design is used to maximize efficiency to map the representation of all five digits. The travelling wave design has been widely used in the visual domain for retinotopic mapping [15, 16, 17], as described in the previous chapter, but this design has not previously been used to form a somatotopic map of individual digits of the hand. Overduin and Servos [8, 18] have implemented a version of the travelling wave protocol, in an attempt to map out the cortical representation of a single digit by using jets of air applied to different points along the digit tip.

The aim of this study was to use fMRI at ultra-high field (7 T) to generate high-resolution maps of the responses in the primary somatosensory cortex (S1) in individual subjects using a traveling wave design in which the fingertips are stimulated in sequence with a piezoelectric device. Data were acquired with a reduced field of view to cover the post-central sulcus at 1 mm isotropic resolution. In addition, the temporal properties of the event-related fMRI responses to brief vibrotactile digit stimulations in which the fingertips experience an equal duration stimulation as for the travelling wave paradigm is characterized. Statistical maps obtained using the traveling wave paradigm are compared with those obtained in the event-related experiment and the haemodynamic lag calculated from each method assessed and compared. To elucidate the contributions of different tissues types to the observed fMRI responses, inversion-recovery images, in which signals from white matter, grey matter, and CSF are selectively nulled were obtained and correlated with the statistical maps on a voxel-by-voxel basis.

6.3 Methods

6.3.1 Subjects

Five subjects experienced in MRI experiments participated in this study with written consent. Procedures were conducted with approval from the University of Nottingham ethics committee. Each subject participated in three scan sessions: one session at 7 T to measure the topographic representation of digits in the somatosensory cortex with a traveling wave paradigm and one session to characterize the spatial and temporal properties of responses to vibrotactile digit stimulation with an event-related design. In addition one session was performed at 3 T to obtain a high-resolution T_1-weighted anatomical volume of the whole brain (MPRAGE, 1mm isotropic) with homogeneous intensity. Data sets from the same individuals across sessions on different days were each registered to these anatomical images.

6.3.2 Stimuli and paradigm

Tactile stimuli were delivered to the digit tips of the left hand using 5 independent custom-built, MR-compatible piezoelectric devices. Each stimulator delivered a somatosensory stimulus at a flutter frequency of 30 Hz with 1 mm displacement applied over a ~ 1 mm^2 area of contact (Dancer Design, UK), Fig. 6.3.A. Two experimental paradigms were performed: a travelling wave paradigm in which the sensory stimulation created a wave of activity across cortical regions containing a somatotopic map of the hand; and an event-related paradigm in which all digits were simultaneously stimulated followed by a rest (OFF period) to allow measurement of event-related fMRI responses to brief stimuli.

The travelling wave paradigm consisted of stimuli applied sequentially to each digit for 3 s, with an OFF period of 1.8 s between stimulation of digits, completing a whole cycle of stimulation of all five digits in 24s. Digits were stimulated in a 'forward' sequence from thumb to little finger (digit 1 to digit
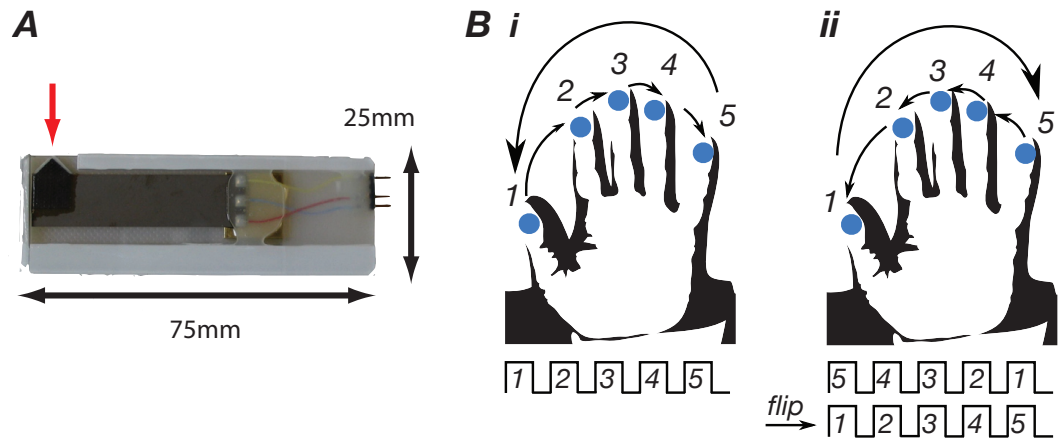
Figure 6.3: Single piezo-electric stimulator device (A). Red arrow, protruding tip which is applied to skin surface (∼1 mm thickness); direction of movement is in and out of the plane. (B) Illustration of the travelling wave paradigm. Vibrotactile stimuli are applied to the fingertips in (i) forward ordering from thumb to little finger or ii) reverse ordering.

5) and in a 'backward' sequence (starting at the little finger and moving to the thumb) (Fig. 6.3. B,C). This resulted in each digit experiencing a 3 s stimulus followed by a 21 s off period. Similar paradigm designs have been used extensively to generate retinotopic maps of visually responsive cortex (as reviewed in [17]). The travelling wave paradigm has previously been applied to the study of somatosensory cortex only at coarse resolution using long cycle lengths [6] or to form an incomplete map of all digits of the hand (Overduin et al. [8] used a similar design to stimulate single digits from tip-to-base but did not use the Fourier-based analysis methods described in this study). In our study, individual scans consisted of 10 cycles, resulting in a total scan duration of 240 s. In a single scan session, six functional scans were acquired with digits stimulated in a 'forward' and 'backward' sequence (in alternating scans). For the event related paradigm all five digits were simultaneously stimulated for an ON period of 3 s (an equal duration to the stimulation in the travelling wave paradigm) with random inter-stimulus intervals of 18, 19 or 20 s. Each functional scan consisted of 12 trials (228 s), and was repeated three times.
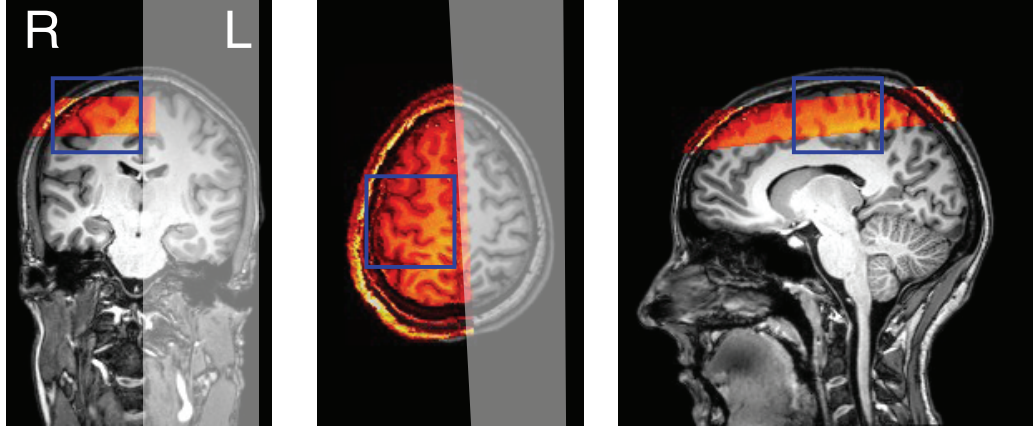
Figure 6.4: Location of imaging stack for zoomed fMRI (red) superimposed on MPRAGE scan for subject. The grey shaded area indicates the location of the outer volume suppression. Blue line, location of shim box.

6.3.3 Functional MRI data acquisition

fMRI data were collected on the 7 T Philips Achieva system (Philips Medical Systems, Netherlands) using a volume transmit head coil and 16-channel receiver array. To minimize head motion, subjects' heads were stabilized using a customized, MR compatible vacuum pillow (B.U.W. Schmidt, Germany) and foam padding. $T_2^\star$-sensitive single shot, gradient echo - echo planar imaging (GE-EPI) was used with the following scan parameters: SENSE factor 2 in the right-left direction, TE = 25 ms, TR = 2.4 s, FA=90°). A total of 22 contiguous axial slices spanning the right primary somatosensory cortex were acquired with 1 mm isotropic resolution, spanning 192 mm in the anterior-posterior (AP) direction and 72 mm in the right-left (RL) direction. The reduced FOV in the phase encoding (PE) direction (RL), required the use of an outer-volume suppression slab to prevent signal fold- over from the left hemisphere into the restricted FOV. The location of the imaging stack and the OVS slab is shown in Fig. 6.4 for a representative subject. Magnetic field inhomogeneity was minimized using local, image-based shimming [19, 20], as described in Section 4.3.3. To classify voxels in the functional, $T_2^\star$- weighted data into different tissue types, we obtained three inversion recovery EP data sets (using the method described in Section 4.3.4) with the same bandwidth,

matrix size, and shim settings to ensure that any residual geometric distortions were matched to the functional data). The inversion delays (TI) of 450 ms, 1200 ms, and 2300 ms were chosen to null white matter, grey matter and CSF respectively (IR images are shown in Fig. 6.11 with a statistical map overlaid). A T_1-weighted anatomical images with the same slice prescription, coverage, and resolution as the functional data (MPRAGE sequence with linear phase encoding order, TE=2.14 ms, TR=14 ms, FA=10°, TI=960 ms, 2 averages) was also acquired during each 7T scanning session. T1-weighted anatomical images of the whole brain (3D MPRAGE, 1 mm isotropic resolution, linear phase encoding order, TE= 3.7 ms, TR= 8.13 ms, TI=960 ms FA= 8°) were acquired from each subject at 3T. These images, which displayed less B_1-inhomogeneity-related signal intensity variation than images acquired at 7T, were used for grey matter segmentation and cortical flattening.

6.3.4 Data preprocesing

All functional image analyses were performed with a combination of custom-written software (mrTools, NYU, http://www.cns.nyu.edu/heegerlab/wiki/; VISTA, Stanford) running in Matlab 7.4 (Mathworks, Natick, MA) and FSL (FMRIB, Oxford [21]). To correct for residual head motion, a motion correction algorithm was applied to the functional data [22]. fMRI data were motion-corrected within and between scans in a given session (for travelling wave and event-related data) and the fMRI data time series were then high-pass filtered to compensate for slow signal drift [23, 24]. Finally, each voxel's time series was divided by its mean intensity to convert the data from image intensity to units of percentage signal change. No spatial filtering was applied to the data. The mean of the $T_2^\star$-weighted fMRI timeseries was calculated and subsequent statistical maps overlaid on this image. For additional visualization, the statistical maps from travelling wave and event-related data were transformed to the space of the anatomical MPRAGE data acquired at 3 T.

6.3.5 Event related design data analysis

A model free deconvolution analysis procedure [25, 26, 27] was used to identify consistently active areas in the event-related data. Specifically, we used the data-driven analysis approach developed by Gardner et al [28] to reconstruct event-related fMRI responses without making any prior assumptions about their shape (or that of the underlying hemodynamic response function). First, the time series of each voxel in the three individual scan repeats was high-pass filtered with a cutoff frequency of 0.01 Hz and converted to percent signal change. Data from the three scans were then concatenated to allow estimation of the response using all acquired event-related data. The event-related fMRI response for a single event-type (all five fingers stimulated for 3 s) at a given voxel was then computed by trial-triggered averaging, solving an equation of the form $\mathbf{y}^T = \mathbf{S} \times \mathbf{H}^T$:

$$
\begin{pmatrix} y_1 \\ y_2 \\ \dots \\ \dots \\ y_n \end{pmatrix} = \begin{pmatrix} 1 & 0 & 0 & \dots \\ 0 & 1 & 0 & \dots \\ \dots & \dots & \dots & \dots \\ 1 & 0 & 0 & \dots \\ \dots & \dots & \dots & \dots \end{pmatrix} \begin{pmatrix} h_1 \\ h_2 \\ \dots \\ \dots \\ h_m \end{pmatrix}
$$

where $\mathbf{y}$ is the measured, mean-subtracted BOLD time course for the voxel (95 points), $\mathbf{S}$ is the stimulus convolution matrix, a design matrix with dimensions $n \times m$ where n is the number of time points in a scan and m is the number of points for which we calculate the estimated response function (11). $\mathbf{H}$ is a m point vector of the unknown haemodynamic response of the stimulus and $[\cdot]^T$ is the transpose operation. The first column of $\mathbf{S}$ contained the value 1 at indices corresponding to the onsets of trials and 0 elsewhere, the second column contained a 1 at indices corresponding to the second time point of those trials and so on. The haemodynamic responses $\mathbf{H}$ to the stimulus that minimized the squared error between $\mathbf{y}^T$ and $\mathbf{S} \times \mathbf{H}^T$ was computed at each voxel by solving the normal equations to the BOLD response for that voxel.
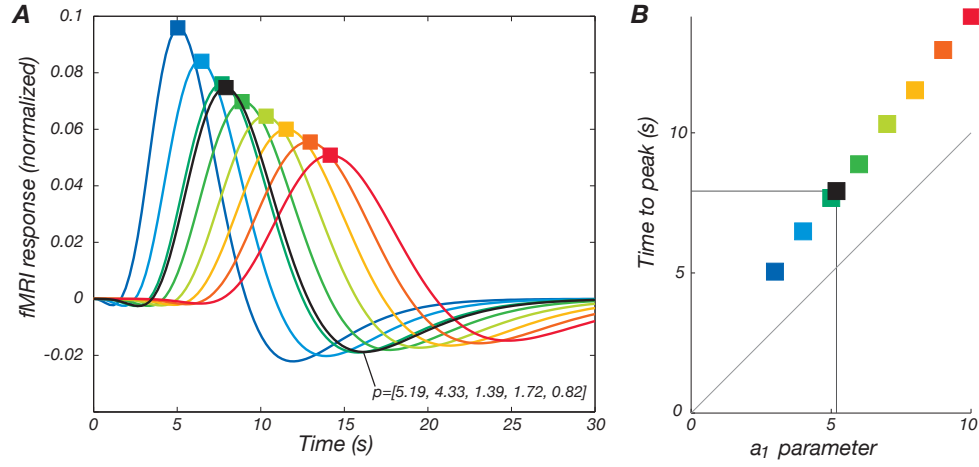
Figure 6.5: Plots of Friston HRF function (A) and time-to-peak (B) as a function of parameter a_1. Coloured lines, range of values for a_1 (3-10s), a_2 is proportionally scaled. (p=[a_1, a_2, b_1, b_2, c]=[a_1,a_2,1.39 s,1.72 s,0.82]). Black line, example fit to event-related data from one subject.

This yields the best least-squares estimate for the event-related fMRI response.

Statistical activation maps were computed from the amount of variance in the original fMRI time course accounted for by the events modelled (using the estimated event-related response) to be time-locked to stimulus presentations. An estimated timecourse is generated by multiplying the estimated hemodynamic response **H** with the stimulus convolution matrix **S**. The amount of variance in the original timecourse which is accounted for by this estimate, r^2, is then

$$r^2 = 1 - \frac{variance(residual)}{variance(original)} \tag{6.1}$$

where the residual was calculated as the difference between the estimated time course (based on the least-squares solution) and the original time course.

To estimate the haemodynamic lag from the event-related data, the measured fMRI responses in ROI's defined for each digit from the phase measured in the travelling wave experiment were fitted using the model of the haemodynamic response function (HRF) corresponding to the difference of two gamma functions [29, 30]:

$$H(t) = \left(\frac{t}{d_1}\right)^{a_1} e^{-\frac{t-d_1}{b_1}} - c\left(\frac{t}{d_2}\right)^{a_2} e^{-\frac{t-d_2}{b_2}} \tag{6.2}$$

where $d_i = a_i b_i$. The time-to-peak depends on the parameters a_1 and a_2 of the Frinston HRF function (a_1 controls the timing of the early positive-going lobe, a_2 controls the undershoot). Simulations of the effect of changing parameter a_1 (with $a_2=2a_1$) on the time to peak of the Frinston function are shown in Fig. 6.5.

The best-fit parameters were estimated by non-linear least squares fitting and the time-to-peak of the fitted haemodynamic response was then determined numerically as an estimate for the haemodynamic delay.

6.3.6 Traveling wave data analysis

Standard Fourier-based analysis methods [16] were applied voxel-by-voxel to generate somatotopic maps. Time series data were analyzed voxel-by-voxel and the following were computed: (1) the coherence between the time series and the best-fitting sinusoid at the 0.04167 Hz stimulus repetition frequency, (2) the phase at that frequency and (3) the amplitude of the best-fitting sinusoid. The coherence measures signal-to-noise [15, 16], taking a value near 1 when the fMRI signal modulation at the stimulus/cue period is large relative to the noise (at the other frequency components) and a value near 0 when there is no signal modulation or when the signal is small compared with noise. The phase measures the temporal delay of the fMRI signal with respect to the onset of the stimulus cycle and for this paradigm, reflects the spatial location of the stimulus (which digit) on the hand. A somatotopic map should therefore be visible on the cortical surface as a smooth progression of early to late phase values, corresponding to the different digits of the hand.

The time series data for the 'forward' (from digit 1 to 5) and 'backward' (from digit 5 to 1) stimulus sequences were combined using a standard approach [15, 31] (Fig. 6.3.A,B) to remove the effect of the haemodynamic delay in visualizing the somatotopic maps. Both the 'forward' and 'backward' scans were time-shifted (advanced by 2 TRs), to approximately cancel any residual haemodynamic lag at each voxel, the 'backward' scans were then time

reversed, and finally the 'forward' and transformed 'backward' scans were averaged. This process is illustrated in Fig. 6.6. The resulting mean time series at each voxel in the average data (and its associated phase value) therefore approximately reflected the timing of the forward ordering scans, in which digits were stimulated sequentially from thumb (digit 1) to little finger (digit 5). We then subdivided the range of phase values in steps of $2\pi/5$ corresponding to the somatotopic representations of digits 1 to 5.

To incorporate information about the local spatial support of statistically significant responses, threshold-free cluster enhancement (TFCE)[32] was applied to the coherence map (H=2, E=0.5, neighbourhood connectivity 6) and voxels in the top 1 percentile of the resulting image were considered for further analysis. Regions-of-interests (ROI) containing voxels included by these criteria were then interrogated for the fMRI timeseries, response (Fourier) amplitude, and related statistics for the different scans.

To estimate the haemodynamic lag from the travelling wave data, the timecourses of the average 'forward' and time-reversed 'backward' scans (to which no time shift had been applied) were compared in detail. Example data showing the relative phase values of the "forward" and time-reversed "backward" scans for small regions of interest (ROI) corresponding to individual digits (as classified from the phase map) are shown in Fig. 6.13. If we assume that after time-reversal of the "backward" scans the time delay of the response is equal, but opposite in sign to that in the forward scans, then the difference in phase of the best-fitting sinusoids to the two time-courses corresponds to twice the haemodynamic delay. However, this method of estimating haemodynamic lag assumes that the fMRI timeseries can be approximated well by a sinusoidal function whose period equals the length of the cycle (24 s) and that the haemodynamic delay and phase of the fitted sinusoidal response are tightly coupled. We therefore performed a simulation to assess any potential bias in the estimation of the haemodynamic lag from travelling wave data.

Simulation

Travelling wave signals were simulated using the known stimulus timing and a model of the haemodynamic response function, *H(t)* as described in Eq. 6.2 [29] for a range of HRF time-to-peak (TTP) values by varying parameter a_1 from 3-9 while other parameters were fixed at: $a_2=2a_1$, $b_1=0.9$ s, $b_2=0.9$ s, c=0.35 [30]. The synthetic data were then analyzed using the Fourier-method applied to the data (as described above) and the corresponding haemodynamic lag was estimated. Based on this analysis, we calculated a correction factor to allow comparison of haemodynamic delays measured in the traveling wave and event-related data.

Figure 6.7 shows the steps of the simulation. The fMRI time series is formed from the asymmetric gamma variate haemodynamic response function Eq. 6.2 convolved with the stimulus input function, as shown by the black line for the 'forward' (A) and 'backward' (B) scans of digit 1. The simulated fMRI response for the 'backward ' scan is time reversed (Fig. 6.7.C) and the responses for the 'forward' and time-reversed 'backward' scans are then fitted to a sinusoid (period 24 s, red line). The sinusoidal waveforms show an earlier time-to-peak compared to the simulated fMRI response from the Frinston model. Assuming the haemodynamic lag is equal and opposite for the 'forward' and time-reversed 'backward' scans, the haemodynamic lag can then be estimated as half the difference between the delays found for the two conditions (red lines in Fig. 6.7.A and 6.7.C). We took care to account of an additional delay of 1.8 s (for the time reversed data), which was included in our stimulus design to provide temporal separation of the stimulation of different digits (See page 162 and Fig. 6.6).

Figure 6.8.B shows the haemodynamic lag in the travelling wave data (as estimated from the phase difference in the sinusoidal fits, Fig. 6.7A,C) plotted as a function of the 'true' lag of the haemodynamic response function (HRF) used in the simulations (cf. Fig. 6.8.A). For our choice of parameters, the haemodynamic lag from the travelling wave analysis (y) is related to the time
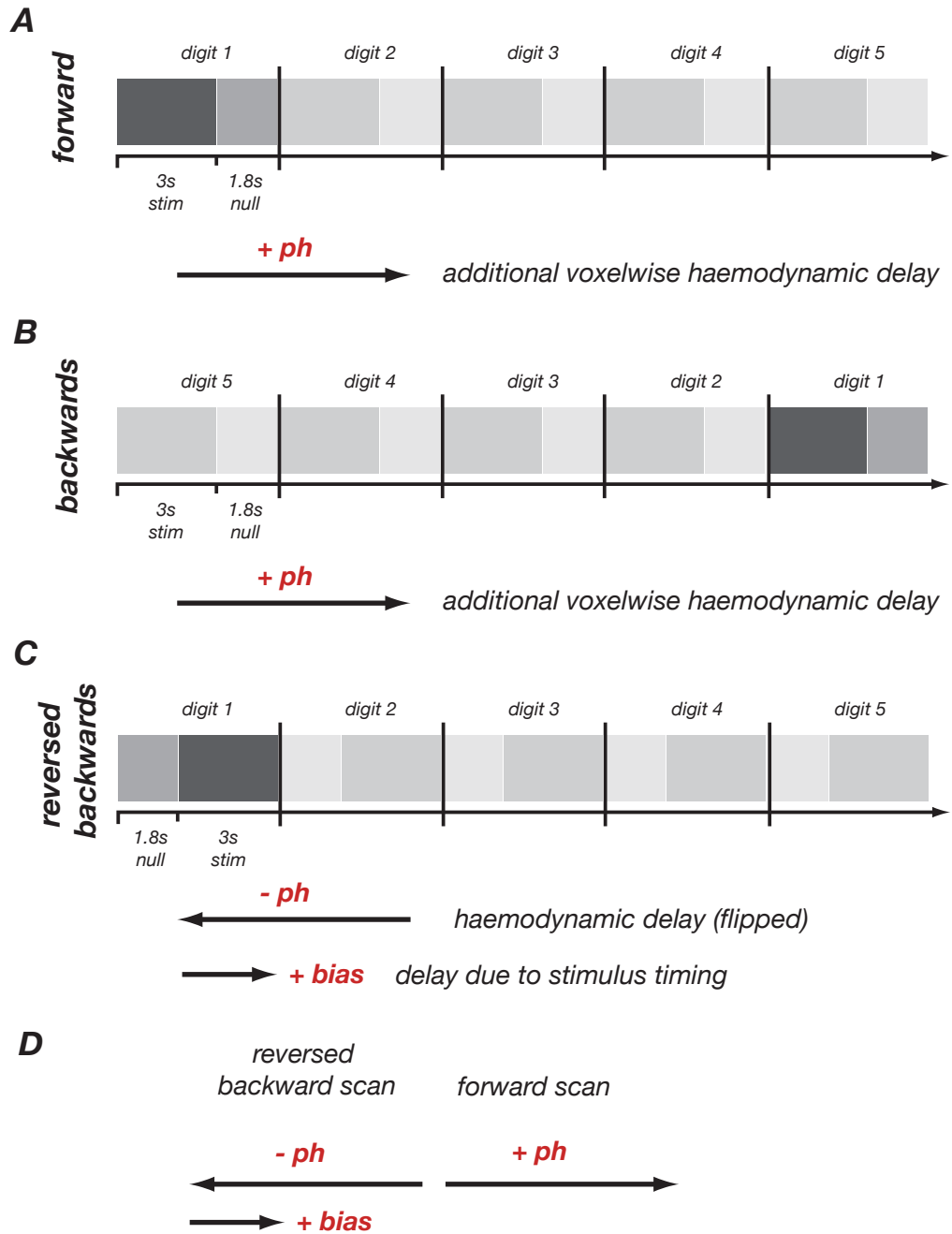
Figure 6.6: Travelling wave analysis. (A) Timing diagram for the forward sequence. Highlighted digit 1 stimulation. Additional arrow indicates delay (+ph). (B) Timing diagram for the backward sequence. (C) When the backward sequence is time-reversed, the inherent haemodynamic delay receives an opposite sign. The asymmetry in the stimulation paradigm means that the sequence is, however, delayed by a bias of 1.8 s. (D) Illustrates that the difference between the two phase values for a given ROI is equivalent to twice the haemodynamic delay minus the bias.
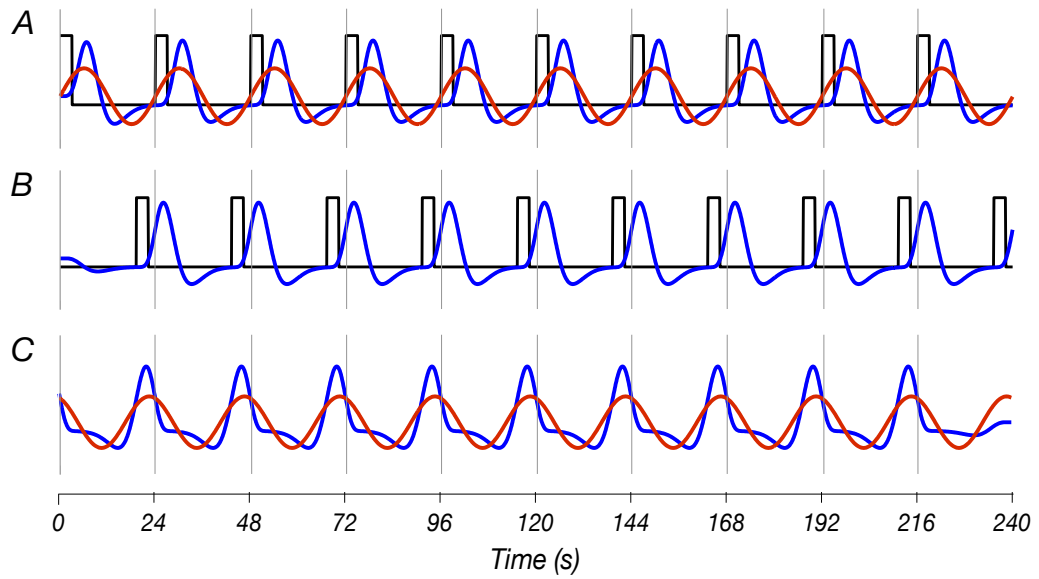
Figure 6.7: (A) The stimulus input function of the 'forward' scan of digit 1 (black line) convolved with HRF (with a_1=6) to simulate the expected fMRI response (blue line). This simulated waveform (blue line) is then fitted to a sinusoidal wave of period 24 s (red line). (B) The stimulus input function of the 'backward' scan for digit one (black line), and the convolution with the same Frinston function to simulate the expected 'backward' fMRI time course (blue line).(C) Time reversed 'backward' scan for digit 1 (blue line) and fitted sinusoidal waveform (red line).
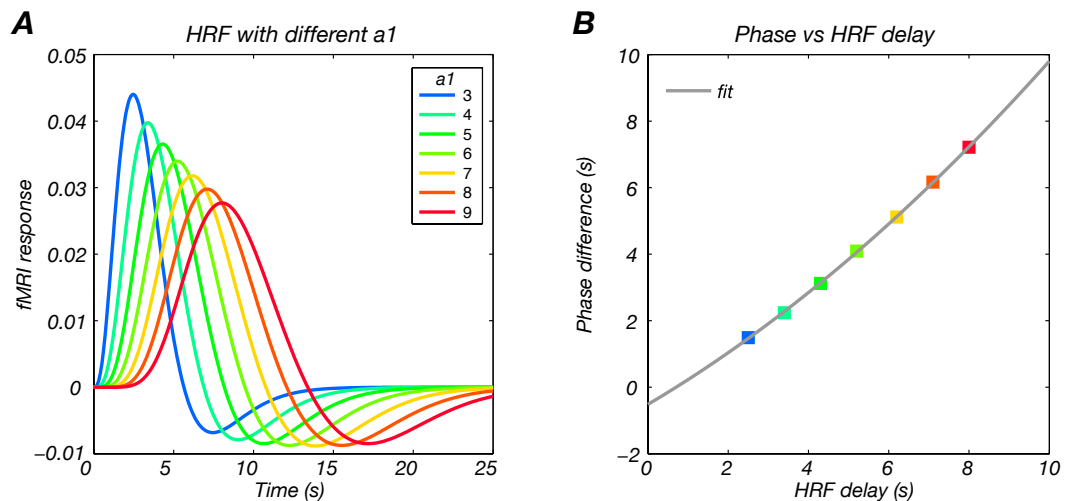

Figure 6.8: (A) Simulated gamma variate functions with a_1 of 3 - 9 to represent the range of delays found in the brain. (B) Simulated haemodynamic lag (phase difference) as determined from the travelling wave analysis versus the true haemodynamic lag from the simulated gamma variate functions in (A).

to peak values of the simulated HRF (x) by a parabolic relationship . An underestimation of the haemodynamic lag was found for the travelling wave data ($y = 0.03x^2 + 0.71x - 0.51$). We used this relationship to correct the haemodynamic delay estimated from the travelling wave analysis to give the results in Table 6.3.

6.3.7 Cortical segmentation and flattening

The inversion recovery data were used to subdivide the EP images into areas of white matter, grey matter, and CSF (Fig. 6.11) to aid classification of the image intensity in the mean EPI $T_2^\star$-weighted data to different tissue types (n=4 clusters in k-means). The specificity of the activity to the cortical grey matter was further examined by plotting the coherence and modulation amplitude against the intensity in the mean EPI $T_2^\star$-weighted image intensity for each voxel in the functional ROI obtained in the travelling wave experiment. The approximate ranges of $T_2^\star$ intensity values for the different tissue types (grey bars in Fig. 6.11) reflect the mean $\pm$ one standard error of the intensity values obtained from the four clusters in the k-means segmentation. To display activation on a cortically flattened surface, an image registration algorithm [22] was first used to align the in-plane MPRAGE anatomical images acquired at the end of each functional session to the co-registered fMRI data. These high-resolution MPRAGE images acquired at 7 T were then registered to the whole head 3T MPRAGE data. The 3T MPRAGE images were then used in a subset of subjects to computationally flatten the grey matter, with functional areas restricted to grey matter voxels, to create flattened visualizations of the cortical activity. Cortical segmentations were obtained based on methods outlined in detail in Chapter 4. It is important to note that data were projected onto surface representations as a final visualization step only. For the flat maps shown in (Results, Fig. 6.14), it was ascertained that the grey/white matter segmentations of the MPRAGE images for each particular subject were in good agreement with the EPI data (see also Section 4.3.3).
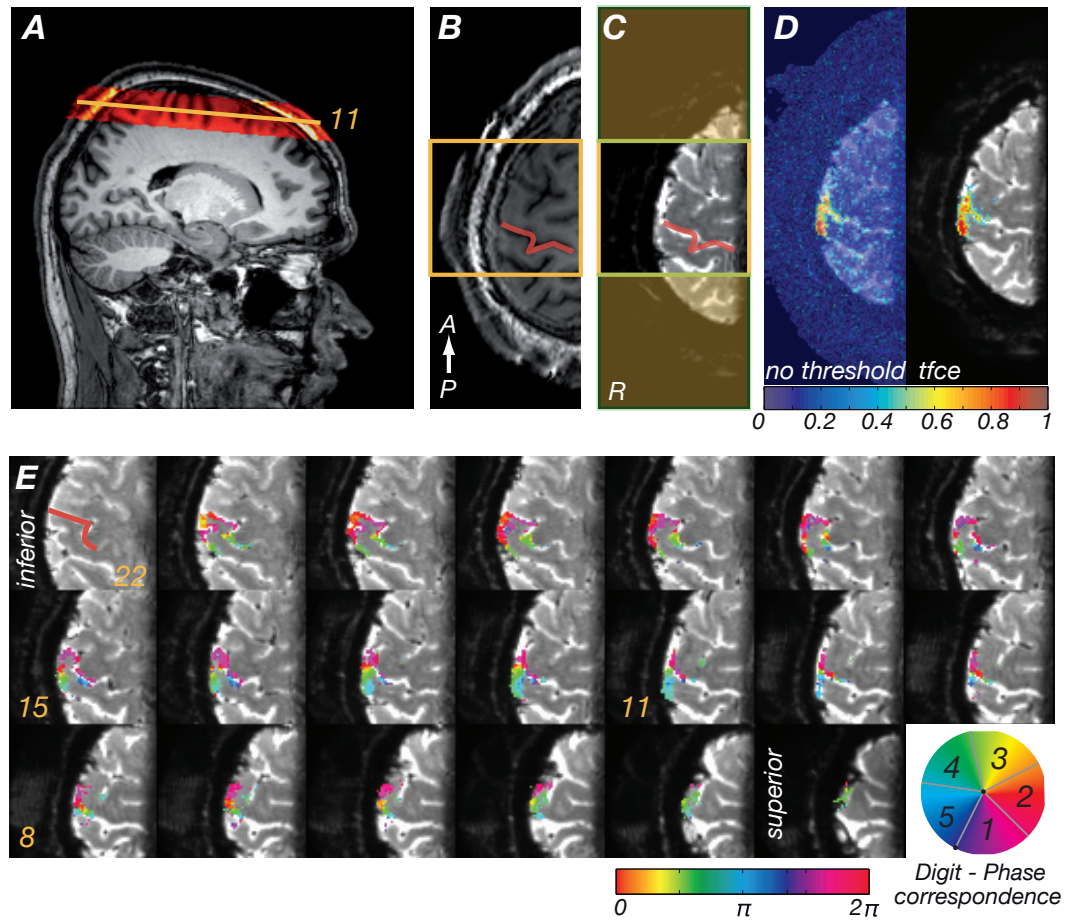
Figure 6.9: (A) Location of the imaging stack and single slice of the (B) MPRAGE image collected in the same location as (C) $T_2^\star$ EPI data. The red line indicates the location of central sulcus, the green box the cropping used in E. (D) Coherence map superimposed on mean EPI image with (left) no thresholding applied and (right) threshold-free cluster enhancement, TFCE. (E) Phase map (from the average of 6 scans) thresholded by a TFCE map (D) superimposed on mean $T_2^\star$-weighted EPI data. Axial slices are numbered from most superior (1) to most inferior (22).

6.4 Results

Analysis of the travelling wave data showed that the signal from a region of grey matter extending along the posterior bank of the central sulcus was significantly modulated at a frequency corresponding to the 24 s period of stimulation in all subjects. Figure 6.9 shows data from a representative subject (Subject 4) with statistical maps superimposed on the mean $T_2^\star$- weighted images from the functional scan. One scan (10 stimulus cycles, 100 volumes)

was sufficient to form statistical maps, but to improve the SNR, responses were averaged over up to 6 scans before performing the standard Fourier analysis. The resulting coherence map (unthresholded) for one subject (average of 6 scans) is shown as a semi-transparent overlay in Fig. 6.9.D (left) and following TFCE correction (right). The coherence map indicates that some voxels show nearly perfectly sinusoidal signal modulation (coherence values close to 1.0). The temporal delay, or phase, of the measured periodic response at a given point in the brain was then used to classify voxels corresponding to each stimulated digit. The resulting phase/'digit' map (Fig. 6.9.E) showed consistency in the inferior-superior direction (across slices in the acquired stack) and an orderly mapping of phase values along the post-central gyrus. Smaller phase delays, corresponding to digits 1 and 2 were present more laterally and inferiorly, whilst larger phase delays, corresponding to digits 3, 4, and 5, more medially and superiorly. For this subject the TFCE corrected ROI encompassing all digits contained 1998 voxels. The mean coherence value was 0.53 (std 0.13, min-to-max range 0.35-0.94) and the mean fMRI response amplitude across all voxels was 3.28 % (std 3.2, range 0.72-21.38). Figure 6.10 shows corresponding phase maps for all five subjects scanned; for each subject a somatotopic map is clearly visible.

Table 6.1 lists the average spatial extent of each individual digit representation and the standard deviation of these values. The latter highlights the variability in sulcal size and position across subjects. A high degree of localization of areas of activation to cortical grey matter is evident from the images,

	D1 $m\pm std$	D2 $m\pm std$	D3 $m\pm std$	D4 $m\pm std$	D5 $m\pm std$
M-L	26.2±5.9	23.2±4.0	20.4±5.0	20.6±4.4	15.2±4.4
A-P	26.2±5.9	23.2±4.0	20.4±5.0	20.6±4.4	15.2±4.4
F-H	18.4±0.9	18.0±0.9	16.6±1.9	16.6±2.6	15.2±2.9
voxels	313±140	373±226	141±47	225±76	120±60

Table 6.1: Maximum spatial spread (mm) and number of voxels of digit representations in travelling wave map.
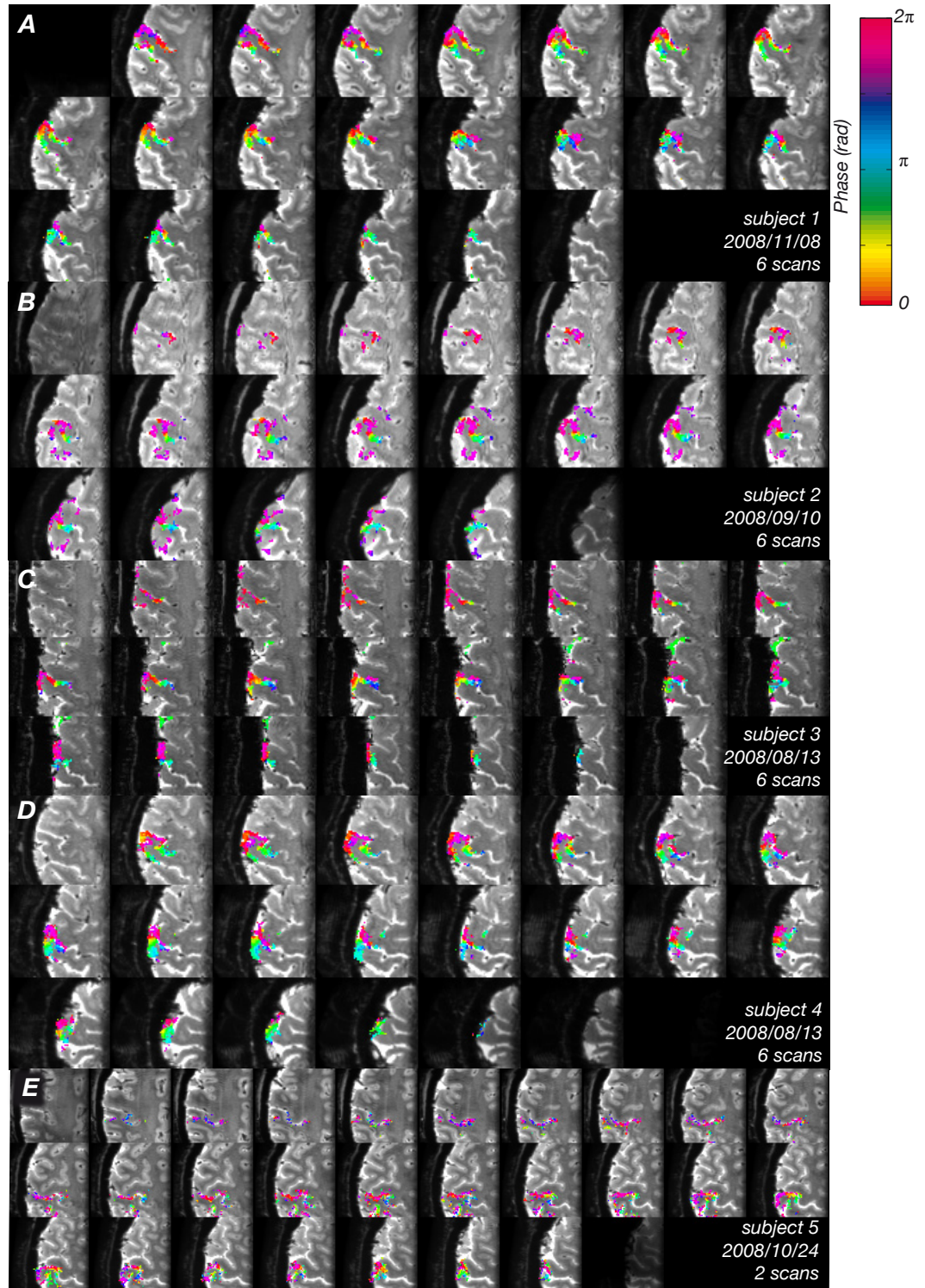
Figure 6.10: Statistical maps (average of 6 scans) for each subject superimposed on mean $T_2^\star$ weighted EPI data, equivalent to Fig. 6.9.E. Colors indicate the phase values from travelling wave paradigm. Statistical maps are thresholded by a TFCE map.
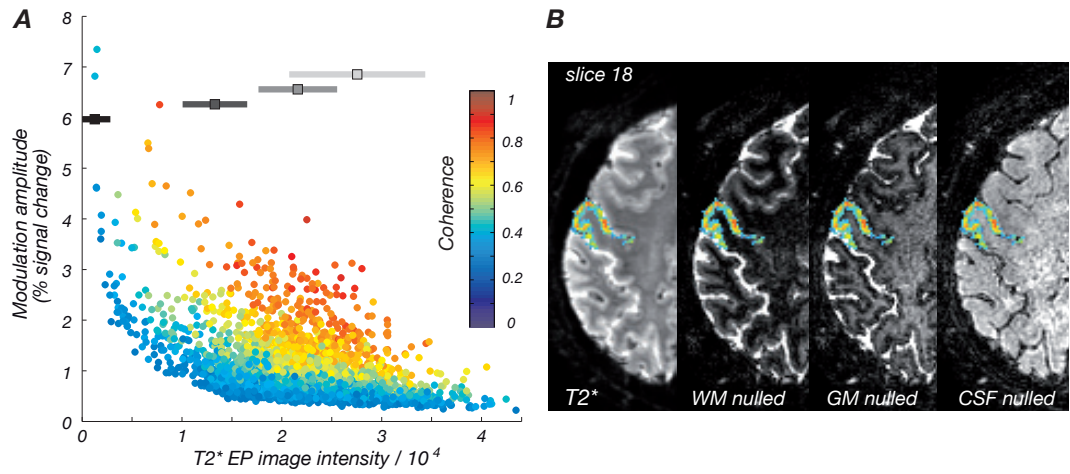
Figure 6.11: (A) Histogram of fMRI response modulation in travelling wave experiment as a function of image intensity in mean $T_2^\star$-weighted EP image. Colours represent coherence with best fitting sinusoid. Grey bands represent the approximate range of intensity to tissue type as classified from the inversion reccovery images. (B) Map of coherence values superimposed on the mean EPI $T_2^\star$ image and inversion recovery images in which grey matter, white matter, and cerebrospinal fluid are selectively nulled.

and this is confirmed by Fig. 6.11.A which shows a scatter plot (for Subject 1) correlating the fMRI response modulation for the travelling wave data as a function of the mean $T_2^\star$- weighted image intensity for different coherence levels. The map of coherence values is also shown on the average $T_2^\star$ image and inversion recovery data (Fig. 6.11.B).

The majority of voxels in the ROI fall in the mid-range of the $T_2^\star$ signal intensities; the voxels with the highest coherence values have $T_2^\star$-weighted image intensities that correspond to grey matter (as determined by clustering of the inversion-recovery data). There is a small group of voxels with high fMRI modulation amplitude, but low statistical coherence and image intensity; these are likely to arise from venous contributions.

For comparison, Table 6.2 shows the distribution of coherence, fMRI response percentage singnal change and contrast-to-noise ratio across the functional ROIs obtained in each subject. The fMRI responses in individual voxels were large (with maximum values of the order of 10-24% peak-to-peak modulation) and robust, with contrast-to-noise ratios of up to 40, but response

Subject	Coherence Value *mean±std (min-max)*	% Signal Change *mean±std (min-max)*	CNR *mean±std*
1	0.57±0.13 (0.27-0.89)	2.62±1.34 (0.68-12.52)	41.7±5.4
2	0.45±0.11 (0.39-0.89)	3.54±1.52 (1.20-15.56)	32.5±6.3
3	0.51±0.12 (0.35-0.89)	2.80±1.38 (0.60-11.92)	36.7±7.0
4	0.53±0.13 (0.35-0.94)	3.28±3.20 (0.72-21.38)	39.5±11.6
5	0.39±0.08 (0.30-0.67)	4.18±2.04 (1.58-24.58)	19.4±3.4

Table 6.2: Details of fMRI response for travelling wave paradigm.

strengths varied across voxels as well as subjects.

The time courses measured in the travelling wave experiments showed high consistency across repeats and locations on the somatotopic map. Figure 6.12 shows the fMRI responses from the travelling wave paradigm (for subject 4) for two small regions of interest: ROI1 (51 mm^3) in slice 11 and ROI2 (51 mm^3) in slice 9, along the posterior bank of the central sulcus for two sets of 3 scan repeats (3 'forward' (f) scans; 3 'backward' (b) scans) which were acquired in interleaved order (f, b, f, b,...). The presence of the large peak at 10 cycles/scan in the Fourier spectrum clearly indicates that the response is dominated by the effects of the somatosensory stimulation. Contributions to the response from frequency components other than the first harmonic are negligible (Fig. 6.12 C,F). Figure 6.13 shows the relative phase values of the 'forward' and 'backward' scans for these two small regions of interest. The mean phase, coherence and response amplitude value for ROI1/2 were 2.8/5.26 rad 0.69/0.57 and 6.68/3.98 % respectively. Figure 6.13 shows the relative phase values of the 'forward' and time-reversed 'backward' scans for these two small regions of interest.

Figure 6.14 compares the the coherence map from the travelling wave analysis (A,B,C) with the r^2 map calculated from the event-related design (D,E,F) on a flattened surface at three different cortical depths (for Subject 1). Similar activation patterns are seen in the primary somatosensory cortex for both the travelling wave and event-related paradigms. The mean time courses of event related data extracted from ROIs, which were independently defined by
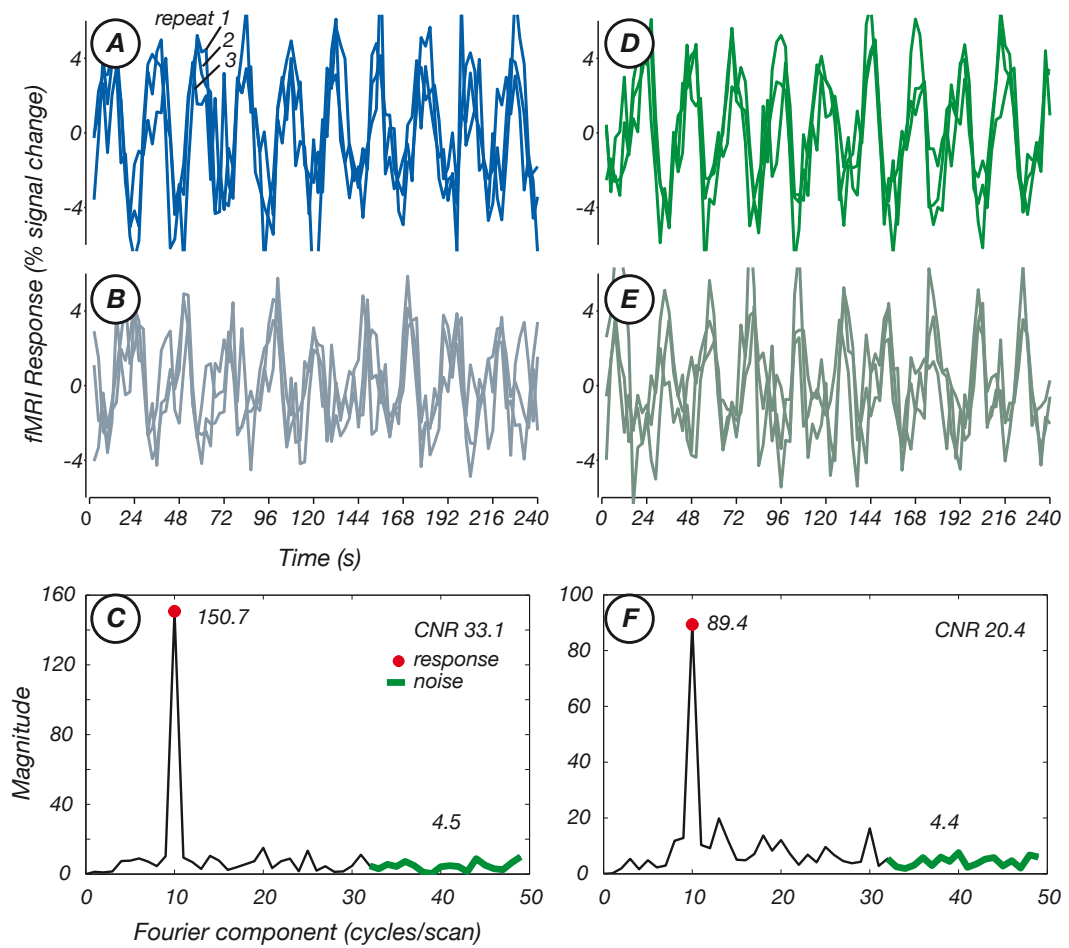
Figure 6.12: Time course plots from two small regions of interest (columns) for two different stimulus conditions (rows). (A) Each trace, mean fMRI response in ROI1 for each of three scans with a 'forward' stimulus (advancing from digit 1 to 5). (B) fMRI responses in ROI1 for 'backward' sequence. (C) Amplitude spectrum of average time course across all scans in ROI1. Red circle, magnitude at stimulus alternation frequency. Thick green line, high-frequency components used to calculate contrast-to-noise ratio (CNR). (D,E, F) corresponding data for ROI2.
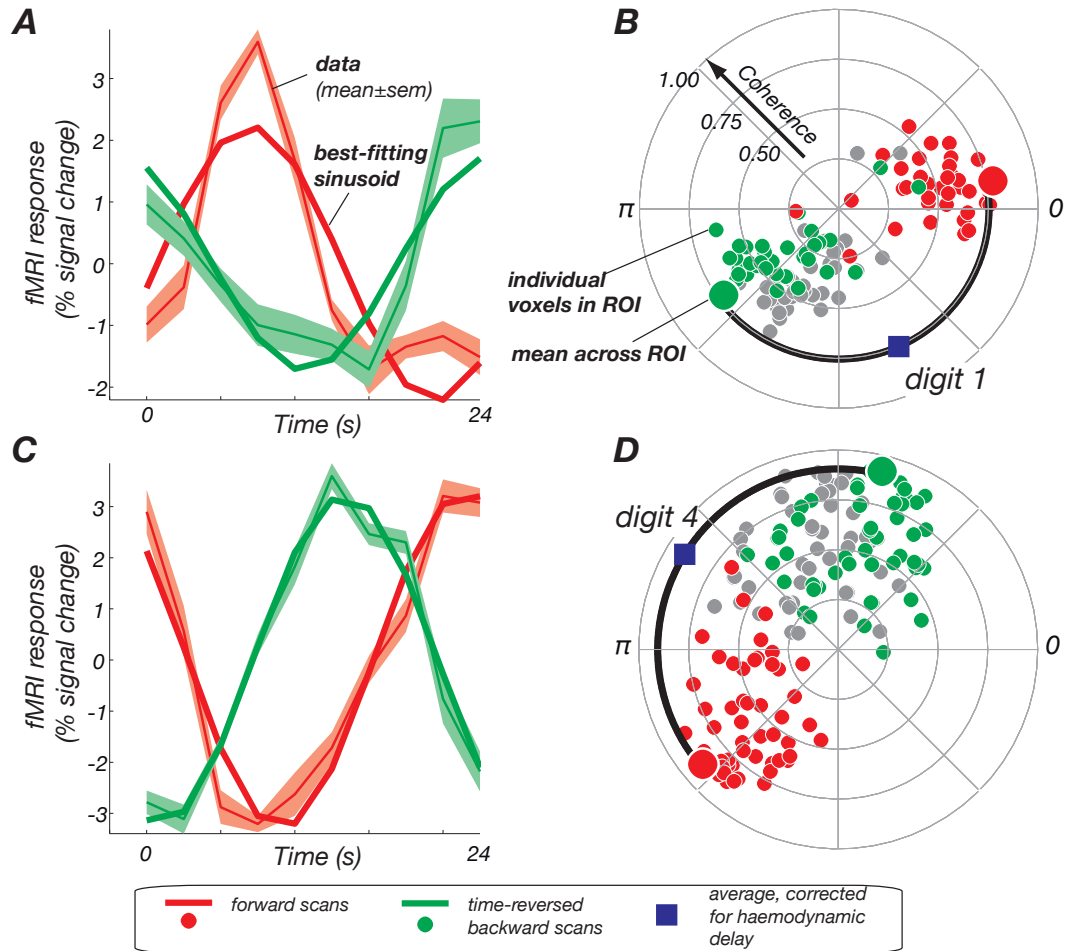
Figure 6.13: (A) The average 'forward' (red) and and time reversed 'backward' (green) fMRI time series and their corresponding sinusoidal fits for digit 1. (B) A polar plot of the phase of the sinusoidal fit for each voxel (for ROI1 - as described in Fig. 6.12) in the ROI (small circles) for 'forward' (red) and time reversed 'backwards' (grey) which is then corrected by a 1.8 s delay (green). The large circles show the 'forward' and time-corrected reversed 'backwards' phases from the best-fitting sinusoid to the mean signal from the ROI. (C and D) show corresponding data for ROI2 (digit 4).
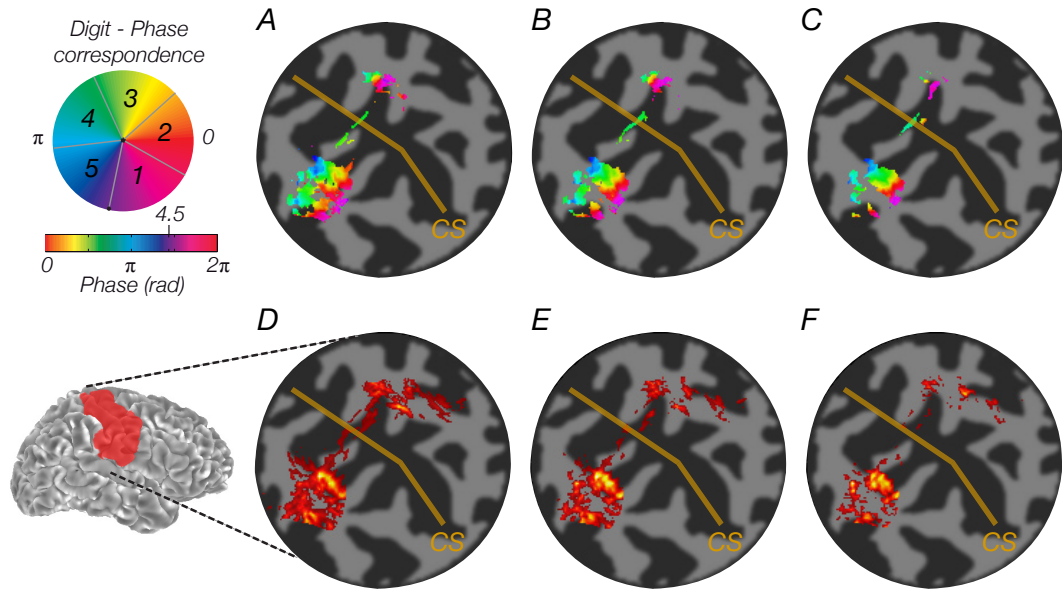
Figure 6.14: Phase map from the travelling wave analysis superimposed onto flattened representation of the cortex in a layer at a fractional cortical depth of (A) 1, (B) 0.8 and (c) 0.6 (where 0 corresponds to the boundary with white matter and 1 to the pial boundary). (D,E,F) Coherence map from the r^2 map from the event-related design for corresponding layers.

the somatotopic mapping are shown in Fig. 6.15.A. Note that the estimated haemodynamic lag from the event-related data does not strongly depend on a particular choice of r^2 threshold (Table 6.3). The solid lines represent the corresponding fits to the haemodynamic response function [30]. Figure 6.15.B indicates that voxels with the highest r^2 values in the event-related data also tend to give most significant responses in the travelling wave experiment. For two of the subjects we compared the average haemodynamic delay estimated from the event-related data to that obtained from the travelling wave analysis (Table 6.3). The degree of approximation fitting a sinusoid to the measured fMRI time-series and the effect of time-reversing the fitted sinusoidal signal was explored in Section 5.3.5. Both methods yield estimates of haemodynamic delay that are comparable, but the delay from the event related paradigm can be seen to be significantly longer.
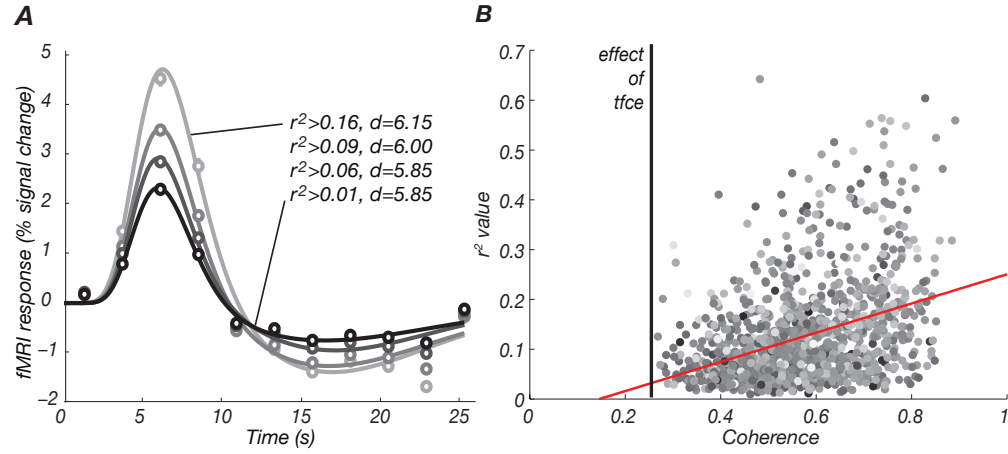
Figure 6.15: (A) Mean event-related fMRI responses in S1. The mean event-related time course for voxels in the functional ROI defined in the travelling wave experiment (symbols) and corresponding fits with difference of gamma model to the haemodynamic response function (solid line) are shown at four different r^2 thresholds. d indicates the haemodynamic lag of each plot. (B) Scatter plot of r^2 values (obtained in the event-related experiment) vs coherence values (obtained from the travelling wave experiment) in ROI.

	Haemodynamic delay (s)				
Subject	Travelling wave	Event-related estimates, ($mean \pm std$)			
	$mean \pm std$	ROIA	ROIB	ROIC	ROID
1	4.33±0.32	6.22±0.23	6.15±0.23	5.95±0.23	5.97±0.22
2	5.08±0.04	6.85±0.50	6.82±0.54	6.74±0.44	6.80±0.54

Table 6.3: Haemodynamic delay of travelling wave and event-related data. ROIs were defined for each digit from the traveling travelling wave statistical map. The table lists the mean and standard deviation across digits. For the event-related data, the haemodynamic delay is estimated for each digit ROI at different r^2 thresholds (ROI A, B C and D threshold levels chosen to include voxels with r^2 values above 0, 25, 50 and 75% of the r^2 distribution).

6.5 Discussion

These results demonstrate that robust maps of the representation of the fingers in human somatosensory cortex can be obtained with 1 mm isotropic resolution at 7 T using a travelling wave paradigm and focal vibrotactile stimulation applied at 30 Hz to the fingertips. The experimental design and analysis methodology used in this study, have been extensively used for retinotopic mapping [15, 16, 17], but this is the first clear demonstration of the method being used to obtain somatotopic maps. An orderly progression of phase values was found along the posterior aspect of the central sulcus corresponding to a map representing digits 1 to 5 in a location thought to contain primary somatosensory cortex (S1). The representation of D1 (thumb) was most inferior and lateral. The representations of D2-D5 were increasingly superior and medial (Fig. 6.9 and 6.10). Areas of significant signal modulation were confined to the posterior aspect of the central sulcus. Unthresholded statistical maps confirm that the pattern of activation is almost exclusively on the post-central side of the sulcus. This is in contrast to some previous reports that have found that somatosensory representations extend further anteriorly to the pre-central aspect of the central sulcus [33].

The fMRI responses in individual voxels were large (up to 10-24 % peak-to-peak modulation, Table 6.2) and robust, with contrast-to-noise ratios of up to 40. This can be compared with signal modulations of 3 - 4 % for most sensory fMRI studies at 3 T [5, 14] using 3 mm isotropic voxels. This large signal modulation at 7 T is expected if a linear increase in BOLD signal with field strength can be realized [34, 35]. Here, the increased CNR at ultra-high field has been exploited to achieve high spatial resolution, reducing partial voluming of activated tissue with non-activated grey matter and white matter/CSF. Potentially this can lead to larger and more consistent haemodynamic response modulations arising from cortical grey matter. In addition, 7 T offers intrinsic improvements in spatial specificity for GE BOLD data compared to lower field strengths due to the supralinear increase in CNR in the microvasculature

[34, 36] and suppression of intravascular signal in draining veins distant from the site of neuronal activity, veins due to shortening of venous blood T_2 (~ 12 ms) [34, 35, 37, 38, 39].

Another factor which may have improved spatial specificity in this experiment compared to previous studies is the paradigm design. First, tactile stimuli were delivered with a piezoelectric device at a stimulation frequency chosen to maximize the response in rapidly adapting somatosensory receptors, whose receptive fields are known to densely tile the glabrous skin on the digits [40]. Second, the travelling wave paradigm [15] is a form of differential paradigm and is likely to suppress non-specific activation common to all digits, such as the BOLD signal in large veins draining from tissue spanning multiple digit representations in the postcentral gyrus, thus improving digit specific mapping. We compared the extent of activation maps for the travelling wave and event-related paradigms and found these to be similar, but the estimates of the haemodynamic lag were shorter for the travelling wave paradigm (Table 6.3). The estimated haemodynamic delay is only slightly affected by the choice of thresholds. The greater lag observed in the event-related estimates may indicate an increased venous contribution [41, 42] that is reduced by using a travelling wave paradigm. In addition, in this study care was taken to retain spatial specificity of the cortical representation of the digits by minimizing data preprocessing to prevent unnecessary blurring.

The spatial resolution of earlier functional MRI measurements (typically with voxel volumes of mm^3 [3, 4, 43] is unfavourable with respect to the size of the somatotopic map. In our high resolution (1 mm isotropic) functional measurements the extent of the sensory maps spanning D1 to D5 was greater in the medial-lateral than anterior-posterior or foot-head directions (Table 6.1). Digits 1 and 2 occupied the largest extent within the somatotopic map, whilst digit 5 has the smallest representation (Table 6.1). Note that the activation lies along the tortuous postcentral gyrus (Fig. 6.14) and with 1 mm isotropic resolution this leads to a band which is approximately 29 voxels in length in the post-central gyrus for D1-D5 mapping. The failure to identify clear soma-

totopic maps in previous studies may have been due to the limits imposed by sampling a relatively small spatial map with comparatively coarse resolution. For example use of 3 mm isotropic resolution would yield somatotopic maps containing at best a third of the number of voxels measured in our study (assuming the best 1D tiling); at worst $1/3^3$ taking into account volume. Even in those previous studies, where high spatial resolution was used, the reduced contrast-to-noise necessarily reduced statistical power [7]. In addition in several previous studies, results were averaged across-subjects, often registered into Talairach/MNI space. This causes blurring, but also doesn't ensure exact alignment of anatomical structures across subjects, especially when their spatial extent is relatively small [12].

Previous studies, some based on relatively coarse resolution measurements, have emphasized the division of significant clusters of fMRI responses in S1 into four anatomical subdivisions (areas 1, 2, 3a and 3b) [8, 33, 43], known to exist from anatomy, histology, and human/non-human single-unit physiology. These areas cannot currently be accurately identified using MRI in vivo, but can be roughly assigned based on anatomical MR images: area 1 is located at the crown of the postcentral gyrus, area 2 in the postcentral sulcus, area 3a in the fundus of the central sulcus and area 3b at the rostral bank of the postcentral gyrus.

Microelectrode mapping studies in primates [44] have suggested that multiple representations of the body arise within primary somatosensory cortex with two complete body surface representations occupying cortical fields 3b and 1. Additionally it has been suggested that area 2 contains an orderly representation of predominantly deep body tissues whilst area 3a may constitute a fourth representation. One study has compared functional data with areas defined using probabilistic cytoarchitectonic maps derived from post-mortem brains [45]. However, thresholding of statistical maps at a single significance value can lead to conclusions about foci of activation corresponding to distinct anatomical subregions (the iceberg effect) which in fact do not exist. Additionally, the spatial information in the probabilistic atlases currently does

not capture the anatomical pattern of sulci and gyri, which makes accurate assignment to Brodmann areas difficult.

In this study, we found statistical maps with spatially contiguous representations of all digits. Stimulation of the fingertips mainly activated the rostral bank of the postcentral gyrus (defined operationally as area 3b), in agreement with a previous study using piezoelectric stimulation where 'apparent' area 3b has shown some evidence of somatotopic organization [7]. However, the spatial extent of the maps reported in [7] was much smaller than our data, suggesting that previous, functionally defined maps, have greatly underestimated the cortical representation of the fingers. Given the relatively low indentation amplitude of our stimuli to the surface of the fingers, we did not expect to see responses dominated by neurons thought to be restricted to areas 3a and 2.

Although the pattern of the somatotopic maps is clearly visible in the axial planes in which our EPI data were acquired, with the direction of changing phase values in the map running along the central sulcus, surface rendering can provide a clearer sense of the spatial layout of topographic maps. Therefore, to ease visualization of the two-dimensional digit topography, the statistical maps were rendered on inflated and flattened representations of the cortical surface (Fig. 6.15). For such visualization, accurate alignment between functional data and anatomical images is essential.

Despite the relatively small residual geometric distortion between EP and anatomical images, problems in assigning responses to different sides of the central sulcus may still result, although these can to some extent be overcome by image processing, and careful segmentation and cortical unfolding (e.g. any voxel whose activation is partial-volumed over voxels, or voxels where there is simultaneous activation on both sides of the sulcus, could be excluded from further analysis). Additionally, small amounts of blurring due to spatial spreading of the haemodynamic response or caused by resampling in the motion correction step can aggravate such effects. To enable more detailed surface-based analysis, segmentations have to be based on anatomical images with higher spatial resolution (e.g. 0.5 mm isotropic voxels) and future studies will assess

the feasibility of using whole head anatomical MPRAGE data acquired at 7T in conjunction with normalization methods that can correct the non-uniform signal intensity [46].

It remains to be seen whether a further reduction in image voxel size below 1 mm can lead to significant improvements in the achievable resolution in cortical maps. Artifacts due to subject motion, respiration and the cardiac cycle may dominate at such small voxel sizes. In this study, subjects' heads were stabilized using customized MR compatible vacuum pillows and foam padding, and realignment results showed that subjects could maintain a stable head position within a fraction of a mm for several minutes. Second, the width of the cortical point spread function (PSF) of the gradient-echo signal, which has been shown to be of the order of 2 mm at 7T [47] (for discussion, see also Logothetis[48]), may ultimately be limiting.

The fMRI responses in this study are based on gradient-echo (GE) BOLD. Degradation of spatial specificity in the functional maps may arise from contributions from large vessels to the BOLD response leading to false activation caused by large draining veins at sites distant from activity. However, undesired extravascular effects can also persist in the small venules and veins immediately following the capillary bed. The PSF can be reduced for spin echo (SE) BOLD acquisition, where the large vessel contributions are substantially reduced due to refocusing of the static dephasing induced by field inhomogeneities around these vessels. Studies in the visual cortex have demonstrated improvements in specificity using SE BOLD [36, 38, 49] and this will be an area of future research for somatotopic mapping. However, SE BOLD has lower sensitivity than GE BOLD, and therefore the implementation of somatotopic mapping will require an increased number of averages, particularly as somatosensory stimulation produces relatively weak fMRI responses compared to those observed in for example, the visual cortex.

Bibliography

[1] W. Penfield and E. Boldrey. Somatic motor and sensory representations in the cerebral cortex of man as studied by electrical stimulation. *Brain*, **60**, 389–443, (1936).

[2] P. A. Gelnar, B. R. Krauss, N. M. Szeverenyi, and A. V. Apkarian. Fingertip representation in the human somatosensory cortex: an fMRI study. *Neuroimage*, **7**(4 Pt 1), 261–283, (1998).

[3] R. Kurth, K. Villringer, G. Curio, K. J. Wolf, T. Krause, J. Repenthin, J. Schwiemann, M. Deuchert, and A. Villringer. fMRI shows multiple somatotopic digit representations in human primary somatosensory cortex. *Neuroreport*, **11**(7), 1487–1491, (2000).

[4] J. A. Maldjian, A. Gottschalk, R. S. Patel, J. A. Detre, and D. C. Alsop. The sensory somatotopic map of the human hand demonstrated at 4 Tesla. *Neuroimage*, **10**(1), 55–62, (1999).

[5] S. T. Francis, E. F. Kelly, R. Bowtell, W. J. Dunseath, S. E. Folger, and F. McGlone. fMRI of the responses to vibratory stimulation of digit tips. *Neuroimage*, **11**(3), 188–202, (2000).

[6] R.-S. Huang and M. I. Sereno. Dodecapus: An MR-compatible system for somatosensory stimulation. *Neuroimage*, **34**(3), 1060–1073, (2007).

[7] R. Schweizer, D. Voit, and J. Frahm. Finger representations in human primary somatosensory cortex as revealed by high-resolution functional MRI of tactile stimulation. *Neuroimage*, **42**(1), 28–35, (2008).

[8] S. A. Overduin and P. Servos. Symmetric sensorimotor somatotopy. *PLOS ONE*, **3**(1), 1505, (2008).

[9] A. Weibull, H. Gustavsson, S. Mattsson, and J. Svensson. Investigation of spatial resolution, partial volume effects and smoothing in functional MRI using artificial 3D time series. *Neuroimage*, **41**(2), 346–353, (2008).

[10] S. Butterworth, S. Francis, E. Kelly, F. McGlone, R. Bowtell, and G. V. Sawle. Abnormal cortical sensory activation in dystonia: an fMRI study. *Mov Disord*, **18**(6), 673–682, (2003).

[11] A. Scouten, X. Papademetris, and R. T. Constable. Spatial resolution, signal-to-noise ratio, and smoothing in multi-subject functional MRI studies. *Neuroimage*, **30**(3), 787–793, (2006).

[12] B. Fischl and A. M. Dale. Measuring the thickness of the human cerebral cortex from magnetic resonance images. *Proc Natl Acad Sci U S A*, **97**(20), 11050–11055, (2000).

[13] C. Triantafyllou, R. D. Hoge, G. Krueger, C. J. Wiggins, A. Potthast, G. C. Wiggins, and L. L. Wald. Comparison of physiological noise at 1.5 T, 3 T and 7 T and optimization of fMRI acquisition parameters. *Neuroimage*, **26**(1), 243–250, (2005).

[14] C. Stippich, R. Hofmann, D. Kapfer, E. Hempel, S. Heiland, O. Jansen, and K. Sartor. Somatotopic mapping of the human primary somatosensory cortex by fully automated tactile stimulation using functional magnetic resonance imaging. *Neurosci Lett*, **277**(1), 25–28, (1999).

[15] S. A. Engel, G. H. Glover, and B. A. Wandell. Retinotopic organization in human visual cortex and the spatial precision of functional MRI. *Cereb Cortex*, **7**(2), 181–192, (1997).

[16] S. A. Engel, D. E. Rumelhart, B. A. Wandell, A. T. Lee, G. H. Glover, E. J. Chichilnisky, and M. N. Shadlen. fMRI of human visual cortex. *Nature*, **369**(6481), 525, (1994).

[17] B. A. Wandell, S. O. Dumoulin, and A. A. Brewer. Visual field maps in human cortex. *Neuron*, **56**(2), 366–383, (2007).

[18] S. A. Overduin and P. Servos. Distributed digit somatotopy in primary somatosensory cortex. *Neuroimage*, **23**(2), 462–472, (2004).

[19] J. L. Wilson, M. Jenkinson, I. de Araujo, M. L. Kringelbach, E. T. Rolls, and P. Jezzard. Fast, fully automated global and local magnetic field optimization for fMRI of the human brain. *Neuroimage*, **17**(2), 967–976, (2002).

[20] M. Poole and R. Bowtell. Volume parcellation for improved dynamic shimming. *MAGMA*, **21**(1-2), 31–40, (2008).

[21] S. M. Smith, M. Jenkinson, M. W. Woolrich, C. F. Beckmann, T. E. J. Behrens, H. Johansen-Berg, P. R. Bannister, M. D. Luca, I. Drobnjak, D. E. Flitney, R. K. Niazy, J. Saunders, J. Vickers, Y. Zhang, N. D. Stefano, J. M. Brady, and P. M. Matthews. Advances in functional and structural MR image analysis and implementation as FSL. *Neuroimage*, **23**, 208–219, (2004).

[22] O. Nestares and D. J. Heeger. Robust multiresolution alignment of MRI brain volumes. *Magn Reson Med*, **43**(5), 705–715, (2000).

[23] B. Biswal, A. E. DeYoe, and J. S. Hyde. Reduction of physiological fluctuations in fMRI using digital filters. *Magn Reson Med*, **35**(1), 107–113, (1996).

[24] B. Biswal, A. G. Hudetz, F. Z. Yetkin, V. M. Haughton, and J. S. Hyde. Hypercapnia reversibly suppresses low-frequency fluctuations in the human motor cortex during rest using echo-planar MRI. *J Cereb Blood Flow Metab*, **17**(3), 301–308, (1997).

[25] G. M. Boynton, S. A. Engel, G. H. Glover, and D. J. Heeger. Linear systems analysis of functional magnetic resonance imaging in human V1. *J Neurosci*, **16**(13), 4207–4221, (1996).

[26] R. L. Buckner, J. Goodman, M. Burock, M. Rotte, W. Koutstaal, D. Schacter, B. Rosen, and A. M. Dale. Functional-anatomic correlates of object priming in humans revealed by rapid presentation event-related fMRI. *Neuron*, **20**(2), 285–296, (1998).

[27] M. A. Burock, R. L. Buckner, M. G. Woldorff, B. R. Rosen, and A. M. Dale. Randomized event-related experimental designs allow for extremely rapid presentation rates using functional MRI. *Neuroreport*, **9**(16), 3735–3739, (1998).

[28] J. L. Gardner, P. Sun, R. A. Waggoner, K. Ueno, K. Tanaka, and K. Cheng. Contrast adaptation and representation in human early visual cortex. *Neuron*, **47**(4), 607–620, (2005).

[29] K. J. Friston, P. Fletcher, O. Josephs, A. Holmes, M. D. Rugg, and R. Turner. Event-related fMRI: characterizing differential responses. *Neuroimage*, **7**(1), 30–40, (1998).

[30] G. H. Glover. Deconvolution of impulse response in event-related BOLD fMRI. *Neuroimage*, **9**(4), 416–429, (1999).

[31] M. I. Sereno, S. Pitzalis, and A. Martinez. Mapping of contralateral space in retinotopic coordinates by a parietal cortical area in humans. *Science*, **294**(5545), 1350–1354, (2001).

[32] S. M. Smith and T. E. Nichols. Threshold-free cluster enhancement: addressing problems of smoothing, threshold dependence and localisation in cluster inference. *Neuroimage*, **44**(1), 83–98, (2009).

[33] C. I. Moore, C. E. Stern, S. Corkin, B. Fischl, A. C. Gray, B. R. Rosen, and A. M. Dale. Segregation of somatosensory activation in the human rolandic cortex using fMRI. *J Neurophysiol*, **84**(1), 558–569, (2000).

[34] J. S. Gati, R. S. Menon, K. Ugurbil, and B. K. Rutt. Experimental determination of the BOLD field strength dependence in vessels and tissue. *Magn Reson Med*, **38**(2), 296–302, (1997).

[35] E. Yacoub, A. Shmuel, J. Pfeuffer, P. F. V. D. Moortele, G. Adriany, K. Ugurbil, and X. Hu. Investigation of the initial dip in fMRI at 7 Tesla. *NMR Biomed*, **14**(7-8), 408–412, (2001).

[36] E. Yacoub, T. Q. Duong, P.-F. V. D. Moortele, M. Lindquist, G. Adriany, S.-G. Kim, K. Ugurbil, and X. Hu. Spin-echo fMRI in humans using high spatial resolutions and high magnetic fields. *Magn Reson Med*, **49**(4), 655–664, (2003).

[37] K. R. Thulborn, J. C. Waterton, P. M. Matthews, and G. K. Radda. Oxygenation dependence of the transverse relaxation time of water protons in whole blood at high field. *Biochim Biophys Acta*, **714**(2), 265–270, (1982).

[38] T. Q. Duong, E. Yacoub, G. Adriany, X. Hu, K. Ugurbil, and S.-G. Kim. Microvascular BOLD contribution at 4 and 7 T in the human brain: gradient-echo and spin-echo fMRI with suppression of blood effects. *Magn Reson Med*, **49**(6), 1019–1027, (2003).

[39] S. Ogawa, R. S. Menon, S. G. Kim, and K. Ugurbil. On the characteristics of functional magnetic resonance imaging of the brain. *Annu Rev Biophys Biomol Struct*, **27**, 447–474, (1998).

[40] I. Darian-Smith, M. Sugitani, J. Heywood, K. Karita, and A. Goodwin. Touching textured surfaces: cells in somatosensory cortex respond both to finger movement and to surface features. *Science*, **218**(4575), 906–909, (1982).

[41] J. Hulvershorn, L. Bloy, E. E. Gualtieri, J. S. Leigh, and M. A. Elliott. Spatial sensitivity and temporal response of spin echo and gradient echo bold contrast at 3 T using peak hemodynamic activation time. *Neuroimage*, **24**(1), 216–223, (2005).

[42] J. A. de Zwart, A. C. Silva, P. van Gelderen, P. Kellman, M. Fukunaga, R. Chu, A. P. Koretsky, J. A. Frank, and J. H. Duyn. Temporal dynamics of the BOLD fMRI impulse response. *Neuroimage*, **24**(3), 667–677, (2005).

[43] A. J. Nelson and R. Chen. Digit somatotopy within cortical areas of the postcentral gyrus in humans. *Cereb Cortex*, **18**(10), 2341–2351, (2008).

[44] J. H. Kaas, R. J. Nelson, M. Sur, C. S. Lin, and M. M. Merzenich. Multiple representations of the body within the primary somatosensory cortex of primates. *Science*, **204**(4392), 521–523, (1979).

[45] S. Geyer, A. Schleicher, and K. Zilles. Areas 3a, 3b, and 1 of human primary somatosensory cortex. *Neuroimage*, **10**(1), 63–83, (1999).

[46] P.-F. V. de Moortele, E. J. Auerbach, C. Olman, E. Yacoub, K. Ugurbil, and S. Moeller. T1 weighted brain images at 7 Tesla unbiased for Proton Density, T2* contrast and RF coil receive B1 sensitivity with simultaneous vessel visualization. *Neuroimage*, **46**(2), 432–446, (2009).

[47] A. Shmuel, E. Yacoub, D. Chaimow, N. K. Logothetis, and K. Ugurbil. Spatio-temporal point-spread function of fMRI signal in human gray matter at 7 Tesla. *Neuroimage*, **35**(2), 539–552, (2007).

[48] N. K. Logothetis. What we can do and what we cannot do with fMRI. *Nature*, **453**(7197), 869–878, (2008).

[49] T. Q. Duong, E. Yacoub, G. Adriany, X. Hu, K. Ugurbil, J. T. Vaughan, H. Merkle, and S.-G. Kim. High-resolution, spin-echo BOLD, and CBF fMRI at 4 and 7 T. *Magn Reson Med*, **48**(4), 589–593, (2002).

Chapter 7

Spin echo fMRI

7.1 Introduction

Conventional gradient echo (GE) blood oxygenation level-dependent (BOLD) contrast monitors brain activity through the vascular response to changes in neural activity. The microvascular components of the BOLD response are believed to be more closely linked to the site of neural activity than the response due to large vessels. Large draining vessels, themselves distant from the site of neuronal activity, receive contributions from a much larger area of the cortex [1, 2, 3], giving rise to signal changes displaced from the site of neuronal activity, limiting the temporal specificity of GE BOLD imaging. Improved spatial sensitivity is intrinsically obtained at high field when imaging at echo times (TE) optimised for grey matter ($\sim$ 25 ms) since GE-BOLD contrast arising from intravascular signal is diminished due to the disproportional shortening of the T_2 of blood compared to tissue [4, 5, 6]. Spin echo (SE) BOLD contrast has been used to selectively suppress the extravascular BOLD component. The difference in spatial sensitivity of gradient echo and spin echo sequences is mainly associated with the extravascular BOLD component. Both the SE and GE signals are affected by diffusion. Diffusion of extravascular water through the field gradients around vessels causes signal loss which is dependent on TE and vessel size. As a water molecule randomly moves through spatially

varying fields, the precession rate of each spin will vary randomly. The effect of these diffusional motions is an averaging of the field offset felt by any one spin, resulting in a reduced phase dispersion. The dispersion of phases after the spins have evolved for a time TE determines the attenuation at that given echo time. The signal attenuation at a given TE is characterized by the change in relaxation rate ($\Delta R_2^\star$, ΔR_2). The magnitude of the diffusion effect on the signal depends on how far a water molecule diffuses and how this distance compares with the spatial scale of field variations. Figure 7.1.A shows the variation of $\Delta R_2^\star$ and ΔR_2 with vessel size as predicted by Monte Carlo simulations by Boxerman et al. If the vessel is a larger venule or vein, the mean path length of the diffusing spins is much smaller than the radius of the vessel, and there is little variation in the field offset felt by the spin. This is called the *static averaging regime* and the gradient echo signal will not be attenuated. Dynamic averaging effects apply to vessels of the size of capillaries, which have a radius smaller than typical diffusion distances. In this case $\Delta R_2^\star$ is reduced by diffusional averaging. For gradient echo experiments, the BOLD effect is dominated by large vessels due to the moderating action of diffusion of the BOLD effect around capillaries. $\Delta R_2^\star$ exceeds ΔR_2 at all radii, reflecting the reduced extravascular SE-BOLD effect. For SE signals, the BOLD effect is largest for the capillaries and smaller venules, with ΔR_2 peaking at a radius of approximately 5 μm at 1.5 T (the peak radius depends on field strength). The extravascular component of the SE BOLD effect is negligible around large vessels as diffusion effects are negligible and the spin echo efficiently refocuses the static dephasing induced by field inhomogeneities. As we move to smaller vessels, diffusion causes the spin echo to be less effective at refocusing the phase dispersions of microscopic field offsets. This sensitivity to vessel size makes SE-BOLD more selective for the small venules and capillaries.

For the extravascular BOLD effect, the ratio $\Delta R_2^\star$ vs ΔR_2 induced by activation decreases with field strength [7, 8]. However, the reported field dependence of the ratio $\Delta R_2^\star/\Delta R_2$ may not be strongly field dependent (Stroman et al. [9] reported ratios of 3.7 and 3.8 at 1.5 T and 3 T respectively, and
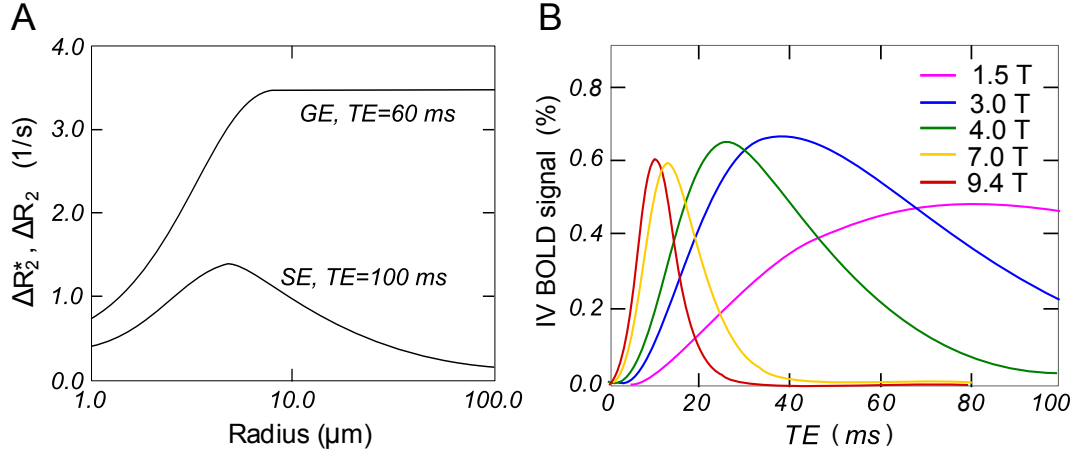
Figure 7.1: (A) Monte Carlo simulations of the dependencies of the extravascular $R_2^\star$ gradient echo (GE) and R_2 spin echo (SE) changes on vessel size at a field strength of 1.5 T. Adapted from [7]. (B) Simulation of the intravascular BOLD signal change, $\Delta S_{blood}/(S_{blood} + S_{tissue})$, as a function of echo time for a spin echo at 1.5, 3, 4, 7, and 9.4 T. Adapted from [6].

Yacoub et al. [10] reported a ratio of 2.6 at 7 T) because of the relative contributions of intravascular vs extravascular effects, which have different field dependence. The intravascular (IV) contribution is diminished with increasing magnetic field due to the rapidly decreasing T_2 of blood, which is much longer than tissue T_2 at 1.5 T but much shorter than tissue T_2 at 7 T [6, 11]. The intravascular contribution (IV) depends strongly on TE and field strength, as shown in Fig 7.1.B. Note that at 7 T, the IV SE-BOLD signal is practically nulled for a TE of 40 ms.

Previous work has provided evidence that SE fMRI has improved spatial specificity relative to GE fMRI at high field strengths, but at the expense of a decrease in BOLD contrast [5, 6, 8, 10, 12, 13]. The need for accuracy in localization must be balanced against the statistical power available to detect the effect under investigation when designing a functional paradigm. To mitigate the reduced BOLD contrast provided by spin-echo sequences, visual stimulus paradigms based on flashing checkerboards (which produce strong activation in the visual cortex) have been used in the work cited above. SE BOLD contrast is more difficult to detect in somatosensory cortex where responses tend

to be low (as described in Chapter 6).

7.2 Methods

7.2.1 Spin echo EPI sequence optimization

Fat Suppression

The measured $T_2^\star$ value for subcutaneous fat is approximately 10 ms, which is much shorter than the echo time of 25 ms generally used to match the $T_2^\star$ of grey matter in GE-EPI studies at 7 T. At this TE, the fat signal is therefore highly attenuated using GE-EPI. However for SE-EPI the fat signal appears bright if no fat suppression is used. The T_2 of the fat is close to 52 ms at 7 T [14]. So for SE-EPI acquisition optimized for BOLD sensitivity the TE used will refocus much of the fat signal and so fat suppression cannot easily be omitted. Fat suppression can be implemented by preceding the imaging sequence with a Spectral Pre-saturation with Inversion Recovery (SPIR) [15]. This uses a spectrally selective inversion pulse as explained in Section 2.3.2. The disadvantage of using fat suppression, particularly at ultra-high field, is that this increases the SAR and can limit the number of slices which can be acquired, particularly for spin echo acquisitions. With the aim of reducing SAR, Speck at al [16] evaluated the efficiency of fat saturation pulses with nominal flip angles ranging from 0° to 130 ° in gradient echo EPI at 7 T. They found that for GE-EPI the fat signal does not contribute significantly, even without any fat saturation, but the signal intensity in cortical grey and white matter was reduced with increasing fat saturation flip angle due to magnetisation transfer effects. To address the issue of the fat signal to spin echo EPI images, Fig. 7.2.A shows a 1.5 mm isotropic resolution SE echo planar axial image acquired without fat suppression and with a reduced field of view in the phase-encoding (right-left) direction ($192{\times}72\text{mm}^2$). A saturation slab is placed (to the right of the red line) to suppress the signal outside the field of view. The fat, which has not been suppressed by the saturation band, wraps
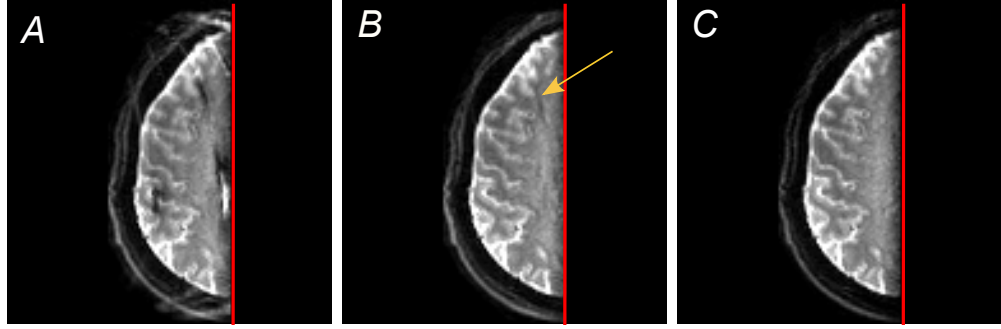
Figure 7.2: SE-EPI slice acquired with (A) no fat suppression, (B) SPIR and (C) both SPIR and SSGR techniques.

into the field of view. Fig. 7.2.B shows the equivalent slice acquired using SPIR prior to the OVS segment. The spectral saturation pulse had a nominal flip angle of 112° and a bandwidth of 135 Hz. The quality of the image has improved considerably but some residual fat artefact remains, indicated by the yellow arrow. This is due to two main factors: first, the low bandwidth of the spectral saturation pulse was chosen to ensure that the water signal is not affected, but it also means that the SPIR might not completely suppress the fat signal, and second, the SPIR pulse may interact with the OVS pulses, resulting in unsatisfactory fat suppression in the transition bands of the pulses. Therefore, in addition to the SPIR pulse preceding the OVS pulses, a Slice Selective Gradient Reversal (SSGR) technique was used [17, 18]. The displacement of the excited fat slice with respect to the water slice is $D = \Delta\delta G_s/B_0$, where (G_s) is the strength of the slice selection gradient and $\Delta\delta$ is the chemical shift in parts per million. The offset frequency between fat and water is ~ 1013 Hz at 7 T. The SSGR technique involves reversing the polarity of the slice selection gradient ($-G_s$) applied with the refocusing pulse (shaded gradient in Fig. 7.3), so that the affected slice of fat will be displaced in the opposite direction. If S is the nominal slice thickness of the excited water, only the overlapping region, S-2D, will experience both excitation and refocusing pulses. Figure 7.2.C shows effective fat suppression with SPIR and gradient reversal. The artefact apparent in Fig. 7.2.B is now totally removed.
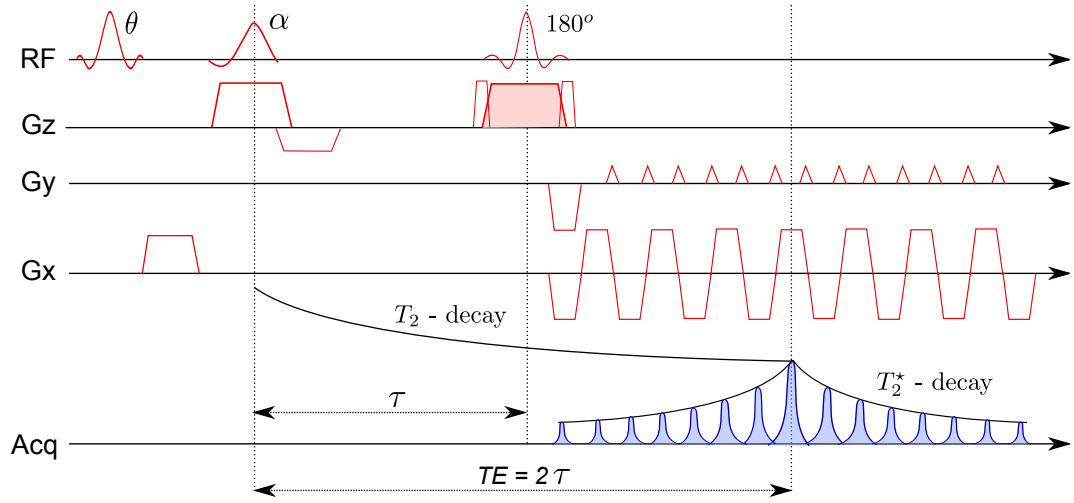
Figure 7.3: Spin-echo, echo planar imaging pulse sequence diagram with SPIR.

Refocusing pulse

The SE sequence was described in detail in Chapter 4. In order to produce T_2-weighting in EP images, a spatially selective refocusing pulse is applied at time τ after the excitation pulse in the spin echo, echo planar imaging (SE-EPI) sequence to rephase the transverse magnetization at time 2τ (See Fig. 7.3). The pulse sequence diagram is shown in Fig. 7.3. A spatially selective refocusing pulse is accompanied by a slice-selection gradient ideally so that only the spins within the selected slice experience the refocusing effect. A pair of crusher gradient pulses [19] are placed immediately before and after the refocusing pulse to eliminate unwanted FID and stimulated echo signal caused by imperfections in the refocusing pulse [20].

The SE-EPI protocol available on the Philips scanner uses a centered SINC pulse as the default refocusing pulse. A SINC pulse [21, 22] consists of several adjacent lobes of alternating polarity, with the central lobe having the highest amplitude and being twice as wide as every other lobe. The Fourier transform of an infinitely long SINC pulse is a top-hat shape frequency profile. In practice, SINC pulses are truncated to have a finite duration. The greater the number of lobes included in the SINC pulse, the better the approximation of the ideal slice profile. Figure 7.4.A shows a SINC pulse envelope with its

corresponding Fourier Transform (FT). The FT of a truncated SINC function has a rectangular-like profile showing ringing effects. When the SINC pulse is played as a refocusing pulse, the side lobes are suppressed (assuming crushers are used) and the bandwidth is narrowed. A slice selective 180° SINC (7 lobes) refocusing pulse results in a narrowing of the bandwidth (as measured by full width at half maximum of the slice profile) of 70 % [23]. In order to compensate for this narrowing of the refocusing region, the amplitude of the slice selection gradient needs to be decreased to extent the width of refocussing. In the Philips software this amplitude is modified with a control parameter, G_{scale}, this scales the amplitude of the gradient while maintaining the same duration. Hence, decreasing this parameter will yield an increase of the thickness of the selected slice.

In order to determine the optimal amplitude for this gradient, we acquired sets of SE EPI data on a head with 1.5 mm isotropic resolution at different G_{scale} values [1 0.8 0.7 0.6 0.5] and a TR of 2.4 s. 20 volumes were acquired for each G_{scale} value. A value of 0.5 doubles the thickness of the selected
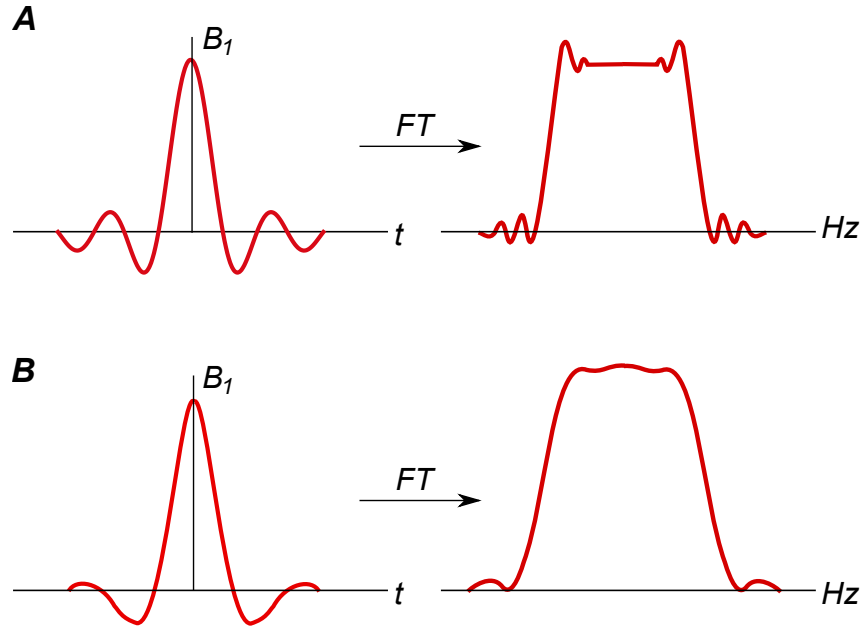

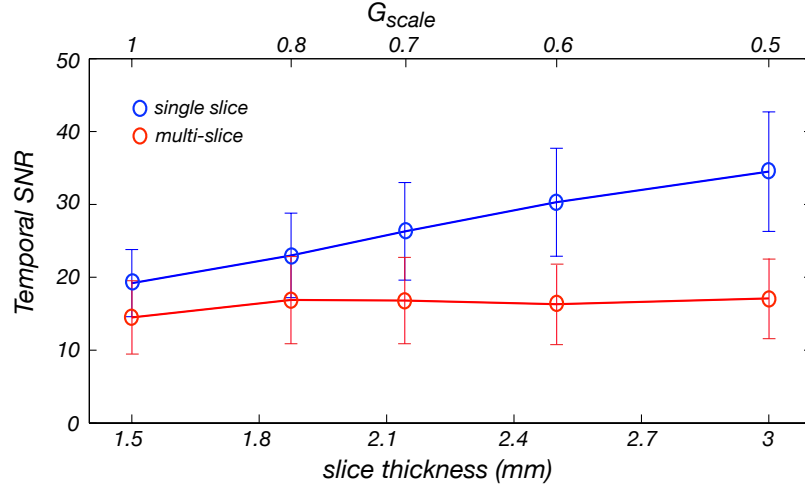Figure 7.4: (A) Truncated SINC RF pulse and an (B) SLR RF pulse with their respective slice profiles.

Figure 7.5: Temporal signal to noise ratio as a function of the slice thickness of refocusing pulse (SINC) slice selection gradient (G_{scale}).

slice improving refocussing, but decreasing the gradient amplitude increases the overlap of adjacent slices even when an acceptable slice-gap is employed. To minimize this 'cross-talk' effect, slices in the volume were acquired in an interleaved manner. This experiment was performed for a single slice and a multislice volume of 11 slices whose centre-slice coincided with a single slice set. The temporal signal to noise ratio (tSNR) was measured across the 20 volumes over a region of interest containing 300 voxels. It was found that for the SINC pulse the mean tSNR for the single slice acquisition increased with increasing slice thickness, from a value of 19.2±4.6 for G_{scale} =1 to a value 34.5±8.2 for G_{scale}=0.5 (See Fig. 7.5). In the case of the multislice acquisition, decreasing the gradient amplitude did not significantly increase the temporal signal to noise ratio (measured over the same ROI). For a TR of 2.4 s, even running with interleaved slice acquisition results in significant cross-talk effects in the head for lower G_{scale}. Furthermore, for the best scenario where G_{scale}=0.5, the mean tSNR measured for the multislice acquisition is reduced to approximately 50% of the equivalent tSNR measured in the single slice acquisition.

Figure 7.5 suggests that the use of SINC pulses for refocusing significantly compromises the signal to noise ratio when contiguous slices are imaged, which is required for high resolution functional mapping. Therefore, a better refocus-

ing pulse is required. Refocusing pulses designed with the Shinnar-Le-Roux (SLR) algorithm [24, 25, 26, 27, 28, 29] can considerably improve the quality of the slice profile (see Fig. 7.4.B) and have largely replaced SINC refocusing pulses in commercial MRI scanners. The Optimum-Echo-2 (bandwidth=679 Hz, length=5.3 ms) is a SLR refocusing pulse available in the Philips software.

To evaluate the performance of the slice profile of the SLR refocusing pulse, we acquired single slice and multi slice sets again for a range of G_{scale} values [1 0.9 0.8 0.7 0.6 0.5] in both the visual and the motor cortex. The multi-slice acquisition consisted of 13 continuous slices (1.5 mm isotropic resolution) with the same centre as the single slice acquisition, so that the centre slice coincides with the acquired single slice. Again 20 volumes of data were acquired for tSNR measurements.

Figure 7.6.A shows the resulting temporal signal to noise ratio measured over an ROI (120 voxels) in the visual cortex plotted versus the effective re-
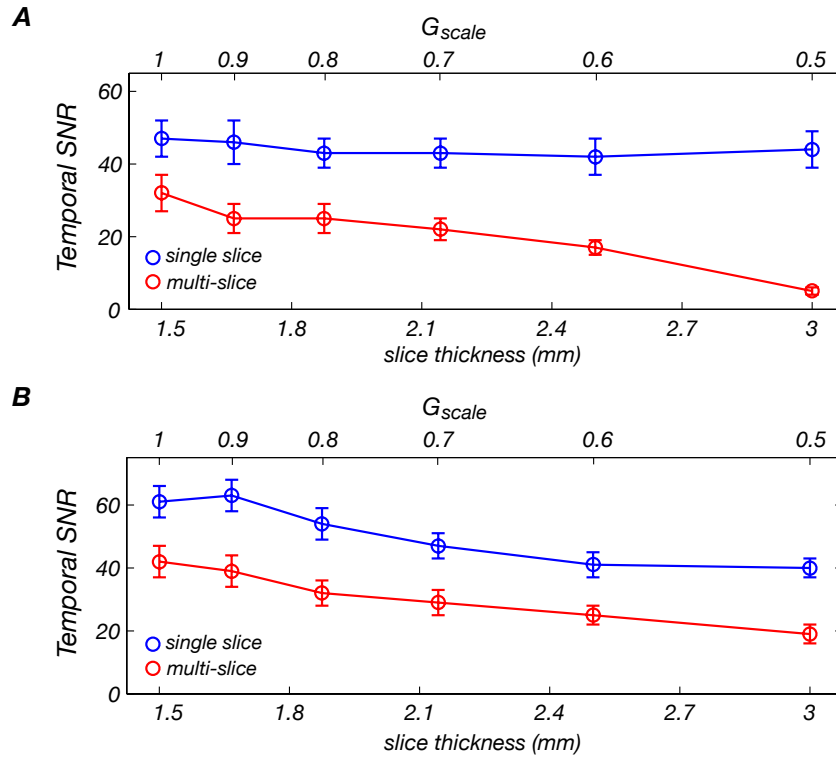
Figure 7.6: Temporal signal to noise ratio as a function of the slice thickness of refocusing pulse (SLR) slice selection gradient (G_{scale}) in (A) visual and (B) motor cortex.

focusing slice thickness for both multislice and single slice acquisitions. In contrast to the SINC refocusing pulse, a higher tSNR is obtained when G_{scale} is set to 1, therefore conserving the original slice thickness of 1.5 mm. For this pulse, the tSNR measured in the multislice acquisition is approximately 70% of that measured in the single slice acquisition, a marked improvement over the SINC pulse. Similar results are obtained for the motor cortex data (Figure 7.6.B.)

It must be noted that the use of the SLR refocusing pulse results in a significantly increased radiofrequency power deposition with respect to the gradient echo sequence. This limits the number of slices that can be acquired within a TR period in the SE-EPI multi-slice acquisition technique. Therefore, for a given TR, a larger slice coverage can be achieved with GE imaging.

7.2.2   Visual Cortex

To compare SE and GE BOLD contrast in the visual cortex, a paradigm which measures the eccentricity component [30] of the retinotopic map was chosen to produce robust activation in the visual cortex. This paradigm consisted of a flickering ring displayed on a white background, which expands along the radial component of the visual field. The ring appears at the centre and expands to the periphery of the visual field in 8 steps to complete a 24 s cycle. Functional scans consisted of 10 cycles and were repeated twice for both SE and GE data sets. T_2-sensitive spin echo single shot, echo planar imaging (SE-EPI) data were acquired with the following scan parameters: SENSE factor 2 in the anterior-posterior direction, flip angle FA=90° (achieved for a requested flip angle of 110°, as described in Section 4.3.2) TR=2.4 s, TE=45 ms. $T_2^\star$-sensitive gradient echo-echo planar imaging (GE-EPI) data were acquired with TE=25 ms. A total of 12 contiguous axial slices aligned parallel to the calcarine sulcus were acquired with both techniques in an interleaved manner with 1.5 mm isotropic resolution. A rectangular field of view (FOV) of 144 mm in the right-left (RL) direction and 126 mm in the anterior-posterior

(AP) direction was used. An outer-volume suppression (OVS) saggital slab was used to prevent signal fold-over and a SPIR sequence was placed before the OVS segment to suppress the signal from fat.

In order to compare the results for contiguous slice acquisition vs acquisition with a slice gap, an experiment as described above was also performed, in which slices were acquired with a slice gap of 0.75 mm.

7.2.3 Motor Cortex

As for the somatosensory cortex, the motor cortex which is located in the dorsal part of the precentral gyrus and the anterior bank of the central sulcus also displays topographic representation of the body. Analogous to the paradigm used in Chapter 6 to acquire somatotopic maps of the digit representation, a 'travelling wave' paradigm in which the motor action created a wave of activity across cortical regions containing a motor map of the hand was used here. In a pilot experiment the subject was visually cued to tap the digits of the left hand sequentially for 3 s (from thumb to little finger) with an OFF period of 1.8 s between adjacent digits, resulting in a 24s cycle of stimulation of all five digits. Functional scans consisted of 10 cycles, resulting in scan duration of 240 s. Spin echo single shot, echo planar imaging (SE-EPI) data were collected with the following scan parameters: SENSE factor 2 in the right-left direction, flip angle FA=90°, TR=2.4 s.

As discussed in Chapter 4, grey matter T_2 values appear to be reduced in the central sulcus compared to the occipital lobe, therefore fMRI of the motor cortex was performed across a range of shorter TE values than are typically used in SE-based fMRI of the visual cortex. A total of six SE-EPI fMRI scans were performed with two repeats at each echo time of 30, 35 and 40 ms in a pilot subject. A total of 13 contiguous axial slices spanning the right primary motor cortex were acquired in an interleaved manner (to reduce cross-talk) with 1.5 mm isotropic resolution, and a field of view (FOV) of 192 mm in the anterior-posterior (AP) direction and 72 mm in the right-left (RL) direction.

The reduced FOV in the phase encoding direction (right-left) allows the use of short echo times without the need for half Fourier Sampling (see Section 4.3.2). An outer-volume suppression (OVS) slab was used to prevent signal fold-over and a spectrally selective saturation pulse was applied for fat suppression.

An additional functional scan was also acquired using GE-EPI with a TE of 25 ms. In order to quantify the T_2 of grey matter, spin echo EPI measurements were made with a range of TE values [30 35 40 45 50 55 ms] at the end of the session. Twenty volumes were acquired at each TE to improve SNR.

A modified experimental protocol was used in studying three additional subjects. For these experiments, 3 SE data sets were acquired with TE=35 ms, 3 SE data sets with TE=40 ms and 2 GE data sets were acquired TE=25 ms. In order to quantify $T_2^\star$, as well as T_2, of grey matter, gradient echo EPI measurements were acquired with TE [25 30 35 40 45 50 50]ms at the end of the session.

7.2.4 Data Analysis

Functional image were analysed using software described previously. fMRI data were motion-corrected within scans [31] and high-pass filtered to compensate for slow signal drift[32, 33]. Each voxel's time series was then divided by its mean intensity to convert the data from image intensity to units of percent signal change. No spatial filtering was applied to the data.

Time series data were analyzed voxel-by-voxel using Fourier-based methods (see Chapters 5 and 6) to compute the topographic maps. The phase measures the temporal delay of the fMRI signal with respect to the onset of the stimulus cycle. For the visual experiment, this corresponds to the spatial location of the ring in the visual field whilst for the motor experiment, this corresponds to tapping a digit; a topographic map should be visible which has a smooth progression of early to late 'phase values', corresponding to different digits.

As described previously, threshold-free cluster enhancement (TFCE) [34] was applied to the coherence map (H=2, E=0.5, neighbourhood connectivity

6) and voxels in the top 1 percentile of the resulting image were considered for further analysis. Regions-of-interests (ROI) of voxels included by these criteria were interrogated for fMRI timeseries and response (Fourier) amplitude.

7.3   Results

7.3.1   Visual cortex

Strong functional activation was observed in the visual cortex for both acquisition schemes (with and without a slice gap) in both the gradient echo and the spin echo data. Greater coherence values are evident in the GE data. The two GE (SE) functional scans were averaged together before performing the standard Fourier analysis. Figure 7.7.A shows the coherence map of the averaged GE functional scan superimposed on the mean $T_2^\star$- weighted images from a single GE functional scan. The corresponding coherence map of the averaged SE functional scan is superimposed on the mean T_2-weighted images from an individual SE functional scan (B). Corresponding coherence maps for GE and SE data acquired with contiguous slices are shown in Fig 7.8.A and Fig 7.8.B respectively. Coherence values are again higher for the GE data. ROIs formed from active voxels using TFCE were interrogated to investigate

	volume	Coherence Value	Response Amplitude
	mm^3	$mean \pm std$ (min-max)	% $mean \pm std$ (min-max)
	Acquisition with a slice gap		
SE ROI	4,306	0.64±0.06 (0.49-0.91)	6.56±4.06 (2.24-44.44)
GE ROI	4,357	0.80±0.06 (0.69-0.96)	9.26±4.46 (2.94-37.82)
GE ROI⋆	10,580	0.68±0.12 (0.49-0.96)	7.20±4.40 (1.38-62.92)
	Contiguous slice acquisition		
SE ROI	4,111	0.56±0.11 (0.40-0.87)	4.90±4.10 (1.36-77.22)
GE ROI	4,043	0.79±0.11 (0.68-0.94)	7.79±6.12 (2.04-60.64)
GE ROI⋆	15,619	0.61±0.14 (0.40-0.94)	4.94±4.82 (0.92-60.64)

Table 7.1: Details of fMRI responses in the visual cortex: GE active ROI and SE active ROI are defined using the TFCE method; GE active ROI⋆ is defined from a coherence threshold of 0.49/0.40 (acquisition with/without a slice gap), chosen to match the coherence threshold of the corresponding SE active ROI.
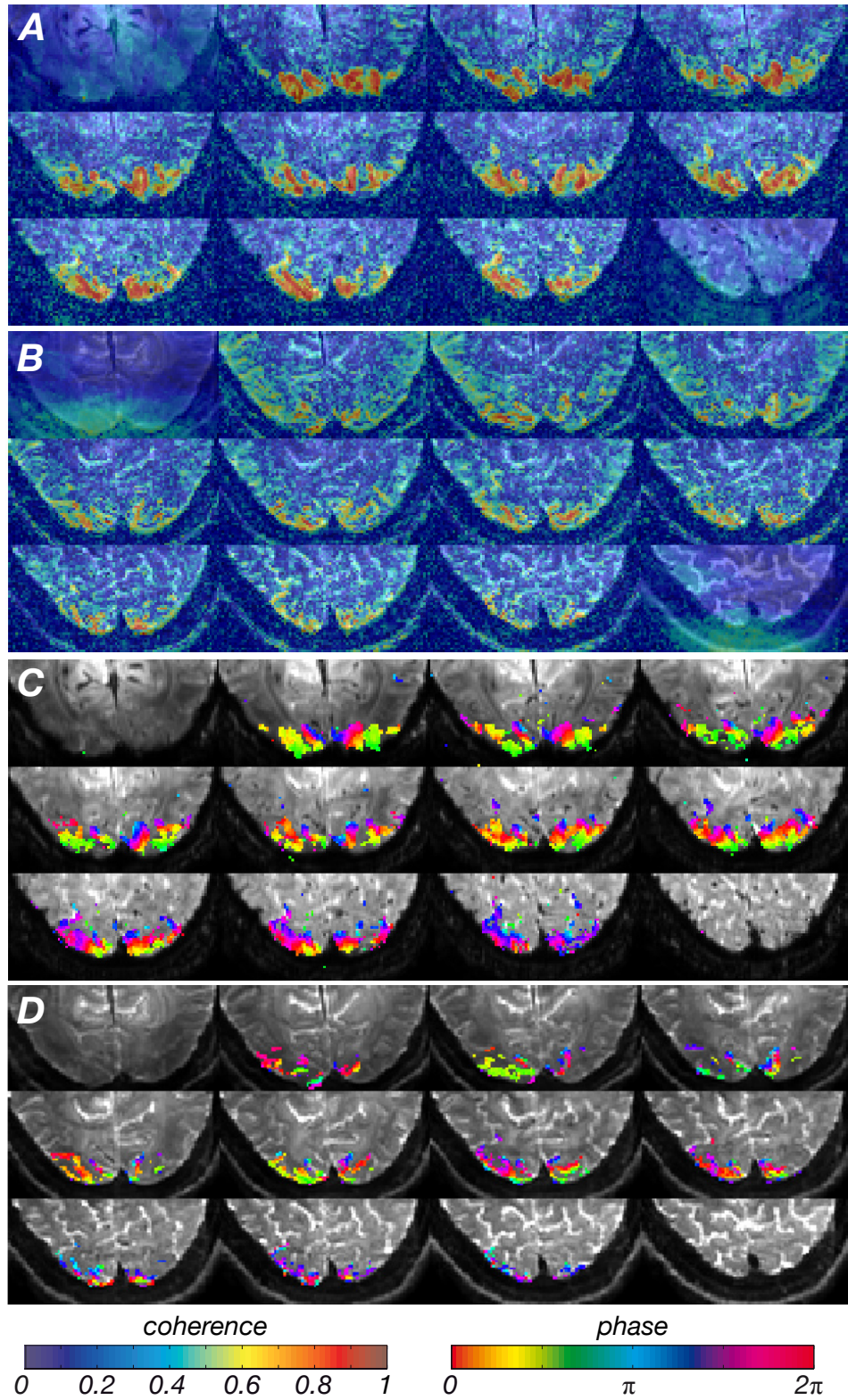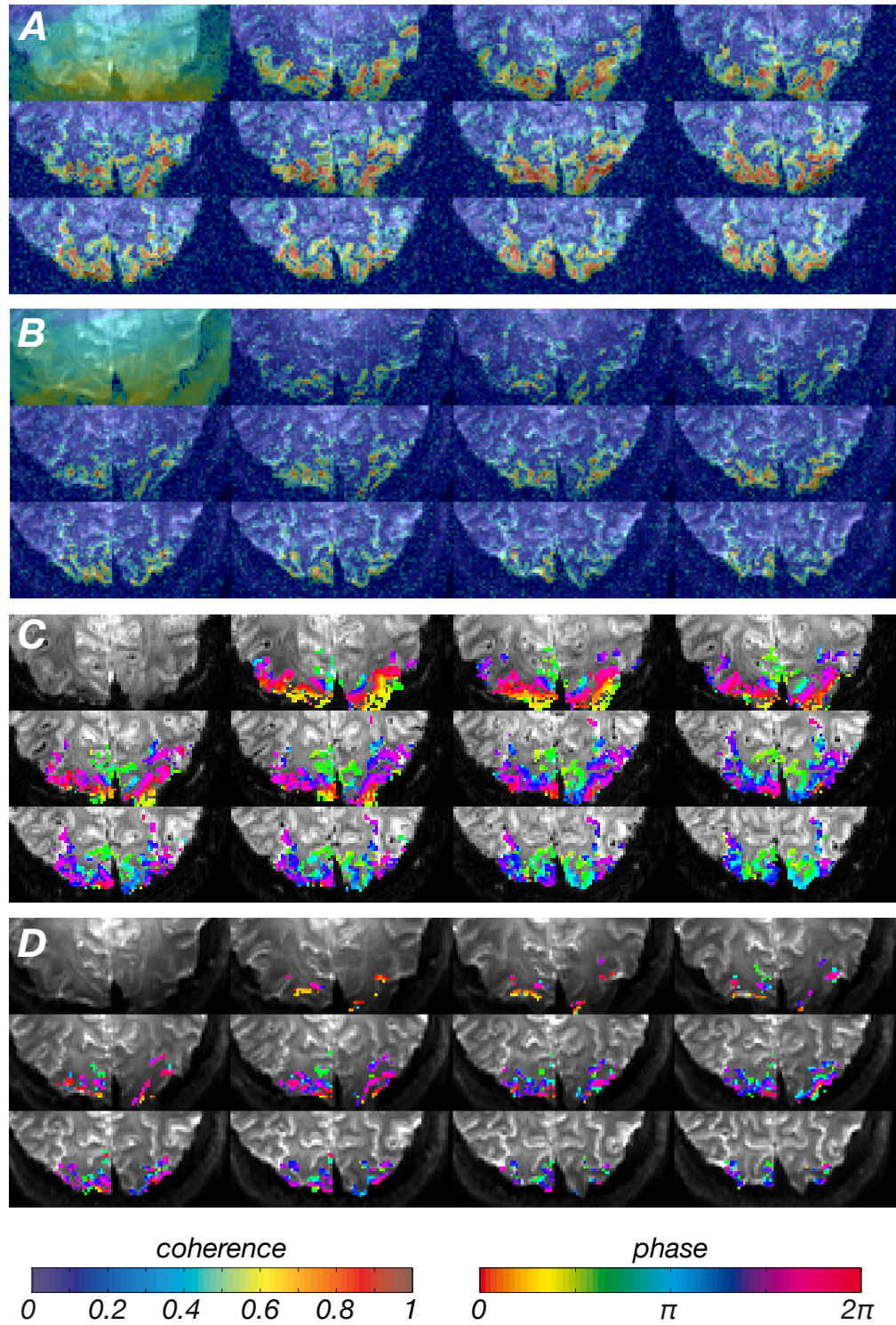
Figure 7.7: Statistical maps of (A,B) coherence and (C,D) phase with best-fitting sinusoid at frequency of stimulus paradigm superimposed on mean EP image for GE (A,C) and SE (B,D) data acquired with a slice gap. Phase maps thresholded at a coherence c>0.49.

Figure 7.8: Statistical maps of (A,B) coherence and (C,D) phase with best-fitting sinusoid at frequency of stimulus paradigm superimposed on mean EP image for GE (A,C) and SE (B,D) data acquired with contiguous slices. Phase maps thresholded at a coherence c>0.4.

differences between SE- and GE-BOLD responses. Table 7.1 details the ROI volume, mean coherence and amplitude values (across voxels) for the active GE and SE ROI in both experiments. The sizes of the GE and SE ROI were comparable, but the lowest coherence value was much higher for the GE (0.69/0.68) than the SE (0.49/0.40) ROIs for acquisitions both with and without a slice gap respectively. A second ROI for the GE data, where the threshold was lowered to 0.49/0.40 (to match that used with the SE data) was also interrogated. Phase maps of active ROI are shown in Fig. 7.7.C and Fig. 7.8.C for GE data (thresholded at c> 0.49/0.40) and Fig. 7.7.D and Fig. 7.8.D for SE data for acquisition with and without a slice gap.

Figure 7.9.A shows the GE fMRI response (red line) and the SE fMRI response (green line) from a region of interest (ROI1) of 1.1 cm^3 size, chosen to correspond to a given stimulus ring (encoded by pink color). A highly significant signal modulation is seen at 10 cycles/scan in the Fourier spectra (B,C) indicates. Contributions to the response from frequency components other than the first and second harmonics are negligible (Fig. 7.9.B,C). The contrast to noise ratio is higher for GE (40.0) than for SE (24.7) data. The mean (across voxels) of the coherence and response amplitude values for this ROI were 0.69/0.56 and 8.02/5.00 % for GE/SE respectively. Figure 7.10 shows the average cycle response (mean across cycles) for ROI1 (A) and ROI2 (B) of 0.5 cm^3 size, chosen to correspond to a different stimulus condition (a ring with a different radius, hence a different phase delay). The phase of the mean response for GE/SE was 5.21/5.44 and 5.21/5.44 for ROI2 respectively. The mean (across voxels) of the coherence and response amplitude values for ROI2 were 0.69/0.56 and 8.02/5.00 % for GE/SE respectively.
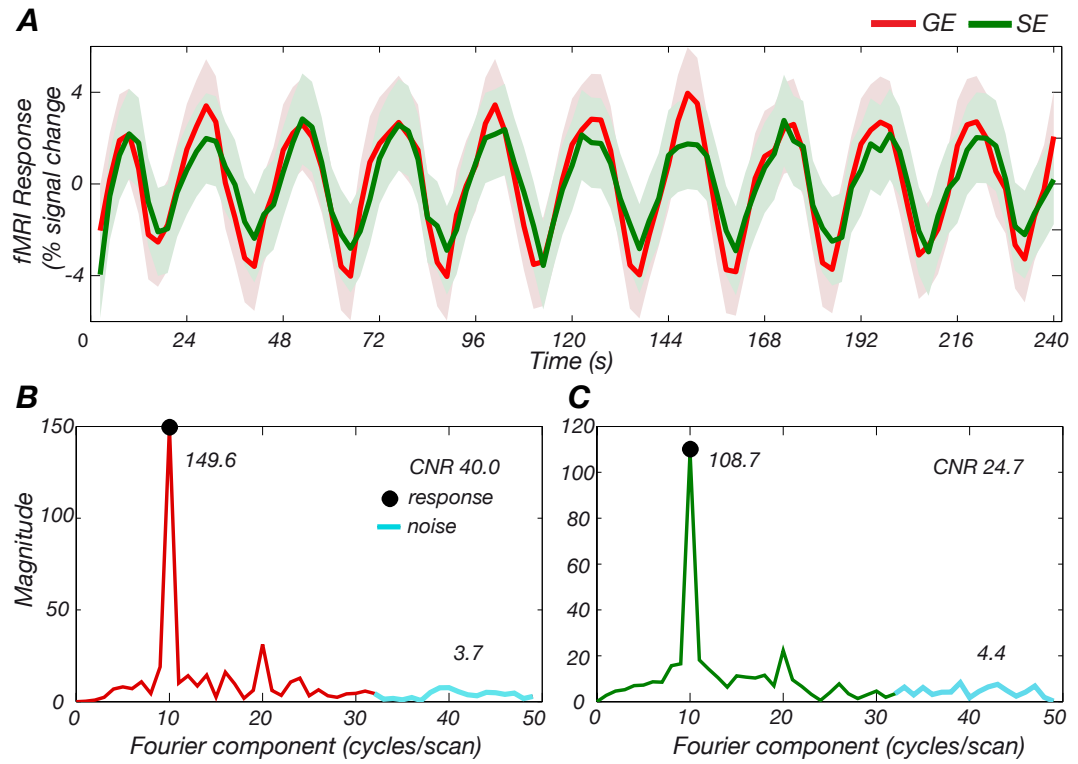
Figure 7.9: (A) Time course plots of GE (red) and SE (green) data from a region of interest in the visual cortex (ROI1). Corresponding Fourier spectra for (B) GE and (C) SE data.
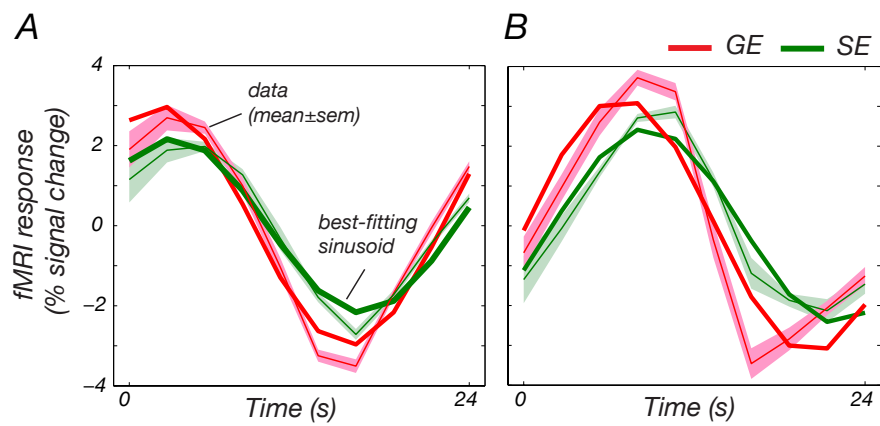

Figure 7.10: Time course plots from (A) ROI1 and (B) ROI2, corresponding to two different stimulus conditions (two rings of different radius). Red (green) line, mean GE (SE) fMRI response in ROI.

active ROI	volume mm^3	Coherence Value $mean \pm std$ (min-max)	Response Amplitude $\% \ mean \pm std$ (min-max)
GE	1,873	0.48±0.11 (0.4-0.87)	4.24±2.68 (1.54-32.94)
SE (TE 30 ms)	270	0.45±0.11 (0.33-0.83)	2.10±0.42 (1.44-3.12)
SE (TE 35 ms)	891	0.41±0.06 (0.33-0.58)	2.48.94±0.62 (1.06-5.58)
SE (TE 40 ms)	631	0.32±0.06 (0.27-0.55)	2.06±0.52 (1.12-3.98)
SE (6 scans)	1168	0.35±0.08 (0.31-0.66)	1.58±0.40 (0.76-2.92)

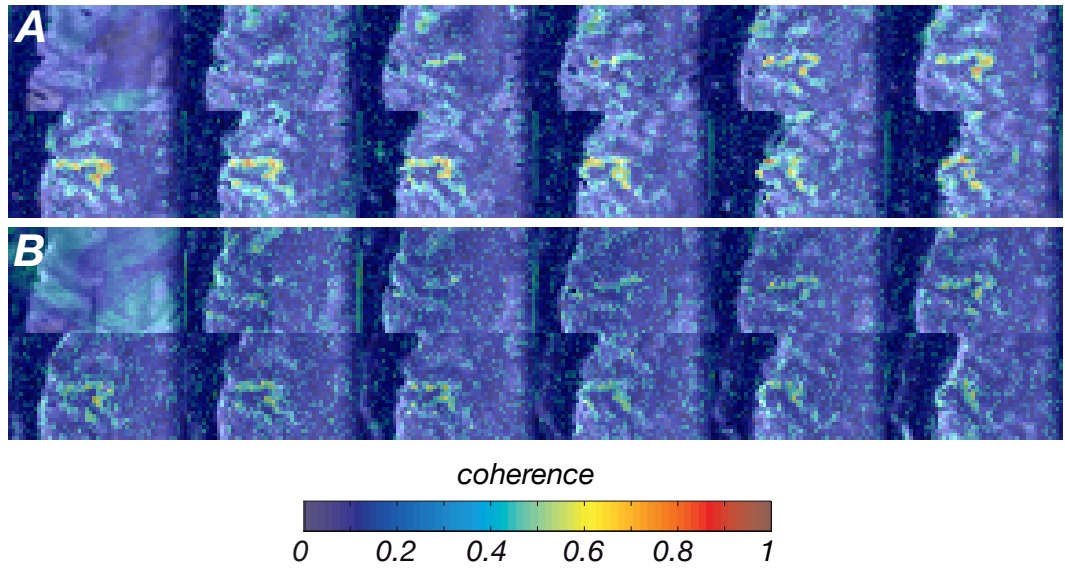Table 7.2: Details of fMRI response in the motor cortex for a pilot subject.

Figure 7.11: Statistical maps of coherence with best-fitting sinusoid at frequency of stimulus paradigm superimposed on mean EP image for (A) individual GE data and (B) SE (average of six scans) data.

7.3.2 Motor cortex

For the motor task, two spin echo fMRI data sets were acquired at TE =30,35 and 40 ms for the pilot subject. The SE functional time series acquired with the same TE values were averaged together before performing the standard Fourier analysis. In addition, an average of all SE scans was also performed. The coherence map of the GE data is shown in Fig. 7.11.A and the corresponding coherence map of the SE data (averaged over 6 scans) is shown in Fig. 7.11.B. Coherence values in the motor cortex are again much higher for the individual GE scan than for the SE data averaged over all scans.
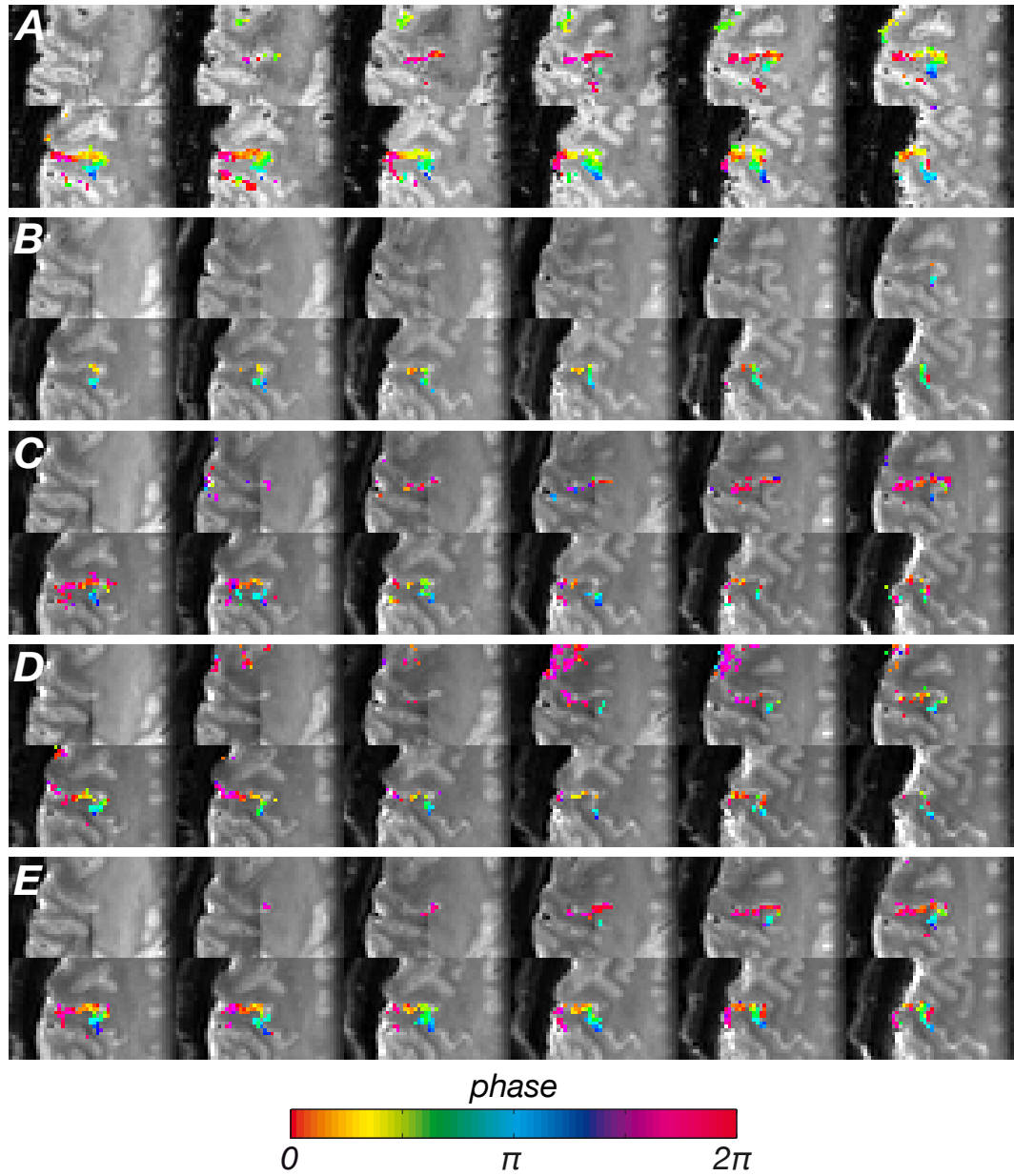
Figure 7.12: Threshold phase map superimposed on mean EP image for (A) GE and SE data with (B) TE=30ms,(C) TE=35ms,(D) TE=40ms and (E) average from six SE scans. Colours indicate digit as shown in colour diagram. Note that the phase map has been thresholded using a TFCE map.

The phase data, thresholded using a TFCE map, are shown in Fig. 7.12 for (A) gradient echo data, and spin echo data at TE of (B) 30, (C) 35, (D) 40 ms and (E) the average of all spin echo functional scans. Different cortical areas can be seen to be active for the different TE values, with the lowest number of active voxels (80) for the shortest TE (TE=35 and TE=40 ms have 264 and
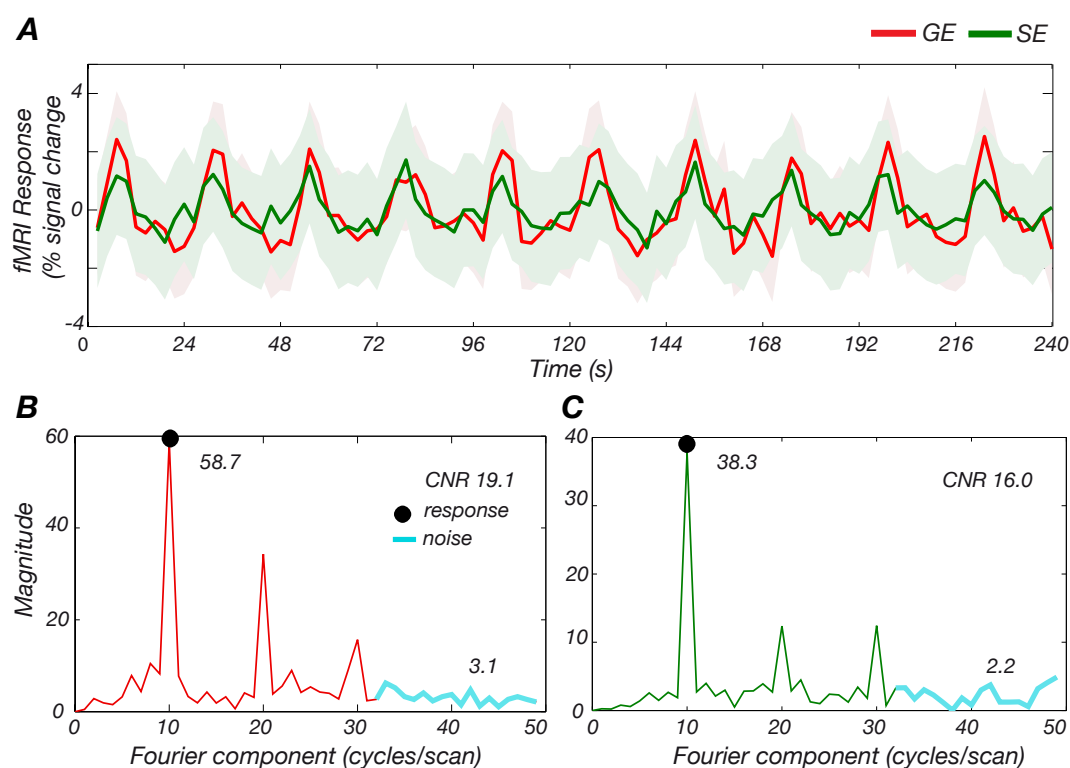
Figure 7.13: A) Time course plots of GE (red) and SE (green) data from a region of interest in the motor cortex corresponding to digit 2. Corresponding Fourier spectrum for (B) GE and (C) SE data.
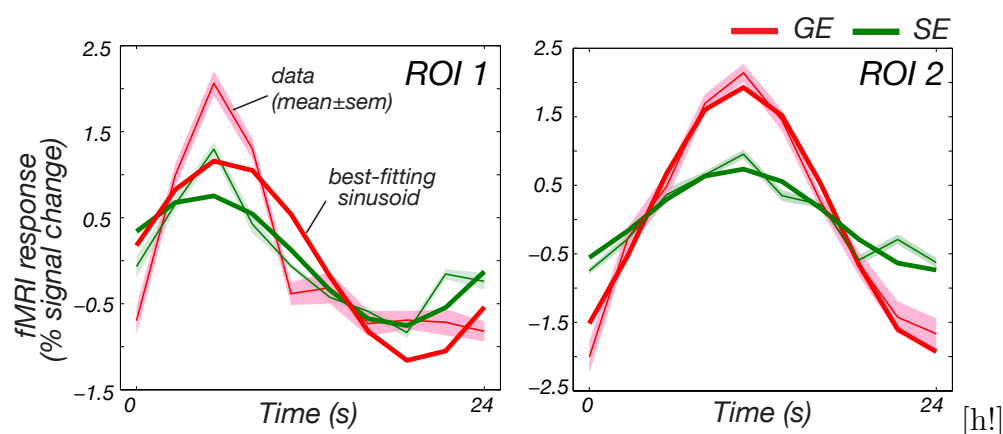

Figure 7.14: Time course plots from a region of interest for two different stimulus conditions (ROI1 and ROI2). Red (blue) line, mean GE (SE) fMRI response in ROI.
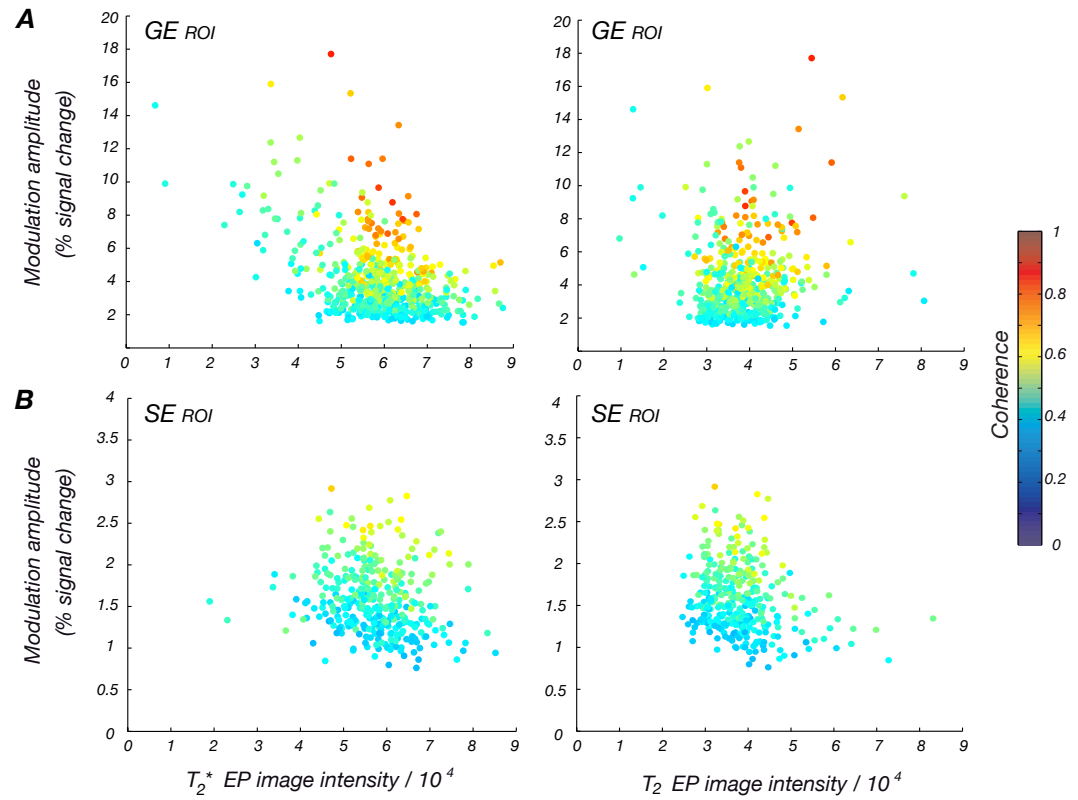
Figure 7.15: Histogram of fMRI response modulation in (A) GE active ROI and (B) SE active ROI, as a function of image intensity in mean $T_2^\star$- (left) and T_2-weighted (right) EP image. Colors represent coherence with best fitting sinusoid.

187 active voxels respectively). By combining the data, the SE recovers the whole progression of phase values in the motor cortex observed in the gradient echo map.

The ROI made of active voxels identified using TFCE for each contrast were interrogated to investigate the coherence and amplitude of the SE response at different TE's and compared with the GE response. Table 7.2 shows details of ROI volume, mean coherence and amplitude values (averaged across voxels) for the ROI identified from the GE and SE data.

Figure 7.13.A shows the GE fMRI response (red line) and the SE fMRI response of the average over 6 scans (green line) from a region of interest corresponding to digit 3 (ROI1, 341 mm^3). A large peak at 10 cycles/scan in the Fourier spectrum for both GE and SE (B,C) indicates highly significant

active ROI	volume mm^3	Coherence Value $mean\pm std$ (min-max)	Response Amplitude $\%$ $mean\pm std$ (min-max)
S1: GE	2,717	0.60±0.13 (0.40-0.94)	4.04±3.10 (0.98-31.72)
S1: SE	2,720	0.36±0.10 (0.24-0.78)	2.04±1.20 (0.52-13.38)
S2: GE	3,149	0.69±0.12 (0.49-0.94)	4.00±2.96 (1.00-24.04)
S2: SE	3,057	0.49±0.12 (0.34-0.88)	1.50±0.92 (0.48-11.02)
S3: GE	3,324	0.61±0.10 (0.47-0.88)	4.68±3.04 (1.20-22.10)
S3: SE	2,733	0.51±0.11 (0.37-0.83)	2.28±1.44 (0.72-11.56)

Table 7.3: Details of fMRI response in the motor cortex for subjects 1,2,3. GE data averaged over 2 scans, SE data averaged over 6 scans.

signal modulation. The frequency components corresponding to the second and third harmonic are also clear (Fig. 7.13.B,C). The contrast to noise ratio is similar for both sets of data; 19.1 (GE) and 16.0 (SE). The mean (across voxels) phase, coherence and response amplitude value for this ROI were 3.72/5.83 rad 0.46/0.42 and 4.06/1.58 % for GE/SE data respectively.

Figure 7.14.A. shows the mean response over a single cycle (mean across cycles) for this ROI. The response to stimulation of digit 3 (ROI2, 196 mm^3) is shown in Fig. 7.14.B. The mean phase, coherence and response amplitude value for ROI2 were 0.93/0.86 rad 0.54/0.49 and 4.66/4.12 % for GE/SE data respectively.

Figure 7.15.A shows a scatter plot of GE fMRI response modulation as a function of the image intensity in the mean $T_2^\star$-weighted image (left) and mean T_2-weighted image acquired with TE=35 ms (right) for the GE active ROI. Corresponding data for the average SE fMRI response modulation for the SE active ROI is shown in Figure 7.15.B for comparison. There are a few voxels of the GE active ROI with low T_2 and $T_2^\star$-weighted intensity values, indicating the presence of blood vessels, but in general the specificity to grey matter tissue is similar for both SE and GE data.

For each activation map from each SE functional scan the T_2 maps were used to determine the T_2 values of voxels which were active. Fig. 7.16.A shows a T_2 map from a representative slice. A dark band is clearly observed in the central sulcus. The normalized histograms of T_2 values of each active ROI for
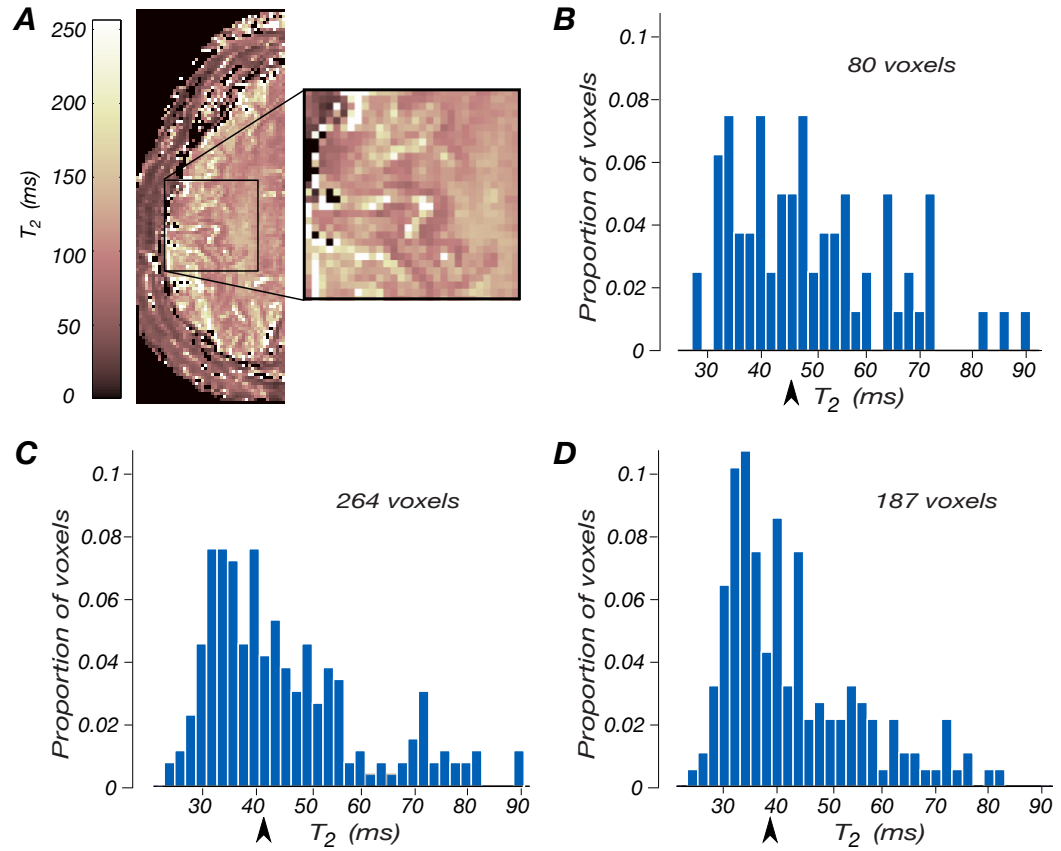
Figure 7.16: (A) T_2 map of a representative slice. Normalized histograms of T_2 values in active ROI of SE data acquired with TE (B) 30, (C) 35 and (D) 40 ms. The arrows indicate the median T_2 value.

the functional scans at different TE (B,C,D) show that there is a high number of active voxels with T_2 values around 35 ms.

Similar results were found for the additional 3 subjects scanned. Table 7.3 shows details of volume, mean coherence and amplitude values (across voxels) for the active GE and SE ROI. Note that the GE data is averaged across 2 scans and SE data averaged across 6 scans. ROI volumes are bigger for subject 2 and 3, since their data comprises 16 slices, compared to subject 1 where only 12 slices were acquired.

Figure 7.17.A shows phase maps of the GE BOLD response overlaid over the mean $T_2^\star$-weighted image for subject 2 and Fig. 7.17.B shows corresponding phase maps of the SE BOLD response overlaid onto the mean T_2-weighted image. Notice phase values are better defined in the GE data.
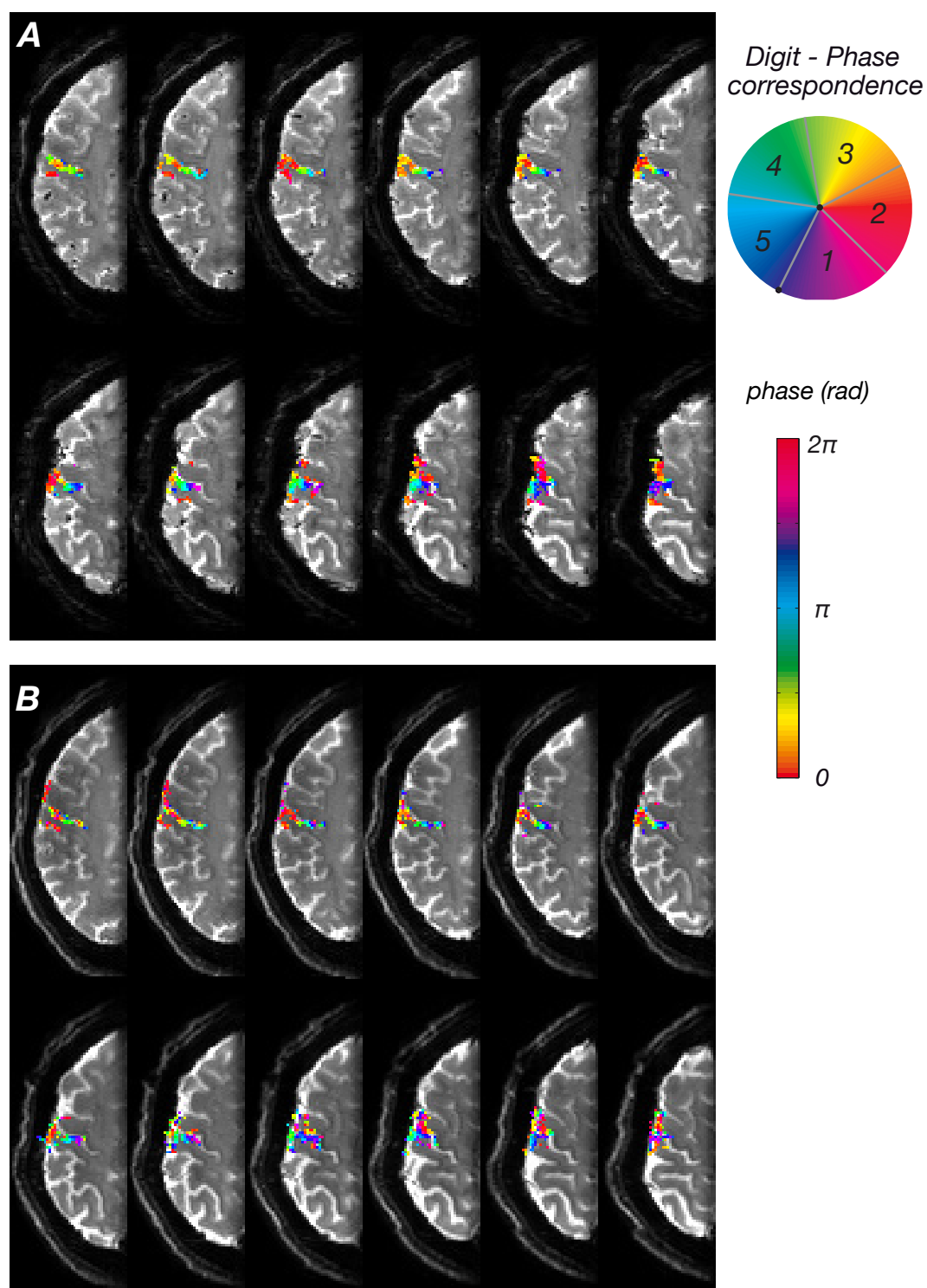
Figure 7.17: Phase data superimposed on mean EP image for (A) GE (average from 2 scans) and SE (average from six scans). Colours indicate digit as shown in colour diagram. Note that the phase map is thresholded using a TFCE map.
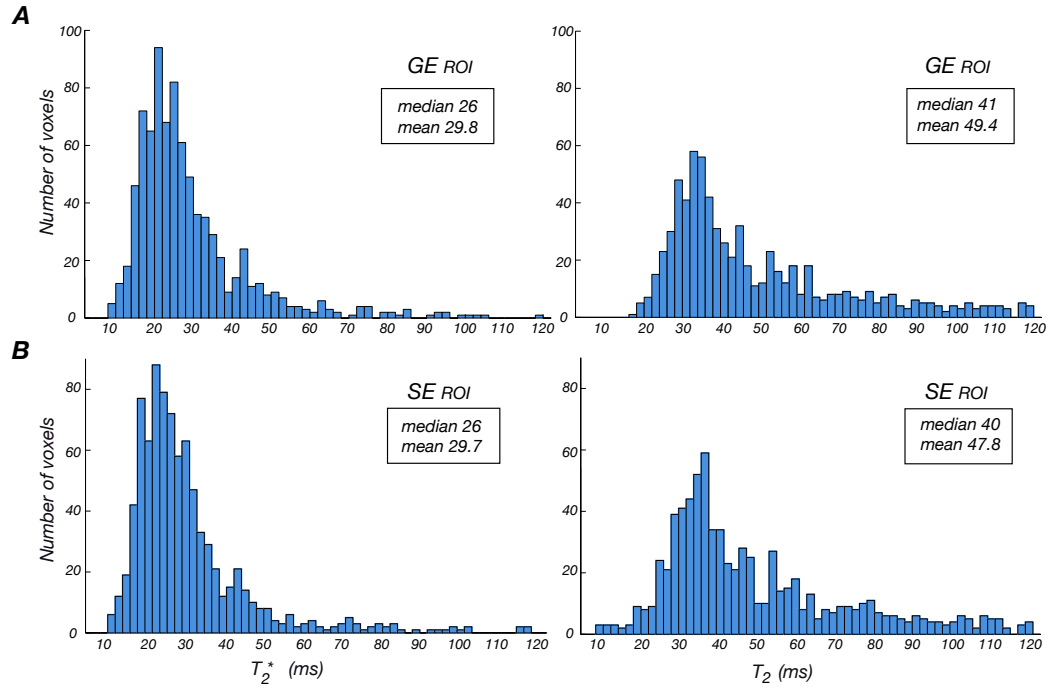
Figure 7.18: Histograms of $T_2^\star$ (left) and T_2 (right) values in active ROI of (1) GE data and (2) SE data for subject 2.

Figure 7.18 shows histograms of $T_2^\star$ (left) and T_2 values (right) of voxels within the GE active ROI (A) and SE active ROI (B). The $T_2^\star$ distribution has a median of 26 ms, which is in agreement with optimal $T_2^\star$ values of 25 ms found in other studies [4].

7.4 Discussion

These results demonstrate that spin echo functional maps in the visual and motor cortex can be acquired in reasonable scanning times at 7 T. The reduced BOLD sensitivity in SE acquisitions results in a reduced contrast to noise ratio of this sequence relative to the GE sequence. The SE contrast achieved in the visual cortex is significantly higher than in the motor cortex, suggesting that application of spin-echo based functional imaging sequences involving more complex stimuli or subtle activation patterns will present challenges in sensitivity. In Chapter 6 somatotopic mapping was studied where mean functional changes across the TFCE ROI for gradient echo were about 3%, compared

to the 4% for gradient echo data in this chapter for the motor cortex with a similar paradigm. Mapping of increased number of averages responses to somatosensory stimulation will require longer acquisition times than mapping the response to motor stimulation.

Some considerations have to be taking into account when using spin echo sequences. The RF power deposition of the refocusing pulse in the spin echo sequences (combined with SAR due to excitation and also fat suppression pulses) limits the slice coverage compared with the gradient echo sequence for a given TR. The choice of TE has to be considered, depending on the area of the brain under study. Echo times of approximately 50 ms have been proved to produce good contrast in spin echo functional studies of the visual cortex at 7 T [6, 8, 10, 12]. However, the results for the motor cortex suggest that the optimal echo time for mapping motor (or somatosensory) activation with SE sequences is about 35-40 ms. This shorter echo time, probably due to a lower T_2, imposes a limit on the field of view/resolution achievable if SENSE factors remain the same.

The travelling wave paradigm [35] used here is a differential paradigm, and as such is likely to suppress the effect of common activation. In particular activation that is common to all digits in the motor task includes the BOLD signal from large veins draining from tissue spanning multiple digit representations in the postcentral gyrus. This effect may diminish the difference in spatial localization between gradient echo and spin echo imaging. Event-related or traditional block design paradigms will delineate the spatial localization differences between SE and GE functional mapping more accurately. Future studies should be performed to compare GE and SE BOLD contrast for travelling wave and event related or block designs to determine the extent of this effect.

Diffusion weighting has been widely used to determine the relative sizes of intravascular and extravascular contribution to the SE and GE BOLD response [6, 8, 13, 36, 37]. Relative sizes of intravascular and extravascular contributions may depend on voxel size. High spatial resolution affords the potential

for increased contrast and better localization of neuronal activity due to the reduced partial voluming effects. High resolution studies will improve the delineation of intra and extra vascular components, hence evaluation of vascular suppression techniques with diffusion weighting at high resolutions may prove valuable in efforts to improve BOLD specificity.

Haemodynamic changes in response to increased neuronal activity occur first in the macrovasculature and then expand to the venous compartment, therefore blood flow changes occur earlier in the capillary and small venules near the activation site and gradually extend to larger draining veins. The temporal delay between capillary and venous haemodynamic responses is on the order of 100 to 2000 ms [38]. Lee et al [39] found using GE-BOLD that grey matter showed a 4 to 8 s delay relative to stimulus onset, whilst in visible vessels the delay was from 8 to 14 s. This larger delay is consistent with the longer time required for blood to reach the larger vessels. In a study of the temporal response of spin echo and gradient echo BOLD at 3T (resolution: $3.75 \times 3.75 \times 4$ mm^3) [40], it was found that SE contrast reaches its maximum amplitude significantly more rapidly than GE contrast, suggesting that the shorter time-to-peak is evidence of the improved localization of the SE signal to the focus of activity. Event-related methods to measure the haemodynamic lag at higher spatial resolution can provide new insight into the temporal ordering of neuronal pathways and activation patterns of complex stimuli using SE BOLD.

Bibliography

[1] S. Lai, A. L. Hopkins, E. M. Haacke, D. Li, B. A. Wasserman, P. Buckley, L. Friedman, H. Meltzer, P. Hedera, and R. Friedland. Identification of vascular structures as a major source of signal contrast in high resolution 2D and 3D functional activation imaging of the motor cortex at 1.5T: preliminary results. *Magn Reson Med*, **30**(3), 387–392, (1993).

[2] C. Segebarth, V. Belle, C. Delon, R. Massarelli, J. Decety, J. F. L. Bas, M. Dcorps, and A. L. Benabid. Functional MRI of the human brain: predominance of signals from extracerebral veins. *Neuroreport*, **5**(7), 813–816, (1994).

[3] R. Turner. How much cortex can a vein drain? Downstream dilution of activation-related cerebral blood oxygenation changes. *Neuroimage*, **16**(4), 1062–1067, (2002).

[4] E. Yacoub, A. Shmuel, J. Pfeuffer, P. F. V. D. Moortele, G. Adriany, K. Ugurbil, and X. Hu. Investigation of the initial dip in fMRI at 7 Tesla. *NMR Biomed*, **14**(7-8), 408–412, (2001).

[5] S. P. Lee, A. C. Silva, K. Ugurbil, and S. G. Kim. Diffusion-weighted spin-echo fMRI at 9.4 T: microvascular/tissue contribution to BOLD signal changes. *Magn Reson Med*, **42**(5), 919–928, (1999).

[6] T. Q. Duong, E. Yacoub, G. Adriany, X. Hu, K. Ugurbil, and S.-G. Kim. Microvascular BOLD contribution at 4 and 7 T in the human brain: gradient-echo and spin-echo fMRI with suppression of blood effects. *Magn Reson Med*, **49**(6), 1019–1027, (2003).

[7] J. L. Boxerman, L. M. Hamberg, B. R. Rosen, and R. M. Weisskoff. MR contrast due to intravascular magnetic susceptibility perturbations. *Magn Reson Med*, **34**(4), 555–566, (1995).

[8] E. Yacoub, T. Q. Duong, P.-F. V. D. Moortele, M. Lindquist, G. Adriany, S.-G. Kim, K. Ugurbil, and X. Hu. Spin-echo fMRI in humans using high spatial resolutions and high magnetic fields. *Magn Reson Med*, **49**(4), 655–664, (2003).

[9] P. W. Stroman, V. Krause, U. N. Frankenstein, K. L. Malisza, and B. Tomanek. Spin-echo versus gradient-echo fMRI with short echo times. *Magn Reson Imaging*, **19**(6), 827–831, (2001).

[10] E. Yacoub, P.-F. V. D. Moortele, A. Shmuel, and K. Ugurbil. Signal and noise characteristics of Hahn SE and GE BOLD fMRI at 7 T in humans. *Neuroimage*, **24**(3), 738–750, (2005).

[11] K. R. Thulborn, J. C. Waterton, P. M. Matthews, and G. K. Radda. Oxygenation dependence of the transverse relaxation time of water protons

in whole blood at high field. *Biochim Biophys Acta*, **714**(2), 265–270, (1982).

[12] T. Q. Duong, E. Yacoub, G. Adriany, X. Hu, K. Ugurbil, J. T. Vaughan, H. Merkle, and S.-G. Kim. High-resolution, spin-echo BOLD, and CBF fMRI at 4 and 7 T. *Magn Reson Med*, **48**(4), 589–593, (2002).

[13] C. R. Michelich, A. W. Song, and J. R. Macfall. Dependence of gradient-echo and spin-echo BOLD fMRI at 4 T on diffusion weighting. *NMR Biomed*, **19**(5), 566–572, (2006).

[14] J. Ren, I. Dimitrov, A. D. Sherry, and C. R. Malloy. Composition of adipose tissue and marrow fat in humans by 1H NMR at 7 Tesla. *J Lipid Res*, **49**(9), 2055–2062, (2008).

[15] E. Kaldoudi, S. C. Williams, G. J. Barker, and P. S. Tofts. A chemical shift selective inversion recovery sequence for fat-suppressed MRI: theory and experimental validation. *Magn Reson Imaging*, **11**(3), 341–355, (1993).

[16] O. Speck, J. Stadler, and M. Zaitsev. High resolution single-shot EPI at 7T. *MAGMA*, **21**(1-2), 73–86, (2008).

[17] J. M. Gomori, G. A. Holland, R. I. Grossman, W. B. Gefter, and R. E. Lenkinski. Fat suppression by section-select gradient reversal on spin-echo MR imaging. Work in progress. *Radiology*, **168**(2), 493–495, (1988).

[18] Z. Nagy and N. Weiskopf. Efficient fat suppression by slice-selection gradient reversal in twice-refocused diffusion encoding. *Magn Reson Med*, **60**(5), 1256–1260, (2008).

[19] P. A. Bottomley and W. A. Edelstein. Methods of eliminating effects of spurious free induction decay NMR signal caused by imperfect 180 degree RF pulses. U. S. Patent 4,484,138., (1984).

[20] J. Hennig, M. Weigel, and K. Scheffler. Multiecho sequences with variable refocusing flip angles: optimization of signal behavior using smooth transitions between pseudo steady states (TRAPS). *Magn Reson Med*, **49**(3), 527–535, (2003).

[21] V. M. Runge, M. L. Wood, D. M. Kaufman, and M. S. Silver. MR imaging section profile optimization: improved contrast and detection of lesions. *Radiology*, **167**(3), 831–834, (1988).

[22] J. R. MacFall, H. C. Charles, and R. Prost. Truncated sinc slice excitation for 31P spectroscopic imaging. *Magn Reson Imaging*, **8**(5), 619–624, (1990).

[23] M. Bernstein, K. F. King, and X. J. Zhou. *Handbook of MRI Pulse Sequences*. Elsevier Academic Press, (2004).

[24] P. L. Roux. French Patent 8610179, (1986).

[25] J. Pauly, P. L. Roux, D. Nishimura, and A. Macovski. Parameter relations for the Shinnar-Le Roux selective excitation pulse design algorithm [NMR imaging]. *IEEE Trans Med Imaging*, **10**(1), 53–65, (1991).

[26] M. Shinnar, L. Bolinger, and J. S. Leigh. The synthesis of soft pulses with a specified frequency response. *Magn Reson Med*, **12**(1), 88–92, (1989).

[27] M. Shinnar, L. Bolinger, and J. S. Leigh. The use of finite impulse response filters in pulse design. *Magn Reson Med*, **12**(1), 81–87, (1989).

[28] M. Shinnar, S. Eleff, H. Subramanian, and J. S. Leigh. The synthesis of pulse sequences yielding arbitrary magnetization vectors. *Magn Reson Med*, **12**(1), 74–80, (1989).

[29] M. Shinnar and J. S. Leigh. The application of spinors to pulse synthesis and analysis. *Magn Reson Med*, **12**(1), 93–98, (1989).

[30] B. A. Wandell. Computational neuroimaging of human visual cortex. *Annu Rev Neurosci*, **22**, 145–173, (1999).

[31] O. Nestares and D. J. Heeger. Robust multiresolution alignment of MRI brain volumes. *Magn Reson Med*, **43**(5), 705–715, (2000).

[32] B. Biswal, A. E. DeYoe, and J. S. Hyde. Reduction of physiological fluctuations in fMRI using digital filters. *Magn Reson Med*, **35**(1), 107–113, (1996).

[33] B. Biswal, A. G. Hudetz, F. Z. Yetkin, V. M. Haughton, and J. S. Hyde. Hypercapnia reversibly suppresses low-frequency fluctuations in the human motor cortex during rest using echo-planar MRI. *J Cereb Blood Flow Metab*, **17**(3), 301–308, (1997).

[34] S. M. Smith and T. E. Nichols. Threshold-free cluster enhancement: addressing problems of smoothing, threshold dependence and localisation in cluster inference. *Neuroimage*, **44**(1), 83–98, (2009).

[35] S. A. Engel, D. E. Rumelhart, B. A. Wandell, A. T. Lee, G. H. Glover, E. J. Chichilnisky, and M. N. Shadlen. fMRI of human visual cortex. *Nature*, **369**(6481), 525, (1994).

[36] J. L. Boxerman, P. A. Bandettini, K. K. Kwong, J. R. Baker, T. L. Davis, B. R. Rosen, and R. M. Weisskoff. The intravascular contribution to fMRI signal change: Monte Carlo modeling and diffusion-weighted studies in vivo. *Magn Reson Med*, **34**(1), 4–10, (1995).

[37] A. W. Song, E. C. Wong, S. G. Tan, and J. S. Hyde. Diffusion weighted fMRI at 1.5 T. *Magn Reson Med*, **35**(2), 155–158, (1996).

[38] P. A. Bandettini. Functional MRI. Ch: The temporal resolution of functional MRI. Springer, Berlin, 205-219, (2000).

[39] A. T. Lee, G. H. Glover, and C. H. Meyer. Discrimination of large venous vessels in time-course spiral blood-oxygen-level-dependent magnetic-resonance functional neuroimaging. *Magn Reson Med*, **33**(6), 745–754, (1995).

[40] J. Hulvershorn, L. Bloy, E. E. Gualtieri, J. S. Leigh, and M. A. Elliott. Spatial sensitivity and temporal response of spin echo and gradient echo bold contrast at 3 T using peak hemodynamic activation time. *Neuroimage*, **24**(1), 216–223, (2005).

Chapter 8

Conclusions

The work described in this thesis was directed towards developing and applying techniques at 7 T to produce anatomical images with high spatial resolution and functional images with high spatial specificity.

Chapter 4 presents a robust methodology for high resolution functional mapping over a restricted field of view (FOV) at 7 T using GE-EPI which involves outer volume suppression (OVS), parallel imaging, localised image-based shimming and acquisition of inversion recovery-EPI data. Image-based shimming[1] reduces residual geometric distortions between EPI and MPRAGE images to less than one voxel, allowing the accurate projection of activation maps onto cortically flattened surfaces and the inversion recovery-EPI images aid the classification of tissue type. In Chapter 4, imaging sequences for high resolution anatomical images are also developed and the detection of the stria of Gennari is also presented. TSE preceded by an inversion recovery (IR) segment provides a mixed T_1/T_2 contrast with very good CNR, but it suffers from long scanning times due to SAR limits. MPRAGE yields T_1-weighted images with good contrast and good slice coverage, 3D GE allows the acquisition of $T_2^\star$-weighted modulus and phase images with good contrast.

Chapter 5 presents an approach for combining high resolution functional data with structural scans in individuals. 3D GE and MPRAGE sequences were used to acquire structural images with 0.4 mm isotropic resolution; $T_2^\star$-

weighted imaging was found to show the best performance with good CNR and a short acquisition time. Using retinotopic mapping we demonstrate the correspondence of functionally defined V1 to striate cortex identified from anatomical MR images and provide evidence of banding within functionally defined V5.

The somatosensory cortex covers a much smaller cortical territory than the visual cortex. With the spatial resolution currently used in most neuroimaging experiments, the reliable localization and unequivocal definition of somatosensory areas has proven much more difficult than for visual areas. Chapter 6 presents a complete, fine-grained topographic map of the five digit representations in S1 at 1 mm resolution, a higher resolution than previously reported in this area. Using a travelling wave paradigm [2], the specificity of the GE-BOLD response was improved.

Spin echo based fMRI offers further gains in spatial accuracy by eliminating extra-vascular effects from large vessels [3], but this comes at the cost of reduced BOLD signal. An optimised SE-EPI acquisition, with improved suppression of fat signals and refocusing pulse profile to allow contiguous slice acquisition is presented in Chapter 7. The use of this sequence demonstrates robust SE-BOLD activation maps in the visual and motor cortex. The specificity of the GE-BOLD maps using a travelling wave paradigm to map the digits in the motor cortex is comparable to that of SE-BOLD maps, suggesting that the travelling wave paradigm suppresses the effect of BOLD signals that are more common to stimulation of multiple digits, which arise from large vessels.

8.1 Further developments

Achieving higher resolution or increased brain coverage in high-resolution fMRI studies requires the use of large matrix sizes and numbers of slices. This leads to long echo trains, potentially producing high sensitivity to distortion, and many RF excitations, which result in long TRs and high SAR particularly

for SE-EPI. The use of a 32-channel RF receiver coil will allow the use of higher parallel imaging acceleration factors to increase the spatial resolution of scanning protocols [4]. Multi-band excitation and SENSE-based reconstruction of signals from multiple slices will allow the reduction of the minimum achievable TR to increase coverage of high resolution data in a given time[5].

The spatial specificity of functional studies can be improved by using SE based fMRI, fMRI-adaptation paradigms [6] for selective mapping of stimulus properties, and travelling wave paradigms [2], which attenuate signal changes in draining veins, for topographic mapping.

These developments will allow the resolution of fMRI studies to be increased to the submillimetre level for the investigation of layer specific activation and columnar organisation.

High resolution fMRI will allow the characterization of responses within specific cortical regions. The quantitative fMRI measurements of specific cortical regions will allow detailed analyses of different pathologies and tracking of cortical reorganization following cortical injury (plasticity).

The benefits of high resolution fMRI can also be extended to larger FOVs and whole brain scanning, encompassing regions of significant field inhomogeneity and short T_2. Extending coverage to inferior brain areas requires that the effects of increased B_1- and B_0-inhomogeneity in these regions be addressed. Multiple element transmit (Multi-Tx) approaches, which have the ability to control SAR and B_1-homogeneity [7], can be used to achieve uniform RF excitation over the head or to produce enhanced sensitivity in targeted regions.

Bibliography

[1] M. Poole and R. Bowtell. Volume parcellation for improved dynamic shimming. *MAGMA*, **21**(1-2), 31–40, (2008).

[2] S. A. Engel, D. E. Rumelhart, B. A. Wandell, A. T. Lee, G. H. Glover, E. J. Chichilnisky, and M. N. Shadlen. fMRI of human visual cortex. *Nature*, **369**(6481), 525, (1994).

[3] E. Yacoub, T. Q. Duong, P.-F. V. D. Moortele, M. Lindquist, G. Adriany, S.-G. Kim, K. Ugurbil, and X. Hu. Spin-echo fMRI in humans using high spatial resolutions and high magnetic fields. *Magn Reson Med*, **49**(4), 655–664, (2003).

[4] S. Moeller, P.-F. V. de Moortele, U. Goerke, G. Adriany, and K. Ugurbil. Application of parallel imaging to fMRI at 7 Tesla utilizing a high 1D reduction factor. *Magn Reson Med*, **56**(1), 118–129, (2006).

[5] S. Moeller, E. Auerbach, P.-F. V. de Moortele, G. Adriany, and K. Ugurbil. fMRI with 16 Fold Reductin Using Multiband Multislice Sampling. *Proceedings of the 16th Meeting ISMRM. Toronto*, (2008).

[6] K. Grill-Spector and R. Malach. fMR-adaptation: a tool for studying the functional properties of human cortical neurons. *Acta Psychol (Amst)*, **107**(1-3), 293–321, (2001).

[7] U. Katscher and P. Boernert. Parallel RF transmission in MRI. *NMR Biomed*, **19**(3), 393–400, (2006).